LNGS - s.s. 17 bis km 18,910 67010 ASSERGI (AQ) ITALY
tel.+39 0862 4371 fax +39 0862 437559
email: document@lngs.infn.it
http://www.lngs.infn.it

Cover Image: CUORE Experiment
© Yura Suvorov - LNGS-INFN

ISBN-978-88-940122-8-6

LNGS/EXP-01/15
July 2015

INFN

Annual Report 2014

Laboratori Nazionali del Gran Sasso

ANNUAL REPORT 2014

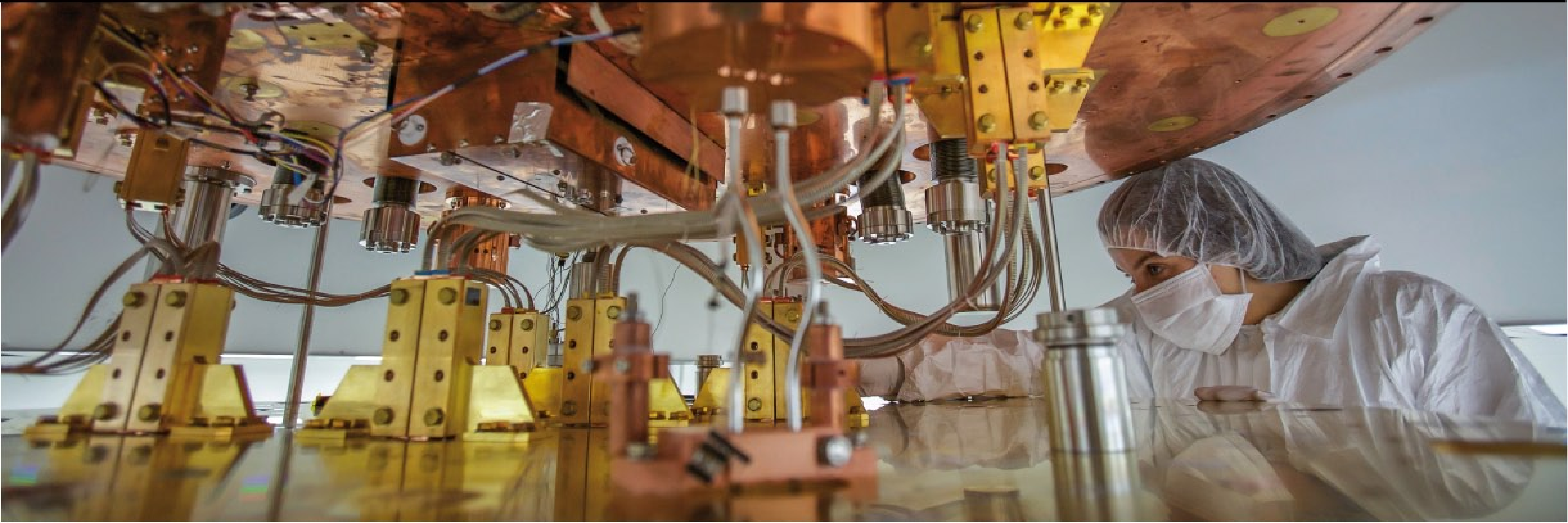

Codice ISBN
978-88-940122-8-6

Annual Report 2014

LNGS Director	Prof. Stefano Ragazzi
Editor	Dr. Roberta Antolini
Technical Assistants	Dr. Alessia Giampaoli Mr. Marco Galeota

Contents

THE BOREXINO EXPERIMENT

Borexino collaboration

M. Agostini[h], K. Altenmuller[h], S. Appel[h], G. Bellini[a], J. Benziger[c], N. Berton[e], D. Bick[v],
G. Bonfini[b], D. Bravo[n], B. Caccianiga[a], L. Cadonati[t], F.P. Calaprice[d], A. Caminata[i], P. Cavalcante[b],
A. Chavarria[d], A. Chepurnov[z], M. Cribier[e], D. D'Angelo[h], S. Davini[x], A. Derbin[u], L. di Noto[i],
M. Durero[e], A. Empl[x], A. Etenko[s], S. Farinon[i], V. Fischer[e], K. Fomenko[m], D. Franco[a], F. Gabriele[b],
J. Gaffiot[e], C. Galbiati[d](*), S. Gazzana[b], C. Ghiano[b], M.G. Giammarchi[a], M. Goeger-Neff[h],
A. Goretti[d], M. Gromov[z] C. Hagner[v], T. Houdy[e], E. Hungerford[x], A. Ianni,[b], A.M. Ianni[d],
N. Jonqueres[f], M. Kaiser[v], V. Kobychev[k], D. Korablev[m], G. Korga[x], D. Kryn[o], T. Lanchenmaier[l],
T. Lassere[e], M. Laubenstein[b], B. Lehnert[y], T. Lewke[h], J. Link[n], E. Litvinovich[s], F. Lombardi[b],
P. Lombardi[a], L. Ludhova[a], G. Lukyanchenko[s], I. Machulin[s], S. Manecki[m], W. Maneschg[j],
S. Marcocci[i], J. Maricic[p], Q. Meindl[h], G. Mention[e], E. Meroni[a], M. Meyer[v], L. Miramonti[a],
M. Misiaszek[q], M. Montuschi[b], P. Mosteiro[d], V. Muratova[u], R. Musenich[i], B. Neumair[h],
L. Oberauer[h], M. Obolensky[o], F. Ortica[g], K. Otis[t], M. Pallavicini[i], L. Papp[b], L. Perasso[a], A. Pocar[d],
G. Ranucci[a](*), A. Razeto[b], A. Re[a], A. Romani[g], N. Rossi[b], R. Saldanha[d], C. Salvo[i], S. Schönert[j],
L. Scola[e], H. Simgen[j], M. Skorokhvatov[s], O. Smirnov[m], A. Sotnikov[m], S. Sukhotin[s], Y. Suvorov[s],
R. Tartaglia,[b], G. Testera[i], C. Veyssiere[e], D. Vignaud[o], M. Vivier[e], B. Vogelaar[n], F. von Feilitzsch[h],
H. Wang[w], J. Winter[h], M. Wojcik[q], A. Wright[d], M. Wurm[h], O. Zaimidoroga[m], S. Zavatarelli[i],
K. Zuber[y], G. Zuzel[j]

[a]Dip. di Fisica dell'Università and Infn Milano - Italy
[b]Laboratori Nazionali del Gras Sasso, Assergi (Aq) - Italy
[c]Dept. of Chemical Engineering, Princeton University - NJ USA
[d]Dept. of Physics, Princeton University - NJ USA
[e]CEA, Centre de Saclay IRFU Gif-sur-Yvette - France
[f]CEA, Centre de Saclay DEN/DM2S/SEMT Gif-sur-Yvette - France
[g]Dip. di Chimica dell'Università and Infn Perugia - Italy
[h]Dept. of Physics, Technische Universität München - Germany
[k]Kiev Institute for Nuclear Research, Kiev, Ukraine
[i]Dip. di Fisica dell'Università and Infn Genova - Italy
[j]Max Planck Inst. für Kernphysik, Heidelberg - Germany
[l]Kepler Center for Astroparticle Physics . Universität Tübingen - Germany
[m]Joint Institute for Nuclear Research Dubna - Russia
[n]Dept. of Physics, Virginia Polytechnic Institute - VA USA
[o]Laboratoire de AstroParticule et Cosmologie, Paris - France
[p]Dept. of Physics and Astronimy, University of Hawaii, Honolulu - HI USA
[q]Institute of Physics, Jagellonian University, Kracow - Poland
[s]RRC Kurchatov Institute, Moscow - Russia
[t]Dept. of Physics, University of Massachusetts, Amherst - MA USA
[u]St. Petersburg Nuclear Physics Institute, Gatchina, Russia
[v]Institut für Experimentalphysik, Universität Hamburg - Germany
[x]Dept. of Physics, University of Houston, Houston - TX USA
[y]Dept. of Physics, Universität Dresden - Germany
[w]Dept. of Physics and Astronomy, University of California, Los Angeles - CA USA
[z]Institute of Nuclear Physics, Lomonosov State University, Moscow, Russia

(*) co-spokespersons

Abstract

The main goal of the Borexino experiment is the study of solar neutrino physics and other rare phenomena. The detector, located in the Hall C of LNGS, became fully operational in 2007 and made possible the first real time measurement of ^{7}Be solar neutrinos, the first experimental evidence of the matter/vacuum transition in solar neutrino oscillations, the observation of geo-neutrinos and the first evidence for solar neutrinos from the pep reaction. In the second phase of the experiment, the first direct measurement of the pp main reaction in the Sun was made. We summarize here the status of the project and outline the perspectives for future measurements.

1 Introduction

Solar neutrino physics is a topic that originally started from the perspective of studying the basic working principle of the core of the Sun, nuclear fusion reactions producing energy and emitting neutrinos. The pioneering Davis experiment [1] was the first one to measure (with radiochemical methods) solar neutrinos as predicted by theoretical models and to detect a significant deficit with respect to the predicted flux. Additional experiments were performed starting from the end of the 80's, both in radiochemical mode [2, 3, 4] and in real-time mode [5, 6] while the most widely accepted model of the Sun evolved into what is now known as the Standard Solar Model [7] [8] [9].

As a general statement, real-time experiments have been performed with large water Cerenkov detectors with an energy threshold of 4-5 MeV, mainly due to natural radioactivity and detector contamination. This implies that only $\sim$0.001% of the total neutrino flux had been observed in real time prior to 2007.

The issue of directly measuring low energy solar neutrinos has been the subject of an intensive research study carried out in the frame of the Borexino development and starting from the very beginning of the 90's. Borexino [10] was designed to study sub-MeV solar neutrinos having as the first experimental goal the detection of the 0.862 MeV ^{7}Be solar neutrino line through the neutrino-electron elastic scattering reaction $\nu e \rightarrow \nu e$. The maximum energy of the recoiling electron is 664 keV and the experimental design threshold is of 50 keV while the analysis threshold is 200 keV. The detection reaction is observed in a large mass (100 tons fiducial volume) of well shielded liquid scintillator viewed by photomultipliers.

The prediction of the ^{7}Be solar flux depends both on the Standard Solar Model and the value of the parameters of the LMA solution of neutrino oscillations [11] [12] [13]. The Borexino experimental program makes it possible to directly test this prediction as well as opening up the unexplored territory of real time sub-MeV solar neutrino spectroscopy.

The main problem of an experiment with such a low energy threshold is the background coming from natural sources such as cosmic rays or radioactivity. This problem has been addressed by means of an intense R&D program focused on low radioactivity materials and purification techniques. This effort was complemented by a comparably thorough research in the field of detection and measurement of very low radioactivity levels [14]. As a part of this program, a prototype of the Borexino detector, called Counting Test Facility [15], was built and operated at LNGS to demonstrate very low radioactive contamination levels (10^{-16} g/g of U-238 equivalent or less [16]) in a ton scale scintillator detector. The CTF was initially used as a measurement facility for quality tests of the Borexino scintillator and is now being exploited by the DarkSide experiment.

The Borexino research and development culminated into the construction and commissioning of the full-scale detector during several years and its final filling with scintillator in 2007.

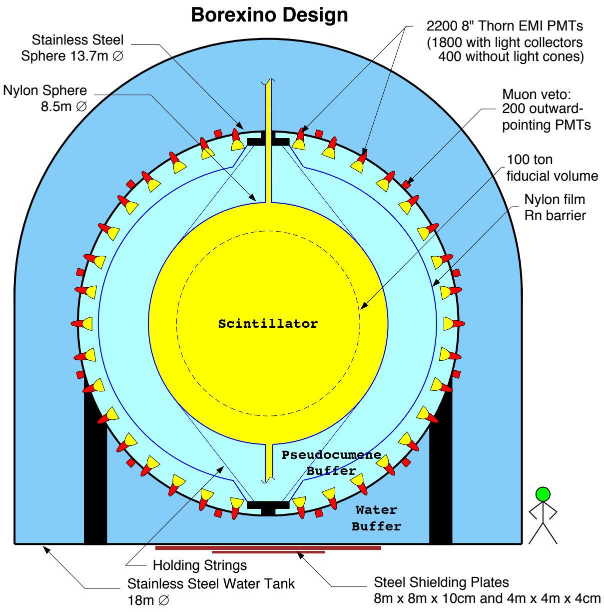

Figure 1: Schematic view of the Borexino detector.

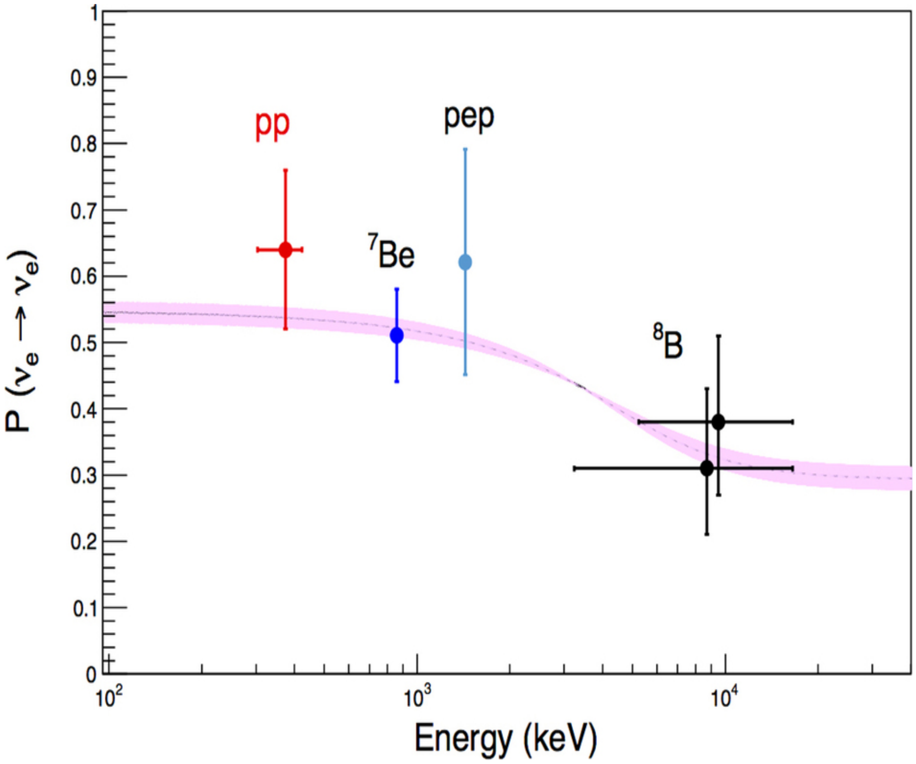

Figure 2: Survival probability of electron-neutrinos produced by the different nuclear reactions in the Sun. All the numbers are from Borexino. The violet band corresponds to the ±1σ prediction of the MSW-LMA solution. [35].

2 The Borexino Detector

Borexino [17] is an unsegmented scintillation detector featuring 300 tonnes of well shielded liquid ultrapure scintillator viewed by 2200 photomultipliers (fig. 1). The detector core is a transparent spherical vessel (Nylon Sphere, 100μm thick), 8.5 m of diameter, filled with 300 tonnes of liquid scintillator and surrounded by 1000 tonnes of high-purity buffer liquid. The scintillator mixture is pseudocumene (PC) and PPO (1.5 g/l) as a fluor, while the buffer liquid consists of PC alone (with the addition of DMP as light quencher). The photomultipliers are supported by a Stainless Steel Sphere, which also separates the inner part of the detector from the external shielding, provided by 2400 tonnes of pure water (water buffer). An additional containment vessel (Nylon film Radon barrier) is interposed between the Scintillator Nylon Sphere and the photomultipliers, with the goal of reducing Radon diffusion towards the internal part of the detector.

The outer water shield is instrumented with 200 outward-pointing photomultipliers serving as a veto for penetrating muons, the only significant remaining cosmic ray background at the Gran Sasso depth (about 3700 meters of water equivalent). The innermost 2200 photomultipliers are divided into a set of 1800 photomultipliers equipped with light cones (so that they see light only from the Nylon Sphere region) and a set of 400 PMT's without light cones, sensitive to light originated in the whole Stainless Steel Sphere volume. This design greatly increases the capability of the system to identify muons crossing the PC buffer (and not the scintillator).

The Borexino design is based on the concept of a graded shield of progressively lower intrinsic radioactivity as one approaches the sensitive volume of the detector; this culminates in the use of 200 tonnes of the low background scintillator to shield the 100 tonnes innermost Fiducial Volume. In these conditions, the ultimate background will be dominated by the intrinsic contamination of the scintillator, while all backgrounds from the construction materials and external shieldings will be negligible.

Borexino also features several external systems conceived to purify the experimental fluids (water, nitrogen and scintillator) used by the experiment (see e.g. [18]).

+

3 Status of the project

The Borexino filling started in January 2007, with scintillator displacing the purified water from inside the detector volumes. The detector was completed and the data taking started in May 2007. The radiopurity of the inner detector has been found in general to be better than the specifications. In particular, among the best radioactivity levels found during the data taking (see, however, [34] for a more complete summary):

1. C-14 contamination of the scintillator was found to be at $\sim 2 \times 10^{-18}$ ^{14}C/^{12}C.
2. The general level of Th-232 contamination - as measured by means of $^{212}Bi/^{212}Po$ delayed coincidences was found to be at $\sim 4 \times 10^{-18}$ g/g.
3. The U-238 family contamination - assessed by studying the $^{214}Bi/^{214}Po$ delayed coincidence rate, was measured to be $\sim 5 \times 10^{-18}$ g/g.
4. Kr-85 contamination, of considerable importance due to the spectral shape similar to the one of the signal searched for was found (by means of the ^{85m}Rb decay and the related β/γ tagging) to be at the level of $\sim$30 counts/day in the 100 tons fiducial volume.

This level of radiopurity, together with the use of muon-related cuts and α/β discrimination techniques has made possible the first real-time detection of the Be-7 solar signal [19] [20] [24], the first observation of the B-8 spectrum with a 3 MeV threshold [21], the first observation of the solar pep nuclear reaction [27] and the observation of geoneutrinos [22] [30].

The direct observation of several solar components by Borexino has allowed to unambiguously detect the matter-vacuum transition of the electron neutrino survival curve as a function of energy (fig. 2).

Several other results were produced over the years, such as the measurement of the Day/Night asymmetry of the Be-7 signal [25], the study of anti-neutrino production in the Sun [23], the study of muons and muon-induced reactions [26] [31], the search rare fenomena such as solar axions [28] and mixing with sterile neutrinos [32]. Studies were also performed of the propagation of neutrinos from CERN to Gran Sasso (CNGS) [29] and high precision measurements of Po isotopes lifetime [33]. All the solar neutrino results before 2013 (the so-called "Phase I") are summarized in [34].

Between 2009 and 2010 an extensive purification campaign (water extraction and Rn stripping) has marked the beginning of the Borexino Phase-II. The new improved radiopurity (less Kr and less Bi) has made it possible to investigate the lowest energy part of the spectrum, to the goal of searching for the more fundamental reaction powering the Sun: the pp fusion which marks the beginning of the whole pp-chain, producing the vast majority of the solar energy.

The analysis for the pp reaction has involved the understanding of the spectrum at low energies, where ^{14}C and its pile-up effects are important and the α/β discrimination is less effective (fig. 3). The relevant analysis has involved a careful modeling of these effects and of all the other backgrounds, like Pb-214, Kr-85 and the (solar) Be-7. The final flux result, published in [35] is $(6.6 \pm 0.7) \times 10^{10}\ cm^{-2}s^{-1}$, in agreement with the solar models.

4 Future perspectives

Additional physics topics are under study or considered for future investigation, depending on the background conditions and on the refinement of the ongoing analysis:

1. Measuring the CNO solar neutrinos.
2. Watch for neutrino bursts from Supernovae events: Borexino is part of the international SNEWS program for early detection of Supernovae with neutrinos.
3. Short baseline oscillation tests with ^{144}Ce-^{144}Pr antineutrino (or Cr-51 neutrino) sources: SOX [36]. This topic is of particular interest in view of the present controversial experimental scenario, encompassing the recently highlighted reactor and Gallium anomalies as well as the long standing LSND puzzle confirmed by the new Miniboone antineutrino data. The emerging picture of an oscillation paradigm comprising 3 active plus 2 sterile neutrinos, the latter with masses at eV scale, could verified with a source test in Borexino for a significant portion of the parameter space, through the search of the oscillation pattern that at the considered L/E values should develop clearly throughout the detector. Moreover, SOX will provide the opportunity of a measurement of the Weinberg angle at MeV energies as well as an improved limit on the neutrino magnetic moment. This test is foreseen for fall 2016; studies about transportation logistic and authorizations are in progress.

5 List of articles published in year 2014

1. G. Bellini et al., *Final results of Borexino Phase-I on low energy solar neutrino spectroscopy.* Physical Review D 89 (2014) 112007.
2. G. Bellini et al., *Neutrinos from the primary proton-proton fusion process in the Sun.* Nature, http://doi:10.1038/nature13702.

References

[1] R. Davis, Nobel Prize Lecture 2002.

[2] W. Hampel et al., Phys. Lett. B 447 (1999) 127.

[3] J.N. Abdurashitov et al., Phys. Rev. Lett. 83 (1999) 4686.

[4] M. Altmann et al., Phys. Lett. B 616 (2005) 174.

[5] S. Fukuda et al., Phys. Rev. Lett. 86 (2001) 5651; Phys. Lett. B 539 (2002) 179.

[6] Q.R. Ahmad et al., Phys. Rev. Lett. 87 (2001) 071301.

[7] J.N. Bahcall and M.H. Pinsonneault, Phys. Rev. Lett. 92 (2004) 121301.

[8] A.M. Serenelli et al., Astr. J. Lett., 705 (2009) L123.

[9] A.M. Serenelli et al., Astr. J. 743 (2011) 24.

[10] G. Alimonti et al., Astroparticle Physics 16 (2002) 205.

[11] J.N. Bahcall et al., JHEP 0408 (2004) 016.

[12] G.L. Fogli et al., Progr. Nucl. Phys., 57 (2006) 742.

[13] J. Beringer et al. (Particle Data Group), The Review of Particle Physics, Phys. Rev. D 86 (2012) 010001.

[14] C. Arpesella et al., Astroparticle Physics 18 (2002) 1.

[15] G. Alimonti et al., Nucl. Instr. & Methods A406 (1998) 411.

[16] G. Alimonti et al., Astroparticle Physics 8 (1998) 141.

[17] G. Alimonti et al., Nucl. Instr. & Methods, A600 (2009) 568.

[18] G. Alimonti et al., Nucl. Instr. & Methods, A609 (2009) 58.

[19] C. Arpesella et al., Phys. Lett. B 658 (2008) 101.

[20] C. Arpesella et al., Phys. Rev. Lett. 101 (2008) 091302.

[21] G. Bellini et al., Phys. Rev. D 82 (2010) 033006.

[22] G. Bellini et al., Phys. Lett. B 687 (2010) 299.

[23] G. Bellini et al., Phys. Lett. B, 696 (2011) 191.

[24] G. Bellini et al., Phys. Rev. Lett. 107 (2011) 141302.

[25] G. Bellini et al., Phys. Lett. B 707 (2012) 22.

[26] G. Bellini et al., Journal of Instrumentation, doi:10.1088/1748-0221/6/05/P05005.

[27] G. Bellini et al., Phys. Rev. Lett. 108 (2012) 051302.

[28] G. Bellini et al., Phys. Rev. D 85 (2012) 092003.

[29] P. Alvarez-Sanchez et al., Phys. Lett. B 716 (2012) 401.

[30] G. Bellini et al., Phys. Lett. B 722 (2013) 295.

[31] G. Bellini et al., Journal of Cosmology and Astroparticle Physics, JCAP08 (2013) 049.

[32] G. Bellini et al., Phys. Rev. D 88 (2013) 072010.

[33] G. Bellini et al., Eur. Phys. J. A (2013) 49.

[34] G. Bellini et al., Phys. Rev. D 89 (2014) 112007.

[35] G. Bellini et al., Nature http://doi:10.1038/nature13702.

[36] G. Bellini et al., Journal of High Energy Physics 2013, 2013:38 http://doi:10.1007/JHEP08(2013)038

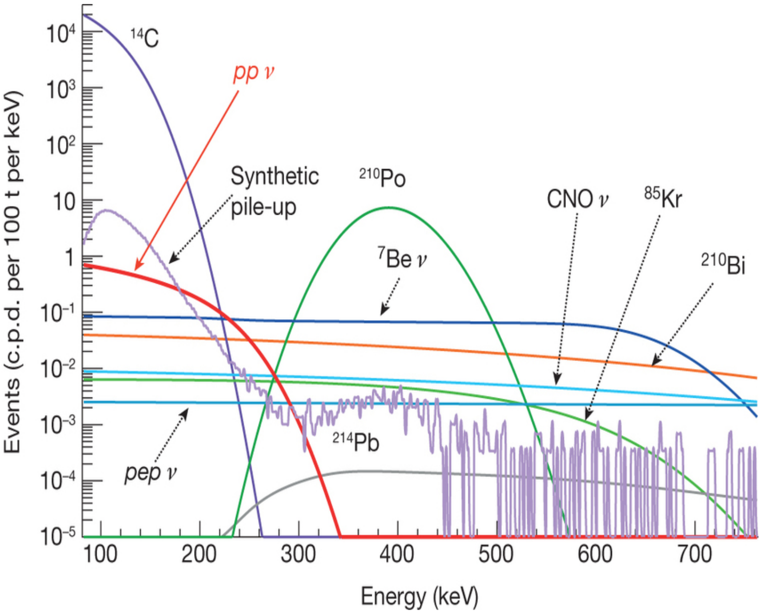

Figure 3: Energy spectral shape of the pp neutrino signal (thick red line), and the other solar neutrino components (^{7}Be, pep and CNO), and of the relevant backgrounds (^{14}C, intrinsic to the organic liquid scintillator; ^{210}Bi; ^{210}Po; ^{85}Kr; and ^{214}Pb) [35].

COBRA Annual Report 2014

K. Zuber[a,*], D. Gehre[a], M. Fritts[a], S. Zatschler[a], K. Rohatsch[a], C. Gößling[b], K. Kröninger[b], R. Klingenberg[b], T. Neddermann[b], S. Rajek[b], J. Tebrügge[b], T. Quante[b], R. Theinert[b], R. Temminghoff[b], C. Nitsch[b], C. Hagner[c], J. Ebert[c], B. Wonsak[c], N. Heidrich[c], J. Timm[c], C. Oldorf[c], H. Rebber[c], T. Michel[d], G. Anton[d], T. Gleixner[d], I. Stekl[e], J. Jose[e], M. Junker[f], J. Suhonen[g], O. Civitarese[h], F. Simkovic[i], O. Schulz[j]

[a] *Technische Universität Dresden* – Germany, [b] *Technische Universität Dortmund* – Germany, [c] *Universität Hamburg* – Germany, [d] *Universität Erlangen–Nürnberg* – Germany, [e] *Technical University of Prague* – Czech Republic, [f] *Laboratori Nazionali del Gran Sasso* – Italy, [g] *University of Jyvaskyla* – Finnland, [h] *University of La Plata* – Argentina, [i] *University of Bratislava, Slovakia* – Slovakia, [j] *MPI Munich* – Germany
(* Spokesperson)

Abstract

The aim of the COBRA experiment (**C**admium Zinc Telluride **0**-Neutrino Double-**B**eta **R**esearch **A**pparatus) is to prove the existence of neutrinoless double beta decay ($0\nu\beta\beta$-decay) and to measure its half-life. The COBRA demonstrator at LNGS is used to investigate the experimental issues of operating CZT detectors in low background mode while additional studies are proceeding in surface laboratories. The experiment consists of 64 monolithic, calorimetric detectors in a coplanar grid (CPG) design. These detectors are $1{\times}1{\times}1\,\mathrm{cm}^3$ in size and are operated in a $4{\times}4{\times}4$ detector array. As a semiconductor material, Cadmium-Zinc-Telluride (CdZnTe or simply CZT) offers the low radioactivity levels and good energy resolution required for the search for $0\nu\beta\beta$-decay. Furthermore, CZT contains naturally several double beta decay candidates. The most promising is ^{116}Cd with a Q-value of 2.8 MeV, which lies above the highest prominent γ-line occurring from natural radioactivity.

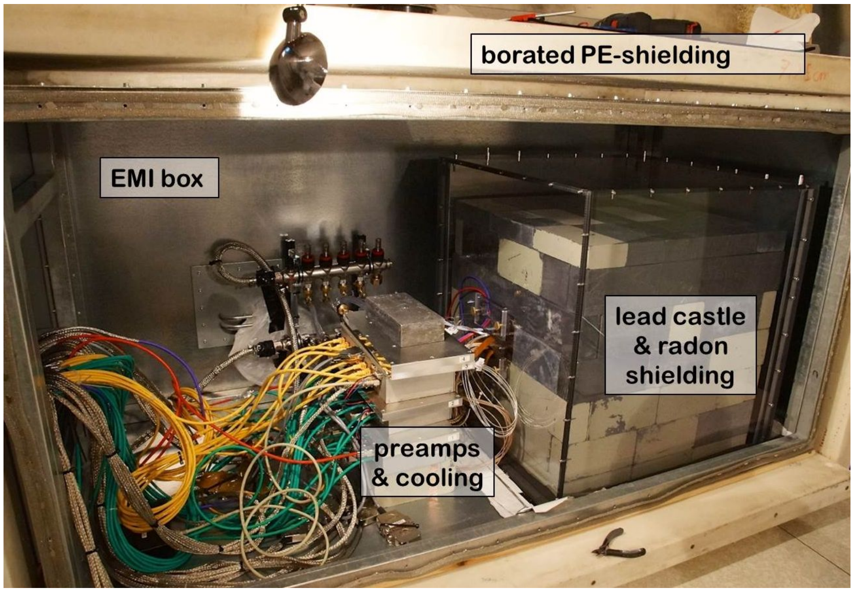

Figure 1: Overview of the experimental setup of the COBRA demonstrator. The different shielding layers can bee seen. The detectors are housed within a copper nest inside the lead castle which can be seen to the right. On the left side the first part of the electronics readout chain can be seen.

1 Status of the COBRA Experiment

The work of the COBRA collaboration in 2014 consisted of three main topics:
The first issue was the operation of the demonstrator setup at LNGS. This setup was taking high quality low background physics data very stable, see section 2.
The second part was the analysis of the data obtained with the demonstrator. This work will be intensified, so that a paper on physics results will be published soon, see section 3.
The third part (see section 4) was the work on the large scale setup to measure the neutrinoless double beta decay. The plan is to build one basic detector module of the proposed large scale experiment. Funding for this has been granted in 2014 by the German Research Foundation (Deutsche Forschungsgemeinschaft DFG), so that first measurements with the required hardware were already accomplished.

2 The COBRA demonstrator setup

In 2014 only minor improvements were done at the COBRA demonstrator, see section 2.1, as the setup was completed in 2013. It has been taking high quality low background physics data. Figure 1 shows a total view of the whole experimental setup of the demonstrator. It consists of several shielding layers. The outermost layer is 7 cm borated polyethylene shielding against neutrons, after that follows a shielding against electromagnetic interferences made of welded metal plates. Inside this volume the inner part of the shielding as well as the first part of the readout electronics is placed. The inner shielding consists of standard lead, ultra low activity lead and copper surrounding the detectors itself.
The demonstrator has been taking data very stable resulting in an increased collected exposure, which is shown in Figure 2. Furthermore, the energy resolution of the demonstrator could be improved with continuous flushing of the inner copper nest with dry nitrogen to reduce the humidity in the inner copper nest (see Figure 1) and the use of a recently installed water-cooling system for the COBRA custom-made preamplifier boxes. The average energy resolution (FWHM) at the Q-value of ^{116}Cd ($Q_{\beta\beta} = 2813.5\,\text{keV}$) as the main isotope of interest is about 1.3%. In 2014 the temperature of the inner setup was constantly decreased while calibration measurements were taken to monitor the effect on the energy resolution of the detectors and the signal quality in general.

2.1 Activities at the LNGS – power supply by UPS units

In 2014 only one working week has been accomplished at the LNGS. There was no need for more, as the COBRA demonstrator has been completed in 2013 and is taking data very stable since then.

In autumn of 2013 several Uninterruptible Power Supply (UPS) units were installed to guarantee a stable power supply of the experimental setup and the data acquisition (DAQ) system. These can power the different parts of the experiment for approximately 20 minutes if a power shortage occurs. The UPS units were supplied by the normal main power lines. Unfortunately, the circuit breakers cut off the power supply to the UPS units several times in the following weeks due to infrequent too high residual currents. As a result the whole experimental setup was without power, turning the benefits of the UPS units into a disadvantage.

A solution to this was the installation of new power lines without circuit breakers directly to the UPS units. This was kindly granted by the LNGS in January 2014. These power lines start at the fuse box next to COBRA's building. One power line goes to the building on the ground floor to the experimental setup, the other line goes to the upper building where the DAQ computer is working. Both new lines have a special connector, in a way that they cannot be used for other purposes by mistake.

By this the advantages of the UPS units could be fully used. The whole experiment did not suffer from power shortages since then and is operating stable and reliable. No power shortages affected the experiment after the power line upgrades although the UPS system had to step in for several times. Therefore, COBRA can report an up-time of 100% since January 2014.

3 Results of the low background measurement

3.1 Data-taking at the LNGS

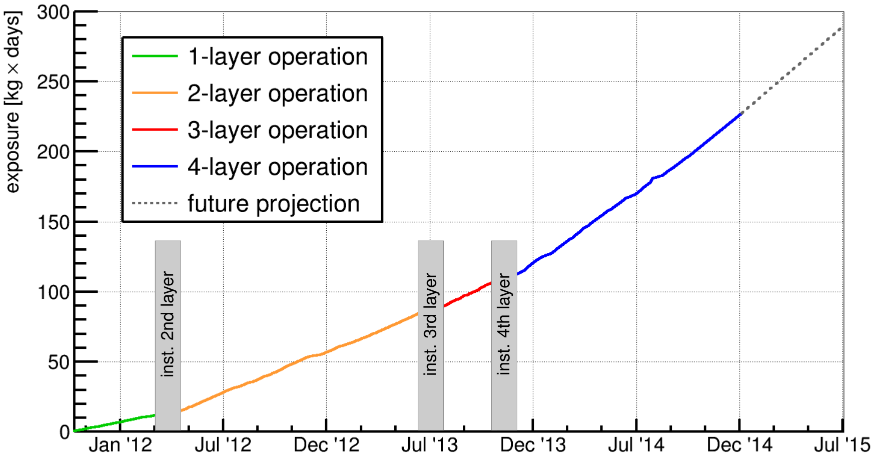

Figure 2: Total exposure of evaluated low-background physics data of the COBRA demonstrator over experimental lifetime.

With the installation of the third and fourth detector layer in late 2013, it became necessary to develop new suitable calibration tools to handle a large number of single detector units with different behavior. The new calibration tools can be scaled very easily with respect to a planned large scale array consisting of several thousand detector units and feature a high accuracy and reliability.

After an extensive testing phase it was decided to perform a complete re-evaluation and re-calibration of all physics data acquired since the commissioning of the demonstrator setup in Sept.'11. This re-evaluation process was finished in summer 2014 leading to an exposure of roughly 110 kg×days incorporating the 3-layer operation period.

During this 3-layer period the third detector layer could not be operated at the nominal high voltage as determined in pre-characterization measurements of each crystal at the TU Dresden. To reduce the amount of potentially radioactive material a new high voltage design using the same HV cable as used for the GERDA experiment was developed for layer three and four. Due to an imperfect fitting connection

between them and the existing HV infrastructure it was necessary to limit the applied HV to -1 kV for layer three to avoid the sudden appearance of sparks. The initial problems with the redesigned high voltage connection could be fixed during the installation of the fourth detector layer in Nov.'13. As a consequence of the HV problems, the accumulated exposure of layer three in the 3-layer operation period is removed from the ongoing analysis of low background physics data. Nevertheless, the exposure loss of 10.8 kg×days is comparable small corresponding to only 5.5% of the currently evaluated total exposure of 195 kg×days.
Furthermore, a run selection was performed to identify physic runs with unstable or obvious bad performance on rather short time scales, which is typical for electromagnetic interference phenomena or problems with the continuous dry nitrogen flushing. Together with the reduced exposure for layer three this leads to about 180 kg×days of exposure suitable for high-quality physics analysis. Another data set obtained between Oct.'14 and Feb.'15 of roughly 40 kg×days is in the final evaluation process and will be available for analysis purposes soon. Currently, a paper on calculating new half-life limits for the isotopes under study is in preparation based on more than 0.5 kg×years evaluated exposure. In summary Figure 2 illustrates the amount of accumulated data until the end of 2014 and the prediction until mid 2015. Assuming an average exposure rate of 2.6 kg×days exposure per layer and month, COBRA will reach very likely an exposure of about 1 kg×year by the end of 2015.

3.2 Low-background physics spectra

The following spectra are based on 180 kg×days exposure of the complete 4-layer operation and have been acquired with full pulse shape sampling. This allows for a complex offline pulse shape analysis (PSA) with the possibility to veto background events in the final data analysis. Furthermore, the co-planar grid (CPG) approach enables the precise determination of the depth of the interaction in-between the electrodes (see [1]), which can be used to reject near-surface events. Furthermore, this allows for the identification of prominent background features such as highlighted in Figure 3 in a two-dimensional plot of reconstructed interaction depth versus deposited energy.

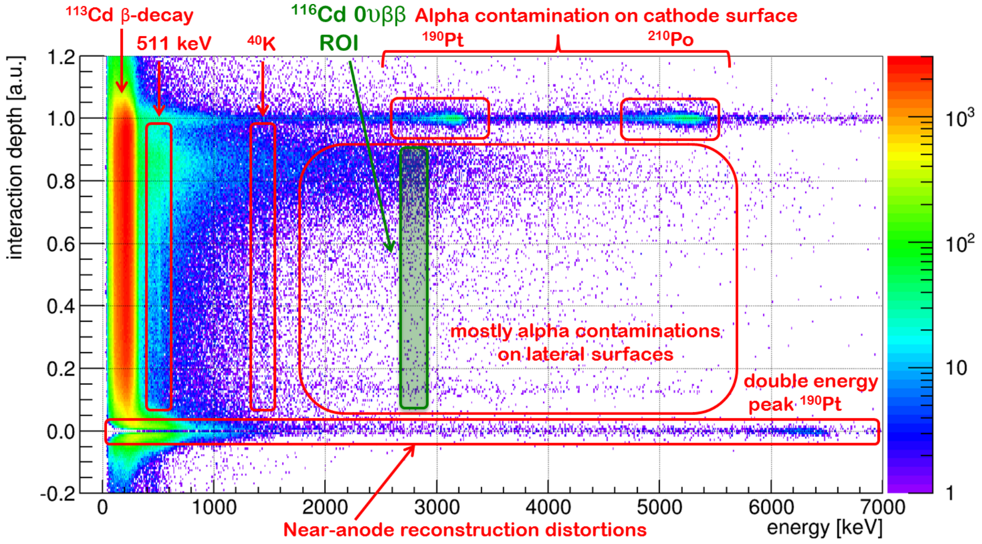

Figure 3: Identified background features using the interaction depth reconstruction of the CPG anode approach. Highlighted are prominent γ-lines visible as straight lines in the two-dimensional plot and features corresponding to near-anode ($z = 0$) or near-cathode ($z = 1$) events. The main region of interest around the Q-value of ^{116}Cd is dominated by alpha-induced events on the lateral detector surfaces.

To further reduce the background index in the main region of interest around the Q-value of ^{116}Cd ($Q_{\beta\beta} = 2813.5\,\text{keV}$) the power of PSA is used to classify specific types of events. The techniques to identify so called lateral surface events (LSE) and the confirmation of those in reliable laboratory measurements are well documented and published in [2].

The most recent improvements in PSA are the discrimination of single-site (SSE) and multi-site events (MSE). Typically, highly energetic photons will interact via multiple interactions within a single crystal and, hence, all identified MSEs can be declared as background. In contrast, the signal of a $0\nu\beta\beta$-event is expected to be almost always single-site. The effects of background understanding and the power of the developed PSA techniques on the measured physics spectrum at the LNGS are illustrated in Figure 4. The newly developed MSE cut seems to have only a small influence, but also shows that the background in the region of interest is only weakly populated by γ-lines from the natural decay chains. Nonetheless, the cut is indispensable for the efficiency estimate of the well-established and excellent working LSE cuts and will be essential for a planned large scale experiment.

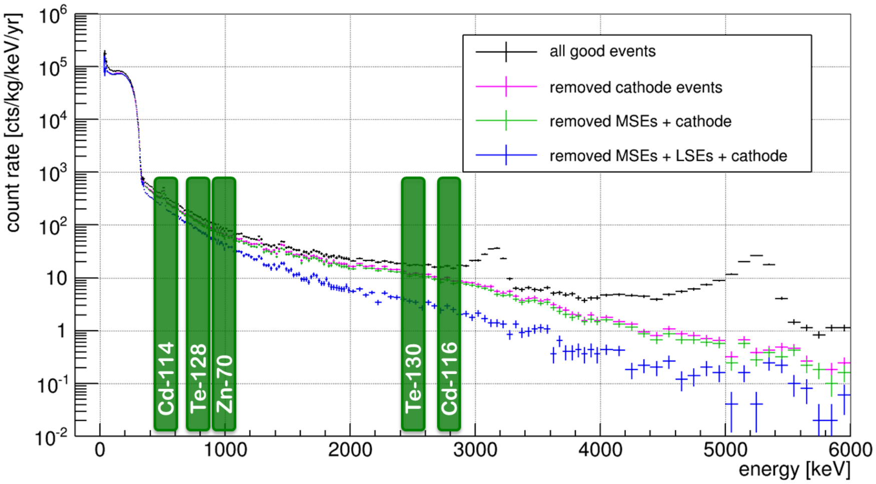

Figure 4: Low-background physics spectra based on 4-layer operation with 180 kg×days exposure accumulated between Sept.'11 and Sept.'14. Several cuts are applied to remove known background features such as alpha-emitting surface contaminations. The combination of all cuts leads to a background index in the region of interest for ^{116}Cd ($Q = 2.8\,\mathrm{MeV}$) of about 2.4 cts/kg/keV/yr. Applying additional fiducial cuts to remove the high-depth region with a significant higher background rate reduces the background index to 0.5 cts/kg/keV/yr.

The experimental setup upgrades done in 2013 such as the installation of an active water-cooling for the preamplifier boxes also achieved a positive effect measurable in the temperature of the inner setup. The ambient temperature dropped from 32°C down to 22°C, which should result in an improved energy resolution. The detector and preamp-temperature could be lowered down to 16°C and will be step-wise lowered further. The decreasing temperature in combination with a continuous dry nitrogen flushing allows for an additional lowering of the individual trigger thresholds. This step is important since COBRA can also measure the fourfold-forbidden non-unique β-decay of ^{113}Cd with an unprecedented precision. The shape of the beta spectrum around and below 50 keV is of general interest in nuclear physics and will be studied in the near future with more accumulated data in the low energy range.

3.3 α/β-discrimination

Because alpha particles and electrons generate charge clouds with different expansions in the semiconductor detector, it should in principle be possible to separate them, at least statistically. To test this hypothesis, one of the usual 1 cm^3 CPG detectors used by COBRA was irradiated from the cathode side with alpha particles and electrons of different energies, up to 2 MeV. The cathode side was chosen because it is not lacquered, allowing alpha particles to enter the sensitive volume. Moreover, this offers the advantage that the drift time of the charge carriers is maximal and so some aspects of pulse shapes are particularly easy to analyze. On the other hand, effects such as diffusion and repulsion that would have a negative impact on the discrimination power, are most prominent there because of the long drift.

Analysis of these data has shown that there are differences for both populations, that are not caused by the transport processes such as diffusion, repulsion and trapping that will increase with particle energy. A weakness of the analysis so far is, that the center of the charge carriers of the alpha- and beta-radiation charge clouds, generated due to the different penetration depths, is also different. This could result in a misinterpretation of the differences. Therefore more work to improve these methods has to be done.

3.4 Coincidence analysis

Coincidence analysis is a powerful tool for background reduction and for the investigation of the background itself. This however, makes a synchronization of the 16 FADCs of the COBRA-setup necessary. For this purpose a pulse generator is operated and an offline software has been written achieving a synchronization with an accuracy of $250\,\mu$s. This allows for the rejection of events with hits in more than one crystal in coincidence as background for the $0\nu\beta\beta$-decay analysis. In addition, the energy spectrum of multi-detector events can be analyzed with regard to the radioactive contamination of the setup. Furthermore, COBRA will look for characteristic coincidences from double beta decays into excited states. Within one FADC the accuracy of the synchronization is only limited by the sampling rate of the FADC of 100 MHz and by the length of the signal pulses. Hence, coincidence studies within a single crystal are very precise. In the near future the multi-site (MSE) analysis will be used to identify several signals within one signal window of $10\,\mu$s. However, a reconstruction of the depth and energy deposit of the individual signals is not possible for multi-site events with the current analysis software. Therefore, only coincident events within one crystal not classified as MSE are used for coincidences between alpha- and beta-decays in the natural decay chains, e.g. ^{214}Bi $\rightarrow$ ^{214}Po. This leads to a list of limits on the crystal contamination using 134.9 kg×days of data. To calculate these, efficiencies for the detection of a given coincidence are needed. These have been calculated with the help of a detailed simulation of the setup as described in section 4.1.

3.5 Background simulation

The first background estimations show that the current background spectrum is far below of all specific material limits. To get more information on the different background components, a Monte Carlo study was started to reproduce the current spectrum. The Monte Carlo simulation chain consists of two stages. The first one simulates the radiation interaction with matter via the GEANT4 libraries, which do not include any charge transport simulation through the detector material. This is equal to a detector with an infinite good energy resolution. Therefore, every detector effect has to be applied in a second step. All necessary parameters which describe the detector response, are estimated with calibration measurements. In the first step the detector geometry and the detector response has to be validated against calibration measurements. In Figure 5 the first version of the detector simulation is shown. Except the excess between 400 keV and 500 keV all features around the γ-lines can be explained by a small calibration offset of the measurement. In the future the detector simulation will also incorporate more known detector effects.

4 Towards a large-scale set-up

4.1 Estimation of the total background rate

For the determination of the total background rate of the COBRA large scale experiment, the proposed structure was implemented in a Monte Carlo geometry. It consists of an outer shielding and a modular detector array of 9×8×8×20 CPGs with a volume of $6\,\mathrm{cm}^3$ and a total of 415 kg detector mass. All previously known details such as mechanical supports, electrode material, cables, lacquer and various shielding components were taken into account in the geometry. For further details see [4]. As background sources the nuclides of the radioactive decay chains of ^{238}U and ^{232}Th were used. Furthermore, ^{40}K and the artificial radionuclide ^{137}Cs were taken into account, both in the form of intrinsic contamination as well as surface contamination. This includes particularly the radon decay products. Moreover, both thermal neutrons from spontaneous fission and (α, n) - reactions as well as muons, muon-induced neutrons

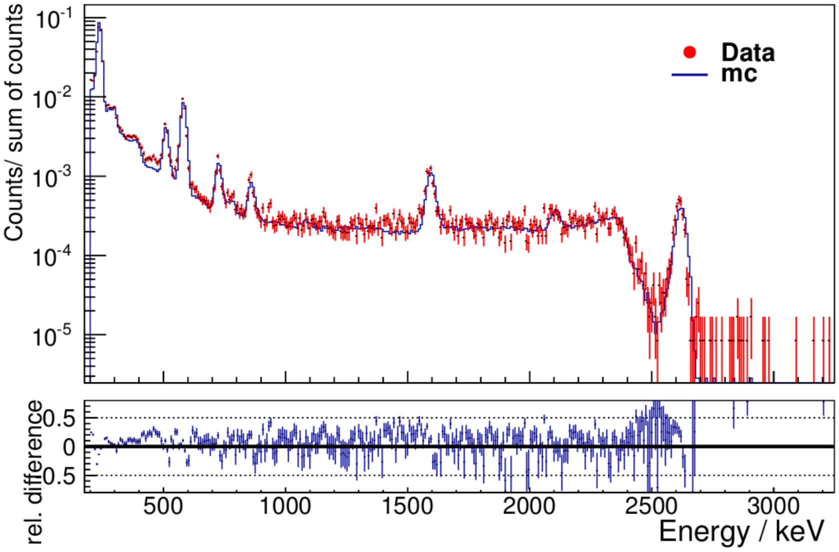

Figure 5: Comparison between simulation and calibration measurement. Only minor differences between simulation and measurement can be seen, which shows the validity of the used approach.

and cosmogenic nuclides are considered. All simulations were performed with GEANT4, with the low-rate physics experiments list 'shielding'.

To calculate the total expected background rate, in addition to the limitation to the region around the Q value of ^{116}Cd, four other conditions were used. The first condition refers to the multiplicity of detectors involved in the event. Furthermore, a restriction on the interaction depth suppresses events on the anode and cathode surfaces in 75% of the cases, which indicates the effectiveness of the corresponding pulse shape analysis. The last condition is that 90% of the γ-induced multi-site events can also be removed by means of pulse shape analysis.

The different background channels were normalized either by their known flux e.g. for neutrons, or in the case of radioactive contamination by comparison with the measured spectrum of the demonstrator. In the latter case, the results of the simulations of the LNGS setup have been fitted to the measured spectrum for each isotope, which is a very conservative procedure. As a result, the sum of the simulated backgrounds exceeds the measured spectrum. This leads to an overestimation of the background in the region of interest (ROI) around 2.8 MeV. Accordingly, the results for the large scale construction need to be seen as a strict upper limit. In order to make reliable statements, a complete background model is needed which will be done as a next step, see section 3.5. In particular, precise limits on the contamination of the individual materials for this are very important. This is because the dominance of the current radon background for the LNGS setup makes it difficult to draw conclusions about other background sources.

The obtained preliminary results for the expected background rate is above the planned background level. This is partly due to the very conservative approach and the above-mentioned uncertainties of the underlying background models. However, it is clear that the background rate is dominated by alpha particles. Gammas, electrons and neutrons contribute less than 1% of the total rate. The alpha particles stem mainly from the paint, the delrin and from the surfaces contamination of radon (27%). The goal of a background rate of less than 1×10^{-3} events/kg/keV/yr is realistic, in case that it is possible to identify either the alpha particles reliably or to reduce the corresponding contamination significantly. It is important to remember that it has not been possible for the COBRA collaboration so far, to keep the detector materials continuously under clean room conditions. Could this or at least a permanent nitrogen atmosphere be guaranteed for the crystal production, installation and operation, the contaminations would be significantly lower than previously observed and assumed in the simulation of the radon decay products.

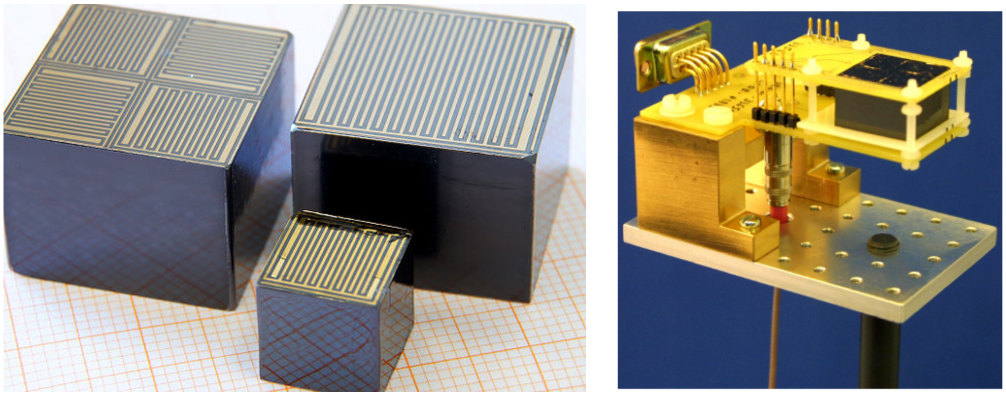

Figure 6: Left: Picture of the two different types of the new 6cm ^{3} detectors, compared to the current 1cm ^{3} approach. Right: Picture of the mounting holder for the large detectors.

HV [kV]	GB [V]	FWHM @ 662 keV
-1.3	-95	8.0%
-1.0	-55	8.0%
-1.5	-50	9.8%
-1.5	-95	7.8%

Table 1:
Energy resolution of the sample single grid detector for different operating parameters.

4.2 Large detectors

CZT detectors with a volume of $2\times2\times1.5\,\mathrm{cm}^3$ and a weight of 35.2 g are under investigation. The smaller surface-to-volume ratio results in a higher full energy detection efficiency and a reduction of surface contributions. A comparison of the dimension of the two detector sizes is shown in Figure 6. There are two approaches for the large detectors. On the one hand a single grid structure like the one on the small detectors and on the other a quad grid structure for the anodes will be tested. For the first investigations four large detectors, two of each type, were bought from Redlen – one of the leading manufactures of high resolution CZT. The new detectors were connected on a board to test the operating mode in principle. Therefore the cathode side of the detector is placed on the high voltage pad of the board and is held in place by its net weight and a delrin holder. The anodes are contacted with wire bonds to the pads for the grid bias (GB), see Figure 6.

4.2.1 Single grid structure

The test measurements are done with a single grid detector of rather poor sample quality using a high voltage (HV) of -1.3 kV and a grid bias of -95 V. Redlen quoted an energy resolution of 5.18% FWHM at 662 keV for this detector. The first measurement shows that it is in principle possible to take an energy spectrum with the new larger single grid detector, but the achieved energy resolution is worse than the result of the measurement from the manufacturer. To improve the energy resolution different operation parameters are tested. The difference in the energy resolution between those suggests that it is important to find the best operation point. The parameters chosen by Redlen for this measurement seem to be adapted but not optimal. With higher HV it is possible to reach an energy resolution of 7.8%. Nonetheless, it was not possible to reach the resolution Redlen quoted. On this account it is important to compare the different operation modes, to test further operation parameters and to characterize the detector response.

4.2.2 Quad grid structure

For testing the general operating mode of the detector with a quad grid structure a sample detector with a high voltage of -1500 V and a grid bias of -80 V is used. Due to problematic grid bias leakage currents Redlen determined the energy resolution of only two grids in their test measurements. They calculated

FWHM	grid 1	grid 2	grid 3	grid 4
@ 662keV	4.0%	4.0%	4.3%	3.6%
@ 2615keV	2.1%	2.2%	2.3%	1.9%

Table 2: Overview of energy resolution achieved with a quad detector for different energies and four working sub-detectors.

an energy resolution of 3.7% and of 2.3%. The circuitry is chosen such that for all four grids the CA side is the outer one and the NCA is in the middle of the detector. It was found that after contacting the detector as shown in Figure 6 one can measure with at least three sub-detectors as will be shown in section 4.2.3. Additionally, a quad grid detector with all four sub-detectors working properly is available for characterization measurements. A recorded spectrum of the deposited energy for all four grids is shown in Figure 7. This measurement shows that all four sub-detectors are functional and that it is possible to determine an energy resolution for every one of them, see Table 2.

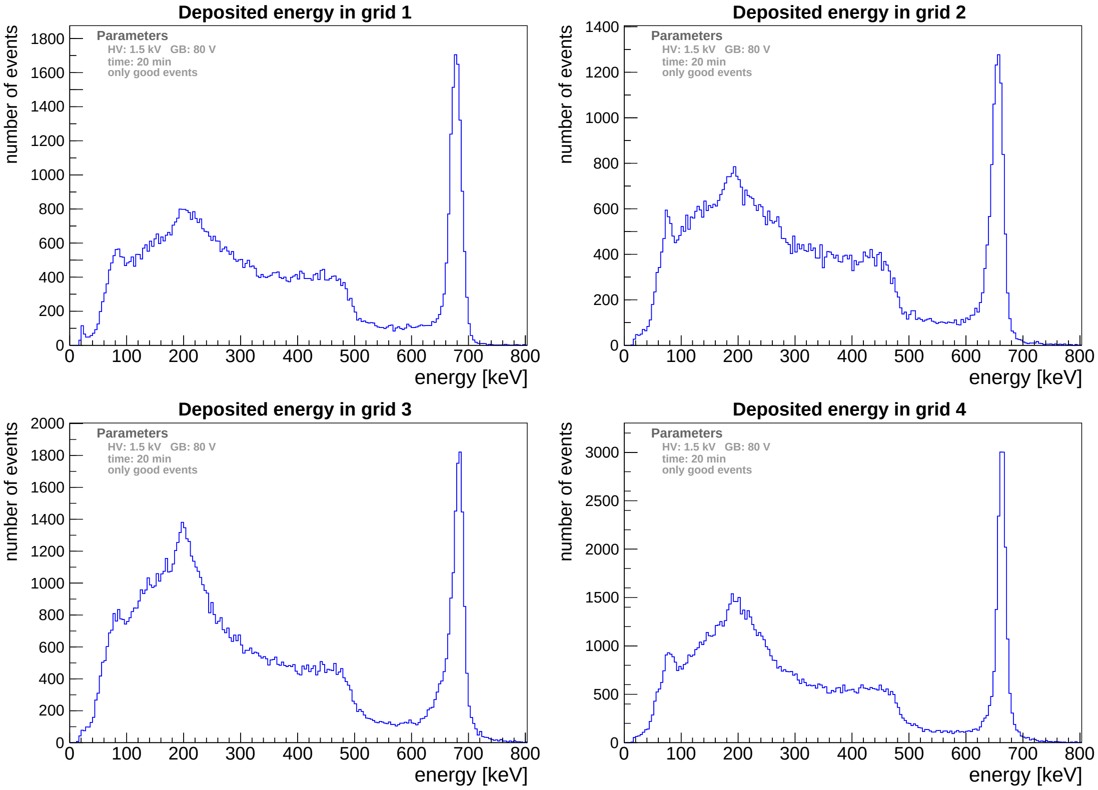

Figure 7: ^{137}Cs energy spectra of the four single sub-detectors of quad grid detector. All four sub-detectors are functional and can be used to investigate the achievable energy resolution.

Furthermore, voltage-current measurements were done to test the general behavior of the new detector approach. The results show that all four sub-detectors behave very similar and show the expected behavior like an ohmic resistor.

The first lab characterization measurements done with the available detectors are very promising but currently do not lead to comparable results in term of achievable energy resolution as for the current 1 cm^3 detector approach. Further studies to improve the achievable resolution by optimizing the operation parameters are described in the next section.

4.2.3 Characterization of quad CPG detectors with gamma sources

In 2015 first lab investigations with the new quad CPG approach for 6 cm^3 crystals have been started with the aim to transfer the existing characterization routines to the new detector generation. As a starting point, one quad CPG detector of sample quality (three properly working sub-CPGs) is used to adapt the procedures to find the optimal operation settings which were developed for the 1 cm^3 detectors installed at the LNGS. The operation settings for HV and GB are chosen to optimize the energy resolution of the detector measured as the FWHM of a specific gamma line. In particular, the spectrum of a ^{137}Cs source is measured for various combinations of HV in the range of 800 ...1500 V and GB in the range of 30 V...90 V based on the experience with the 1 cm^3 detectors. Each spectrum is then fitted with a Gaussian to obtain the FWHM for the full energy peak at 661.6 keV. In a first step, all working sub-CPGs are treated as if they were individual single CPG detectors meaning that only one sub-CPG is supplied with a grid bias while all other grids are floating. For standard CPG detectors such as used for the COBRA demonstrator it is a known feature that the achievable energy resolution can be improved by using a so called weighting factor which corrects for electron trapping effects at the same time (see [1]). The effect of the optimal weighting factor can be seen in Figure 8.

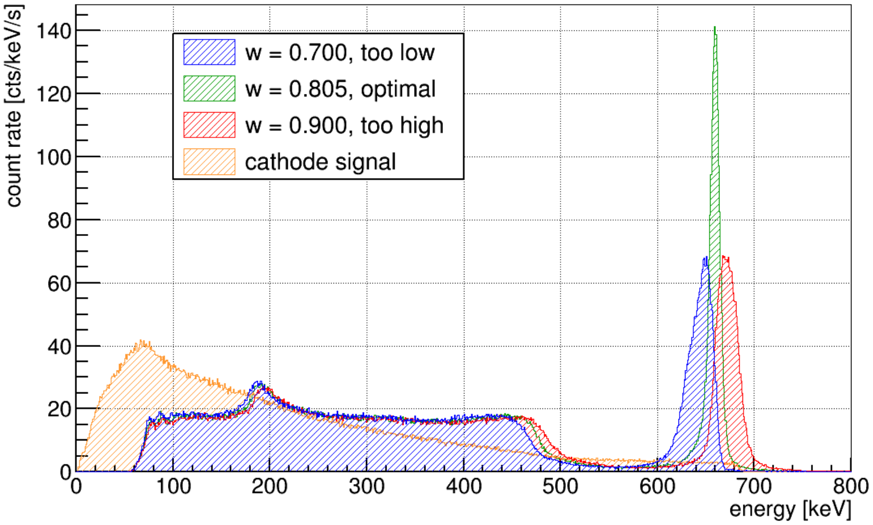

Figure 8: Comparison of ^{137}Cs spectra with (green) and without (blue/red) the use of an optimal weighting factor for a 1 cm^3 CPG detector. By using the optimal weighting factor, the energy resolution can be improved from 4.7% FWHM at 661.6 keV to 1.9%. Additionally the reconstructed cathode signal (orange) is shown, which corresponds roughly to a planar electrode design. In this case no full energy peak at all is visible in the spectrum due to the specific charge transport properties of CZT (taken from [5]).

The crucial point in the working point determination process is to find the optimal weighting factor for each HV and GB combination using empirical methods as will be described in the following. Firstly, the weighted difference signal CA$-w\cdot$NCA is calculated for each event while the weighting factor is varied in a specific range. Secondly, each spectrum for a certain value of w is fitted with a Gaussian to extract the FWHM of the ^{137}Cs full energy peak. The optimal weighting factor can then be found at the minimum of a parabola fit of a FWHM versus weighting factor. The optimal weighting factor is then used to reprocess the data to perform the final fit of the full energy peak to determine the FWHM for each HV and GB combination. An illustration of the resulting three-dimensional plots can be seen in Figure 9 for the three working sub-CPGs of the available sample quad detector.

In a second step, the working point characterization is repeated with all sub-CPGs active at the same time. If there is a trigger in one channel, all channels are readout as well to preserve the complete information of the event. Subsequently, the same routine as above can be used to find the optimal working point of each sub-CPG separately. It was found that this treatment leads to similar results for the individual sub-CPGs like for the single measurements but with only a fraction of the required measurement time. Finally, the information of all sub-CPGs can be combined to reconstruct the overall deposited energy as the sum of the calibrated single sub-CPG entries. This method requires some adjustments to the existing

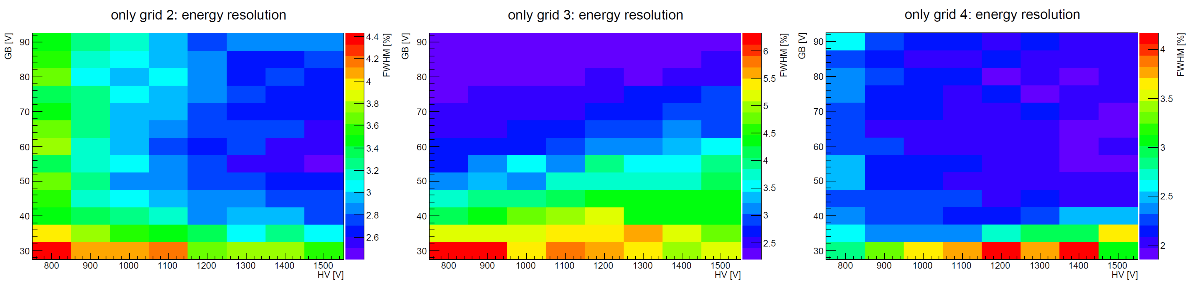

Figure 9: Heat map of energy resolution at 661.6 keV dependent on applied HV and GB for the three working sub-CPGs of a sample quad CPG detector. Higher HV and GB are preferred by each sub-CPG but the overall resolution of the quad detector could be possibly improved further by applying individual GB for the sub-CPGs as will be studied in the near future.

routines but leads at this point to the most promising results as shown in Figure 10.

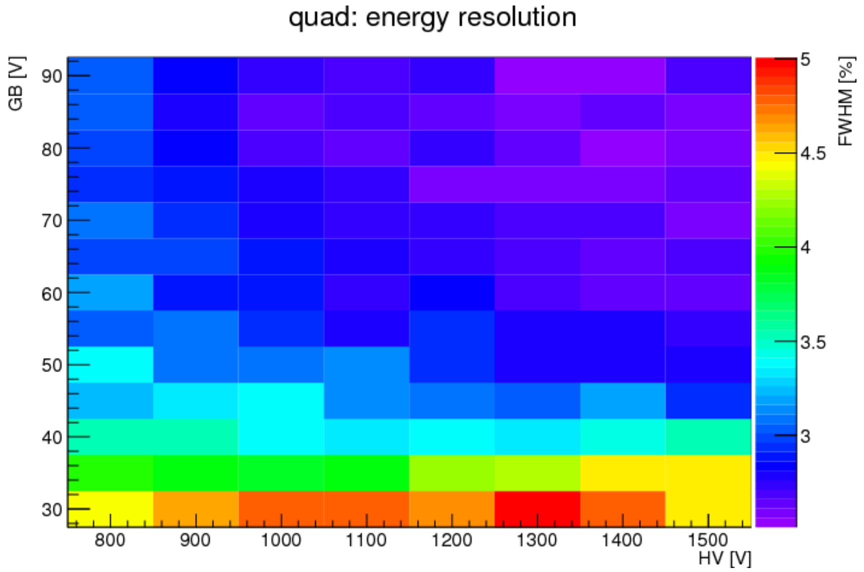

Figure 10: Heat map of energy resolution at 661.6 keV dependent on applied HV and GB for sample quad-CPG detector. The total energy deposition is the sum of the individual energy entries of the three working sub-CPGs. The working point settings were determined to HV/GB= 1400/80 V resulting in an energy resolution of 2.6% FWHM, which is a very promising result taking into account the poor quality of the sample detector.

In the near future the working point investigations on quad CPG detectors will be extended using a new voltage supply system which allows for individual grid bias for the sub-CPGs. Furthermore, the improved characterization routines will be applied on all detectors selected for a prototype detector module consisting of nine 6 cm^3 quad CPGs.

Another investigation which has just been started is a localized radiation with a strongly collimated ^{137}Cs source of high activity. The collimated source is mounted on a two-dimensional scanning table with a step accuracy of 0.1 mm which allows for a precise scanning of four detector sides. The collimator channel has a diameter of 0.5 mm and a length of 60 mm. This ensures a spatial resolution of better than 1 mm^2 to investigate the local response of the new detector generation. Of special interest is the localized radiation of the area in between the four sub-CPGs to study the effect of charge sharing for events near those regions. Other subjects of interest are the experimental verification of the adjusted depth reconstruction method for the quad approach and to test the possibility of identifying the x-y-position of interactions. The last point is very promising to improve the efficiency of multi-site event identification.

4.3 ASIC-based electronics readout system

For the large scale setup a readout system based on integrated circuits is necessary due to the huge amount of electronic channels. A commercially available ASIC-based readout system which serves COBRA's purposes was identified, tested and bought. The work on this has just begun, a spectrum showing the results of first test measurements is shown in Figure 11. The energy resolution in that measurement is limited by the detector which was of lower quality.

5 Pixel detectors

In the past, the COBRA collaboration investigated the possibilities of using hybrid pixel detectors with CdTe sensor layers (for example Timepix) in the search for neutrinoless double beta decay (see [9], [10]). It turned out that with the existing electrical layout of the Timepix, a sensor thickness of 3 mm and a pixel pitch between 165 μm and about 220 μm would be optimal with respect to sensitivity to the effective Majorana neutrino mass for a wide range of possible specific single electron background rates. It could be shown that energy resolutions (FWHM) from 1.3% to 1.6% can be expected for these sensor configurations. For an assumed specific background rate of 0.001 counts/kg/keV/yr at the Q-value the analysis of the track topology, which is partly resolved with such a fine pixel pitch, allowed the identification of 75% of single electrons as such in the simulations. Thus the background can be reduced by about a factor of four by analysis of recorded track topologies. On the other hand, 23% of neutrinoless double beta decays would be classified as background events. After topology analysis with a random decision forest, the detection efficiency amounts to 42% according to simulations. The net benefit of topology analysis was equivalent to a reduction in the background level by only a factor of 2.2 for single electrons. This rather limited potential is a consequence of the current design of pixel detectors: no information about the structure of tracks along the charge carrier drift axis is accessible. After 5 years of measuring time, the sensitivity to the effective Majorana neutrino mass (90% C.L.) would be 59 meV for 420 kg CdTe realized as 3 mm thick layer on a pixel detector with 165 μm pixel pitch, the single assemblies facing each other so that 6 mm thick layers are effectively formed.

Simulations showed that the background level could effectively be reduced by about a factor of 6.5 with a position resolution in the order of 110 μm. The COBRA pixel group developed an algorithm which can reconstruct the average depth of charge carrier generation from the energy signals measured with the pixelated (anode) and the common electrode (cathode) and the recording of the moment the discriminator threshold is exceeded. The Timepix detector cannot deliver all this information for each event, but the new Timepix3 detector in principle can. As the new Timepix3 detector was not available at the moment of this study, the algorithm was tested with the Timepix for the special case for high energy electrons traversing the CdTe sensor layer completely. The experiment was carried out at DESY. At a reduced

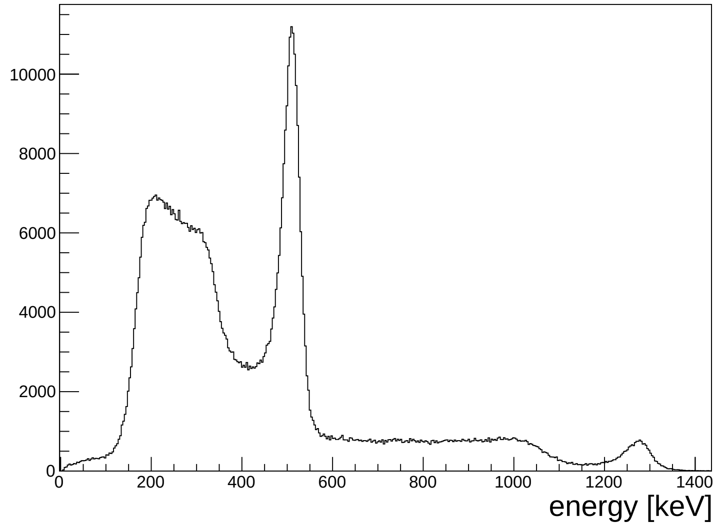

Figure 11: Spectrum of a ^{22}Na source obtained with the ASIC-based readout system which will be used for COBRA's first detector module of the large scale setup.

bias voltage, it was demonstrated that a position resolution of about $63\,\mu$m (σ of Gaussian) could be achieved (see [11]). The three dimensional structure of the high energy electron tracks could be nicely reconstructed. Thus, a single layer solid state TPC has been demonstrated in [11].
Furthermore, it was already demonstrated (see [12]) that the Timepix detector is in principle able to detect the signal of double electron captures. Using this technique a part of the collaboration was able to measure the probability of double vacancy creation in the ordinary electron capture decay of ^{55}Fe with a statistical error that was reduced by at least a factor of two compared to literature. In this experiment, two Timepix detectors were operated in coincidence with silicon sensors facing each other with a ^{55}Fe source in between.
It was also shown experimentally in [13] – by exposing a CdTe Timepix detector to alpha particles with 2.8 MeV energy – that alpha particle background can be reduced by at least a factor of 450 000 by analysis of the topology of the set of triggered pixels. In contrast to electrons, alpha particles usually trigger a circularly shaped region of pixels, as the track of typical alpha particle in CdTe is only a few micrometers long. Diffusion of charge carriers during drift to the pixel electrodes leads to the triggering of pixels in circularly shaped region.

References

[1] M. Fritts, J. Durst, T. Göpfert, T. Wester and K. Zuber, *Analytical model for event reconstruction in coplanar grid CdZnTe detectors.* NIM A, 708, 1-6, 2013. `http://dx.doi.org/10.1016/j.nima.2013.01.004`.

[2] M. Fritts, J. Tebrügge et al, *Pulse-shape discrimination of surface events in CdZnTe detectors for the COBRA experiment.* NIM A, 749, 27-34, 2014. `http://dx.doi.org/10.1016/j.nima.2014.02.038`.

[3] T. Neddermann, *Material Screening by means of Low-level Gamma Ray Spectrometry with the Dortmund Low Background HPGe Facility*, PhD thesis, TU Dortmund, 2014.

[4] N. Heidrich, *Monte-Carlo-based Development of a Shield and Total Background Estimation for the COBRA Experiment*, PhD thesis, U Hamburg, 2014.

[5] S. Zatschler, *Identification of Multi-Site Events in Coplanar-Grid CdZnTe-Detectors for the COBRA-Experiment*, diploma thesis, TU Dresden, 2014.

[6] F. Kandzia, *Investigation on intrinsic Alpha Particle Events in CdZnTe Detector*, diploma thesis, TU Dresden, 2014.

[7] R. Theinert, *Performance and efficiency studies of CdZnTe semiconductor detectors for the COBRA experiment*, master thesis, TU Dortmund, 2014.

[8] C. Nitsch, *Upgrade of the Muon Veto and Measurements with the Dortmund Low Background Facility*, master thesis, TU Dortmund, 2014.

[9] M. Filipenko, T. Gleixner et al.(2013) 'Characterization of the energy resolution and the tracking cap1abilities of a hybrid pixel detector with CdTe-sensor layer for a possible use in a neutrinoless double beta decay experiment', The European Physical Journal C, vol. 73, no. 4, 2374

[10] T. Michel, T. Gleixner et al., (2013) 'The Potential of Hybrid Pixel Detectors in the Search for the Neutrinoless Double-Beta Decay of 116Cd', Advances in High Energy Physics, Special issue on Neutrino Masses and Oscillations, vol. 2013, 105318

[11] M. Filipenko, T. Gleixner et al. (2014) '3D Particle Track Reconstruction in a Single Layer Cadmium-Telluride Hybrid Active Pixel Detector', The European Physical Journal C, accepted for publication on July 30, 2014

[12] T. Michel, B. Bergmann et al. (2014) 'Measurement of the double K-shell vacancy creation probability in the electron capture decay of 55Fe with active pixel detectors', Physical Review C, vol. 89, no. 1, 014609

[13] T. Gleixner, M. Filipenko et al., Rejection of alpha-particle background for neutrinoless double beta decay search with pixel detectors, 2014 JINST 9 P10015

The CRESST dark matter search

G. Angloher[a], A. Bento[a,b], C. Bucci[c], L. Canonica[c], A. Erb[d,e], F. von Feilitzsch[d], N. Ferreiro[a],
P. Gorla[c], A. Gütlein[f,g], D. Hauff[a], J. Jochum[h], M. Kiefer[a], H. Kluck[f,g] H. Kraus[i],
J.C. Lanfranchi[d], J. Loebell[h], A. Münster[d], F. Petricca[a,+], W. Potzel[d], F. Pröbst[a], F. Reindl[a],
S. Roth[d], C. Sailer[h], K. Schäffner[c], S. Schönert[d], J. Schieck[f,g] W. Seidel[a], M. von Sivers[d]
L. Stodolsky[a], C. Strandhagen[h], R. Strauss[a], A. Tanzke[a], M. Uffinger[h], A. Ulrich[d], I. Usherov[h],
S. Wawoczny[d], M. Willers[d], M. Wüstrich[a], A. Zöller[d]

[a] *Max-Planck-Institut für Physik, 80805 Munich, Germany*
[b] *Departamento de Fisica, Universidade de Coimbra, 3004 516 Coimbra, Portugal*
[c] *Laboratori Nazionali del Gran Sasso, 67010 Assergi, Italy*
[d] *Technische Universität München, Physik Department, 85747 Garching, Germany*
[e] *Walther-Meißner-Institut für Tieftemperaturforschung, 85748 Garching, Germany*
[f] *Institut für Hochenergiephysik der Österreichischen Akademie der Wissenschaften, 1050 Wien, Austria*
[g] *Atominstitut, Vienna University of Technology, 1020 Wien, Austria*
[h] *Eberhard-Karls-Universität Tübingen, 72076 Tübingen, Germany*
[i] *University of Oxford, Department of Physics, Oxford OX1 3RH, UK*
[+] Spokesperson e-mail address: petricca@mpp.mpg.de

Abstract

The aim of CRESST (Cryogenic Rare Event Search with Superconducting Thermometers) is to search for particle dark matter via their elastic scattering off nuclei in scintillating $CaWO_4$ crystals. The experiment is located at the Laboratori Nazionali del Gran Sasso (LNGS), Italy, and it uses low background cryogenic detectors with superconducting phase-transition thermometers for the direct detection of WIMP-nucleus scattering events.

1 Dark Matter

Deciphering the nature of dark matter is one the challenges of modern particle physics and cosmology. Despite the prove of existence of dark matter in many astrophysical and cosmological observations and strong arguments that it cannot be made of ordinary matter, a direct detection of this elusive component of the universe has not yet been confirmed. Unfortunately the astrophysical and cosmological observations do not completely constrain the nature of dark matter and the type of interaction with ordinary matter, therefore many different particle candidates can provide a solution for the dark matter problem. WIMPs (Weakly Interacting Massive Particles) are among the best motivated candidates as they naturally arise from extensions of the standard model of particle physics and achieve the correct thermal relic abundance in the early Universe.

In the last few years, many direct dark matter projects have probed with increasing sensitivity the mass-cross section parameter space for WIMP-nucleus elastic scattering [1]. Most of these experiments are suitable for WIMP masses $\gtrsim 30$ GeV/c^2, where the sensitivity gain is mainly driven by the exposure. Nevertheless, a number of theoretical models favoring lighter WIMP candidates (e.g. [2, 3, 4, 5, 6]) have recently moved the interest of the community to the mass region below 10 GeV/c^2. As such light WIMPs produce only very low-energy nuclear recoils (below keV), the challenge for their detection is to achieve a sufficiently low threshold in terms of recoil energy, with enough background discrimination at these low energies.

2 Detector principle

Cryogenic detectors are low-temperature (mK) calorimeters that measure the energy deposited in the absorber by a particle interaction as an increase of temperature in an appropriate temperature sensor. Such cryogenic calorimeters provide the best energy threshold for nuclear recoils and the sensitivity which are fundamental requirements for dark matter searches.

Experiments based on this type of detectors developed strategies to distinguish background from a possible WIMP signal on an event-by-event base. In the case of scintillating materials, e.g. $CaWO_4$ as used in CRESST, such discrimination is obtained by pairing each scintillating crystal with a light detector measuring the scintillation light, that is different according to the type of interaction. Crystal and light detector are operated as independent cryogenic calorimeters, each equipped with a transition edge sensor (TES).

The TES is a thin tungsten film, stabilized in the transition from the normal to the superconducting state. In the region of the transition, the tiny change of the film temperature ($O(\mu$K)) induced by the absorption of the phonons produced by an energy deposition in the absorber leads to a measurable change in resistance which is read out by SQUID-based electronics.

A crystal and the corresponding light detector form a *detector module*. For each particle interaction, a detector module yields two coincident signals (one from the crystal and one from the light detector). The signal in the target crystal provides a sensitive measurement of the total energy deposition (approximately independent of the type of interacting particle), while the signal in the light detector is used for discriminating different types of interactions.

3 The CRESST Setup at LNGS

The main part of the facility at LNGS is a cryostat, whose design had to combine the requirements of low temperature with those of low background. As can be seen in Fig. 1, the dilution unit of the cryostat and the dewars containing cryogenic liquids do not extend into the experimental volume.

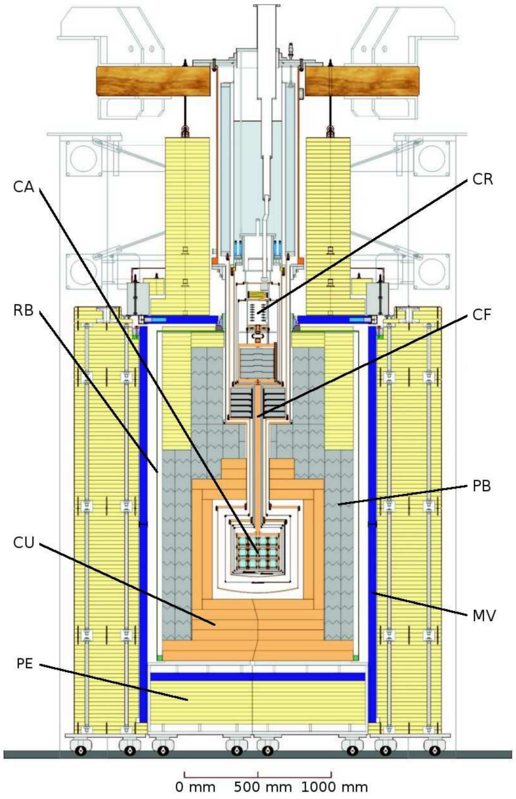

Figure 1: Schematic drawing of the CRESST setup. A cold finger (CF) links the cryostat (CR) to the experimental volume, where the detectors are arranged in a common support structure, the so called carousel (CA). This volume is surrounded by layers of shielding from copper (CU), lead (PB), and polyethylene (PE). The copper and lead shieldings are additionally enclosed in a radon box (RB). An active muon veto (MV) tags events which are induced by cosmic radiation.

The low temperatures are provided by a ^{3}He-^{4}He dilution refrigerator and transferred to the detectors via a 1.3 m long copper cold finger. The detectors are arranged in a common support structure, the so-called *carousel*, and mounted inside the *cold box* which consists of five concentric radiation shields surrounding the experimental volume and the cold finger. Two internal cold shields consisting of low-level lead are attached to the mixing chamber and to a thermal radiation shield at liquid N_2 temperature, respectively, in order to block any line-of-sight from the non-radio-pure parts of the dilution refrigerator to the detectors inside the cold box. The cold box is surrounded by several layers of shielding against the main types of background radiation: layers of highly pure copper and lead shield against γ-rays, while polyethylene serves as a moderator for neutrons. The inner layers of shielding are contained in a gas tight box to prevent radon from penetrating them. In addition, an active muon veto using plastic scintillator panels is installed to tag muons. The veto surrounds the lead and copper shielding and covers 98.7 % of the solid angle around the detectors, a small hole on top is necessary to leave space for the cryostat.

4 Measures for background reduction

The main goal of the current run of the CRESST experiment (run33) was to clarify the nature of the signal excess reported in [7], reducing neutron, α and ^{206}Pb recoil backgrounds by more than one order of magnitude. To achieve this goal various actions have been taken.

4.1 Neutron background

The existing neutron shielding, consisting of ∼40 cm of polyethylene (PE) surrounding the Pb/Cu shielding, has been supplemented with a 5 cm thick PE layer inside the Pb/Cu shield. This was expected to reduce the background from neutrons originating in the Pb/Cu shield by more than an order of magnitude, as estimated by a GEANT4 simulation purposely performed. Part of this additional shielding is placed in the vacuum inside the cold box (see Fig. 2) and another overlapping part is placed outside. The outside part may be removed to still allow a neutron test with an external neutron source during the run.

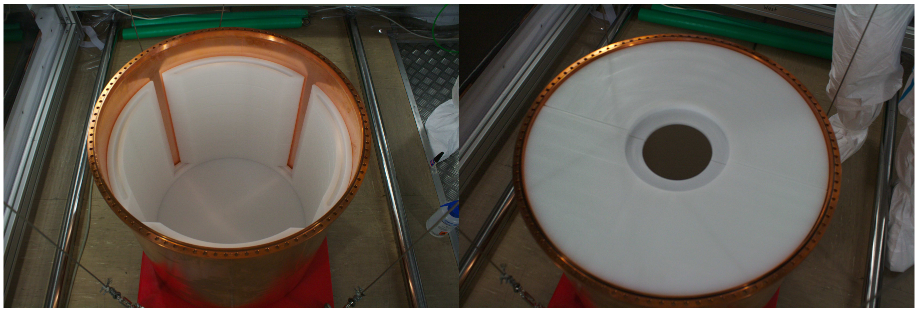

Figure 2: PE shielding placed inside the outer vacuum can of the cryostat.

4.2 Degraded alphas and ^{206}Pb nuclear recoil background

The origin of the degraded alphas and ^{206}Pb nuclear recoil background has been extensively discussed in [7].

4.2.1 Passive reduction

Passive reduction of these backgrounds is aimed in the current run by equipping conventional detector modules with new holding clamps from purpose-produced ultra pure CuSn6 and by avoiding radon exposure during production of clamps and assembling of detectors. Out of the 18 modules installed for the current run, 12 have a conventional design with new ultra-pure CuSn6 clamps.

4.2.2 Active reduction

Active reduction of the ^{206}Pb nuclear recoil background is pursued by using new 'actively discriminating detector" designs which allow to tag α decays originating from all inner surfaces of the detector module. Three new detector designs, tested during the last years in our R&D cryostat in the underground lab, are used in the current run. Fig. 3 shows two of them sharing the use of a cylindrical $CaWO_4$ disk (carrier crystal) glued to the target crystal. Common for both designs is that the holding clamps are not in contact with the target, but only with the carrier crystal. The module on the left side has a fully scintillating holder design which allows to distinguish the background from surface α decays by using the additional light signal of the α as a veto. The module uses clamps covered with Parylene which was measured to be a good scintillator even at low temperatures. The module on the right side does not use a conventional light detector, but the light detector is instead a silicon beaker completely surrounding the target crystal which allows to actively discriminate surface α decays with full efficiency. Both designs rely on the possibility to distinguish between events in the carrier and in the target crystal. For the left design this is needed to distinguish possible stress-relaxation events originating from the contact between the Parylene coated clamps and the crystal. In the right design there is no line of sight between target crystal and clamps. In this case non scintillating clamps can be used and the discrimination is needed to identify possible recoiling nuclei in the carrier crystal originating from the clamps.

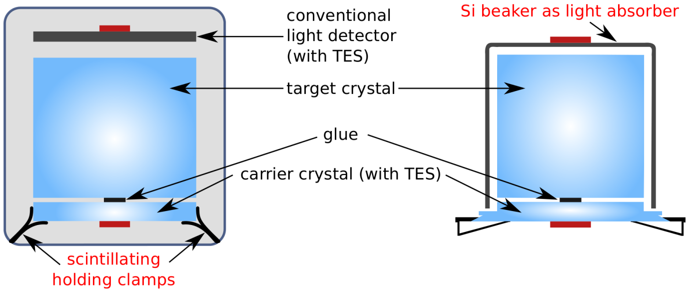

Figure 3: Scheme of the actively discriminating detector designs with crystal clamped on carrier.

The third new detector design (see Fig. 4) uses $CaWO_4$ sticks to hold the crystal (a detailed description can be found in [8]). The sticks are held in place by clamps outside the scintillating housing and therefore also this design is fully scintillating. Further innovation in this design is the use of a cuboidal crystal instead of a cylindrical one for improved light collection.

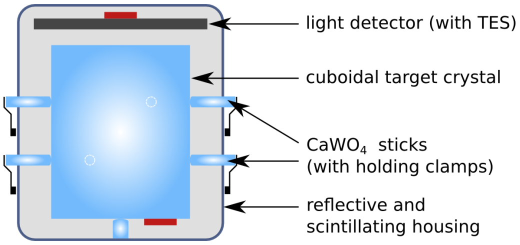

Figure 4: Scheme of the actively discriminating detector design which uses $CaWO_4$ sticks to hold the target crystal.

Two modules of each of the new detector designs are currently installed.

5 Current status of the experiment

The experiment has been acquiring data since July 30th 2013. The data set until January 7th 2014 has been used for a first evaluation of the detector performance and of the impact of the various actions for background reduction which have been implemented for this run.
The data set shows that the residual neutron background has been efficiently suppressed with the introduction of the additional PE layer inside the Pb/Cu shield. The background of degraded αs has also been completely removed by introducing the new holding clamps. The ^{206}Pb nuclear recoil background, however, was impossible to suppress with passive techniques such as cleaning and shielding the detectors. This background is efficiently suppressed only in the three new "actively discriminating detector" designs that were introduced.

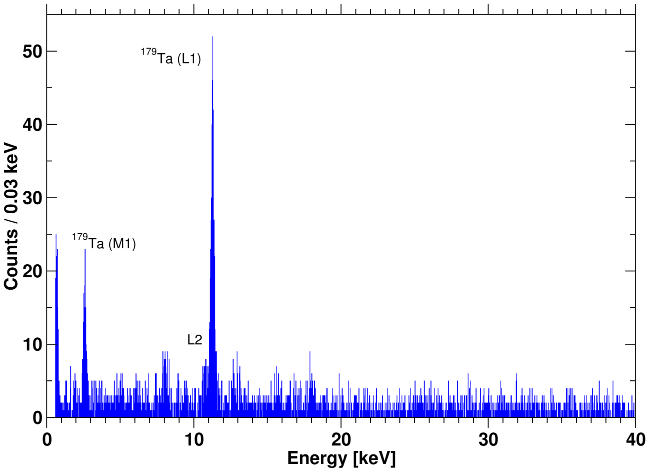

Figure 5: Low-energy spectrum of all events recorded with a TUM grown CaWO$_4$ crystal, corresponding to an exposure of 29.35 kg live days. The average rate of e^-/γ background in the region shown is about 3.5/[kg keV day]. The visible lines mainly originate from cosmogenic activation (see text).

Four of the 18 CaWO$_4$ crystals operated in the present run have been produced at the crystal growing facility of the Technische Universität München [9]. Due to the improved selection of raw materials and the control of all production steps, these crystals show a significant gain in terms of radiopurity with respect to the commercially available ones (a factor of 2 to 10 lower e^-/γ background in the region of interest and a significant reduction of the α contamination corresponding to a total intrinsic alpha activity from natural decay chains of about 3 mBq/kg [10, 11]). The low energy spectrum of the crystal named TUM40 is shown in Fig. 5. The prominent peaks at $\sim$2.6 keV and $\sim$11.3 keV can be attributed to M1 and L1 electron capture decays of cosmogenically produced ^{179}Ta. The fitted peak positions agree with the tabulated values of the binding energy of the Hf M1 and L1 shells [12] within deviations of 0.5 eV and 2 eV, respectively.
The improved radiopurity has a great impact on the low energy region, where it allows a significant gain in sensitivity for low WIMP masses.

6 Results

The data set from a single "actively discriminating detector" module of the design shown in Fig. 4, corresponding to an exposure of about 29 kg days, has been used to derive a limit for the cross section of spin-independent WIMP-nucleon scattering presented in [13].

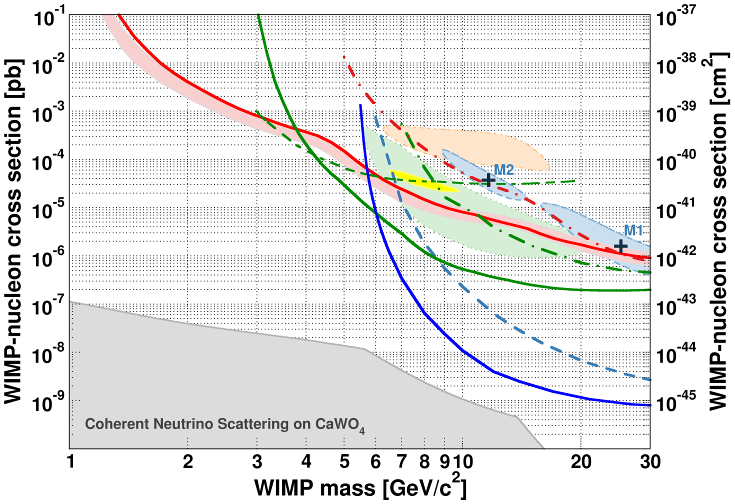

Figure 6: WIMP parameter space for spin-independent ($\sigma \propto A^2$) WIMP-nucleon scattering. The 90 % C.L. upper limit (solid red) is depicted together with the expected sensitivity (1 σ C.L.) from the background-only model (light red band). The CRESST 2 σ contour reported in [13] is shown in light blue. The dash-dotted red line refers to the reanalyzed data from the CRESST commissioning run [14]. Marked in grey is the limit for a background-free CaWO$_4$ experiment arising from coherent neutrino-nucleus scattering, dominantly from solar neutrinos. Shown in green are the limits (90 % C.L.) from Ge-based experiments: Super-CDMS (solid) [15], CDMSlite (dashed) [16] and EDELWEISS (dash-dotted) [17]. The parameter space favored by CDMS-Si [18] is shown in light green (90 % C.L.), the one favored by CoGeNT (99 % C.L. [19])and DAMA/Libra (3 σ C.L. [20]) in yellow and orange. The exclusion curves from liquid xenon experiments (90 % C.L.) are drawn in blue, solid for LUX [21], dashed for XENON100 [22]. Marked in grey is the limit for a background-free CaWO$_4$ experiment arising from coherent neutrino scattering, dominantly from solar neutrinos [23].

The exclusion limit we get is shown as solid red line in Fig. 6. A Monte Carlo simulation, based on a background model assuming the presence of e^-/γ-backgrounds only [11], gives the light-red band (1 σ CL). The limit derived from data and this simulation agree throughout the whole WIMP mass range indicating that the events in the acceptance region may be solely explained by leakage of the e^-/γ-background.

The CRESST exclusion limit rises more moderately and has lower systematic uncertainty than the limits from other experiments when going to low WIMP masses. These distinctive features, which come from the possibility to simultaneously probe a possible WIMP signal on different nuclei (including the very light oxygen nuclei) and to measure nuclear recoil energies with little systematic uncertainty, mark the uniqueness of the experimental technique [13].

The result from the data obtained already excludes the lower mass maximum (M2), but more statistics is required to improve the limit at higher WIMP masses and, thus, to clarify the origin of the higher mass maximum (M1). For this reason the current run will go on until an exposure of about 500 kg days is collected with the actively discriminating modules, which is expected to be achieved in 2015 (see Fig. 7).

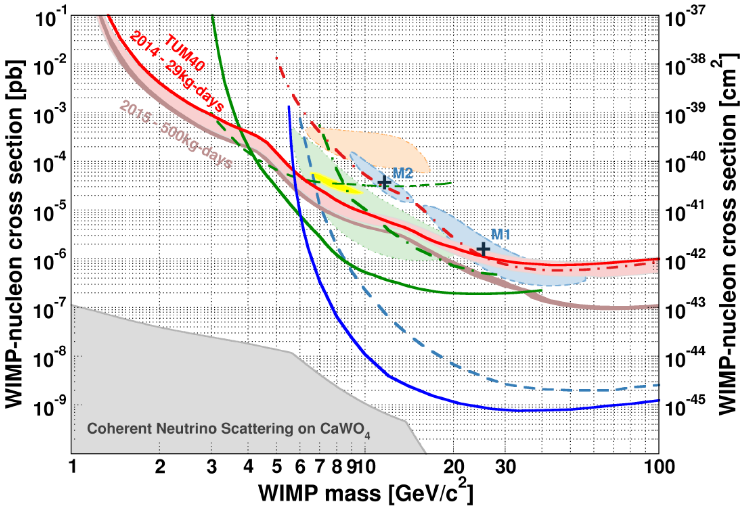

Figure 7: In addition to the limits shown in Fig. 6, the expected sensitivity for an exposure of about 500 kg days with the actively discriminating modules is shown.

7 Conclusions

With an exposure of 29.35 kg live days collected in 2013 we set in [13] a limit on spin-independent WIMP-nucleon scattering which probes a new region of parameter space for WIMP masses below 3 GeV/c^2, previously not covered in direct detection searches. The improved performance of the upgraded detector manifests itself in a significantly improved sensitivity of CRESST-II for very low WIMP masses. A possible excess over background discussed for the previous CRESST-II phase [7] is not confirmed.

8 List of Publications

1. G. Angloher et al.: Results on low mass WIMPs using an upgraded CRESST-II detector (2014)
   Eur. Phys. J. C. Volume 74, Number 12 (2014), arXiv:1407.3146 [astro-ph.CO]

2. A. Mnster et al.: Radiopurity of CaWO4 Crystals for Direct Dark Matter Search with CRESST and EURECA
   JCAP 2014, 018 (2014), arXiv:1403.5114 [astro-ph.IM]

3. R. Strauss et al.: Precision Measurements of Light Quenching in CaWO4 Crystals at mk Temperatures
   Eur. Phys. J. C (2014) 74, arXiv:1401.3332 [astro-ph.IM]

4. R. Strauss et al.: A detector module with highly efficient surface-alpha event rejection operated in CRESST-II Phase 2
   arXiv:1410.1753 [physics.ins-det]

5. R. Strauss et al.: Electron/gamma and alpha backgrounds in CRESST-II Phase 2 arXiv:1410.4188 [physics.ins-det]

Acknowledgements

We are grateful to LNGS for their generous support of CRESST, in particular to Marco Guetti for his constant assistance.

References

[1] P. Cushman et al.: arXiv:1310.8327 [hep-ex].

[2] T. Cohen et al.: Phys. Rev. D82 (2010) 056001, arXiv:1005.1655 [hep-ph].

[3] D. E. Kaplan et al.: Phys. Rev. D79 (2009) 115016, arXiv:0901.4117 [hep-ph].

[4] K. Sigurdson et al.: Phys. Rev. D70 (2004) 083501, arXiv:astro-ph/0406355.

[5] J. Fortin et al.: Phys. Rev. D85 (2012) 063506, arXiv:1103.3289 [hep-ph].

[6] J. Feng et al.: Phys. Lett. B 704 (2011) 534, arXiv:1102.4331 [hep-ph].

[7] G. Angloher et al.: EPJC 72, (2012) 1971.

[8] R. Strauss et al.: arXiv:1410.1753 [physics.ins-det].

[9] A. Erb and J.-C. Lanfranchi, CrystEngComm 15, 2301 (2013).

[10] A. Münster et al.: JCAP 05 (2014) 018.

[11] R. Strauss et al.: arXiv:1410.4188 [physics.ins-det].

[12] R.B. Firestone, C. Baglin, S.Y.F. Chu, Table of isotopes: 1998, update with CD-ROM (Wiley, New York, 1998)

[13] G. Angloher et al.: EPJC 74, (2014) 3184.

[14] A. Brown et al.: Phys. Rev. D 85, 021301 (2012).

[15] R. Agnese et al.: Phys. Rev. Lett. 112, 241302 (2014).

[16] R. Agnese et al.: Phys. Rev. Lett. 112, 041302 (2014).

[17] E. Armengaud et al.: Phys. Rev. D 86, 051701 (2012).

[18] R. Agnese et al.: Phys. Rev. Lett. 111, 251301 (2013).

[19] C.E. Aalseth et al.: Phys. Rev. D 88, 012002 (2013).

[20] C. Savage, G. Gelmini, P. Gondolo, K. Freese: JCAP 0904, 010 (2009).

[21] D.S. Akerib et al.: Phys. Rev. Lett. 112, 091303 (2014).

[22] E. Aprile et al.: Phys. Rev. Lett. 109, 181301 (2012).

[23] A. Gütlein et al.:arXiv:1408.2357 [hep-ph]

CUORE
2014 LNGS Report

C. Alduino,[1] K. Alfonso,[2] D. R. Artusa,[1,3] F. T. Avignone III,[1] O. Azzolini,[4] M. Balata,[3] T. I. Banks,[5,6,3] G. Bari,[7] J.W. Beeman,[8] F. Bellini,[9,10] A. Bersani,[11] D. Biare,[6] M. Biassoni,[12,13] C. Brofferio,[12,13] A. Buccheri,[10] C. Bucci,[3] C. Bulfon,[10] A. Camacho,[4] A. Caminata,[11] L. Canonica,[3] X.G. Cao,[14] S. Capelli,[12,13] M. Capodiferro,[10] L. Cappelli,[3,15] L. Carbone,[13] L. Cardani,[9,10] M. Cariello,[11] N. Casali,[3,16] L. Cassina,[12,13] R. Cereseto,[11] G. Ceruti,[13] A. Chiarini,[7] D. Chiesa,[12,13] N. Chott,[1] M. Clemenza,[12,13] S. Copello,[17] C. Cosmelli,[9,10] O. Cremonesi,[13,†] C. Crescentini,[7] R. J. Creswick,[1] J. S. Cushman,[18] I. Dafinei,[10] A. Dally,[19] C. J. Davis,[18] F. Del Corso,[7] S. Dell'Oro,[3,20] M. M. Deninno,[7] S. Di Domizio,[17,11] M. L. di Vacri,[3,16] L. DiPaolo,[6] A. Drobizhev,[5,6] L. Ejzak,[19] G. Erme,[3,15] D. Q. Fang,[14] M. Faverzani,[12,13] J. Feintzeig,[6] G. Fernandes,[17,11] E. Ferri,[12,13] F. Ferroni,[9,10] S. Finelli,[7] E. Fiorini,[13,12] M. A. Franceschi,[21] S. J. Freedman,[6,5,‡] B. K. Fujikawa,[6] R. Gaigher,[13] A. Giachero,[12,13] L. Gironi,[12,13] A. Giuliani,[22] L. Gladstone,[23] P. Gorla,[3] C. Gotti,[12,13] M. Guerzoni,[7] M. Guetti,[3] T. D. Gutierrez,[24] E. E. Haller,[8,25] K. Han,[18,6] E. Hansen,[23,2] K. M. Heeger,[18] R. Hennings-Yeomans,[5,6] K. P. Hickerson,[2] H. Z. Huang,[2] M. Iannone,[10] L. Ioannucci,[3] R. Kadel,[26] G. Keppel,[4] Yu. G. Kolomensky,[5,26] A. Leder,[23] C. Ligi,[21] K. E. Lim,[18] X. Liu,[2] Y. G. Ma,[14] M. Maino,[12,13] L. Marini[17,11] M. Martinez,[27] R. H. Maruyama,[18] R. Mazza,[13] Y. Mei,[6] R. Michinelli,[7] N. Moggi,[28,7] S. Morganti,[10] P. J. Mosteiro,[10] T. Napolitano,[21] M. Nastasi,[12,13] S. Nisi,[3] C. Nones,[29] E. B. Norman,[30,31] A. Nucciotti,[12,13] T. O'Donnell,[5,6] F. Orio,[10] D. Orlandi,[3] J. L. Ouellet,[5,6] C. E. Pagliarone,[3,15] M. Pallavicini,[17,11] V. Palmieri,[4] G. Pancaldi,[7] L. Pattavina,[3] M. Pavan,[12,13] R. Pedrota,[32] A. Pelosi,[10] M. Perego,[13] G. Pessina,[13] V. Pettinacci,[10] G. Piperno,[9,10] C. Pira,[4] S. Pirro,[3] S. Pozzi,[12,13] E. Previtali,[13] C. Rosenfeld,[1] C. Rusconi,[13] E. Sala,[12,13] S. Sangiorgio,[30] D. Santone,[3,16] N. D. Scielzo,[30] V. Singh,[5] M. Sisti,[12,13] A. R. Smith,[6] F. Stivanello,[4] L. Taffarello,[32] L. Tatananni,[3] M. Tenconi,[22] F. Terranova,[12,13] M. Tessaro,[32] C. Tomei,[10] S. Trentalange,[2] G. Ventura,[33,34] M. Vignati,[10] S. L. Wagaarachchi,[5,6] J. Wallig,[35] B. S. Wang,[30,31] H. W. Wang,[14] L. Wielgus,[19] J. Wilson,[1] L. A. Winslow,[23] T. Wise,[18,19] A. Woodcraft,[36] L. Zanotti,[12,13] C. Zarra,[3] G. Q. Zhang,[14] B. X. Zhu,[2] S. Zimmermann,[35] S. Zucchelli[37,7]

(The CUORE Collaboration)

[1]Department of Physics and Astronomy, University of South Carolina, Columbia, SC 29208 - USA
[2]Department of Physics and Astronomy, University of California, Los Angeles, CA 90095 - USA
[3]INFN - Laboratori Nazionali del Gran Sasso, Assergi (L'Aquila) I-67010 - Italy
[4]INFN - Laboratori Nazionali di Legnaro, Legnaro (Padova) I-35020 - Italy
[5]Department of Physics, University of California, Berkeley, CA 94720 - USA
[6]Nuclear Science Division, Lawrence Berkeley National Laboratory, Berkeley, CA 94720 - USA
[7]INFN - Sezione di Bologna, Bologna I-40127 - Italy
[8]Materials Science Division, Lawrence Berkeley National Laboratory, Berkeley, CA 94720 - USA
[9]Dipartimento di Fisica, Sapienza Università di Roma, Roma I-00185 - Italy
[10]INFN - Sezione di Roma, Roma I-00185 - Italy
[11]INFN - Sezione di Genova, Genova I-16146 - Italy
[12]Dipartimento di Fisica, Università di Milano-Bicocca, Milano I-20126 - Italy
[13]INFN - Sezione di Milano Bicocca, Milano I-20126 - Italy

[14]Shanghai Institute of Applied Physics, Chinese Academy of Sciences, Shanghai 201800 - China
[15]Dipartimento di Ingegneria Civile e Meccanica, Università degli Studi di Cassino e del Lazio Meridionale, Cassino I-03043 - Italy
[16]Dipartimento di Scienze Fisiche e Chimiche, Università dell'Aquila, L'Aquila I-67100 - Italy
[17]Dipartimento di Fisica, Università di Genova, Genova I-16146 - Italy
[18]Department of Physics, Yale University, New Haven, CT 06520 - USA
[19]Department of Physics, University of Wisconsin, Madison, WI 53706 - USA
[20]INFN - Gran Sasso Science Institute, L'Aquila I-67100 - Italy
[21]INFN - Laboratori Nazionali di Frascati, Frascati (Roma) I-00044 - Italy
[22]Centre de Spectrométrie Nucléaire et de Spectrométrie de Masse, 91405 Orsay Campus - France
[23]Massachusetts Institute of Technology, Cambridge, MA 02139 - USA
[24]Physics Department, California Polytechnic State University, San Luis Obispo, CA 93407 - USA
[25]Department of Materials Science and Engineering, University of California, Berkeley, CA 94720 - USA
[26]Physics Division, Lawrence Berkeley National Laboratory, Berkeley, CA 94720 - USA
[27]Laboratorio de Fisica Nuclear y Astroparticulas, Universidad de Zaragoza, Zaragoza 50009 - Spain
[28]Dipartimento di Scienze per la Qualità della Vita, Alma Mater Studiorum - Università di Bologna, Bologna I-47921 - Italy
[29]Service de Physique des Particules, CEA / Saclay, 91191 Gif-sur-Yvette - France
[30]Lawrence Livermore National Laboratory, Livermore, CA 94550 - USA
[31]Department of Nuclear Engineering, University of California, Berkeley, CA 94720 - USA
[32]INFN - Sezione di Padova, Padova I-35131 - Italy
[33]Dipartimento di Fisica, Università di Firenze, Firenze I-50125 - Italy
[34]INFN - Sezione di Firenze, Firenze I-50125 - Italy
[35]Engineering Division, Lawrence Berkeley National Laboratory, Berkeley, CA 94720 - USA
[36]SUPA, Institute for Astronomy, University of Edinburgh, Blackford Hill, Edinburgh EH9 3HJ - UK
[37]Dipartimento di Fisica e Astronomia, Alma Mater Studiorum - Università di Bologna, Bologna I-40127 - Italy
[‡]Deceased
[†]Spokesperson

Abstract

CUORE is a challenging experiment designed to exploit the cryogenic bolometer technique to reach a sensitivity of the order 10^{26} years on the $\beta\beta(0\nu)$ half-life of ^{130}Te, thus approaching the inverted hierarchy region of the neutrino masses. The detector will consist of a close-packed array of TeO_2 crystals containing $\sim$ 206 kg of ^{130}Te in total and cooled to an operating temperature of $\sim$ 10 mK inside a large, dedicated cryostat.

CUORE has almost completed the construction phase and is now in an advanced stage of installation and commissioning. For more than two years, assembly and commissioning activities have been underway on site. All detector construction-related activities have been completed essentially on schedule. The 19 towers of CUORE are now safely stored underground inside their cases waiting for the final installation inside the CUORE cryostat. The finalization and commissioning of the cryogenic system still represents the most serious challenge towards the final installation of the detector and the start of the data taking. The recently obtained, successful cool down of the CUORE cryostat below the design temperature of 10 mK is therefore a crucial milestone which strengthen the expectations for a successful completion of the commissioning plan in 2015.

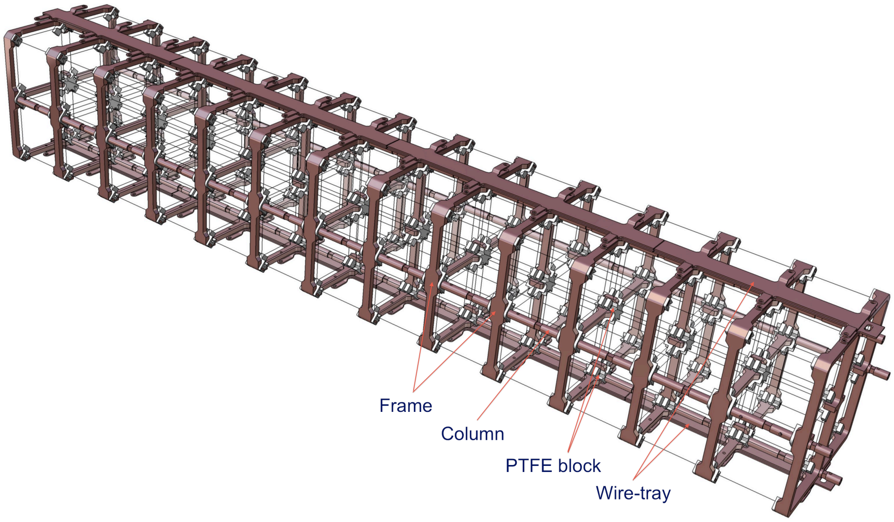

Figure 1: Detailed view of the components of a single CUORE tower.

1 Detector components

The CUORE detector will consist of 988 TeO_2 crystals arranged into 19 identical towers. Each tower will contain 52 crystals held securely inside a copper structure by specially-designed PTFE brackets (Fig. 1).

A temperature sensor (neutron-transmutation doped (NTD) Germanium thermistor) and a Joule heater are glued to one face of each crystal. After a tower is assembled, gold wires are bonded directly from the thermistor and heater to readout ribbons held in specially designed copper trays fixed to the tower structure. A complex procedure for cleaning the tower copper parts—the so-called "TECM" process, based on a sequence of mechanical, electro-chemical, chemical, and magneto-plasma treatments—has been developed in order to guarantee that background contributions from radioactive surface contaminants are reduced to an acceptable level.

A detector-part database has been developed to store relevant information about every component of the CUORE detector, i.e. production time, cleaning history, sea-level exposure time intervals, and so on.

1.1 Crystals

The $5 \times 5 \times 5$ cm^3 TeO_2 crystals were grown at the Shanghai Institute of Ceramics, Chinese Academy of Sciences (SICCAS). Crystal production has proceeded steadily since 2009 at a dedicated clean room facility in Jiading, China, and batches of finished crystals were shipped to LNGS every 1–2 months, traveling by sea to limit cosmogenic activation. All 1063 TeO_2 absorbers have now been delivered to LNGS. After a visual inspection, the delivered crystals are stored in nitrogen-fluxed cabinets in CUORE's underground Part Storage Area (PSA). Of the 1063 delivered crystals only a fraction (24) were found to have some visible internal flaws, whose origin is unknown. These crystals were returned to SICCAS and replaced with new ones.

Approximately 4% of the delivered crystals are tested as cryogenic bolometers to verify their radio-purity and to check overall performance. In these so-called CUORE Crystal Validation Runs (CCVRs), four crystals are randomly selected from the most recent shipments, assembled into a detector module, and cooled to 10 mK inside the CUORE R&D cryostat in Hall C at

LNGS. Each CCVR typically lasts for ~ 1 month, which is the time needed to acquire sufficient statistics to verify that the crystals meet contract specifications. The last CCVR has been performed in summer 2013. All of the tested crystals have met or exceeded the desired energy resolution and the contract specifications for bulk radioactivity and dimensional tolerances. Based on this, we expect all crystals to meet the requirements for CUORE.

In June 2013, three workers from SICCAS spent two weeks at LNGS to reprocess the surfaces of a total of 44 TeO_2 crystals which had been used for CCVRs or which suffered a failure during the gluing procedure. The polishing of the crystal surfaces was accomplished using the same procedures followed at the Chinese plant. Crystals were then vacuum-packed in a double-layered PET bag, before returning to the PSA storage. All crystals have now been assembled into towers.

1.2 NTD thermistors

Each CUORE crystal is instrumented with a NTD Ge thermistor for signal readout. These devices are produced by irradiating pure Ge wafers at the MIT research reactor for precise lengths of time. This procedure dopes the semiconductor very homogeneously and also very close to the metal-insulator transition, a necessary characteristic of these specialized thermistors. After a nine-month radioactive-decay “cool-off” period, the wafers are further processed into sensors at LBNL. To date, more than 1500 CUORE-specific thermistors have been prepared in this manner. About 1000 are needed to fully instrument CUORE, including 988 used for direct event detection and the remainder used for monitoring temperatures around the cryostat.

In August 2013, the assembly team encountered unusual wire-bonding problems with some of the thermistors in Towers 5 and 6 (Towers 1, 2, 3, and 4 were bonded successfully). Wires were not adhering properly to the gold contact pads on the NTDs during the usual ball-bonding process. Rutherford backscattering (RBS) and Secondary Ion Mass Spectrometry (SIMS) measurements conducted on both bondable and problematic NTDs revealed significant contact metal/Ge alloying within the problematic bonding pads. The measurements are consistent with an overheating of the Ge substrate during the vacuum-deposition plating process. Two batches of thermistors that show this phenomenon were identified: those produced in December 2011 and a second set delivered in mid-2013.

In light of this, we have sampled all remaining NTD batches to identify those that are easily bondable prior to gluing the thermistors onto the TeO_2 crystals. We have also developed specific techniques that allow us to successfully wire bond to the alloyed-contact devices that are already installed in towers. Concurrent with this work, we designed and fabricated a new mask for producing all remaining thermistors. The new mask incorporates the use of high thermal-conductivity materials, reflective coatings, and a thermal shield to reduce the overall heat load on the NTDs during contact formation. These improvements have shown to be quite effective and the new mask has subsequently been used to fabricate two new batches of devices.

The remaining towers were then assembled with “certified bondable” NTDs and were successfully wire bonded. The 19 towers of CUORE are now complete and are safely stored underground inside their cases waiting for the final installation inside the CUORE cryostat.

1.3 Copper parts

The copper parts that form the scaffolding for the CUORE detector towers are fabricated in the Milano Bicocca and Legnaro workshops, cleaned at LNL (Laboratori Nazionali di Legnaro) according to a special protocol (see Section 1), and then placed in underground storage at LNGS (PSA) until the time comes for assembly. Both the design of the tower structure and the surface cleaning methods are rather different with respect to those used in Cuoricino. A complete test of

Figure 2: A phase of the chemical cleaning of the CUORE detector suspension plate (TSP).

the copper fabrication, cleaning, and assembly sequence was possible only via the construction and operation of the CUORE-0 tower.

The production of all the copper parts for the 19 towers of CUORE and a some spare parts was completed by the end of 2013. Based on the successful completion of the detector parts cleaning plan and in order to exploit the experience of the Legnaro group, the possibility to clean with the same accuracy the cryostat interfaces was discussed at the end of 2013. Many of these components directly face or are very close to the detector and special care was devoted to their preparation (material procurement, machining and cleaning) with radio-purity constraints comparable with those of the detector parts. A full inventory and detailed cleaning plan together was completed in Spring 2014. The inventory included:

- the tower support plate (TSP) together with a large number of ancillary parts for the routing and shielding of the sense wires from the detectors
- the detector copper cage and its ancillary parts (screws and supporting elements)
- lowest part of the cold lead shield on the top of the detector
- terminations of the suspending systems of the TSP and of the above mentioned lead shield.

In September 2014, a new chemical plant and an upgrade the old plasma system was completed and the Legnaro group started to clean the more than 2200 copper cryostat components. In order to reduce the cleaning time and respect the CUORE schedule, three protocols were implemented: chemical low protocol, chemical high protocol, and the standard CUORE protocol. The chemical low protocol consists in pre-cleaning plus cold chemical etching. The chemical high protocol proposes pre-cleaning, chemical etching and SUBU. The standard CUORE protocol references to pre-cleaning, tumbling where possible, electropolishing, SUBU and plasma cleaning. These protocols replace the original plan to apply a polyethylene wrap to the most critical copper interfaces. Selection of the protocol was based on the position of the component inside of cryostat, and the distance from the detector. The Detector interface copper components, top lead, suspension, thermalization, TSP (fig. 2), wiring, DCS, FCS, Top Shield, Bottom Shield) were completed in December 2014. The last components, Side Shields, MC Vessel, Fast Cooling, will be completed by May 2015. After the completion of the cryostat components, the spare tower copper parts, presently stored in the Baradello cave, will be cleaned.

2 Electronics and data acquisition

The goal of the CUORE electronics is to provide an effective low-noise system for reading and monitoring CUORE detectors. It is interfaced to the CUORE data acquisition system (DAQ) which records the data and provides a link with the slow-control and data analysis tools.

2.1 Front-end electronics

The Front-end electronics system is almost complete with only a couple components waiting for their final testing. The design of the system was done at INFN of Milano-Bicocca, the production was done at the University of South Carolina, while testing and calibration was done at the University of California at Los Angeles, and at INFN Milano-Bicocca. The system consists of several sections. From the detectors to the DAQ system, they can be listed as:

- the connecting links between the detectors and the mixing chamber
- the connecting links between the mixing chamber and the room temperature connectors on the fridge
- the connections between the fridge connectors and the very front-end inputs
- the preamplifiers
- the very front-end, located on the mainboards, on top of the fridge
- the antialising filters, close to the DAQ system

In addition to the components for extracting data from the detectors, a pulser/DC generator is used to correct gain instabilities. This device is a very stable voltage source capable of generating pulses and DC signals with a very high stability, at the level of a ppm/ °C. The power supply to all these boards consists of a 3 stages system: AC/DC, DC/DC and the linear power regulator, several units are provided.

All the listed parts are fully programmable and can also be monitored thanks to a series of 32 bit CISC ARM micro-controllers located on the boards themselves. Communication between the micro-controllers and the DAQ is through a CAN-bus interface on fiber optics. A series of additional secondary boards such as backplanes and similar, have also been developed.

All the the Front-end main boards, the Bessel filter boards, the Pulser boards and the power supply DCDC and linear regulators were produced and tested. The full set of Bessel boards has also been already pre-installed in Milan and delivered to LNGS (see fig.3). Pre-installation of the main boards is ongoing. Presently, the only part still in production is the FE underplane, a secondary board to provide the power supply distribution to the FE main boards. These units are expected to be available in spring 2015.

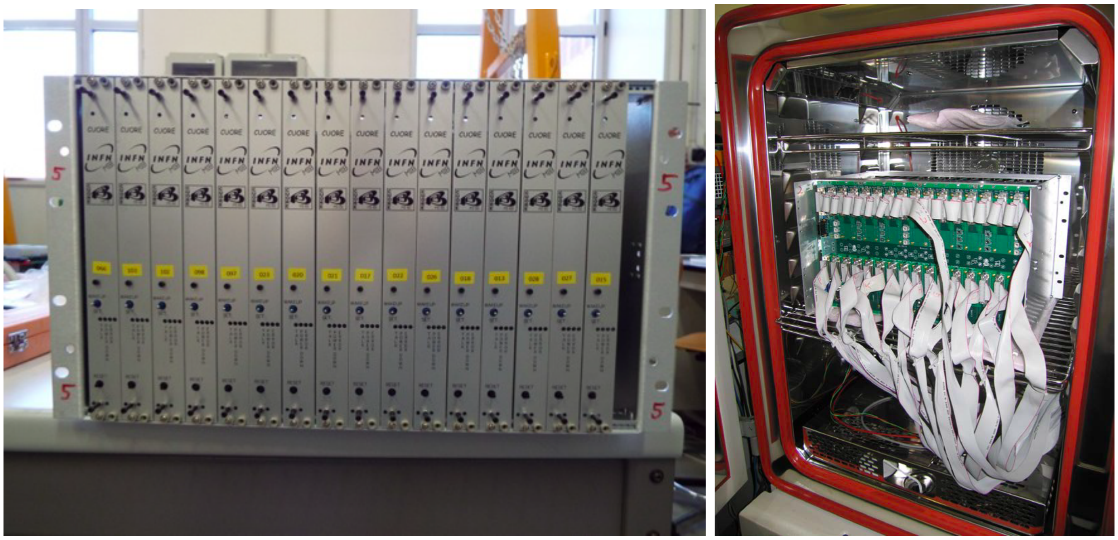

Figure 3: One of the crates with the bessel filters (left) and the climatic chamber used for the front-end pre-installation tests (right).

2.2 Faraday cage

The Faraday Cage is mainly needed to shield the high-impedance signal links between the detectors and the front-end electronics from disturbances coming from the main power line (50 Hz), cryogenic pumps and all other EMI interferences which may be injected from the outside. Located on the second floor of the CUORE building, the cage will exploit the existing vertical beams (building steel work) as a mechanical support. The current design consists of a room 6x6 m^2 wide, 2.5 m tall, made of panels chosen for their shielding properties supported by Aluminum profiles. The interfaces between panels were optimized with simulations.

The shielding panels (Skudal S3022 by Selite) are currently being manufactured by the company. The panels are made of Skudotech, a flexible high magnetic permeability material, held between Aluminum layers, with a total thickness of 5 mm and a weight of about 15 kg per square meter. The order for the Aluminum profiles to support the panels was also placed. All the hardware needed to mount the Faraday room is expected to be ready before summer 2015.

2.3 Slow control

The CUORE Slow Control System (CUORE-SCS) development is carried out by the INFN groups of Bologna, LNGS, Milano-Bicocca, by the University of Cassino and Southern Lazio and by the US group at MIT. The Cassino Group has developed the CUORE-Cryogeny Monitor and Control System (CMCS) and part of the related equipment and acquisition system. TheCMCS is a LabView based slow control system that fully acquire and monitor all the parameters coming from the CUORE-Cryogeny instrumentation (Thermometry and related readout electronics, Pressure Gauges, Pulse Tubes, Fast Cooling System, Cryomech Compressors, Diluition Unit, Gas Handling Systems, Vacum Pumps, Gas Blowers, Water cooling System) and takes active decisions on all the vital components of the CUORE Cryogenic System. All the information coming from the mentioned devices reach the CMCS Rack where the cryogenic temperature monitors (AVS 47B, LakeShore 218 TM, etc.), Thermometer Remapping Boxes (TRB), controllers for pumps, valves and other devices are located. The heart of the CMCS is aReal Time NI PXI Express with its modules that allow us to acquire and control each single

CUORE-Cryogeny device.

The LabVIEW data from the CMCS is logged to a local computer. The MIT group then copies this data to a general slow monitoring computer where it is archived and uploaded to a MongoDB database. This database is part of the CORC system which provides high level viewing through a webpage for both the data acquisition and slow monitoring system, especially for shifters. The development of the high level interface is ongoing by the MIT group.

To ensure that the whole system runs smoothly, the Bologna group has setup a Nagios monitoring system onsite onsite. Nagios is an open-source package that has the ability to remotely monitor: services (ssh, http, tcp/udp ports, ping...), resources (CPU load, disk space, memory, swap, single processes...) and network devices (host, switch, routers...). It is used within the slow-control system to monitor:

- that each LabView VI is running (either on pc or PCI) and updating the data sent to upper level;
- that CORC is active;
- that the relevant databases are running (and eventually their metrics);
- that the DAQ system is running;
- that the internal network is active.

Nagios runs inside the CUORE internal network and pushes the information collected there to an external instance that can be reached from the internet. The status of monitored systems is shown on a web page. Additionally, in case of problems or failures, emails will be automatically sent to the people in charge of the various subsystems.

3 Data acquisition system

All the hardware for the CUORE data acquisition system is now procured. The system has been pre-installed in Genova and is ready for delivery at LNGS. It is composed by 66 NI-PXI-6284 digitizer boards, for a total of 1056 analog input channels. The digitizer boards are hosted in six PXI chassis that are contained in two rack cabinets (3 chassis each). These two rack cabinets also contain the DAQ-Bessel interface boards. A third rack cabinet hosts the six computers dedicated to the data readout (one per chassis) and the event builder computer. The three DAQ rack cabinets will be delivered to LNGS and placed on the second floor of the CUORE hut as soon as the CUORE faraday room installation will be complete.

4 Readout system for the commissioning of the CUORE cryostat

A complete readout system for the commissioning of the CUORE cryostat was installed in the second floor of the CUORE hut in decembre 2014. The detectors have been organized in what was called mini-tower, consisting in 31 channels (8 bolometers plus diagnostic NTD thermometers). This was a very good occasion to test the Electronics and the DAQ systems, as we installed a full, although reduced in quantity, readout system. Several achievements have been obtained: system layuout, pre-installation, installation, working condition, detector characterization and signal acquisition. The readout system consisted in:

- A set of 6 fridge to very front-end cables: the mini-tower and the thermometers were connected on several output ports.
- One complete very front-end chassis hosting 13 complete boards, 76 channels, of which only 31 connected to the detectors. The chassis was competed by its linear power supplies. We used a complete chassis because the detector channels were distributed over several cables from one side, and to study the working condition in the experimental area on the other side (input channels not connected to the detectors can be shorted to ground).
- One chassis hosting 7 CUORE Bessel filter boards, 84 channels.
- One calibration CUORE pulser board, with 4 pulser channels.
- A complete usb to can bus communication system between the DAQ and every board for slow control. A set of, specially developed, glue boards were used to convert to fibre optic the electrical digital signals.
- A supply chain consisting of an ACDC followed by DCDC and a filter to supply the linear power supply.
- One chassis with 5 digitizer boards, 80 channels total. Four boards were for standard bolometer signal readout, while the last board was devoted to tests of a PID system for the temperature stabilization of the detectors.
- One chassis hosting 4 DAQ-Bessel interface boards, 96 channels total.

The DAQ, Bessel, and DAQ-Bessel interface chassis were hosted in a rack cabinet, that also hosted a power distribution unit. The front end and pulser boards were placed on top of the 300 K flange of the CUORE cryostat, over the Y-beam. The signal connection between the front end and the Bessel boards, and between the Bessel boards and the DAQ-Bessel interface boards, was made of commercial DB-25 shielded cables. The signal connection between the DAQ-Bessel interface boards and the DAQ boards was made with commercial NI-SHC68 shielded cables. The CUORE data acquisition and electronics control software was hosted on a dedicated computer. The data transmission between the DAQ chassis and computer was provided by a commercial optical link (NI-PCI-PXI-8336).

The installed readout system was successfully used during the commissioning test of the CUORE cryostat (Run2, december 2014). This was the first time that the CUORE electronics was used for the readout of bolometric detectors. An extensive test of the readout system could not be performed as the cryogenic system was maintained cooled for a short time. However, a lot of useful information could be obtained. The basic functionalities of all the components of the system were successfully checked, and only a few minor bugs in software and firmware have been identified and solved. Apart for minor improvements, the readout system is ready for being used for the next cold commissioning run of the CUORE cryostat, foreseen for summer 2015.

5 Cryogenics

In September 2014 the cryostat reached ∼6 mK under stable conditions. This was a major milestone for the cryogenic commissioning. The cryostat performance was then characterized and a cooling power at 10 mK that fully matches the experimental requirements, was eventually

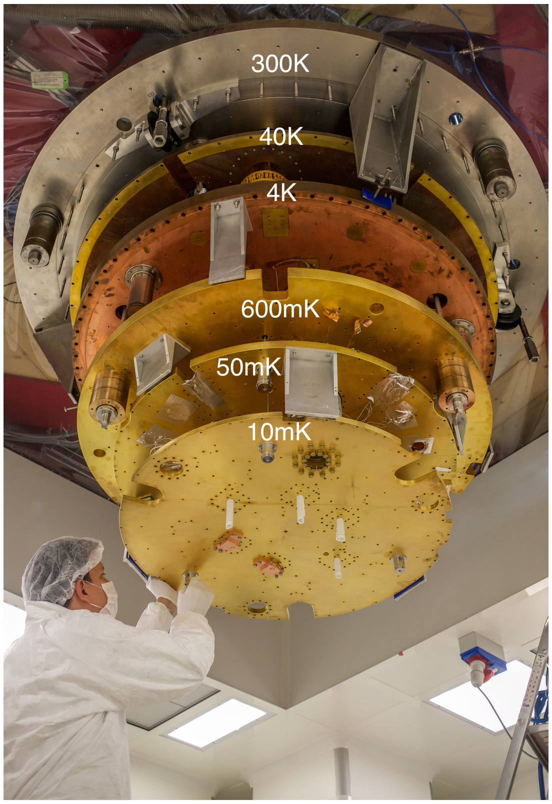

Figure 4: Global view of all the cryostat plates.

measured. This completed the first (Run 1) of the three successive cool downs to base temperature which characterize the Phase 2 of the cryogenics commissioning. Each run is characterized by an increasing level of complexity due to the addition of new elements of the cryogenic system. The preparation of Run 2 (inclusion of the wiring system) was immediately started. A thousand of readout channel for the CUORE detectors were successfully installed.

The start of Run 2 cool down is expected for mid November 2014. Meanwhile the preparation of the components for Run 3 (full load) is progressing with the machining of the Roman lead for the cold shields and the recent delivery at LNGS of the Fast Cooling System for the last phase of commissioning.

5.1 Installation and test of the cryogenic set-up

Phase 2 of the Cryostat commissioning is devoted to the test and optimization of all the components of the cryostat (plates, vessels, wires, Pb shields, and suspensions, fig. 5) at base temperature, before the installation of the 19 towers. Run 1 of Phase 2, the so called “no load test run”, was focused on reaching a stable base temperature on the 10 mK vessel and plate and showing the aspected cooling power. The Run was actually the sum of 3 successive cool downs in which the system was debugged to the level of meeting the CUORE specifications. In run 1.3 the 10 mK vessel reached the expected temperature and actually the record temperature of 6 mK with the $\sim$400 kg of copper of the innermost vessel and plate. This is by far the largest mass ever cooled to this temperature.

The characterization of the system at base T showed the expected cooling power ($\sim$10 μW) at 10 mK. After the conclusion of Run 1.3, in September 2014 the preparation for Run 2, the

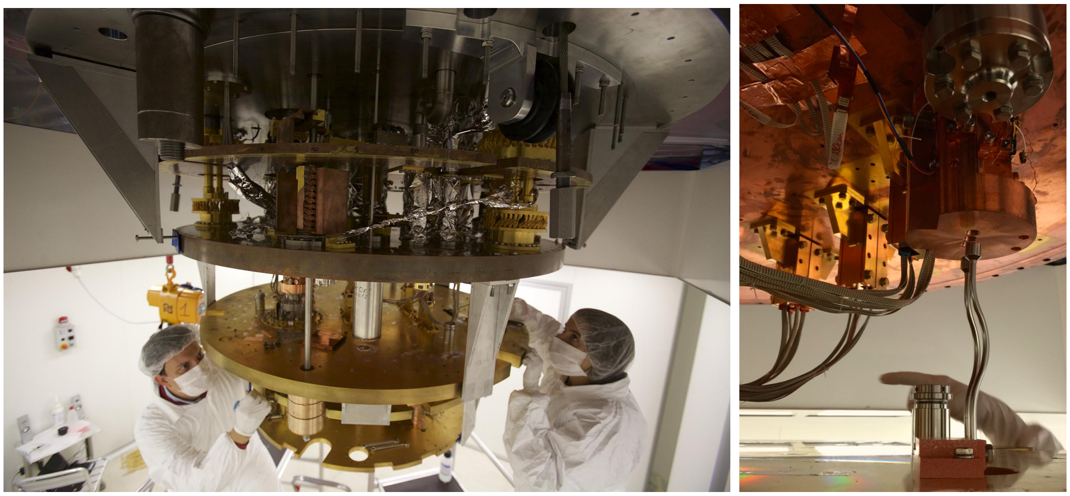

Figure 5: Details of the internal sections of the cryostat

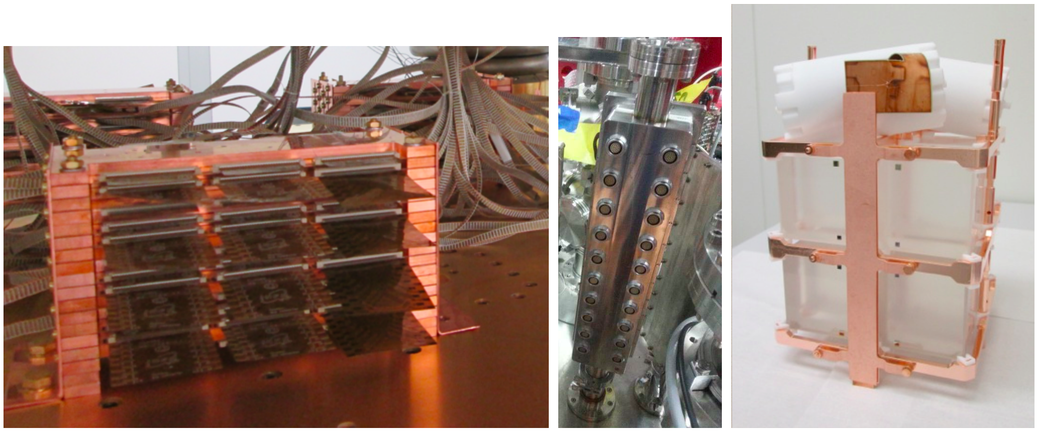

Figure 6: Cryostat wiring system: details of one of the 5 junction boxes (left) and of one of the room temperature connector boxes (center). The 2-floor CUORE test tower installed in run 2 (right).

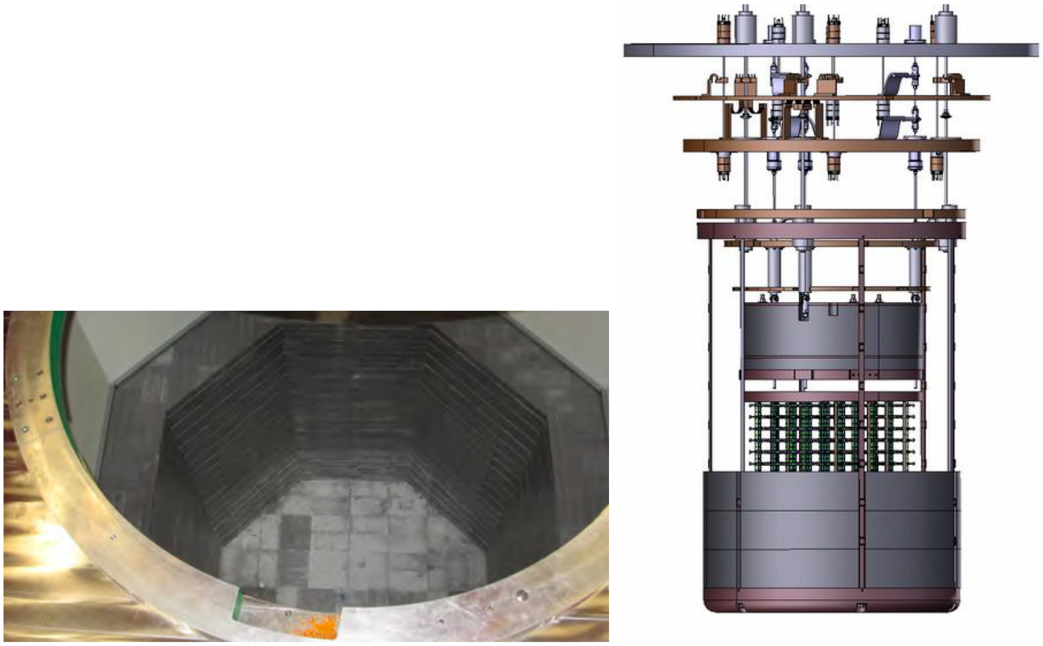

Figure 7: Top view of the room temperature ("external") shield (left). The missing 1/3 of the modern lead side wall is going to be installed in the upcoming weeks.Scheme of the ancient roman lead cold shield (right).

so called Wire Test Run, was started.

The full set of wires for the CUORE bolometers was installed, including all the detector thermistors, heaters and thermometry channels ($\sim$ 3500 wires). All the wires, divided in 6 output Fischer boxes, were properly thermalized at each T step (4 K, 600 mK, and 50 mK) and connected to the Junction Boxes on the 10 mK plate (Fig. 6). All the wires were electrically tested for continuity and grounding.

A revamping of the IVC and OVC thermometry for full cryostat cool down and operation monitoring (over 60 thermometers) has been completed. This includes different kinds of thermometers for the different T stages: silicon diodes are used for the 300 K - 2 K range, Ruthenium oxide sensors are used from few K down to 50 mK. Fixed Point Sensor and two CMN thermometers were installed on the 10 mK plate for T <40 mK. Also, recently a Noise Thermometer was installed on the 10 mK for base T monitoring. It should provide complementary information with respect to the CMN. The start of the Run 2 cool down procedure is expected for mid November. It includes also the first measurement with an actual detector: a "mini-tower" (2 floors, fig. 6 right) assembled with the same parts and procedures of CUORE. It will be also read-out with a full CUORE electronics and DAQ chain.

5.2 External Shield

The external shield is designed to screen the cryostat from environmental neutrons and γ's. Neutron thermalization and absorption is achieved by a borated polyethylene terephthalate (PET) floor and by lateral walls of PET followed by boric-acid powders, which are poured in plastic frames. The B-PET shield is followed by lead blocks. To ease its installation on the ground floor of the hut, the steel structure holding the shield was divided into three horizontal rings. The rings were produced by Comasud (Teramo, Italy) and delivered to LNGS. The

Figure 8: Part of the ready-to-mount detector towers in their storage inside the CUORE clean room.

installation of the shield was interleaved with commissioning activities at the ground floor of the CUORE building. The shield is presently completely installed, apart from one third of the lateral lead ring that will be installed during cold Run 2, after all the vessels will be installed back on the cryostat (fig. 7 left).

5.3 Cold Lead shield

The cold lead shield is designed to screen the detector from the residual environmental γ radioactivity (unshielded by the external lead shield) and from the radioactivity of the cryostat components. It consists of 30 cm thick (modern) lead disk (and its copper supporting and thermalizing structure) on the top, and a 6 cm thick cylindrical structure (side and bottom) realized with ancient lead from a roman ship sunk near Oristano (fig. 7 right). 270 ingots were granted to INFN in exchange for the recovery of 1000 ingots and a series of archeometric measurements on the lead samples. Ingots could be melted after cutting the top part with the roman inscriptions. Roman lead ingots are covered with a thick layer of fouling and has therefore to be cleaned before melting. The ingots cut have been performed in the last months at LNGS using a proper band saw. Ingots cleaning will be performed in the next days by an italian company with a cryoblasting technique based on the use of dry ice. The resulting ingots will be transferred within the end of this year to a german company where they will be melted with a specially designed technique characterized by a controlled atmosphere (nitrogen flux) and minimum machining to get the requested mechanical tolerances.

6 Detector assembly

The assembly of the CUORE detector towers started in late February 2013. The aim was to complete all 19 towers by Summer 2014. Apart from minor details, the assembly of the 19th tower was completed in the second half of July 2014, in excellent agreement with the CUORE schedule. The 19 CUORE towers are presently stored in the underground CUORE building waiting for their installation inside the CUORE cryostat during the summer 2015 (fig. 8). The details of the assembly procedure were amply described in previous reports. Except for cleaning, all of the activities have been carried out inside the clean room on the first floor of the CUORE hut. The assembly of the detector has been an excellent example of a successful collaboration effort characterized by a very good organization and an effective share of the resources.

7 CUORE-0

The goal of CUORE-0 is to test the mechanical assembly and cleaning procedures developed for the CUORE detector. CUORE-0 is a single CUORE tower built in full accordance with the CUORE procedures and using the CUORE assembly line. After solving a number of serious problems related to the aging cryogenic setup of CUORICINO, the detector was finally successfully cooled down in March 2013. It is expected that with a little more than one year of CUORE-0 physics data that the experiment will exceed the sensitivity of CUORICINO. As of the writing of this report, we are preparing to release this result.

7.1 Detector operation

After we reached the base temperature of $\sim$10 mK on all the detectors, in April 2013 the detector optimization phase started. A lot of effort was spent in order to understand and reduce all possible sources of noise that worsen the performance of the detectors.

At the end of April 2013, data taking started. Even though some interruptions occurred due to cryostat maintenance, we run the detector for 4 months, up to the end of August 2013, collecting a total statistics of 6.86 kg·y. After the long maintenance stop in September 2013, the operating conditions of the cryogenic system have dramatically improved and the system was run smoothly for about 1 year, with a run time efficiency of $\sim$80% (Phase II). On October 2014 the data taking was stopped, in order to further maintain the cryogenic system, and the data taking resumed on November 7th. CUORE-0 data taking continues with several special calibrations until CUORE data taking starts.

As was reported in previous reports, the total spectrum obtained by summing all calibration spectra of all active channels (49 out of 52) acquired during Phase II shows a FWHM resolution at 2.615 MeV of 4.8 keV, demonstrating that the 5 keV CUORE goal is reached. An exposure of 18.1 kg·y ($\sim$5 kg·y of ^{130}Te) was obtained in the period from March 2013 until May 2014 (Phase I + Phase II). The background rate in the α continuum is 0.020 ± 0.001counts/(keV·kg·y), that is a factor of $\sim$6 less than CUORICINO (0.110 ± 0.001counts/(keV·kg·y). The background rate in the ROI is 0.063 ± 0.006 counts/(keV·kg·y) (was 0.153 ± 0.006 counts/(keV·kg·y) in CUORICINO. This corresponds to a background reduction in the ROI of a factor of $\sim$2.5 with respect to CUORICINO. These results validate the enhanced cleaning and assembly techniques undertaken for CUORE and confirm the background model developed from CUORICINO.

The expected CUORE-0 sensitivity surpassed the sensitivity of the CUORICINO in February 2015. The collaboration anticipates releasing a CUORE-0 result shortly.

8 Publications in 2014

1. D.R. Artusa *et al.*, "Initial performance of the CUORE-0 experiment", Eur.Phys.J. C **74** (2014) 8, 2956.
2. D.R. Artusa *et al.*, "Searching for neutrinoless double-beta decay of ^{130}Te with CUORE', Adv.High Energy Phys. (2015) 879871.
3. D.R. Artusa *et al.*, "Exploring the Neutrinoless Double Beta Decay in the Inverted Neutrino Hierarchy with Bolometric Detectors", Eur.Phys.J. C **74** (2014) 10, 3096.

DAMA

Collaboration:

P. Belli[a], R. Bernabei[a,@], A. Bussolotti[a,*], S. d'Angelo[a,**], A. Di Marco[a], F. Emiliani[a], F. Montecchia[a], A. d'Angelo[b], F. Cappella[b], A. Incicchitti[b], A. Mattei[b,*], O.G. Polischuk-Shkulkova[b,g], R. Cerulli[c], V. Caracciolo[c], S. Castellano[c], C.J. Dai[d], H.L. He[d], H.H. Kuang[d], X.H. Ma[d], X.D. Sheng[d], R.G. Wang[d], Z.P. Ye[d,e]

in some detector developments, by-product results and small scale experiments: A.S. Barabash[r], R.S. Boiko[g], V.B. Brudanin[h], D.M. Chernyak[g], F.A. Danevich[g], E. Galenin[n], E.N. Galashov[l], A. Gektin[n], V. Isaienko[i], V.V. Kobychev[g], S.I. Konovalov[r], G.P. Kovtun[m], N.G. Kovtun[m], B.N. Kropivyansky[g], V.M. Kudovbenko-Mokina[g], M. Laubenstein[c], S. Nisi[c], D.V. Poda[c,g], R. B. Podviyanuk[g], A.P. Shcherban[m], V.N. Shlegel[l], D.A. Solopikhin[m], Yu.G. Stenin[l], J. Suhonen[o], A.V. Tolmachev[q], S. Tkachenko[n], V.I. Tretyak[g], I.A. Tupitsyna[n], V.I. Umatov[r], Ya.V. Vasiliev[l], I.M. Vyshnevskyi[g], R.P. Yavetskiy[q]

in some studies on $\beta^+\beta^+$, EC/β^+, EC/EC decay modes (under the joint Indo-Italian DST-MAE project and inter-universities agreement): P.K. Raina[p], A.K. Singh[p], P.K. Rath[p], S. Ghorui[p]

[a]Dip. Fisica, Univ. Roma "Tor Vergata" and INFN Tor Vergata, 00133 Roma, Italy.
[b]Dip. Fisica, Univ. Roma "La Sapienza" and INFN-Roma, 00185 Roma, Italy.
[c]Laboratorio Nazionale del Gran Sasso, INFN, 67010 Assergi (Aq), Italy.
[d]IHEP, Chinese Academy of Sciences, P.O. Box 918/3, Beijing 100049, China.
[e]Physics Dept, Jing Gangshan University 343009, Jiangxi, China.
[g]Institute for Nuclear Research, MSP 03680, Kiev, Ukraine.
[h]Joint Institute for Nuclear Research, 141980 Dubna, Russia.
[i]National University of Kyiv-Mohyla Academy, 04655 Kyiv, Ukraine
[l]Nikolaev Institute of Inorganic Chemistry, 630090 Novosibirsk, Russia.
[m]National Science Center Kharkiv Institute of Physics and Technology, Kharkiv, Ukraine.
[n]Institute for Scintillation Materials, 61001 Kharkiv, Ukraine.
[o]Dep. of Physics, University of Jyvaskyla, P.O. Box 35, FIN-40351, Jyvaskyla, Finland
[p]Indian Institute of Technology, Kharagpur, India.
[q]Institute for Single Crystals, 61001 Kharkiv, Ukraine
[r]Institute of Theoretical and Experimental Physics, 117259 Moscow, Russia
[@] Spokesperson; * technical staff; ** deceased.

Abstract

DAMA is as an observatory for rare processes located deep underground at the Gran Sasso National Laboratory of the I.N.F.N. (LNGS) that develops and exploits low background scintillators. In 2014 the main experimental activities have been performed with:

i) the second generation DAMA/LIBRA set-up (sensitive mass: $\simeq$ 250 kg highly radiopure NaI(Tl)), upgraded in 2008, 2010 and at the end of 2012; ii) the DAMA/LXe set-up (sensitive mass: $\simeq$ 6.5 kg liquid Kr-free Xenon enriched either in ^{129}Xe or in ^{136}Xe); iii) the DAMA/R&D set-up (a facility dedicated to perform relatively small scale experiments, mainly investigating double beta decay modes in various isotopes); iv) the DAMA/Ge set-up (mainly dedicated to sample measurements and to specific measurements on rare processes); some activities are also performed with the detector Ge-Multi of the STELLA facility; v) a small set-up (named DAMA/CRYS) for prototype tests and detectors' qualification. The main DAMA activities during 2014 are summarized in the following.

1 DAMA/LIBRA

DAMA/LIBRA (Large sodium Iodide Bulk for Rare processes) is a unique apparatus for its sensitive mass, target material, intrinsic radio-purity, methodological approach and all the controls performed on the experimental parameters (c.f.r. [1, 2, 3, 4, 5, 6, 7, 8, 9, 10, 11] and the 2014 publication list). It is the successor of DAMA/NaI [12, 13, 14, 15, 16, 17, 18, 19, 20, 21, 22, 23, 24], with a higher exposed mass, higher duty cycle and increased sensitivity. The main goal of DAMA/LIBRA is the investigation of the Dark Matter (DM) particles in the galactic halo by exploiting the DM model independent annual modulation signature [25, 26].

The granularity of the apparatus (25 detectors in a matrix 5×5) is an important feature to study Dark Matter and for background identification since Dark Matter particles can just contribute to events where only one of the 25 detectors fires (*single-hit* events) and not to whose where more than one detector fire in coincidence (*multiple-hit* events). The apparatus has also the unique feature (as well as DAMA/NaI) that gamma calibrations are regularly performed down to the software energy threshold in the same conditions as the production runs, without any contact with the environment and without switching-off the electronics. The high light yield and other response features have allowed working in a safe and reliable way down to 2 keV (DAMA/LIBRA- phase1). At the end of 2010 new photomultipliers (PMTs) with higher quantum efficiency [6] have been installed, some other optimizations have been done and the data taking of DAMA/LIBRA-phase2 then started. Among the scientific goals of this set-up we also recall here: i) investigation with high sensitivity of the DM particle component in the galactic halo by the model independent approach known as DM annual modulation signature, with highly precise determination of the modulation parameters (which carry crucial information); ii) corollary investigations on the nature of the candidate and on the many possible astrophysical, nuclear and particle physics scenarios; iii) investigations on other possible model dependent and/or model independent approaches to study Dark Matter particles, second order effects and some exotic scenarios; iv) improved search for processes of Pauli exclusion principle violation in ^{23}Na and ^{127}I; v) search for possible electric charge non-conservation (CNC) processes, as the electron decay into invisible channels and in the $e^- \to \nu_e + \gamma$ channel, and excitations of nuclear levels of ^{23}Na and ^{127}I after CNC electronic capture, ... ; vi) search for possible nucleon, di-nucleon and tri-nucleon decay into invisible channels in ^{23}Na and ^{127}I; vii) search for solar axions by Primakoff effect in NaI(Tl); viii) search for nuclear rare decays in ^{23}Na, ^{127}I and Tl isotopes (as e.g. superdense states, cluster decay, ...); ix) search for neutral particles (QED new phase) in ^{241}Am decays, etc.

Most of these investigations require further dedicated data taking and high exposure to reach competitive sensitivities. As regards the DM features, which can be suitably exploited further collecting very large exposure, see e.g. the Sect 6 of Ref. [17] and the Appendix of Ref. [2]. In particular, the latter shows how the decreasing of the software energy threshold as in the present

DAMA/LIBRA-phase2 offers the unique possibility to investigate the modulation amplitude at the lowest energy, where a discrimination power can disentangle among many of the possible DM scenarios.

1.1 Final model-independent result of DAMA/LIBRA-phase1 on DM annual modulation

The results obtained with the total exposure of 1.04 ton × yr collected by DAMA/LIBRA-phase1 during 7 annual cycles have been presented at international conferences and the paper on the final model independent result of DAMA/LIBRA-phase1 was published [4].

Fig. 1 shows the time behaviour of the experimental residual rates of the *single-hit* scintillation events measured by DAMA/LIBRA–phase1 in the (2–4), (2–5) and (2–6) keV energy intervals as a function of the time.

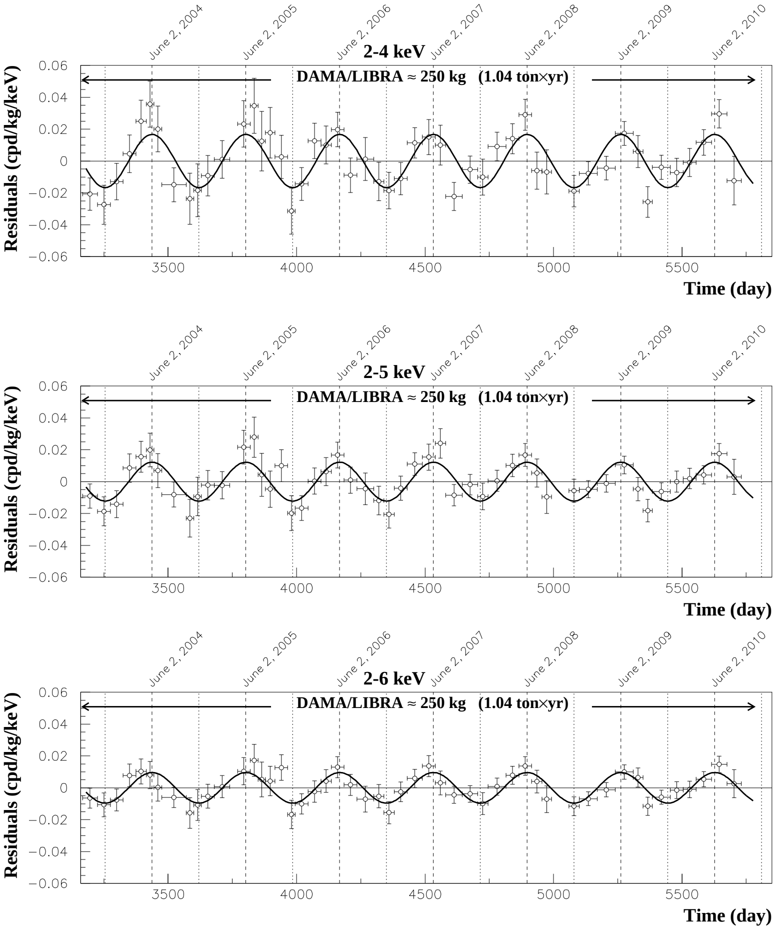

Figure 1: Experimental residual rate of the *single-hit* scintillation events measured by DAMA/LIBRA–phase1 in the (2–4), (2–5) and (2–6) keV energy intervals as a function of the time. The time scale is maintained the same of the previous DAMA papers for coherence. The data points present the experimental errors as vertical bars and the associated time bin width as horizontal bars. The superimposed curves are the cosinusoidal functions behaviours $A\cos\omega(t-t_0)$ with a period $T = \frac{2\pi}{\omega} = 1$ yr, a phase $t_0 = 152.5$ day (June 2^{nd}) and modulation amplitudes, A, equal to the central values obtained by best fit on the data points of the entire DAMA/LIBRA–phase1. The dashed vertical lines correspond to the maximum expected for the DM signal (June 2^{nd}), while the dotted vertical lines correspond to the minimum.

tion events in the (2–4), (2–5) and (2–6) keV energy intervals for the complete DAMA/LIBRA–phase1. The residuals of the DAMA/NaI data (0.29 ton × yr) are given in Refs. [2, 16, 17]. We remind that these residual rates are calculated from the measured rate of the *single-hit* events after subtracting the constant part: $< r_{ijk} - flat_{jk} >_{jk}$. Here r_{ijk} is the rate in the considered i-th time interval for the j-th detector in the k-th energy bin, while $flat_{jk}$ is the rate of the j-th detector in the k-th energy bin averaged over the cycles. The average is made on all the detectors (j index) and on all the energy bins (k index) which constitute the considered energy interval. The weighted mean of the residuals must obviously be zero over one cycle.

In general it is worth noting that rejection strategies cannot safely be applied to the data when a model-independent signature based on the correlation of the measured experimental rate with the Earth galactic motion is pursued; in fact, the effect searched for (which is typically at level of few %) would be largely affected by the uncertainties associated to the rejection procedure. On the other hand, the signature itself acts as an effective background rejection.

The DAMA/LIBRA-phase1 data give evidence for the presence of DM particles in the galactic halo, on the basis of the exploited model independent DM annual modulation signature by using highly radio-pure NaI(Tl) target, at 7.5 σ C.L.. Including also the first generation DAMA/NaI experiment (cumulative exposure 1.33 ton × yr, corresponding to 14 annual cycles), the C.L. is 9.3 σ. At present status of technology the DM annual modulation is the only model independent signature available in direct dark matter investigation that can be effectively exploited. All the many specific requirements of the signature are fulfilled by the data and no systematic or side reaction able to mimic the exploited DM signature is available (see e.g. Refs.[2, 3, 4, 15, 16, 17, 27, 28, 29, 30, 31, 32, 7] and the 2014 publication list). In particular, only systematic effects or side reactions simultaneously able to fulfil all the specific requirements of the DM annual modulation signature and to account for the whole observed modulation amplitude could mimic this signature; thus, no other effect investigated so far in the field of rare processes offers a so stringent and unambiguous signature.

Studies on other DM features, second order effects, and several other rare processes are in progress with the aim to reach very high sensitivity. Studies for measurements with data taking dedicated to other rare processes are continuing.

It is also worth noting that in the DM field DAMA/LIBRA is the set-up still having the highest intrinsic radio-purity, the largest exposed sensitive mass[1], the largest collected exposure, the deepest controlled running condition and stability, and the only one with highly sensitive ULB (Ultra-Low Background) NaI(Tl) detectors.

The DAMA obtained model independent evidence is compatible with a wide set of scenarios regarding the nature of the DM candidate and related astrophysical, nuclear and particle Physics. For example, some of the scenarios available in literature and the different parameters are discussed in Refs. [16, 17, 13, 18, 19, 20, 21, 22, 23, 5, 33, 34] and in Appendix A of Ref. [2]. A further large literature is available on the topics; many possibilities are open.

No other experiment exists, whose result – at least in principle – can directly be compared in a model independent way with those by DAMA/NaI and DAMA/LIBRA. In particular, all the results presented so far in the field are not in conflict with the model independent DM annual modulation result of DAMA in many scenarios, also considering the large uncertainties in theoretical and experimental aspects, the same holds for indirect approaches; see e.g. some arguments in 2014 publication list and quoted references.

---

[1] In this case the sensitive mass is the total mass of the NaI(Tl) crystals and not a reduced fiducial mass.

1.2 DAMA/LIBRA-phase2

- During 2014 DAMA/LIBRA has continued to take data in the new phase2 configuration with the PMTs of higher quantum efficiency [6] and new preamplifiers.
- In September 2014 DAMA/LIBRA-phase2 has concluded the data taking of the 3th full annual cycle, and started the data taking of the 4th cycle.
- Designs for the developments of some other new electronic modules were realized for further implementation of the apparatus for low energy studies.
- A further review paper on the results of DAMA/LIBRA-phase1 has been published. There, after summarizing some introductory arguments, a review of the already released model independent positive results by the DAMA/NaI and DAMA/LIBRA setups is presented and discussed in various aspects.
- Studies on other DM features, second order effects, and several other rare processes are in progress with the aim to reach very high sensitivity thanks to the progressive increasing of the exposure. In particular, the analyses on possible diurnal effect in the DAMA/LIBRA-phase1 data have been concluded and the paper published (see Sect. 1.2.1).
- A paper which summarizes in a simple and intuitive way why the neutrons, the muons and the solar neutrinos cannot give any significant contribution to the DAMA annual modulation results has been released (see Sect. 1.2.2). A number of these arguments have already been presented in individual papers; they are recalled there. Afterwards, few simple considerations are summarized which already demonstrate the incorrectness of the claim reported in PRL 113 (2014) 081302.
- Studies for further measurements with dedicated data taking to investigate other rare processes are continuing.

1.2.1 Model independent result on possible diurnal effect in DAMA/LIBRA–phase1

Search for possible diurnal effect in the *single-hit* low energy data collected by DAMA/LIBRA–phase1 (total exposure: 1.04 ton × yr) has been carried out both in terms of sidereal and solar time. Actually a diurnal effect with the sidereal time is expected for DM because of Earth rotation. This effect is model-independent and has several requirements as the DM annual modulation effect does. The interest in this signature is that the ratio R_{dy} of this diurnal modulation amplitude over the annual modulation amplitude is a model independent constant; considering the LNGS latitude one has:

$$R_{dy} = \frac{S_d}{S_m} \simeq 0.016 \tag{1}$$

Taking into account R_{dy} and the DM annual modulation effect pointed out by DAMA/LIBRA–phase1 for *single-hit* events in the low energy region, it is possible to derive the diurnal modulation amplitude expected for the same data. In particular, when considering the (2–6) keV energy interval, the observed annual modulation amplitude in DAMA/LIBRA–phase1 is: (0.0097 $\pm$ 0.0013) cpd/kg/keV [4] and the expected value of the diurnal modulation amplitude is $\simeq 1.5 \times 10^{-4}$ cpd/kg/keV.

Fig. 2 shows the time and energy behavior of the experimental residual rates of *single-hit* events both as a function of solar (*left*) and of sidereal (*right*) time, in the (2–6) keV and (6–14) keV intervals. The used time bin is 1 (either solar or sidereal) hour.

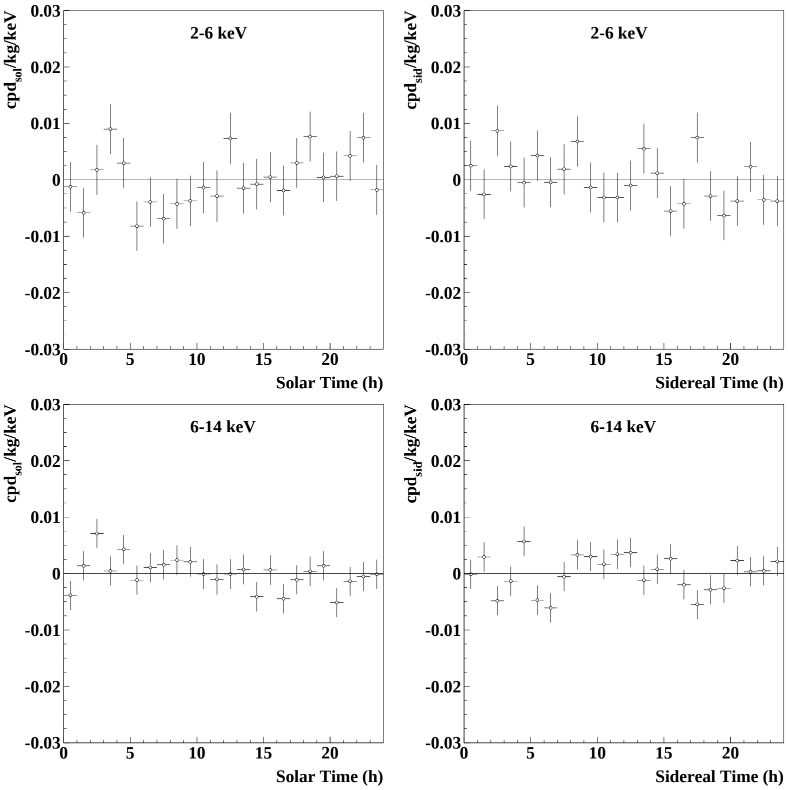

Figure 2: Experimental model-independent diurnal residual rate of the *single-hit* scintillation events, measured by DAMA/LIBRA–phase1 in the (2–6) and (6–14) keV energy intervals as a function of the hour of the solar (*left*) and sidereal (*right*) day. The experimental points present the errors as vertical bars and the associated time bin width (1 hour) as horizontal bars. The cumulative exposure is 1.04 ton × yr. More on 2014 publication list.

The null hypothesis (absence of residual rate diurnal variation) has been tested by a χ^2 test, obtaining the results given in Table 1; there the upper tail probabilities (P-values), calculated by the standard χ^2 distribution, are also reported. Thus, no diurnal variation with a significance of 95% C.L. is found at the reached level of sensitivity.

In addition to the χ^2 test, another independent statistical test has been applied: the run test (see 2014 Publication list); it verifies the hypothesis that the positive and negative data points are randomly distributed. The lower tail probabilities are equal to: 7% and 26% in the (2–6) and (6-14) keV energy region, respectively, for the solar case and 78% and 16% in the (2–6) and (6-14) keV energy region, respectively, for the sidereal case. Thus, in conclusion the presence of any significant diurnal variation and of time structures can be excluded at the reached level of sensitivity (see e.g. the error bars in Fig. 2).

In order to compare the experimental data with the DM diurnal effect due to the Earth rotation around its axis, the sidereal diurnal modulation amplitude of the (2–6) keV energy interval is taken into account: $A_d^{exp} = -(1.0 \pm 1.3) \times 10^{-3}$ cpd/kg/keV. Following the Feldman-Cousins procedure an upper limit can be obtained for the measured diurnal modulation amplitude:

Table 1: Test of absence of diurnal effect in the DAMA/LIBRA–phase1 data. The P-values, calculated by the standard χ^2 distribution, are also shown. As can be seen, the χ^2 test supports the hypothesis that the diurnal residual rates in DAMA/LIBRA–phase1 are simply fluctuating around zero.

Energy	Solar Time	Sidereal Time
2–6 keV	χ^2/d.o.f. = 25.8/24 → P = 36%	χ^2/d.o.f. = 21.2/24 → P = 63%
6–14 keV	χ^2/d.o.f. = 25.5/24 → P = 38%	χ^2/d.o.f. = 35.9/24 → P = 6%

$A_d^{exp} < 1.2 \times 10^{-3}$ cpd/kg/keV (90% C.L.); thus, the DAMA/LIBRA–phase1 experimental sensitivity is not sufficient to point out this second order diurnal effect (expected amplitude $\simeq 1.5 \times 10^{-4}$ cpd/kg/keV).

For further details see 2014 Publication list.

In conclusion, at that level of sensitivity the presence of any significant diurnal variation and of diurnal time structures in the data can be excluded for both the cases of solar and sidereal time. In particular, the sidereal diurnal modulation amplitude expected – because of the Earth diurnal motion – on the basis of the DAMA DM annual modulation results is below the present sensitivity; it will be possible to investigate this diurnal effect with adequate sensitivity when a suitably large exposure will be available. DAMA/LIBRA–phase2, presently running, with a lower software energy threshold [6] can also offer an alternative possibility to increase sensitivity to such an effect.

1.2.2 No role for neutrons, muons and solar neutrinos in the DAMA DM annual modulation results

A paper which summarizes in a simple and intuitive way why neutrons (of whatever origin), muons and solar neutrinos cannot give any significant contribution to the DAMA annual modulation results has been released (see 2014 Publication list). Table 2 summarizes the safety upper limits on the contributions (if any) to the observed modulation amplitude due to the total neutron flux at LNGS, either from (α,n) reactions, from fissions and from muons' and solar-neutrinos' interactions in the rocks and in the lead around the experimental set-up; the direct contributions of muons and solar neutrinos are also reported there. As seen in Table 2, they are all negligible and they cannot give any significant contribution to the observed modulation amplitude; in addition, neutrons, muons and solar neutrinos are not a competing background when the DM annual modulation signature is investigated since they cannot mimic this signature.

For details see the 2014 Publication list and references therein. A number of these arguments were already presented in individual papers. Afterwards, few simple considerations were summarized which already demonstrated the incorrectness of the claim reported in PRL 113 (2014) 081302.

2 DAMA/1ton

A multi-purpose 1 ton (full sensitive mass) set-up made of highly radio-pure NaI(Tl) was proposed in 1996 to INFN-CSN2, and the funded R&D-II, DAMA/LIBRA and R&D-III were considered as intermediate steps. We have already cited some items in the report to CSLNGS on March 2011. It is worth noting that the 1 ton will be fully sensitive to the processes of interest. As mentioned there, the final design is based on the fulfillment of three additional replica of the present DAMA/LIBRA set-up, solution that offers many technical and scientific advantages; thus, the technical design is completely known, since DAMA/LIBRA is operative. As already mentioned, some activities were/are/will-be carried out in the light of overcoming the present problems regarding the supplying and purifications of high quality NaI and, mainly, TlI powders and the creation of updated protocols.

During 2014 activities on materials and improved designs have also been carried out in the framework of a POR fellowship.

3 DAMA/LXe

We pointed out since 1990 [35] the possible interest in using the liquid Xenon as target-detector material for particle DM investigations. Since the end of 80's (former Xelidon experiment of the INFN) we have built several liquid Xenon (LXe) prototype detectors. Since 1996 we pointed out to the INFN-CSN2 the intrinsic problems of this detector medium for large scale experiments dedicated to DM investigation (poor collection of the far UV light, response disuniformity on large detectors, self-absorption, rebuilding of the sensitive part for each liquefaction with no proof of the same condition, no possibility of routine calibration in keV region, degassing of materials, operating parameters stability, etc.) and agreed to pursue the activity by exploiting

Table 2: Summary of the contributions to the total neutron flux at LNGS; the value, the relative modulation amplitude, and the phase of each component is reported. It is also reported the counting rate in DAMA/LIBRA for *single-hit* events, in the $(2-6)$ keV energy region induced by neutrons, muons and solar neutrinos, detailed for each component. The modulation amplitudes, A_k, are reported as well, while the last column shows the relative contribution to the annual modulation amplitude observed by DAMA, $S_m^{exp} \simeq 0.0112$ cpd/kg/keV [4]. As can be seen, they are all negligible and they cannot give any significant contribution to the observed modulation amplitude. In addition, neutrons, muons and solar neutrinos are not a competing background when the DM annual modulation signature is investigated since in no case they can mimic this signature. For details see the 2014 Publication list and references therein.

Source		$\Phi^{(n)}_{0,k}$ (neutrons cm^{-2} s^{-1})	η_k	t_k	$R_{0,k}$ (cpd/kg/keV)	$A_k = R_{0,k}\eta_k$ (cpd/kg/keV)	A_k/S_m^{exp}
SLOW neutrons	thermal n ($10^{-2} - 10^{-1}$ eV)	1.08×10^{-6}	$\simeq 0$ however $\ll 0.1$	–	$< 8 \times 10^{-6}$	$\ll 8 \times 10^{-7}$	$\ll 7 \times 10^{-5}$
	epithermal n (eV-keV)	2×10^{-6}	$\simeq 0$ however $\ll 0.1$	–	$< 3 \times 10^{-3}$	$\ll 3 \times 10^{-4}$	$\ll 0.03$
FAST neutrons	fission, $(\alpha, n) \to$ n (1-10 MeV)	$\simeq 0.9 \times 10^{-7}$	$\simeq 0$ however $\ll 0.1$	–	$< 6 \times 10^{-4}$	$\ll 6 \times 10^{-5}$	$\ll 5 \times 10^{-3}$
	$\mu \to$ n from rock (> 10 MeV)	$\simeq 3 \times 10^{-9}$	0.0129	end of June	$\ll 7 \times 10^{-4}$	$\ll 9 \times 10^{-6}$	$\ll 8 \times 10^{-4}$
	$\mu \to$ n from Pb shield (> 10 MeV)	$\simeq 6 \times 10^{-9}$	0.0129	end of June	$\ll 1.4 \times 10^{-3}$	$\ll 2 \times 10^{-5}$	$\ll 1.6 \times 10^{-3}$
	$\nu \to$ n (few MeV)	$\simeq 3 \times 10^{-10}$	0.03342^*	Jan. 4th*	$\ll 7 \times 10^{-5}$	$\ll 2 \times 10^{-6}$	$\ll 2 \times 10^{-4}$
	direct μ	$\Phi^{(\mu)}_0 \simeq 20\ \mu$ m^{-2}d^{-1}	0.0129	end of June	$\simeq 10^{-7}$	$\simeq 10^{-9}$	$\simeq 10^{-7}$
	direct ν	$\Phi^{(\nu)}_0 \simeq 6 \times 10^{10}\ \nu$ cm^{-2}s^{-1}	0.03342^*	Jan. 4th*	$\simeq 10^{-5}$	3×10^{-7}	3×10^{-5}

* The annual modulation of solar neutrino is due to the different Sun-Earth distance along the year; so the relative modulation amplitude is twice the eccentricity of the Earth orbit and the phase is given by the perihelion.

Kr-free enriched Xenon gases in limited volume.

The presently running set-up (with a Cu inner vessel filled by $\simeq$ 6.5 kg, that is $\simeq$2 l, of liquid Xenon) can work either with Kr-free Xenon enriched in ^{129}Xe at 99.5% or Kr-free Xenon enriched in ^{136}Xe at 68.8% [36, 37, 38]. Many competing results were achieved on several rare processes [36, 37, 38, 39, 40, 41]. It is worth noting that e.g. the mass exposed when using the Xenon enriched in ^{129}Xe corresponds for spin-dependent coupled particles to expose 24.5 kg (full sensitive mass) of natural Xenon, while the exposed mass when using the Xenon enriched in ^{136}Xe corresponds for spin-independent coupled particles to an exposed mass of 50.4 kg (full sensitive mass) of natural Xenon.

In the period of interest, the annual maintenance of the cryogenic system has been carried out. The vacuum and purification procedures have been performed and the set-up has then been in data taking filled with Xenon enriched in ^{136}Xe, still mainly focusing the high energy region. Some preliminary analyses are continuing.

4 DAMA/R&D

The DAMA/R&D installation is a general-purpose low background set-up used for measurements on low background prototypes and for relatively small-scale experiments [42, 43, 44, 45, 46]

The measurements mainly investigate 2β decay modes in various isotopes; both the active and the passive source techniques have been exploited as well as the coincidence technique. Particular attention is dedicated to the isotopes allowing the investigation of the $2\beta^+$ processes and in particular to resonant 2ϵ or $\epsilon\beta^+$ decay channels. In particular, in the first case an enhancement of the rate by some orders of magnitude is predicted for the case of coincidence between the released energy and the energy of an excited state. In the second case the investigation of neutrino-less 2ϵ and $\epsilon\beta^+$ processes can refine the understanding of the contribution of right-handed currents to neutrino-less 2β decay; therefore developments of experimental technique to search for 2ϵ, $\epsilon\beta^+$, and $2\beta^+$ processes are strongly required considering also that in the $2\beta^+$ investigations a gap of several orders of magnitude between theoretical expectations and experimental results is the usual situation and the better achieved sensitivities do not exceed the level of $T_{1/2} \simeq 10^{21}$ yr. Even more important motivation to search for double electron capture appears from a possibility of a resonant process thanks to energy degeneracy between initial and final state of mother and daughter nuclei. Such a resonant process could occur if the energy of transition ($Q_{2\beta}$) minus the energies of two bounded electrons on K or/and L atomic shells of daughter nucleus is near to the energy of an excited level (E_{exc}) of the daughter isotope.

Therefore developments of experimental technique to improve the reachable sensitivity in the searches for 2ε, $\varepsilon\beta^+$, and $2\beta^+$ processes are strongly required.

Finally, investigations on various kinds of new scintillators and preliminary works for the future measurements are also in progress.

Some of the main results during 2014 are listed in the following.

- The experiment by using cadmium tungstate crystal scintillators (total mass 1.175 kg) developed from enriched to 82% ^{116}Cd (^{116}CdWO$_4$) is in progress. The activity of β active ^{238}U daughters was determined thanks to the improvement of the pulse-shape discrimination between beta and alpha events and the increase of the experimental statistics. More precise model of the background was built, allowing improvement of the accuracy on ^{116}Cd half-life relatively to the two neutrino double beta decay to the ground state of ^{116}Sn. The background in the vicinity of the $0\nu2\beta$ decay of ^{116}Cd (2.7–2.9 MeV) is reduced to 0.12 cnt/(yr keV kg) by the improvement of the pulse-shape discrimination of

^{212}Bi–^{212}Po events. The total live time of the experiment is 2.503 yr. A partial exposure has been already released in Conferences (see Sect. 4.1). The experiment is running.

- The results of the experiment with a BaF_2 scintillation crystal in the low-background DAMA/R&D set-up have been published. The radioactive contamination of a BaF_2 scintillation crystal with mass of 1.714 kg was measured over 101 hours. The half-life of ^{212}Po (present in the crystal scintillator due to contamination by radium) was measured. The half-life limits of ^{212}Pb, ^{222}Rn and ^{226}Ra relatively to 2β decays are also improved in comparison with the earlier results. A R&D of a fast scintillation detector containing thorium and radium is in progress to prepare new measurements with the aim to improve the half-life value of ^{212}Po. Besides, non-exponential deviations in the decay of ^{212}Po and ^{214}Po at very short times after the nuclei appearance can be searched for (see Sect. 4.2).
- Investigation of radioactive elements segregation in crystals to develop ultra-radio-pure scintillators for rare events experiments is in progress.
- Analyses towards the further investigation of the beta decay of ^{113m}Cd have been started.
- The final version of a paper to search for super-heavy eka-tungsten with the help of $ZnWO_4$ and BGO crystal scintillators has been prepared.
- The work for the future (some years from now) installation of the $^{116}CdWO_4$ detectors in the low-background GeMulti set-up has further been progressed and other future measurements (among them: developments on new SrI_2(Eu) crystals, on new enriched $CdWO_4$ depleted in ^{113}Cd, on highly radio-pure $ZnWO_4$, further pursuing the goals of our project for achieving highly radio-pure scintillators for the search of rare processes) have been prepared.

This DAMA/R&D set-up is as a general-purpose set-up and will assure us also in future the possibility to produce many kinds of low background measurements in an efficient way at well reduced cost. In particular the present measurements with the $^{116}CdWO_4$ crystals are planned with further improvements to continue over about 4 years as needed to reach the proposed goal; then, the other measurements will start in the DAMA/R&D setup after preliminary measurements in DAMA/CRYS (see later).

4.1 Search for 2β decay of ^{116}Cd with the help of enriched $^{116}CdWO_4$ crystal scintillators

A low-background experiment using enriched $^{116}CdWO_4$ scintillators (total mass of 1.16 kg, enrichment by ^{116}Cd to 82%) is in progress at LNGS. Two $^{116}CdWO_4$ crystal scintillators (586 g and 589 g) were fixed inside polystyrene light-guides ($\oslash 70 \times 194$ mm). The cavities inside the light-guides were filled with the radiopure liquid scintillator. Two high purity quartz light-guides ($\oslash 70 \times 200$ mm) were glued to the polystyrene light-guide on both sides. The detectors were viewed from the opposite sides by two low radioactive 3" photomultipliers. The detector modules, covered by the 3M foil to improve the light collection, were installed inside a low radioactive air-tight Cu box at the DAMA/R&D setup. Copper bricks 5 cm thick were used as an additional passive shield.

The exposure of the experiment at the last stage of the data taking is 1.15 kg×yr (see 2014 Publication list). The applied data analysis is similar to the one described in Ref. [46]. The energy spectrum of $\gamma(\beta)$ events accumulated with the $^{116}CdWO_4$ detector and selected off-line by the pulse shape and the front edge analyzes is shown in Fig. 3.

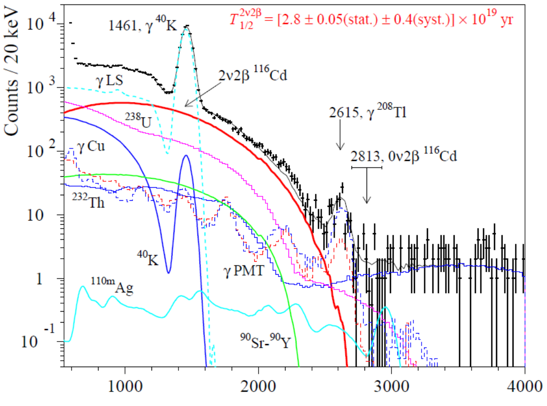

Figure 3: (Color online) The energy spectrum of $\gamma(\beta)$ events measured with the ^{116}CdWO$_4$ scintillation detector over 8696 h in the low-background set-up (points with error bars) together with the fit (solid black line). The main components of the background are also shown: $2\nu2\beta$ decay of ^{116}Cd, the distributions of internal ^{40}K, ^{90}Sr-^{90}Y, ^{232}Th, ^{238}U, and cosmogenic ^{110m}Ag, the contribution from external γ quanta from the details of the detector (LS, PMT) and set-up (Cu). The energies are in keV.

The energy resolution of the ^{116}CdWO$_4$ detector is FWHM = 4.3% at $Q_{2\beta}$ of ^{116}Cd, the background counting rate was reduced to 0.12(2) counts/yr/kg/keV in the region of interest 2.7 – 2.9 MeV, where the $0\nu2\beta$ peak is expected. The main components of the background in this region remain γ quanta of ^{208}Tl from the contamination of the set-up and internal contamination of the ^{116}CdWO$_4$ crystals by ^{228}Th.

The half-life relatively to the $2\nu2\beta$ decay of ^{116}Cd to the ground level of ^{116}Sn was measured as $T_{1/2}^{2\nu2\beta}$ = [2.8 ± 0.05(stat.) ± 0.4(syst.)] × 10^{19} yr, in agreement with the results of the previous experiments. The half-life limit on $0\nu2\beta$ decay of ^{116}Cd to the ground state of ^{116}Sn was established as $T_{1/2}^{0\nu2\beta} \geq 1.0 \times 10^{23}$ at 90% C.L. The sensitivity can be advanced to the level of lim $T_{1/2} \sim 10^{24}$ yr (which corresponds to the effective neutrino mass $m_\nu = 0.4 - 1.4$ eV) after improvement on the background; a R&D to further reduce the background conditions of the experiment is in progress.

4.2 Rare nuclear decays with BaF$_2$ scintillator contaminated by radium

The radioactive contamination of a BaF$_2$ crystal scintillator ($\oslash 3'' \times 3''$, 1.714 kg) was measured over 101 hours in the low-background DAMA/R&D set-up (see 2014 Publication list). The BaF$_2$ crystal scintillator was viewed through two light-guides ($\oslash 3'' \times 100$ mm) by two low radioactive 3″ photomultipliers. The detector was surrounded by Cu bricks and installed inside a low radioactive air-tight Cu box at the DAMA/R&D set-up.

The radioactive contaminations were estimated to be at level of few Bq/kg for ^{226}Ra and ^{228}Th. Taking into account 3 orders of magnitude lower activity of ^{238}U and ^{232}Th (only limits <0.0002 Bq/kg for ^{238}U and <0.004 Bq/kg for ^{232}Th were obtained) and broken equilibrium in the chains, one can conclude that the BaF$_2$ crystal is contaminated by radium (which is chemically close to barium).

The response of the BaF$_2$ crystal scintillator to α particles has been investigated in a wide energy interval (4.8 – 9.0 MeV) and the capability of pulse-shape discrimination between α particles and γ quanta (electrons) has been demonstrated (see Fig. 4).

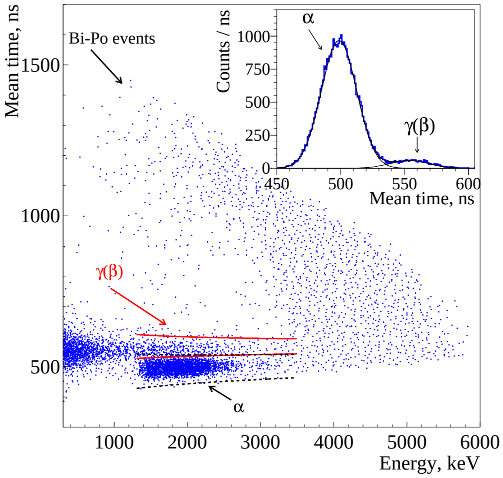

Figure 4: Scatter plot of the mean time of the pulse versus energy accumulated by the BaF_2 scintillation detector during a background run ($\simeq 2$ h). The contours give regions where 99% of α or β/γ events are concentrated. The population of events in the energy interval $\simeq 1-6$ MeV with mean time values mainly above the β/γ and α regions are caused by the decays of the fast ^{212}Bi–^{212}Po sub-chain of ^{228}Th (Bi-Po events). (Inset) The mean time spectrum in the energy interval $2000-2100$ keV.

The analysis of the distribution of the time intervals between β and α decays in the fast Bi-Po chains allowed us to estimate the half-life of ^{212}Po as $T_{1/2} = 298.8 \pm 0.8$(stat.) ± 1.4(syst.) ns, which is in agreement with the table value [47, 48].

The quite-high level of contamination of the BaF_2 detector by Ra gives the possibility to search for rare β and 2β decays of some nuclides in U/Th chains, which cannot be easily studied in the usual way since they quickly decay through α and/or β channels and cannot be accumulated in big quantities. The ^{222}Rn nuclide is known as 100% decaying via emission of α particle with $T_{1/2} = 3.82$ d; however, its β decay is also energetically allowed with $Q_\beta = 24 \pm 21$ keV. Search for decay chains of events with specific pulse shapes characteristic for α or for β/γ signals and with known energies and time differences allowed us to set, for the first time, the limit on the branching ratio of ^{222}Rn relatively to β decay as $B_\beta < 0.13\%$ at 90% C.L. (equivalent to limit on partial half-life $T^\beta_{1/2} > 8.0$ y, still quite far from the theoretical estimation $T^\beta_{1/2}(^{222}\mathrm{Rn}) = 4.8 \times 10^5$ y).

The half-life limits of ^{212}Pb, ^{222}Rn and ^{226}Ra relatively to 2β decays were also improved in comparison to the earlier work (see Table 3).

The obtained results can be highly improved with a detector with smaller dead time and better energy resolution.

5 DAMA/CRYS

DAMA/CRYS is a small test set-up mainly dedicated to tests on new detectors' performances and small scale experiments. In the period of interest:

- Low background measurements of a cadmium tungstate crystal scintillator enriched in ^{116}Cd (326 g) have been concluded; they have been performed in the DAMA/CRYS set-up with the aim to investigate the segregation of thorium, uranium and radium during the

Table 3: Branching ratios and half-life values or limits (at 90% C.L.) obtained in this work in comparison with other results. $T_{1/2}$ limits in [49] were given at 68% C.L.

Nuclide	Main channel of decay and $T_{1/2}$ [47]	$T_{1/2}$ This work	Other works	
^{212}Po	α 299 ± 2 ns	298.8±0.8(stat.)±1.4(syst.) ns	294.7±0.6(stat.)±0.8(syst.) ns	[50]
			299 ± 2 ns	[48]
^{212}Pb	β 10.64 h	$2\beta2\nu$ > 75 h	> 146 h	[49]
		$2\beta0\nu$ > 20 y	> 6.7 y	[49]
^{222}Rn	α 3.8235 d	β > 8.0 y	–	
		$2\beta2\nu$ > 8.0 y	> 40 d	[49]
		$2\beta0\nu$ > 8.0 y	> 2.8 y	[49]
^{226}Ra	α 1600 y	$2\beta2\nu$ $> 1.2 \times 10^6$ y	$> 4.5 \times 10^3$ y	[49]
		$2\beta0\nu$ $> 1.2 \times 10^6$ y	$> 4.1 \times 10^4$ y	[49]

crystal growth process (see also above). We have observed a very low segregation of thorium, which opens the possibility to improve radiopurity of ^{116}CdWO$_4$ crystal scintillators in ^{228}Th (the most harmful contamination in the experiment to search for $0\nu2\beta$ decay of ^{116}Cd) by recrystallization.

- At present a new ZnWO$_4$ crystal is in measurements.
- The automatic moving system has been installed.
- The cryogenic part of DAMA/CRYS (to allow also measurements of the responses of various new/improved scintillators as a function of the temperature) will be installed when the presently running measurements will be concluded.

6 DAMA/Ge and LNGS STELLA facility

The measurements on samples and on various R&D developments are performed by means of the DAMA low background Ge detector, specially built with a low Z window; it is operative deep underground in the STELLA facility of the LNGS. Some selected materials are in addition measured with high sensitivity ICP-MS and mass spectrometers. In addition other Ge detectors (in particular, GeMulti) are also used for some peculiar measurements. Published results can be found in Ref. [51] and in the 2014 Publication list.

In particular, the main data takings/results during year 2014 with DAMA/Ge and LNGS STELLA facility are summarized in the following.

- The data taking of the experiment to search for double beta processes in ^{106}Cd by using cadmium tungstate crystal scintillator enriched in ^{106}Cd (^{106}CdWO$_4$, mass of 215 g) in coincidence with the four crystals HPGe detector GeMulti (the volume of each detector is 225 cm^3) has continued during 2014 at the STELLA facility. The ^{106}CdWO$_4$ scintillator is viewed by a low-background photomultiplier tube through a lead tungstate crystal light-guide produced from deeply purified archaeological lead to suppress γ quanta from the photomultiplier. Preliminary results have already been presented at Conference. Then, we intend to develop a scintillation coincidence detector (with two large area CdWO$_4$ crystal scintillators placed in a very closed geometry to the ^{106}CdWO$_4$ detector) with aim to improve the coincidence efficiency and suppress background caused by trace radioactive contamination of the GeMulti cryostat. Besides, developed procedures for obtaining

^{106}CdWO$_4$ depleted in ^{113m}Cd will be applied to further increase the experimental sensitivity (see Sect. 6.1).

- The search for double beta decay of ^{184}Os, ^{192}Os (^{184}Os is of especial interest thanks to possibility of resonant neutrinoless double electron capture) and alpha decay of ^{184}Os to excited levels of daughter nuclei is further under study. The ultra-pure osmium samples (with diameter in the range 4-7 mm) were cut in 0.8-1.0 mm plates to improve the detection efficiency. A next stage of the experiment is planned to start as soon as it will become operative at STELLA facility – with an ultra-low background broad energy HPGe detector especially designed for low energy gamma-ray spectrometry.

- The results of the experiment to search for double beta processes in ^{136}Ce and ^{138}Ce by using deeply purified cerium oxide sample with mass more than 0.7 kg using HPGe spectrometry (^{136}Ce is of especial interest taking into account one of the largest energy of decay and promising theoretical predictions) have been published. Further purification of the cerium from thorium contamination to increase the experimental sensitivity is in preparation towards higher sensitivities (see Sect. 6.2).

- The deeply purified neodymium oxide samples with a total mass about 2.5 kg (original 5 kg) was pressed to improve detection efficiency in an experiment to search for 2β decay of ^{150}Nd to excited levels of ^{150}Sm with the help of low background HPGe detectors. As already pointed out, the radioactive contamination of the samples was found to be below the sensitivity of the HPGe gamma and ICP-MS analyzes available at the LNGS. The experiment plans to use the four crystal HPGe detectors, GeMulti, after the completion of the presently running 106Cd experiment.

- The R&D of low background GSO(Ce) crystal scintillators to investigate double beta processes in ^{152}Gd and ^{160}Gd has been progressed.

- A R&D of methods to purify dysprosium and erbium elements is further in progress. The materials are of special interest, taking into account recent theoretical estimates of neutrino-less resonant double electron capture processes in ^{156}Dy and ^{164}Er. Works to prepare the measurements of new samples have been progressed.

- The R&D of methods to purify samarium, ytterbium and erbium has been progressed. The materials are of special interest taking into account recent theoretical estimates of neutrino-less resonant double electron capture processes in ^{144}Sm, ^{162}Er, ^{164}Er and ^{168}Yb. The radioactive contamination of samarium, ytterbium and erbium oxide samples has been measured by using the HPGe gamma spectrometry. Deep purification of the samples is under investigation in order to improve the sensitivity reachable in the measurements in preparation.

- Preparations of other future measurements are in progress.

6.1 First results in the search for 2β decay of ^{106}Cd with ^{106}CdWO$_4$ crystal scintillator in coincidence with four HPGe detectors

An experiment to search for double beta decay processes in ^{106}Cd with the help of enriched in ^{106}Cd (to 66%) low background ^{106}CdWO$_4$ scintillation detector has been in measurement during 2014 at the STELLA facility. First preliminary results have been presented at Conferences (see 2014 Publication list).

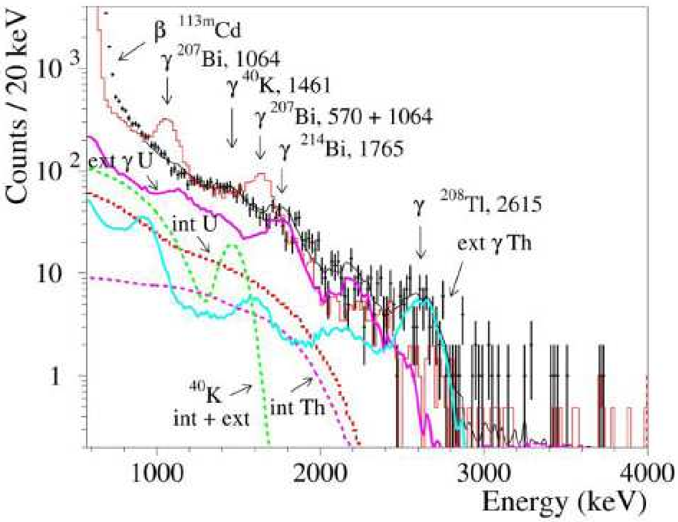

Figure 5: Energy spectrum of the $\gamma(\beta)$ events accumulated over 3233 h in the low background set-up with the ^{106}CdWO$_4$ crystal scintillator (points) together with the background model (black continuous line). The main components of the background are shown: the distributions of internal and external ^{40}K, internal ^{228}Th and ^{238}U, and the contributions from the external γ quanta from U and Th contamination of the set-up. It is also shown a spectrum (solid histogram) taken before cleaning the crystal's surface from ^{207}Bi.

The ^{106}CdWO$_4$ crystal scintillator (mass of 215 g) is viewed through a lead tungstate (PbWO$_4$) crystal light-guide ($\oslash 40 \times 83$ mm) by 3 inches low radioactive photomultiplier. The PbWO$_4$ crystal was developed from deeply purified archaeological lead. The detector is installed in coincidence with the four HPGe crystals mounted in one cryostat with a well in the center.

The mean-time pulse shape discrimination method was used to discriminate $\gamma(\beta)$ events from α events caused by internal contamination of the crystal by uranium and thorium. The energy spectrum of the $\gamma(\beta)$ events is shown in Fig. 5.

The sensitivity of the experiment after 3233 h of data taking is at level of lim $T_{1/2} \sim 10^{19} - 10^{21}$ yr for the double β processes in ^{106}Cd with emission of γ quanta. In particular, a new improved half-life limit is set to the two neutrino electron capture with positron emission in ^{106}Cd as $T_{1/2} \geq 8.4 \times 10^{20}$ yr (at 90% C.L.). The aim is to improve further the sensitivity of the experiment particularly for this channel of the decay to the level of theoretical predictions ($T_{1/2} \sim 10^{20} - 10^{22}$ yr) by increasing the statistics and by construction of a more precise model of the background.

6.2 Search for double beta decay of ^{136}Ce and ^{138}Ce

Cerium contains three potentially 2β active isotopes: ^{136}Ce, ^{138}Ce and ^{142}Ce [52]. The ^{136}Ce isotope is of particular interest because of one of the highest energy of decay which enables even $2\beta^+$ decay allowed only for six nuclei [52].

Search for double beta processes in ^{136}Ce and ^{138}Ce was performed with the help of an ultra-low background HPGe γ detector (see 2014 Publication list). Cerium oxide powder of 99.99% grade was tested by the low-background HPGe detector GeBer at the STELLA facility, showing a considerable contamination. To reduce radioactive contamination, the material was purified by the liquid-liquid extraction method. The radioactive contamination of the sample by potassium, radium and uranium was reduced by more than one order of magnitude. However, the purification procedure was not efficient enough to remove thorium, which still is present in the material at the level of 0.6 Bq/kg and remains the main source of the background.

A sample of the purified cerium oxide with mass 732 g was used in the experiment carried out in the STELLA low background facility. The sample in a thin plastic container was placed on the end-cap of the ultra-low background HPGe detector GeCris. The energy spectra with and without the sample, normalized to the time of measurements, are presented in Fig. 6. The counting rate of the detector with the cerium sample substantially exceeds the background of the spectrometer mainly due to the residual radioactive contamination of the sample by thorium.

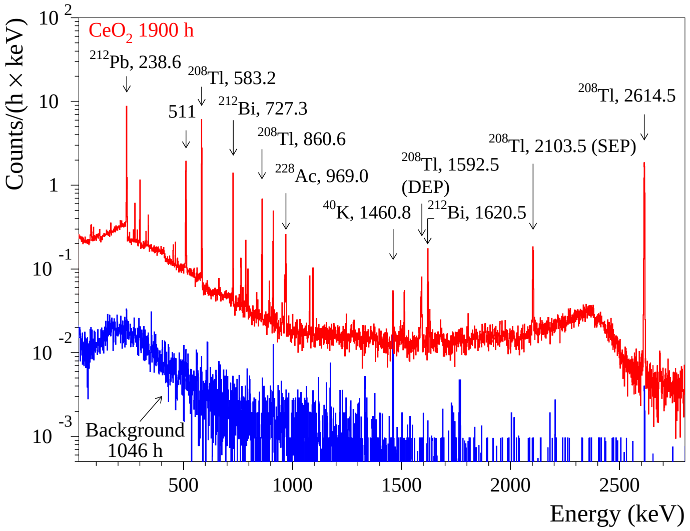

Figure 6: Energy spectra accumulated with the CeO_2 sample over 1900 h and without sample over 1046 h by the ultra-low background HPGe γ spectrometer. Energy of γ quanta are in keV.

There are no peculiarities in the spectrum accumulated with the CeO_2 sample which could be attributed to the 2β processes in ^{136}Ce or ^{138}Ce. Thus, only lower half-life limits can be estimated. New improved half-life limits were set on double beta processes in ^{136}Ce and ^{138}Ce at the level of $T_{1/2} \sim 10^{17} - 10^{18}$ yr; many of them are even two orders of magnitude larger than the best previous results. At the same time, the sensitivity of the present experiment is still far from the theoretical predictions.

Further experimental progress can be achieved by deep purification of cerium from radioactive contamination (mainly by thorium), using of enriched cerium isotopes, and by increasing the experiment scale. In fact, it should be stressed that the activity of ^{228}Th in the $CeCl_3$ crystal is three orders of magnitude lower than that in CeO_2. One can expect that further purification of cerium from thorium traces is possible, for instance, by using a chemistry similar to the applied to produce the $CeCl_3$ crystal scintillators.

7 Other activities

In 2014 it continued the investigation on the so called directionality, i.e. – in case of DM candidates inducing just nuclear recoils – on the correlation of their impinging direction (through the recoiling nuclei) with the Earth galactic motion.

In particular for directionality in recent years we have made extensive efforts and measurements with $ZnWO_4$ crystal scintillators, already interesting to investigate double beta decay of Zn and W isotopes [43]. These scintillators [53] have the particular feature to be anisotropic in the light output and in the pulse shape for heavy particles (p, α, nuclear recoils) depending on the direction with respect to the crystal axes. The response to γ/β radiation is isotropic instead. Among the anisotropic scintillators, the $ZnWO_4$ has unique features, which make it an excellent candidate for this type of research, and there is still plenty of room for the improvement of its performances. The possibility of a low background pioneer experiment (named ADAMO, Anisotropic detectors for DArk Matter Observation) to exploit deep underground the directionality approach by using anisotropic $ZnWO_4$ scintillators has been explored [53]. We have also discussed as first in written project and Conferences the potentiality to build detectors with anisotropic features by using Carbon Nanotubes (CNT) [54].

8 Conclusions

During 2014 DAMA/LIBRA has continued to take data in the phase2 configuration. The strictly quality control allows DAMA/LIBRA to be still the highest radio-pure set-up in the field with the largest exposed sensitive mass, the full control of running conditions, the largest duty-cycle and an exposure orders of magnitude larger than any other activity in the field, etc..

Studies on other DM features, second order effects, and several other rare processes are in progress with the aim to reach very high sensitivity also thanks to the progressive increasing of the exposure. In particular, analyses on possible diurnal effect in the DAMA/LIBRA-phase1 data have been released. In addition, a paper which summarizes in a simple and intuitive way why the neutrons, the muons and the solar neutrinos cannot give any significant contribution to the DAMA annual modulation results has been published.

Studies are under way towards possible DAMA/LIBRA–phase3 and/or DAMA/1ton (proposed since 1996).

In addition the work for the future (some years from now) installation of the ^{116}Cd detectors in the low-background GeMulti set-up has been progressed as well as the preparations for the future search for super-heavy eka-tungsten with the help of $ZnWO_4$ scintillation and the preparation of the other future measurements (among them: developments on new SrI_2(Eu) crystals, on new enriched $CdWO_4$ depleted in ^{113}Cd, on highly radio-pure $ZnWO_4$, further developing the goals of our project to develop highly radio-pure scintillators for the search of rare processes).

Finally, in 2014 all the DAMA set-ups have regularly been in data taking and various kinds of measurements are in progress and planned for the future.

During 2014 the results of the ANVUR VQR 2004-2010 evaluation appeared and for DAMA it is: 24/27 full-rank products; i.e. total score 25.6/27.

9 List of Publications during 2014

1. R. Bernabei, P. Belli, F. Cappella, V. Caracciolo, R. Cerulli, C.J. Dai, A. d'Angelo, S. d'Angelo, A. Di Marco, H.L. He, A. Incicchitti, X.H. Ma, F. Montecchia, D. Prosperi, X.D. Sheng, R.G. Wang, Z.P. Ye, DAMA/LIBRA results and perspectives of phase 2, Nucl. Instr. and Meth. A 742 (2014) 177

2. R. Bernabei, P. Belli, F. Cappella, V. Caracciolo, S. Castellano, R. Cerulli, C.J. Dai, A. d'Angelo, S. d'Angelo, A. Di Marco, H.L. He, A. Incicchitti, H.H. Kuang, X.H. Ma, F. Montecchia, X.D. Sheng, R.G. Wang, Z.P. Ye,, The annual modulation signature for Dark

Matter: DAMA/LIBRA-phase1 results and perspectives, Advances in High Energy Physics 2014 (2014), Article ID 605659, 10 pages (http://dx.doi.org/10.1155/2014/605659)

3. R. Bernabei, P. Belli, F. Cappella, V. Caracciolo, S. Castellano, R. Cerulli, C.J. Dai, A. d'Angelo, S. d'Angelo, A. Di Marco, H.L. He, A. Incicchitti, H.H. Kuang, X.H. Ma, F. Montecchia, D. Prosperi, X.D. Sheng, R.G. Wang, Z.P. Ye, Model independent result on possible diurnal effect in DAMA/LIBRA-phase1, Eur. Phys. J. C 74 (2014) 2827 [arXiv:1403.4733]

4. P. Belli, A. Incicchitti, F. Cappella, Inorganic scintillators in direct dark matter investigation, Int. J. of Mod. Phys. A 29 (2014) 1443011 (44 pages)

5. P. Belli, R. Bernabei, F. Cappella, V. Caracciolo, R. Cerulli, F.A. Danevich, A. Di Marco, A. Incicchitti, D.V. Poda, O.G. Polischuk, V.I. Tretyak, Investigation of rare nuclear decays with BaF_2 crystal scintillator contaminated by radium, Eur. Phys. J. A 50 (2014) 134

6. P. Belli, R. Bernabei, R.S. Boiko, F. Cappella, R. Cerulli, F.A. Danevich, A. Incicchitti, B.N. Kropivyansky, M. Laubenstein, D.V. Poda, O.G. Polischuk, V.I. Tretyak, Search for double beta decay of ^{136}Ce and ^{138}Ce with HPGe gamma detector, Nucl. Phys. A 930 (2014) 195

7. R. Bernabei, P. Belli, F. Cappella, V. Caracciolo, R. Cerulli, C.J. Dai, A. d'Angelo, S. d'Angelo, A. Di Marco, H.L. He, A. Incicchitti, H.H. Kuang, X.H. Ma, F. Montecchia, X.D. Sheng, R.G. Wang and Z.P. Ye, No role for neutrons, muons and solar neutrinos in the DAMA annual modulation results, Eur. Phys. J. C 74 (2014) 3196

8. R. Bernabei, Preface, Int. J. of Mod. Phys. A 29-19 (2014) 1402003

9. P. Belli, New particle detectors (and possible R&D's) of interest in NON-accelerator physics, Il N.Cim. 37 (2014) 45.

10. R. Bernabei, Crystal scintillators for low background measurements, EPJ Web of Conf. 65 (2014) 01001 (DOI: 10.1051/epjconf/20146501001)

11. P. Belli, R. Bernabei, F. Cappella, R. Cerulli, F.A. Danevich, S. d'Angelo, A. Incicchitti, V.V. Kobychev, D.V. Poda, V.I. Tretyak, Search for rare processes with $ZnWO_4$ crystal scintillators, EPJ Web of Conf. 65 (2014) 01002 (DOI: 10.1051/epjconf/20146501002)

12. V.I. Tretyak, P. Belli, R. Bernabei, V.B. Brudanin, F. Cappella, V. Caracciolo, R. Cerulli, D.M. Chernyak, F.A. Danevich, S. d'Angelo, A. Incicchitti, M. Laubenstein, V.M. Mokina, D.V. Poda, O.G. Polischuk, R.B. Podviyanuk, I.A. Tupitsyna, First results of the experiment to search for 2β decay of ^{106}Cd with $^{106}CdWO_4$ crystal scintillator in coincidence with four crystals HPGe detector, EPJ Web of Conf. 65 (2014) 01004 (DOI: 10.1051/epjconf/20146501004)

13. D.V. Poda, A.S. Barabash, P. Belli, R. Bernabei, F. Cappella, V. Caracciolo, S. Castellano, D.M. Chernyak, R. Cerulli, F.A. Danevich, S. d'Angelo, A. Incicchitti, V.V. Kobychev, S.I. Konovalov, M. Laubenstein, R.B. Podviyanuk, O.G. Polischuk, V.N. Shlegel, V.I. Tretyak, V.I. Umatov, Ya.V. Vasiliev, Search for 2β decay of ^{116}Cd with the help of enriched $^{116}CdWO_4$ crystal scintillators, EPJ Web of Conf. 65 (2014) 01005 (DOI: 10.1051/epjconf/20146501005; arXiv1312.0743)

14. R.S. Boiko, A.S. Barabash, P. Belli, R. Bernabei, F. Cappella, R. Cerulli, F.A. Danevich, A. Incicchitti, M. Laubenstein, V.M. Mokina, S. Nisi, D.V. Poda, O.G. Polischuk, V.I. Tretyak, Purification of cerium, neodymium and gadolinium for low background experiments, EPJ Web of Conf. 65 (2014) 04001 (DOI: 10.1051/epjconf/20146504001)

15. P. Belli, R. Bernabei, F. Cappella, V. Caracciolo, R. Cerulli, A. Di Marco, F.A. Danevich, A. Incicchitti, D.V. Poda, O.G. Polischuk, V.I. Tretyak,Radioactive contamination of BaF$_2$ crystal scintillator, EPJ Web of Conf. 65 (2014) 04004 (DOI: 10.1051/epjconf/20146504004)

16. R. Bernabei, P. Belli, F. Cappella, V. Caracciolo, R. Cerulli, C.J. Dai, A. d'Angelo, A. Di Marco, H.L. He, A. Incicchitti, X.H. Ma, F. Montecchia, X.D. Sheng, R.G. Wang, Z.P. Ye, The Dark Matter annual modulation results from DAMA/LIBRA, EPJ Web of Conf. 70 (2014) 00043

17. R. Bernabei, P. Belli, F. Cappella, V. Caracciolo, R. Cerulli, C.J. Dai, A. d'Angelo, A. Di Marco, H.L. He, A. Incicchitti, H.H. Kuang, X.H. Ma, F. Montecchia, X.D. Sheng, R.G. Wang, Z.P. Ye, New results and perspectives of DAMA/LIBRA, EPJ Web of Conf. 71 (2014) 00011

18. R. Bernabei, P. Belli, F. Cappella, V. Caracciolo, S. Castellano, R. Cerulli, C.J. Dai, A. dAngelo, S. dAngelo, A. Di Marco, H.L. He, A. Incicchitti, X.H. Ma, F. Montecchia, X.D. Sheng, R.G. Wang, Z.P. Ye, Results from DAMA/LIBRA and perspectives, in the volume of Proceedings of the 9th Patras Workshop on Axions, WIMPs and WISPs 2013, Ed. Verlag Deutsches Elektronen-Synchrotron, (2014), pag. 179-183 (ISBN 978-3-935702-83-6)

19. R. Bernabei, P. Belli, F. Cappella, V. Caracciolo, S. Castellano, R. Cerulli, C.J. Dai, A. d'Angelo, S. d'Angelo, A. Di Marco, H.L. He, A. Incicchitti, X.H. Ma, F. Montecchia, X.D. Sheng, R.G. Wang, Z.P. Ye, New results from DAMA/LIBRA, to appear in the volume of Proceedings of the 16th Lomonosov Conference on Elementary Particle Physics, Moscow, 22 - 28 August, 2013

20. R. Bernabei, P. Belli, S. d'Angelo, A. Di Marco, F. Cappella, A. Incicchitti, O.G. Polischuk, R.S. Boiko, D.M. Chernyak, F.A. Danevich, V.V. Kobychev, V.M. Mokina, D.V. Poda, V.I. Tretyak, V. Caracciolo, S. Castellano, R. Cerulli, M. Laubenstein, A.S. Barabash, S.I. Konovalov, V.I. Umatov, V.B. Brudanin, Recent Results on the Search for 2β decay processes with Scintillators and pure samples, to appear in the volume of Proceedings of the 16th Lomonosov Conference on Elementary Particle Physics, Moscow, 22 - 28 August, 2013

21. R. Bernabei, Dark Matter particles in the galactic halo, Bled Workshops in Physics vol. 15, no. 2 (2014) 10 (ISSN 1580-4992; Proc. of the 17th workshop "What Comes Beyond the Standard Models?", Bled 20-28 July 2014, Slovenia)

22. O.G. Polischuk, P. Belli, R. Bernabei, V.B. Brudanin, F. Cappella, V. Caracciolo, R. Cerulli, D.M. Chernyak, F.A. Danevich, S. d'Angelo, A. Incicchitti, M. Laubenstein, V.M. Mokina, D.V. Poda, V.I. Tretyak, I.A. Tupitsyna, Search for 2β processes in ^{106}Cd with ^{106}CdWO$_4$ crystal scintillator, to appear in the Proc. of the Conf. "Functional materials for science and technology", Kharkiv, 18-19 September 2014, Ukraine

23. P. Belli, Direct Detection of Dark Matter, to appear in the Proceed. of RICAP 2014, Noto (Italy), October 2014

24. R. Bernabei, P. Belli, F. Cappella, V. Caracciolo, R. Cerulli, C.J. Dai, A. d'Angelo, S. d'Angelo, A. Di Marco, H.L. He, A. Incicchitti, H.H. Kuang, X.H. Ma, F. Montecchia, X.D. Sheng, R.G. Wang, Z.P. Ye, DAMA/LIBRA-phase1 results and perspectives of phase2, to appear in the Proceed. of RICAP 2014, Noto (Italy), October 2014

25. R. Bernabei, P. Belli, F. Cappella, V. Caracciolo, R. Cerulli, C.J. Dai, A. d'Angelo, S. d'Angelo, A. Di Marco, H.L. He, A. Incicchitti, H.H. Kuang, X.H. Ma, F. Montecchia, X.D. Sheng, R.G. Wang, Z.P. Ye, Recent results from DAMA/LIBRA- phase1 and perspectives, to appear in the Proceed. of ICHEP 2014, Valencia (Spain), July 2014

26. R. Bernabei, P. Belli, F. Cappella, V. Caracciolo, R. Cerulli, C.J. Dai, A. d'Angelo, S. d'Angelo, A. Di Marco, H.L. He, A. Incicchitti, H.H. Kuang, X.H. Ma, F. Montecchia, X.D. Sheng, R.G. Wang, Z.P. Ye, DAMA/LIBRA-phase1 results and perspectives of the phase2, to appear in the Proceed. of ICNFP 2014, Kolymbari (Greece), July-August 2014

27. R. Bernabei, P. Belli, F. Cappella, V. Caracciolo, R. Cerulli, C.J. Dai, A. d'Angelo, S. d'Angelo, A. Di Marco, H.L. He, A. Incicchitti, H.H. Kuang, X.H. Ma, F. Montecchia, X.D. Sheng, R.G. Wang, Z.P. Ye, DAMA results at Gran Sasso Underground lab, to appear in the Proceed. of the Workshop on Theory, Phenomenology and Experiments in Flavour Physics, Capri (Italy), May 2014

28. R. Bernabei, P. Belli, S. d'Angelo, A. Di Marco, F. Montecchia, F. Cappella, A. d'Angelo, A. Incicchitti, V. Caracciolo, R. Cerulli, C.J. Dai, H.L. He, X.H. Ma, X.D. Sheng, R.G. Wang, Z.P. Ye, New results from DAMA/LIBRA: Final model independent results of DAMA/LIBRA-phase1 and perspectives of phase2, to appear in the Proceed. of the Vulcano Workshop 2014 "Frontier objects in Astrophysics ans Particle Physics", Vulcano (Italy), May 2014

References

[1] R. Bernabei et al., Nucl. Instr. and Meth. A 592 (2008) 297.

[2] R. Bernabei et al., Eur. Phys. J. C 56 (2008) 333.

[3] R. Bernabei et al., Eur. Phys. J. C 67 (2010) 39.

[4] R. Bernabei et al., Eur. Phys. J. C 73 (2013) 2648.

[5] P. Belli et al., Phys. Rev. D 84 (2011) 055014.

[6] R. Bernabei et al., J. of Instr. 7 (2012) P03009.

[7] R. Bernabei et al., Eur. Phys. J. C 72 (2012) 2064.

[8] R. Bernabei et al., Int. J. of Mod. Phys. A 28 (2013) 1330022 (73 pages).

[9] R. Bernabei et al., Eur. Phys. J. C 62 (2009) 327.

[10] R. Bernabei et al., Eur. Phys. J. C 72 (2012) 1920.

[11] R. Bernabei et al., Eur. Phys. J. A 49 (2013) 64.

[12] P. Belli, R. Bernabei, C. Bacci, A. Incicchitti, R. Marcovaldi, D. Prosperi, DAMA proposal to INFN Scientific Committee II, April 24^{th} 1990.

[13] R. Bernabei et al., Phys. Lett. B 389 (1996) 757; R. Bernabei et al., Phys. Lett. B 424 (1998) 195; R. Bernabei et al., Phys. Lett. B 450 (1999) 448; P. Belli et al., Phys. Rev. D 61 (2000) 023512; R. Bernabei et al., Phys. Lett. B 480 (2000) 23; R. Bernabei et al., Phys. Lett. B 509 (2001) 197; R. Bernabei et al., Eur. Phys. J. C 23 (2002) 61; P. Belli et al., Phys. Rev. D 66 (2002) 043503.

[14] R. Bernabei et al., Il Nuovo Cim. A 112 (1999) 545.

[15] R. Bernabei et al., Eur. Phys. J. C18 (2000) 283.

[16] R. Bernabei el al., La Rivista del Nuovo Cimento 26 n.1 (2003) 1-73.

[17] R. Bernabei et al., Int. J. Mod. Phys. D 13 (2004) 2127.

[18] R. Bernabei et al., Int. J. Mod. Phys. A 21 (2006) 1445.

[19] R. Bernabei et al., Eur. Phys. J. C 47 (2006) 263.

[20] R. Bernabei et al., Int. J. Mod. Phys. A 22 (2007) 3155.

[21] R. Bernabei et al., Eur. Phys. J. C 53 (2008) 205.

[22] R. Bernabei et al., Phys. Rev. D 77 (2008) 023506.

[23] R. Bernabei et al., Mod. Phys. Lett. A 23 (2008) 2125.

[24] R. Bernabei et al., Phys. Lett. B408 (1997) 439; P. Belli et al., Phys. Lett. B460 (1999) 236; R. Bernabei et al., Phys. Rev. Lett. 83 (1999) 4918; P. Belli et al., Phys. Rev. C60 (1999) 065501; R. Bernabei et al., Il Nuovo Cimento A112 (1999) 1541; R. Bernabei et al., Phys. Lett. B 515 (2001) 6; F. Cappella et al., Eur. Phys. J.-direct C14 (2002) 1; R. Bernabei et al., Eur. Phys. J. A 23 (2005) 7; R. Bernabei et al., Eur. Phys. J. A 24 (2005) 51; R. Bernabei et al., Astrop. Phys. 4 (1995) 45.

[25] K.A. Drukier et al., Phys. Rev. D 33 (1986) 3495.

[26] K. Freese et al., Phys. Rev. D 37 (1988) 3388.

[27] R. Bernabei et al., AIP Conf. Proceed. 1223, 50 (2010) (arXiv:0912.0660).

[28] R. Bernabei et al., J. Phys.: Conf. Ser. 203, 012040 (2010) (arXiv:0912.4200); http://taup2009.lngs.infn.it/slides/jul3/nozzoli. pdf, talk given by F. Nozzoli.

[29] R. Bernabei et al., in the volumeFrontier Objects in Astrophysics and Particle Physics (Vulcano 2010), S.I.F. Ed. (2011), 157 (arXiv:1007.0595).

[30] R. Bernabei et al., Can. J. Phys. 89 (2011) 11.

[31] R. Bernabei et al., to appear on Proceed. of the Int. Conf, TIPP 2011.

[32] R. Bernabei et al., arXiv:1210.6199; arXiv:1211.6346.

[33] A. Bottino et al., Phys. Rev. D 85 (2012) 095013.

[34] A. Bottino et al., arXiv:1112.5666.

[35] P. Belli et al., Il Nuovo Cim. 103A (1990) 767.

[36] P. Belli et al., Phys. Lett. B 387 (1996) 222 and Phys. Lett. B 389 (1996) 783 (erratum); R. Bernabei et al., New J. Phys. 2 (2000) 15.1; Eur. Phys. J.-direct C11 (2001) 1; Phys. Lett. B 436 (1998) 379; R. Bernabei et al., in the volume “Beyond the Desert 2003”, Springer (2003) 365.

[37] R. Bernabei et al., Nucl. Instr. & Meth. A482 (2002) 728.

[38] R. Bernabei et al., Phys. Lett. B 546 (2002) 23; F. Cappella, PhD Thesis, Università di Roma ”Tor Vergata”, 2005.

[39] P. Belli et al., Il Nuovo Cim. C 19 (1996) 537; Astrop. Phys. 5 (1996) 217.

[40] R. Bernabei et al., Phys. Lett. B 527 (2002) 182.

[41] P. Belli et al., Phys. Rev. D 61 (2000) 117301; Phys. Lett. B 465 (1999) 315; R. Bernabei et al., Phys. Lett. B 493 (2000) 12; Eur. Phys. J. A 27 s01 (2006) 35.

[42] R. Bernabei et al., Astropart. Phys. 7 (1997) 73; R. Bernabei et al., Il Nuovo Cim. A 110 (1997) 189; P. Belli et al., Astropart. Phys. 10 (1999) 115; P. Belli et al., Nucl. Phys. B 563 (1999) 97; R. Bernabei et al., Nucl. Phys. A 705 (2002) 29; P. Belli et al., Nucl. Instr. Meth.

A 498 (2003) 352; R. Cerulli et al., Nucl. Instr. Meth. A 525 (2004) 535; R. Bernabei et al., Nucl. Instr. Meth. A 555 (2005) 270; R. Bernabei et al., Ukr. J. Phys. 51 (2006) 1037; P. Belli et al., Nucl. Phys. A 789 (2007) 15; P. Belli et al., Phys. Rev. C 76 (2007) 064603; P. Belli et al., Eur. Phys. J. A 36 (2008) 167; P. Belli et al., Nucl. Instr. Meth. A 615 (2010) 301; P. Belli et al., J. Phys. G 38 (2011) 015103; D. Poda et al., Radiation Measurements 56 (2013) 66.

[43] P. Belli et al., Nucl. Phys. A 826 (2009) 256; P. Belli et al., Phys. Lett. B 658 (2008) 193; P. Belli et al., Nucl. Instrum. and Meth. A 626-627 (2011) 31.

[44] P. Belli et al., Phys. Rev. C 85 (2012) 044610.

[45] P. Belli et al., J. Phys. G: Nucl. Part. Phys. 38 (2011) 115107.

[46] A.S. Barabash et al., JINST. 6 (2011) P08011.

[47] R.B. Firestone et al., Table of Isotopes (John Wiley & Sons, N.Y., 1996) and 1998 CD update.

[48] E. Browne, Nucl. Data Sheets 104, 427 (2005).

[49] V.I. Tretyak et al., Europhys. Lett. 69, 41 (2005) more detailed version: arXiv:nucl-ex/0404016.

[50] G. Bellini et al., Eur. Phys. J. A 49, 92 (2013).

[51] P. Belli et al., Nucl. Instr. and Meth. A 572 (2007); P. Belli et al., Nucl. Phys. A 806 (2008) 388; P. Belli et al., Nucl. Phys. A 824 (2009) 101; O. P. Barinova et al., Nucl. Instr. and Meth. A 607 (2009) 573; P. Belli et al., Eur. Phys. J. A 42 (2009) 171; P. Belli et al., Nucl. Phys. A 846 (2010) 143; P. Belli et al., Nucl. Phys. At. Energy 11 (2010) 362; P. Belli et al., Nucl. Phys. A 859 (2011) 126; P. Belli et al., Phys. Rev. C 83 (2011) 034603; P. Belli et al., Eur. Phys. J. A 47 (2011) 91; P. Belli et al., Nucl. Instr. and Meth. A 670 (2012) 10; P. Belli et al., Phys. Lett. B 711 (2012) 41; P. Belli et al., Nucl. Instr. and Meth. A 704 (2013) 40; P. Belli et al., Eur. Phys. J. A 49 (2013) 24; P. Belli et al., Phys. Rev. C 87 (2013) 034607.

[52] V.I. Tretyak, Yu.G. Zdesenko, Tables of double beta decay data, At. Data Nucl. Data Tables 61 (1995) 43; V.I. Tretyak, Yu.G. Zdesenko, Tables of double beta decay data – an update, At. Data Nucl. Data Tables 80 (2002) 83.

[53] F. Cappella et al., Eur. Phys. J. C 73 (2013) 2276.

[54] FIRB 2013: "Sviluppo di rivelatori a risposta anisotropa", PI: Cappella Fabio, Reference number: RBFR13THVM; Talk by R. Cerulli at Int. Conf. Dark matter, Dark Energy and their detection, Novosibirsk, Russia, July 2013, http://people.roma2.infn.it/∼dama/pdf/cerulli_novosibirsk2013.pdf; Talk by P. Belli at What Next workshop, Tor Vergata University, Rome, Italy, March 2014, http://people.roma2.infn.it/∼belli/belli_TorVergata_mar14.pdf.

The DarkSide-50 Experiment

P. Agnes,[1] L. Agostino,[2] I. Albuquerque,[3] T. Alexander,[4] A. Alton,[5] K. Arisaka,[6] H. Back,[3] B. Baldin,[7] K. Biery,[7] G. Bonfini,[8] M. Bossa,[9] B. Bottino,[10] A. Brigatti,[11] J. Brodsky,[3] F. Budano,[12] S. Bussino,[12] L. Cadonati,[4] M. Cadoni,[13] H. Cao,[3] F. Calaprice,[3] N. Canci,[6] A. Candela,[8] M. Cariello,[10] M. Carlini,[8] S. Catalanotti,[14] P. Cavalcante,[15] A. Chepurnov,[16] A.G. Cocco,[14] C. Condon,[3] G. Covone,[14] D. D'Angelo,[11] M. D'Incecco,[8] S. Davini,[9,17] S. De Cecco,[2] M. De Deo,[8] M. De Vincenzi,[12] A. Derbin,[18] A. Devoto,[13] F. Di Eusanio,[3] G. Di Pietro,[11] C. Dionisi,[19] E. Edkins,[20] A. Empl,[17] A. Fan,[6] G. Fiorillo,[14] K. Fomenko,[21] J.P. Fontaine,[9] G. Forster,[4] D. Franco,[1] F. Gabriele,[8] C. Galbiati,[3] S. Giagu,[19] C. Giganti,[2] A. Goretti,[3] L. Grandi,[22] M. Gromov,[16] M.Y. Guan,[23] Y. Guardincerri,[7] B. Hackett,[20] K. Herner,[7] E. Hungerford,[17] Al. Ianni,[8] An. Ianni,[3] I. James,[12] C. Jollet,[24] K. Keeter,[25] C. Kendziora,[7] S. Kidner,[15] V. Kobychev,[26] G. Koh,[3] D. Korablev,[21] G. Korga,[17] A. Kurlej,[4] P.X. Li,[23] M. Lissia,[13] P. Lombardi,[11] L. Ludhova,[11] S. Luitz,[27] G. Lukyachenko,[26] Y.Q. Ma,[23] I. Machulin,[26] A. Mandarano,[9] S. Mari,[12] J. Maricic,[20] L. Marini,[10] D. Markov,[26] C.J. Martoff,[28] A. Meregaglia,[24] E. Meroni,[11] P. Meyers,[3] T. Miletic,[28,29] R. Milincic,[20] D. Montanari,[7] A. Monte,[4] M. Montuschi,[8] M.E. Monzani,[27] P. Mosteiro,[3] B. Mount,[25] V. Muratova,[18] P. Musico,[10] A. Nelson,[3] S. Odrowski,[8] A. Odrzywolek,[30] M. Okounkova,[3] M. Orsini,[8] F. Ortica,[31] L. Pagani,[10] M. Pallavicini,[10] E. Pantic,[32] L. Papp,[15] S. Parmeggiano,[11] K. Pelczar,[30] N. Pelliccia,[31] L. Perasso,[10] S. Perasso,[1] A. Pocar,[4] S. Pordes,[7] D. Pugachev,[26] H. Qian,[3] K. Randle,[4] G. Ranucci,[11] A. Razeto,[8] K. Recine,[28] B. Reinhold,[20] A. Renshaw,[6] M. Rescigno,[19] A. Romani,[31] B. Rossi,[14,3] N. Rossi,[8] D. Rountree,[15] D. Sablone,[17,8] P. Saggese,[11] R. Saldanha,[22] W. Sands,[3] S. Sangiorgio,[33] C. Savarese,[9] E. Segreto,[8] D. Semenov,[18] E. Shields,[3] M. Skorokhvatov,[26] M. Smallcomb,[5] O. Smirnov,[21] A. Sotnikov,[21] C. Stanford,[3] Y. Suvorov,[6] R. Tartaglia,[8] J. Tatarowicz,[28] G. Testera,[10] A. Tonazzo,[1] E. Unzhakov,[18] A. Vishneva,[21] B. Vogelaar,[15] M. Wada,[3] S. Walker,[14] H. Wang,[6] Y. Wang,[23] A.W. Watson,[28] S. Westerdale,[3] M. Wojcik,[30] X. Xiang,[3] J. Xu,[3] C.G. Yang,[23] J. Yoo,[7] S. Zavatarelli,[10] A. Zec,[4] C. Zhu,[3] and G. Zuzel[30]

[1]*APC, Université Paris Diderot, Sorbonne Paris Cité, Paris 75205, France*
[2]*LPNHE, Université Pierre et Marie Curie, Université Paris Diderot, CNRS/IN2P3, Paris 75252, France*
[3]*Department of Physics, Princeton University, Princeton, NJ 08544, USA*
[4]*Amherst Center for Fundamental Interactions and Physics Department, University of Massachusetts, Amherst, MA 01003, USA*
[5]*Physics and Astronomy Department, Augustana College, Sioux Falls, SD 57197, USA*
[6]*Physics and Astronomy Department, University of California, Los Angeles, CA 90095, USA*
[7]*Fermi National Accelerator Laboratory, Batavia, IL 60510, USA*
[8]*Laboratori Nazionali del Gran Sasso, Assergi (AQ) 67010, Italy*
[9]*Gran Sasso Science Institute, L'Aquila 67100, Italy*
[10]*Physics Department, Università degli Studi and INFN, Genova 16146, Italy*
[11]*Physics Department, Università degli Studi and INFN, Milano 20133, Italy*
[12]*Physics Department, Università degli Studi Roma Tre and INFN, Roma 00146, Italy*
[13]*Physics Department, Università degli Studi and INFN, Cagliari 09042, Italy*
[14]*Physics Department, Università degli Studi Federico II and INFN, Napoli 80126, Italy*
[15]*Physics Department, Virginia Tech, Blacksburg, VA 24061, USA*
[16]*Skobeltsyn Institute of Nuclear Physics, Lomonosov Moscow State University, Moscow 119991, Russia*
[17]*Department of Physics, University of Houston, Houston, TX 77204, USA*
[18]*Saint Petersburg Nuclear Physics Institute, Gatchina 188350, Russia*
[19]*Physics Department, Sapienza – Università di Roma and INFN, Roma 00185, Italy*
[20]*Department of Physics and Astronomy, University of Hawai'i, Honolulu, HI 96822, USA*
[21]*Joint Institute for Nuclear Research, Dubna 141980, Russia*
[22]*Kavli Institute, Enrico Fermi Institute and Dept. of Physics, University of Chicago, Chicago, IL 60637, USA*
[23]*Institute of High Energy Physics, Beijing 100049, China*
[24]*Institut Pluridisciplinaire Hubert Curien, Strasbourg 67037, France*
[25]*School of Natural Sciences, Black Hills State University, Spearfish, SD 57799, USA*
[26]*National Research Centre Kurchatov Institute, Moscow 123182, Russia*
[27]*SLAC National Accelerator Laboratory, Menlo Park, CA 94025, USA*
[28]*Physics Department, Temple University, Philadelphia, PA 19122, USA*
[29]*Department of Chemistry and Physics, Arcadia University, Glenside, PA 19038, USA*
[30]*Smoluchowski Institute of Physics, Jagiellonian University, Krakow 30059, Poland*
[31]*Chemistry Department, Università degli Studi and INFN, Perugia 06123, Italy*
[32]*Physics Department, University of California, Davis, CA 95616, USA*
[33]*Lawrence Livermore National Laboratory, Livermore, CA 94550, USA*

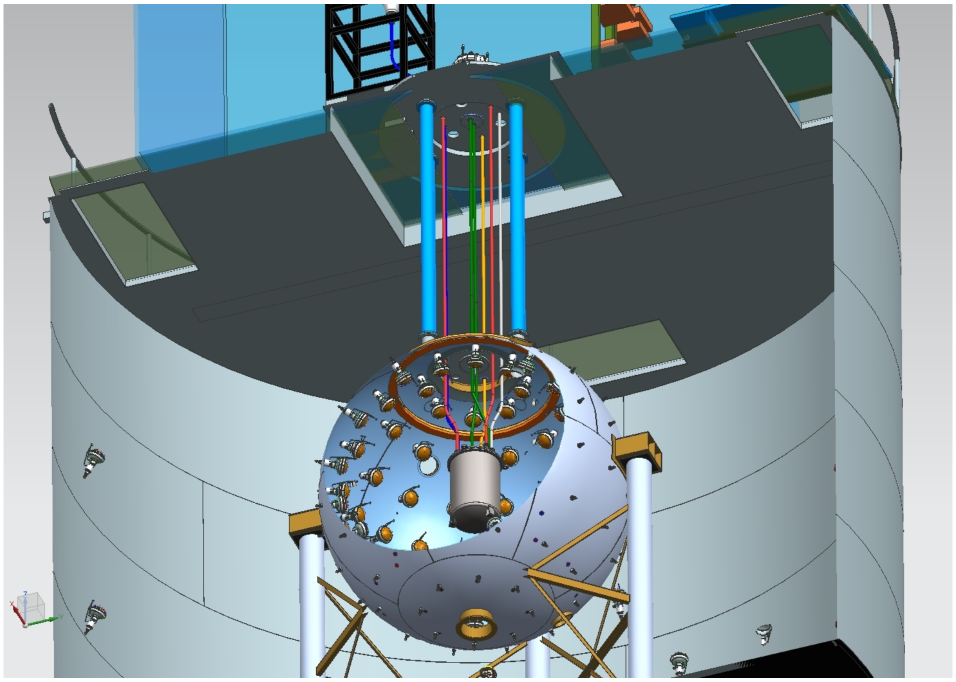

FIG. 1. The DarkSide-50 apparatus.

I. INTRODUCTION AND STATUS OF DARKSIDE-50 AS OF MAY, 2015

The DarkSide-50 experiment is a direct search for WIMP Dark Matter using a liquid argon time projection chamber (LAr-TPC). The LAr-TPC has pulse-shape discrimination with rejection power of $\sim 10^7$ for gamma-ray and beta decay backgrounds while retaining high efficiency for WIMP recoils in the energy range expected for medium and high mass WIMPs. Neutron backgrounds are rejected with very high efficiency by a sophisticated veto system (see below) surrounding the TPC.

The DarkSide-50 apparatus consists of three nested detectors. Innermost is the Liquid Argon Time Projection Chamber (LAr-TPC), with its 50 kg active mass (150 kg mass total). This is surrounded by the 4.0 m diameter (30 tonne) borated Liquid Scintillator Veto (LSV), which lies within the 1 kt water Cherenkov detector (WCD). The organic scintillator mix consists of pseudocumene (PC) and trimethylborate (TMB), with the wavelength shifter (2,5) diphenyloxazole (PPO).

The experiment published its first results in [1], from an initial 50 live days ((1422 ± 67) kg d) of data with an Atmospheric Argon (AAr) fill in the LAr-TPC and the full veto system functioning. The published results are discussed in Sec. II below. Most importantly, the pulse-shape discrimination combined with other analysis cuts was sufficient to completely suppress the $\sim 1.5 \times 10^7$ background events from ^{39}Ar in the AAr exposure, giving a background-free WIMP region in the final acceptance plot.

Several major operations have been successfully performed on DarkSide-50 after the initial AAr data taking period ended. These included completely reconstituting the liquid scintillator, calibration measurements using radioactive sources inserted within the LSV, and finally the filling of the LAr-TPC with low-^{39}Ar underground argon. As a result, the full detector system is now functioning in a low background mode appropriate for an extended dark matter search.

The veto reconstitution was necessary in order to correct the previously reported compromise of the liquid scintillator by a high ^{14}C content. This was caused by inadvertent use of a batch of TMB made from biological precursors containing modern carbon, rather than from petroleum. Removing the TMB by repeated distillation during June, 2014 reduced the ^{14}C trigger rate in the LSV from 150kBq to 0.3kBq. In January, 2015, further operations were performed to re-distill the PC, restore the PPO thereby removed, and finally replace the TMB with radiopure material, albeit at a lower concentration (5% instead of 50%). No increase of the ^{14}C trigger rate was observed on adding the new TMB. Details on the present performance of the veto are given below in Sec. IV.

Two TPC and LSV calibration campaigns were performed using neutron and gamma sources. The sources were inserted within the LSV using the newly commissioned source insertion device CALIS. The calibration campaigns and their first results are discussed in Sec. III.

The goal of DarkSide-50 is to conduct a dark matter search with the TPC filled with underground argon (UAr)[2, 3]. UAr has greatly reduced ^{39}Ar content relative to AAr[4], which is necessary for the future extension of the DarkSide program to tonne-scale detectors. Years of work by members of the collaboration toward this goal culminated on April 1, 2015 when DarkSide-50 was topped off with essentially the entire world's supply of UAr. Re-commissioning of the TPC with UAr is nearly complete at time of writing, but the early data already show that the detector is performing very well. The argon cryogenic system is stable; the UAr light yield is indistinguishable from that of AAr, and the UAr electron drift lifetime (a stringent indicator of any electronegative contaminants such as water or oxygen) is more than 4 milliseconds. Preliminary estimates of the radioactive ^{39}Ar level in the UAr are significantly below the upper limits previously established by counting small samples of UAr[4]. Details of the TPC performance with UAr are presented below in Sec. V.

II. PUBLISHED RESULTS FROM ATMOSPHERIC ARGON FILL:

In Ref[1], we presented results from 50 live days ($(1422 \pm 67)\,\mathrm{kg\,d}$) of data with the LAr-TPC filled with Atmospheric Argon (AAr) and the full veto system functioning. This initial run established important technical results such as the stability of the innovative closed-loop argon circulation system with external purification and cooling, and demonstrated an electron drift lifetime in the LAr-TPC of > 5 ms. The photoelectron yield was measured *in situ* using a source of short-lived ^{85m}Kr injected into the LAr circulation, as well as the ^{39}Ar beta decay spectrum. The yield for primary argon scintillation at null field was $(7.9 \pm 0.4)\,\mathrm{PE/keV}$. Achieving such a high photoelectron yield was a key technical goal of the experiment, since photoelectron statistics dominate the background rejection power of the pulse shape discrimination.

Another technical innovation proven in the AAr exposure was the use of cryogenic preamplifiers designed at LNGS to read out the LAr-TPC photomultipliers. The resulting very high signal to noise ratio, combined with the high photoelectron yield, further increased the performance of the pulse shape discrimination.

The LSV was also commissioned, achieving a photoelectron yield of $(0.54 \pm 0.04)\,\mathrm{PE/keV}$. It was successfully used to remove a handful of neutron candidates from the AAr dataset, despite a high LSV background rate caused by the inadvertent use of TMB containing ^{14}C from organic carbon precursors (this has since been remediated; see below).

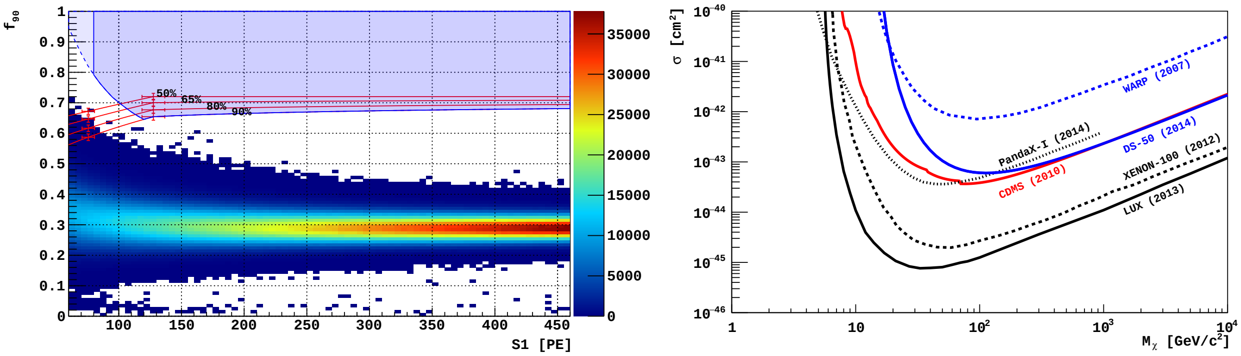

FIG. 2. *left*: Scatterplot of pulse shape discrimination parameter F90 vs. primary scintillation pulse height S1, for the 50 day AAr data sample (from Ref. [1]) after all data quality and physics cuts. The shaded blue region is the dark matter search box in the f90 vs. S1 plane. Percentages label the f90 acceptance contours for nuclear recoils drawn by connecting points (shown with error bars) determined from the SCENE measurements. No events are found in the search box. *right*: The spin-independent WIMP-nucleon cross section 90% C.L. exclusion plot derived from the AAr data sample shown to the left is represented by the solid blue line. Other results shown are from LUX [7] (solid black), XENON100 [8] (dashed black), PandaX [9] (dotted black), CDMS [10] (solid red), and WARP [11] (dashed blue)

Combined with other analysis cuts, the pulse shape discrimination was sufficient to completely suppress the $\sim 1.5 \times 10^{7}$ background events from ^{39}Ar decays, i.e. to give a background-free WIMP region in the final acceptance plot. This plot is shown in Fig. 2, left. The DarkSide-50 spin-independent WIMP search exclusion plot derived from this analysis is shown in Fig. 2, right. The upper limit is as low as $6.1 \times 10^{-44}\,\mathrm{cm}^2$ at $100\,\mathrm{GeV/c^2}$ WIMP mass, the best result achieved to date with an argon target.

The background-free result obtained with such a large sample of ^{39}Ar decay events has important implications for measurements with UAr, with its much lower rate from ^{39}Ar. The reported AAr exposure contained at least as many ^{39}Ar events as $0.6\,\mathrm{t\,yr}$ of running with UAr, implying that the background rejection in DarkSide-50 is powerful enough to give a background-free result from a UAr run *twenty years* long. For a more realistic ∼3 year UAr run, the demonstrated ^{39}Ar rejection power would allow the acceptance region to be significantly widened without admitting any background, giving even higher WIMP acceptance at low energies than in the publication.

III. RADIOACTIVE SOURCE CALIBRATION OF DARKSIDE-50

During 2014, DarkSide collaborators developed calibration hardware to deploy radioactive sealed sources within the LSV. CALIS (CALibration Insertion System) is designed to calibrate both the LAr-TPC and the LSV. The device has been constructed, tested at Fermilab and LNGS, precision cleaned, and successfully installed into the LSV with entry *via* the DarkSide CRH clean room (Fig. 3, left).

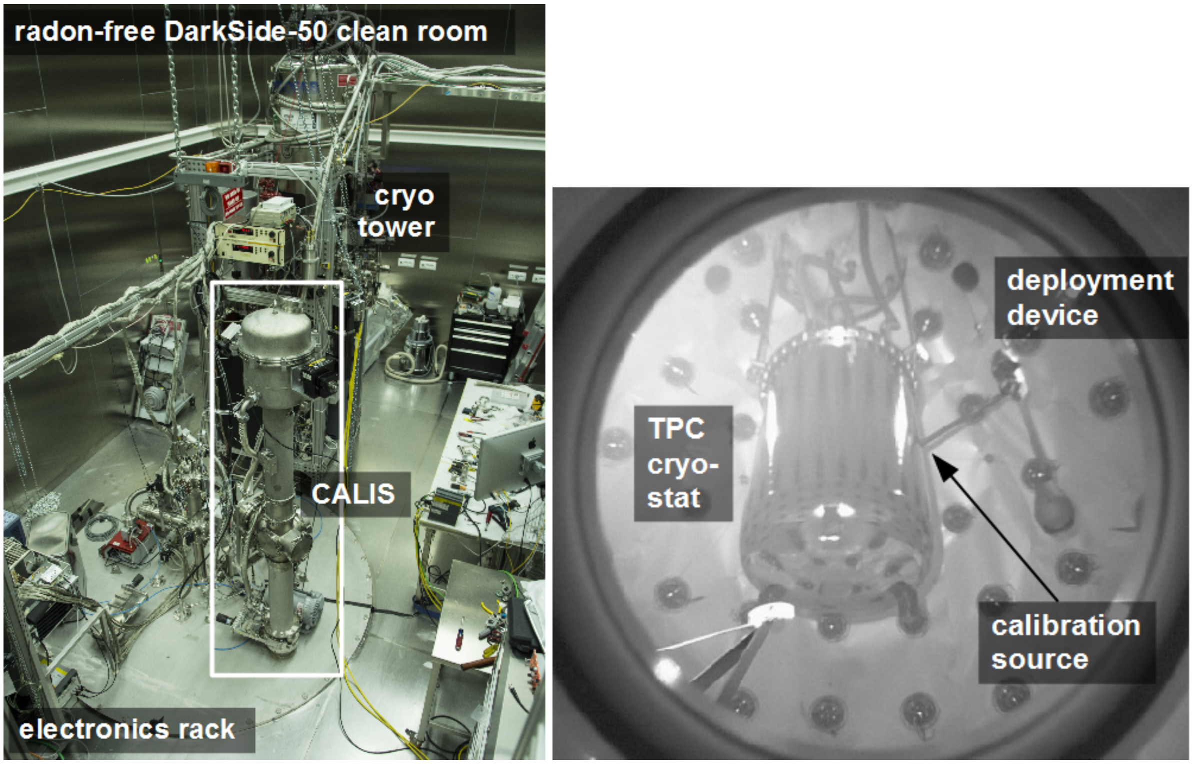

FIG. 3. *left*: CALIS after installation inside the CRH radon-suppressed clean room atop the WCD. *right*: Photograph taken with a camera looking into the LSV from the WCD. It shows a source deployed next to the cryostat of the LAr-TPC.

Source Deployment: In order to deploy a radioactive source next to the LAr-TPC, the source is brought into the CRH radon-suppressed clean room atop the WCD tank, and mounted in a source holder connected to the deployment device within CALIS. A stainless steel cable allows the source holder to be lowered into the LSV through a load lock on a dedicated access port, to a position next to the cryostat. The source holder is on the end of a 60 cm long articulated arm, which can be moved and rotated to position the source in 3-D relative to the cryostat (Fig. 3, right). Throughout the deployment a slightly pressurized nitrogen atmosphere is maintained in order to avoid exposing the liquid scintillator to oxygen or water, which would degrade it. All materials used for CALIS, such as stainless steel, teflon, and viton, that come in contact with the scintillator are certified for contact with the liquid scintillator. The system includes several safety features to ensure safe deployment and retrieval of the source without affecting the stability and performance of the LSV. After data taking, the deployment device is retracted into the load lock and a sequence of N_2 purging and evacuation removes all traces of scintillator. The source holder can then be removed from the deployment device and the radioactive source returned to storage. Tests in air at LNGS established the deployment system's positioning accuracy to be about ±1 cm after its 7 meter journey into the LSV. This result is being compared to calibration campaign data in an ongoing analysis. The CALIS concept has the built-in flexibility to deploy different devices next to the cryostat, e.g. the deployment of a (d,d) neutron generator is considered in the future.

Calibration Campaigns: After the calibration device and the deployment procedures were approved by the DarkSide scientific committee, two extensive calibration campaigns were performed during October through December

2014 and January through February 2015. The performance and stability of the LSV and LAr-TPC were not affected by these campaigns.

Since these were the first exposures of DarkSide-50 to external radioactive sources, several different gamma sources were explored (^{57}Co, ^{133}Ba and ^{137}Cs), in addition to two Am-Be neutron sources differing significantly in activity. The Am-Be neutron source deployments allowed the full DarkSide-50 system (LAr-TPC, LSV, WCD) response to neutrons to be measured *in situ* for the first time. Data was taken while conditions such as the TPC drift field (null field, 100 V/cm, 150 V/cm, 200 V/cm) and the source positions relative to the TPC were systematically varied. This was done to improve our understanding of the detector and to allow accurate tuning of the detector optics and LAr microphysics embodied in G4DS, the DarkSide-50 Monte Carlo.

DarkSide-50 Monte Carlo: G4DS is a Geant-4 based simulation of the energy deposits of each type of particle in LAr and in the materials of the detector, the generation of scintillation signals, and the light collection. The program contains accurate representations of the materials and geometry of the entire detector (including the vetoes), the optical parameters of materials which affect the photon propagation, and also an LAr scintillation and ionization model to accurately simulate light generation by various modes of energy deposition. This effective model had to be developed due to the lack of complete experimental and theoretical information about electron-ion recombination in LAr in the literature. The model includes a functional form for the recombination probability based on literature data, with parameter values fitted to make the MC agree with the high statistics ^{39}Ar spectrum. The overall photoelectron yield of the MC was normalized at the ^{39}Ar endpoint. The entire Monte Carlo chain was then tested by comparisons with data from the external calibration sources, ^{57}Co, ^{133}Ba and ^{137}Cs.

Early Results: Fig. 4, left shows a comparison of ^{57}Co calibration source S1 scintillation spectrum to the G4DS MC simulation. The calibration source data was analyzed with minimal cuts but restricting the sample to single-site interactions having one S1 and one S2 pulse. To reproduce this condition, the MC clusterizes its calculated energy deposits and rejects events with clusters sufficiently separated to fail the single-site cut applied to the data. The ^{57}Co gamma ray spectrum reaching the TPC is also significantly degraded by Compton interactions in the stainless steel source holder, the cryostat, and the copper field cage rings of the TPC. These effects change the observed spectrum significantly, and appear to be well accounted for by the MC. Also, the short attenuation length of the 122 keV gammas from ^{57}Co causes the interactions to be concentrated near the detector's edge, which is harder to describe in MC than the central region of the detector. While some improvements are yet to be made, the level of agreement between the simulation and the various complex features of the data is very encouraging.

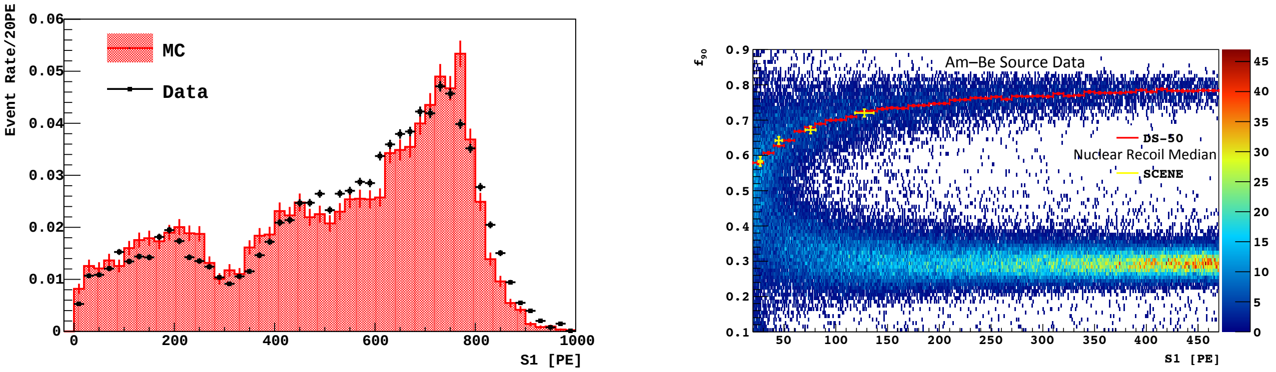

FIG. 4. *left*: Data-MC comparison for the S1 primary scintillation spectrum from a ^{57}Co source deployed next to the cryostat. While some improvements are yet to be made, the level of agreement between the simulation and the various complex features of the data is very encouraging. *right:* Plot of F90 vs. scintillation signal S1 from a high rate Am-Be neutron source calibration of DarkSide-50. The red line shows the mean F90 for the nuclear recoil band, while the points in yellow show the corresponding F90 values scaled from SCENE measurements and used in our publication Ref. [1]. There is very good agreement between the two. Inelastic scattering of the high energy neutrons, the high source intensity, and correlated neutron and γ-ray emission by the Am-Be source all contribute events outside the nuclear recoil and electron recoil bands.

The WIMP search box and nuclear recoil acceptance in our paper [1] were established without the availability of neutron calibration data in DarkSide-50. Pulse shape discrimination in DarkSide-50 is based on a parameter called F90, which is the fraction of S1 scintillation occurring in the first 90 ns of a pulse. F90 mean values were measured in the SCENE experiment [6] as a function of energy and then scaled to the light yield of DarkSide-50, and the electron and nuclear recoil acceptance curves were determined from an analytic statistical model of the F90 distributions as a function of energy. While we have full confidence in this approach, the Am-Be neutron source

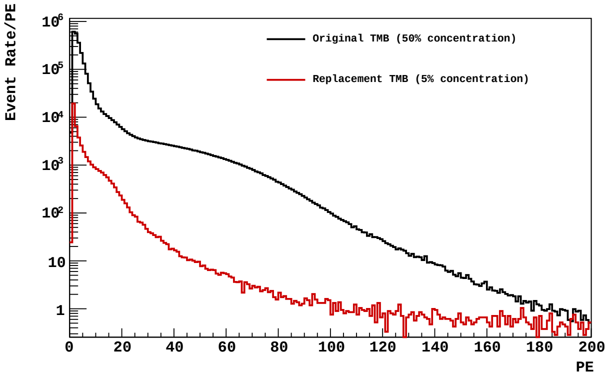

FIG. 5. The low energy spectrum seen in the LSV in the original configuration, with ^{14}C-rich TMB, at 50% concentration, compared to the current low-^{14}C TMB at $\sim$ 5% concentration. The dramatic decrease in ^{14}C background is evident.

data now allow the approach to be directly verified. The mean F90 for nuclear recoils in DarkSide-50 is found to agree closely with the corresponding scaled SCENE results, as shown in Fig. 4, right). (Events in this plot outside the nuclear recoil and electron recoil bands are contributed by inelastic scattering of energetic neutrons from the Am-Be source, along with its correlated neutron and gamma ray emissions.)

In January and February 2015 the reconstitution of the LSV scintillator was completed and a second Am-Be neutron source calibration was performed, mainly to study the LSV response in the various neutron detection channels. With a borated scintillator, a critical aspect of the neutron detection efficiency is the capability to observe the 6.4 % capture branch leading to a 1775 keV α + ^{7}Li(g.s.) without any accompanying γ-ray. Veto results are described in further detail below in Sec. IV.

IV. DARKSIDE NEUTRON VETO PERFORMANCE

Several major operations were performed on the LSV between November 2014 and February 2015:

- many repeated distillations of the entire 30 t of PC-TMB-PPO mixture to remove the ^{14}C-rich TMB and purify the PC beginning in June 2014
- cycling of the entire scintillator inventory through external pumps to allow the re-insertion of PPO in two aliquots during December 2014 and February 2015
- cycling to insert the radiopure TMB in January 2015
- two calibration campaigns involving the insertion of radioactive sources during October through December 2014 and January through February 2015 (Sec. III).
- disposal of the ^{14}C-rich TMB during November, 2014

These operations were successfully carried out without incident, with generous assistance and hard work from the LNGS staff and Health and Safety Department.

First PPO addition: The first PPO addition campaign took place on December 1 and 2, 2014. It restored the PPO concentration from a few ppm remaining after PC distillation, to 680 ± 30 ppm ($\sim$ 0.7 g/l). The addition of PPO increased the light yield of the LSV from $\sim$ 0.4 PE/keV to $\sim$ 0.5 PE/keV with no increase of ^{14}C or other backgrounds.

Radiopure TMB addition: During the TMB addition campaign, which took place between January 8th and 15th, a total of 1.44 tons of TMB were added to the LSV. The mass fraction of TMB was increased to $\sim$ 5%, corresponding to a neutron capture time in the LSV of about 20 μsec. The trigger rate and the light yield of the LSV were unchanged by this operation. Fig. 5 compares the ^{14}C spectra with the original ^{14}C-rich TMB, at 50% concentration, to that of the current low-^{14}C TMB at $\sim$ 5% concentration. The dramatic decrease in ^{14}C background allows much more stringent veto cuts to be imposed on the WIMP search events than was the case during the data taking for Ref[1], without introducing significant dead time.

Neutron calibration and second PPO addition: A neutron source calibration of the LSV followed the TMB addition operation. The main goal of this calibration was to observe the neutron captures on ^{10}B in the TMB, which occurs *via* two channels:

$$\begin{array}{lll} ^{10}\mathbf{B} + n \rightarrow {}^{7}\mathbf{Li} + \alpha & & 6.4\% \\ ^{10}\mathbf{B} + n \rightarrow {}^{7}\mathbf{Li}^{*} + \alpha, & {}^{7}\mathbf{Li}^{*} \rightarrow {}^{7}\,\mathbf{Li} + \gamma(\mathbf{478keV}) & 93.6\% \end{array}$$

The first channel listed leaves the ^{7}Li daughter in its ground state, with a kinetic energy of 1015 keV. The accompanying α has kinetic energy 1775 keV. Due to scintillation quenching, this channel is expected to have a pulse height in the LSV at or below $\sim$50 keV$_{ee}$. This channel, with its highly quenched scintillation signal, must be detected with high efficiency in order to achieve the very high radiogenic neutron detection efficiency (99.5 %) desired for the DarkSide program. The second listed channel gives a much larger pulse height in the LSV due to the un-quenched signal of the 478 keV γ-ray in prompt coincidence with the 839 keV ^{7}Li nucleus and the 1471 keV α.

During the neutron calibration campaign of February, 2015, a second PPO addition was performed. This increased the PPO concentration from $\sim$ 0.7 g/l to $\sim$ 1.5 g/l. This further addition of PPO slightly decreased the light yield of β and γ interactions but also slightly increased the light yield for α+^{7}Li products, by decreasing the α+^{7}Li scintillation quenching [12]. The trigger rate due to ^{14}C or other radioactive backgrounds in the LSV did not increase during the calibration and second PPO campaign.

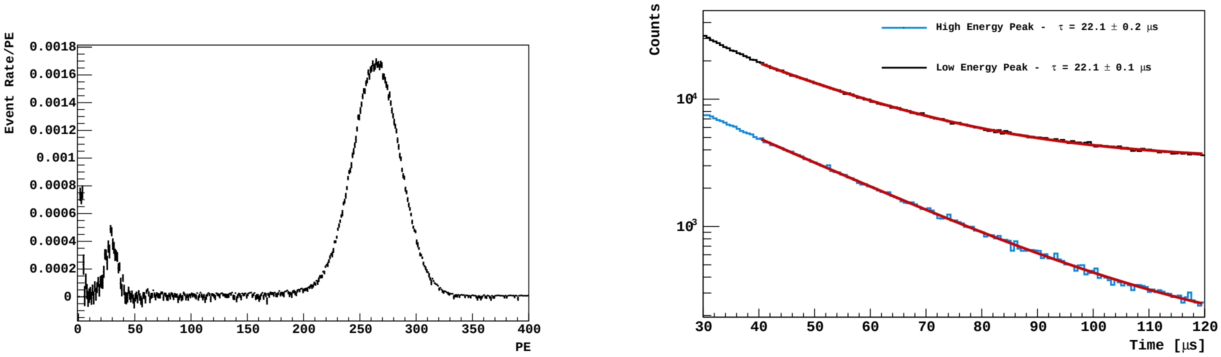

FIG. 6. *left*: Scintillation pulse height spectrum seen in the LSV at 1.5 g/l PPO, for signals in delayed coincidence with a large LSV signal from the 4.4 MeV gamma ray accompanying many Am-Be neutrons. The peak on the left is from the 6.4 % of captures which lead to an α + ^{7}Li(g.s.), while the peak on the right is from the 93.6 % of captures that lead to the ^{7}Li excited state, piled up with the accompanying 478 keV γ-ray. *right*: The delay time distributions for the two peaks in the left panel. Note the arbitrary displacement of the curves for clarity. The expected neutron capture time for a 5% TMB sctintillator is about 20 μsec. The capture times (τ) shown in the legend were found by fitting an exponential decay plus a constant to the time distributions. Both peaks show the time dependence of neutron capture in the scintillator, with a non-negligible constant background still evident in the case of the ground state transition.

Figure 6, left shows a pulse height spectrum of scintillation pulses in the LSV as seen during one of the Am-Be source calibration campaigns with the PPO concentration at 1.5 g/l. The LSV was self-triggered on a large signal from the 4.4 MeV gamma rays accompanying a large fraction of Am-Be neutrons. The low pulse-height peak, which we associate with the ^{7}Li ground state channel, lies between 20–30 PE, which is well above our detection threshold. Since the TPC cryostat can block some scintillation light, the energy and apparent branching ratio for the two possible decays are expected to depend on the position of the source relative to the TPC, which is consistent with observations. To verify that the two peaks seen in this figure are from neutron captures, the time distributions relative to the trigger are shown in Fig. 6, right. Both peaks drop off with a time constant of 22 μsec, roughly consistent with the 20 μsec capture time expected at this TMB concentration. The time distribution of the ground state channel shows a non-negligible constant background term.

In the analysis of the 50 day AAr campaign [1], the sensitivity of the LSV was largely determined by the high ^{14}C background rate. The threshold for applying an LSV veto could not be set low enough in energy to see the ^{7}Li(g.s.) neutron capture channel without introducing excessive dead time. Now that the ^{14}C rate is so much lower, cuts can be made which allow these events in the 20–30 PE range to be efficiently vetoed. This should allow the LSV to operate with significantly lower veto inefficiency than that reported in the 50 day AAr campaign [1].

With the present TMB concentration, $\sim$ 8% of neutrons will capture on ^{1}H. Neutron capture on ^{1}H produces a 2.2 MeV γ-ray, which is energetic enough to be easily seen if most of the energy is deposited in the scintillator.

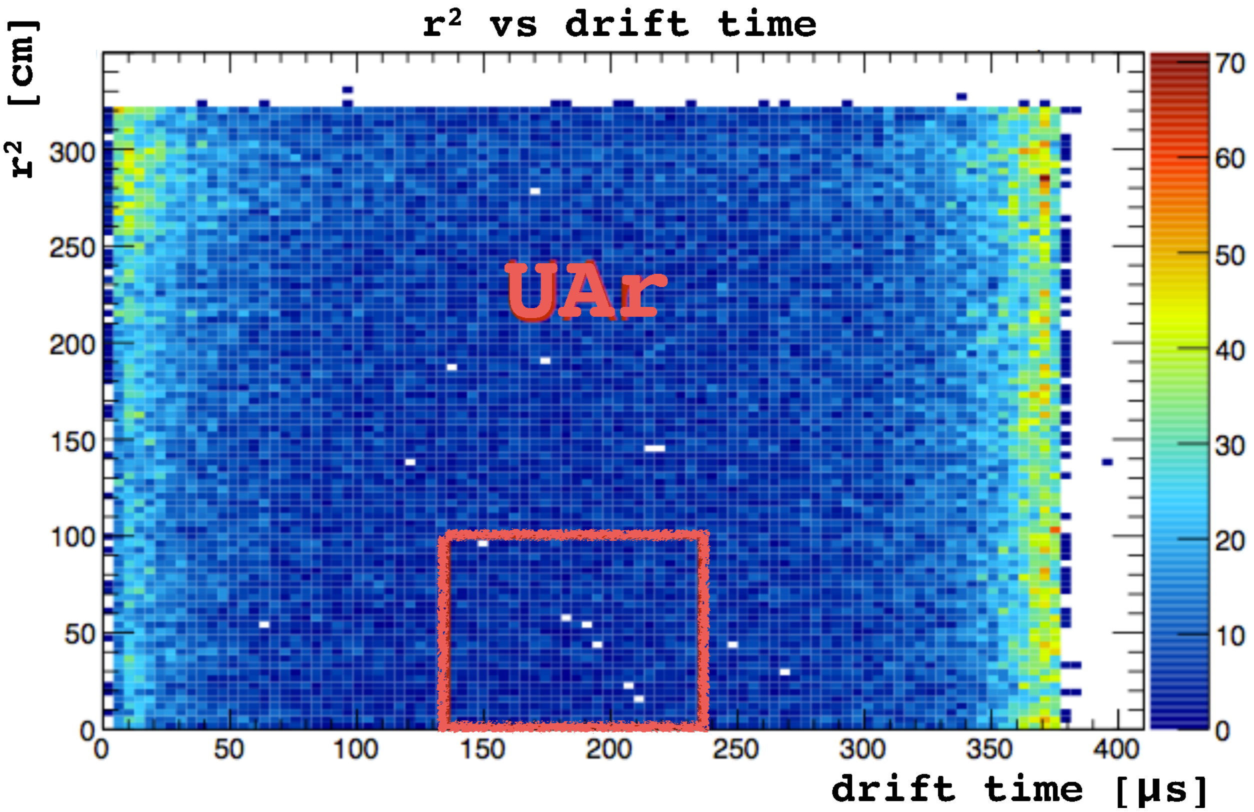

FIG. 7. Scatterplot of radius squared vs.drift time (z position) for all single-site events from UAr in the TPC. Events are seen to be concentrated along the boundaries of the detector, showing the self-shielding effect described in the text. The position cut imposed in Fig.8 (right) is shown as a pink box.

However, for neutron captures occurring near the TPC cryostat, the γ-ray may strike the cryostat and be absorbed without depositing enough energy in the LSV to be detected. If this happens and if in addition the neutron's slowing down signal is below threshold, the LSV may fail to detect and veto the neutron. While the loss of sensitivity due to this effect is still being studied, we suspect that this may be the limit on the veto efficiency that can be achieved with the present TMB concentration.

V. COMMISSIONING OF DARKSIDE-50 WITH UAR AND FIRST RESULTS

When DarkSide-50 is filled with AAr, background from the beta decay of cosmogenic ^{39}Ar dominates the event rate below that nuclide's 565 keV endpoint. Extension of the DarkSide program to ton-scale LAr-TPCs requires this background to be eliminated by procuring argon free of ^{39}Ar. Members of our collaboration have achieved this by constructing a plant at a gas well in Cortez, Colorado [2] to extract argon from the underground gas stream, and a cryogenic distillation plant at Fermilab[3] to purify this material. After years of effort, over 150 kg of underground argon (UAr) has been extracted, purified, and shipped to LNGS from its final purification site at Fermilab. Shipment was by sea, to avoid activation by cosmic rays. The UAr arrived at LNGS on February 11, 2015.

Several large pieces of new equipment needed for the UAr fill were also delivered, installed and commissioned at LNGS in preparation for the UAr fill. These included a very high-capacity heated getter system designed and built by Darkside collaborators to polish the UAr as it came out of its shipping bottles, as well as components for the UAr recovery system with a 200 bar compressor to ensure that the "genie" could be put back in his bottle(s) in case of emergency. In March, 2015 the DarkSide-50 TPC was turned off and the AAr was removed. Extensive realistic testing was performed on the new equipment and the UAr recovery system, and the stability of the cryogenic systems under complete power failure was verified. At last, the detector was prepared for re-filling with UAr.

After these six weeks of intense effort by members of the collaboration assisted by LNGS staff, the UAr filling operation started on March 25, and was completed on April 1. The step-by-step re-commissioning of the detector started immediately.

The first step was to take primary scintillation-only (S1) data with no drift field. This setting also allowed high resolution study of the residual background with the UAr fill. Within hours the positions of identified primordial radionuclide lines lying above the ^{39}Ar endpoint showed that the photoelectron yield was indistinguishable from that seen with AAr (Fig.8, left). These lines originate from the very low levels of U and Th in the detector construction materials.

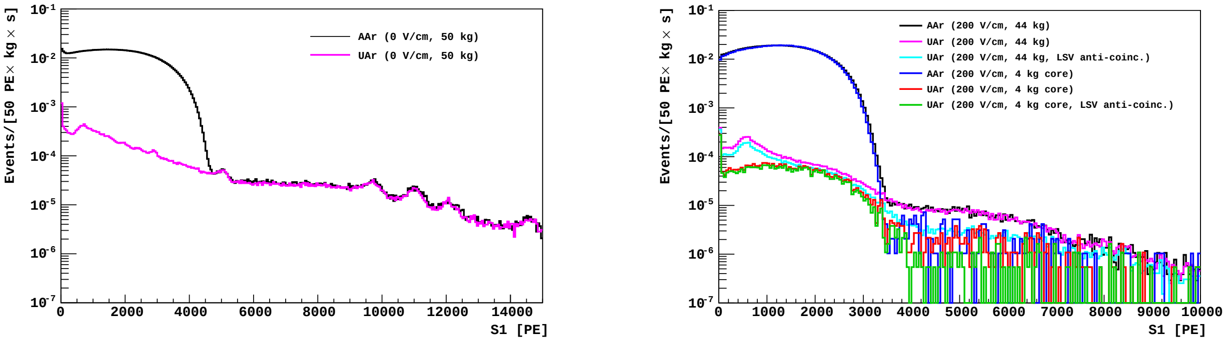

FIG. 8. *left*: S1 pulse height spectra with zero drift field, comparing very early UAr data to a live time-normalized sample of zero-field AAr data. Based on the agreement of gamma ray lines above 565 keV, the light yield of UAr data is seen to match that of AAr data. The lines are due to identified members of the U and Th decay chains and ^{60}Co present in construction materials. *right*: S1 pulse height spectra from early UAr running with drift field on at 200 V/cm, compared to a live-time normalized sample of 200 V/cm AAr data . Cuts restricting events to the central ∼10% of the LAr volume (red curve) reveal a small ^{39}Ar signal from the UAr. The ^{39}Ar level relative to AAr is estimated by taking the ratio of areas as discussed in the text, giving a level 300 ±7 (stat) times lower than AAr. Imposing a veto cut in addition, shows that additional Compton background is present in the UAr both above and below the ^{39}Ar endpoint. The absence of gamma ray photopeaks peaks in the field-on data is expected due to the single scatter cut needed for event localization, since energetic gamma ray photopeak events would require multiple interactions.

When the drift field was turned on, it rapidly became apparent that the initial purity of the UAr fill was extraordinary, with a drift lifetime exceeding 4 ms. The drift time and (x,y) localization information available with field on showed that the residual UAr background events were strongly concentrated at the periphery of the sensitive volume (Fig. 7). This represented a long awaited confirmation of the self-shielding effect that will provide added powerful background rejection in much larger detectors.

Fig. 8, right, shows a comparison of S1 pulse height spectra from UAr vs. AAr with the TPC fields on.

To seek a clean sample of ^{39}Ar events, a single scatter cut and a strong fiducial volume cut were imposed. The cut was $r < 10$ cm and 13 cm $< z <$ 22 cm, with the full detector radius being 17.8 cm and the full height 35.6 cm. The cut thus restricts events to lie in the central ∼10% of the detector volume. This left a hint of the ^{39}Ar spectral shape visible in the UAr data. The UAr/AAr agreement above the ^{39}Ar endpoint was preserved, as expected since both are dominated by the same gamma ray backgrounds in that energy region. The relative livetime normalization of these event samples was confirmed from the ratio of the integrated numbers of events above the ^{39}Ar endpoint, which is 1.06 ± 0.02 (stat). The agreement can be seen by comparing the dark blue and red lines in Fig. 8, right.

For an energy interval within the flat part of the ^{39}Ar spectrum, the ratio of events in the fiducialized AAr/UAr spectra is 300±7 (stat). This is a conservative value for the ^{39}Ar ratio in AAr/UAr, because the AAr spectral area is totally dominated by high rate ^{39}Ar while the UAr spectral area contains both ^{39}Ar and some additional background. Some of the background can be seen by comparing the red and green lines in Fig.8, right, which shows the effect of imposing an LSV veto cut on the fiducialized UAr data. The veto removes a small number of events, presumed to be multiply Compton scattered gamma rays with one interaction in the LSV and one in the LAr-TPC. The great majority of events below the ^{39}Ar endpoint are unaffected by the veto cut, as expected for fully contained low energy betas from ^{39}Ar.

This analysis confirms that the ^{39}Ar background in the full inventory of UAr is well below the upper limit previously established by counting small samples [4]. That published upper limit was already sufficient for the extension of the DarkSide program to ton-scale detectors.

VI. CONCLUSIONS AND OUTLOOK

DarkSide has now opened a new chapter in which the full potential of the LAr-TPC technology can begin to be realized. With the detector systems now in a very stable and extremely low background condition, we are looking forward to an extended dark matter search run, and to developing a further understanding of the remaining, non–^{39}Ar backgrounds.

Acknowledgements: DarkSide-50 was built, commissioned, and operated with support from NSF (NSF PHY-1004072, NSF PHY-1242585, and associated grants), DOE (DE-FG02-91ER40671 and DE-AC02-07CH11359), and INFN.

---

[1] P. Agnes et al, Physics Letters B 743, 456 (2015).
[2] H.O. Back et al., arxiv:1204.6024.
[3] H.O. Back et al., arxiv:1204.6061.
[4] J. Xu et al., Astropart. Phys. **66**, 53 (2015).
[5] T. Alexander et al. (SCENE Collaboration), Phys. Rev. D **88**, 092006 (2013).
[6] T. Alexander et al. (SCENE Collaboration), arxiv:1406.4825.
[7] D.S. Akerib et al. (LUX Collaboration),Phys. Rev. Lett. **112**, 091303 (2014).
[8] E. Aprile et al. (XENON100 Collaboration), Phys. Rev. Lett **109**, 181301 (2012).
[9] M. Xiao et al. (PandaX Collaboration), arxiv:1408.5114.
[10] Z. Ahmed et al. (CDMS II Collaboration), Science **327**, 1619 (2010).
[11] P. Benetti et al. (WARP Collaboration), Astropart. Phys. **28**, 495 (2008).
[12] I. Berlman, J. Chem. Phys. **34**, 598 (1961)

GERDA - the search for $0\nu\beta\beta$ decay

M. Agostini[o], M. Allardt[d], A.M. Bakalyarov[m], M. Balata[a], I. Barabanov[k], L. Baudis[s], C. Bauer[g], N. Becerici-Schmidt[n], E. Bellotti[h,i], S. Belogurov[l,k], S.T. Belyaev[m], G. Benato[s], A. Bettini[p,q], L. Bezrukov[k], T. Bode[o], D. Borowicz[c,e], V. Brudanin[e], R. Brugnera[p,q], A. Caldwell[n], C. Cattadori[i], A. Chernogorov[l], V. D'Andrea[a], E.V. Demidova[l], A. di Vacri[a], A. Domula[d], E. Doroshkevich[k], V. Egorov[e], R. Falkenstein[r], O. Fedorova[k], K. Freund[r], N. Frodyma[c], A. Gangapshev[k,g], A. Garfagnini[p,q], C. Gooch[n], P. Grabmayr[r], V. Gurentsov[k], K. Gusev[m,e,o], C. Hahne[d], A. Hegai[r], M. Heisel[g], S. Hemmer[p,q], G. Heusser[g], W. Hofmann[g], M. Hult[f], L.V. Inzhechik[k], L. Ioannucci[a], J. Janicskó Csáthy[o], J. Jochum[r], M. Junker[a], V. Kazalov[k], T. Kihm[g], I.V. Kirpichnikov[l], A. Kirsch[g], A. Kish[s], A. Klimenko[g,e], K.T. Knöpfle[g], O. Kochetov[e], V.N. Kornoukhov[l,k], V.V. Kuzminov[k], M. Laubenstein[a], A. Lazzaro[o], V.I. Lebedev[m], B. Lehnert[d], H.Y. Liao[n], M. Lindner[g], I. Lippi[q], A. Lubashevskiy[g,e], B. Lubsandorzhiev[k], G. Lutter[f], C. Macolino[a], B. Majorovits[n], W. Maneschg[g], G. Marissens[f], E. Medinaceli[p,q], M. Miloradovic[s], M. Misiaszek[c], P. Moseev[k], I. Nemchenok[e], S. Nisi[a], D. Palioselitis[n], K. Panas[c], L. Pandola[b], K. Pelczar[c], A. Pullia[j], M. Reissfelder[g], S. Riboldi[j], N. Rumyantseva[e], C. Sada[p,q], F. Salamida[i], M. Salathe[g], C. Schmitt[r], B. Schneider[d], J. Schreiner[g], O. Schulz[n], B. Schwingenheuer[g], S. Schönert[o], A-K. Schütz[r], H. Seitz[n], O. Selivanenko[k], E. Shevchik[e], M. Shirchenko[m,e], H. Simgen[g], A. Smolnikov[g], L. Stanco[q], M. Stepaniuk[g], H. Strecker[g], L. Vanhoefer[n], A.A. Vasenko[l], A. Veresnikova[k], K. von Sturm[p,q], V. Wagner[g], M. Walter[s], A. Wegmann[g], T. Wester[d], C. Wiesinger[o], H. Wilsenach[d], M. Wojcik[c], E. Yanovich[k], I. Zhitnikov[e], S.V. Zhukov[m], D. Zinatulina[e], K. Zuber[d], and G. Zuzel[c].

a) INFN Laboratori Nazionali del Gran Sasso and Gran Sasso Science Institute, Assergi, Italy

b) INFN Laboratori Nazionali del Sud, Catania, Italy

c) Institute of Physics, Jagiellonian University, Cracow, Poland

d) Institut für Kern- und Teilchenphysik, Technische Universität Dresden, Dresden, Germany e)Joint Institute for Nuclear Research, Dubna, Russia

f)Institute for Reference Materials and Measurements, Geel, Belgium

g)Max-Planck-Institut für Kernphysik, Heidelberg, Germany

h)Dipartimento di Fisica, Università Milano Bicocca, Milano, Italy

i)INFN Milano Bicocca, Milano, Italy

j)Dipartimento di Fisica, Università degli Studi di Milano e INFN Milano, Milano, Italy

k)Institute for Nuclear Research of the Russian Academy of Sciences, Moscow, Russia

l)Institute for Theoretical and Experimental Physics, Moscow, Russia

m)National Research Centre "Kurchatov Institute", Moscow, Russia

n)Max-Planck-Institut für Physik, München, Germany

o)Physik Department and Excellence Cluster Universe, Technische Universität München, Germany

p)Dipartimento di Fisica e Astronomia dell'Università di Padova, Padova, Italy

q)INFN Padova, Padova, Italy

r)Physikalisches Institut, Eberhard Karls Universität Tübingen, Tübingen, Germany

s)Physik Institut der Universität Zürich, Zürich, Switzerland

Spokesperson: B. Schwingenheuer (*B.Schwingenheuer@mpi-hd.mpg.de*)
Co-Spokesperson: S. Schönert (*Stefan.Schoenert@ph.tum.de*)

physics coordinator:	L. Pandola	chair of collaboration board:	R. Brugnera
technical coordinator:	B. Majorovits	chairs of speakers bureau:	R. Brugnera, K. Zuber
GLIMOS/RAE:	M. Balata	chair of editorial board:	P. Grabmayr

URL: `http://www.mpi-hd.mpg.de/gerda/`

Abstract

The GERmanium Detector Array (GERDA) at the Laboratori Nazionali del Gran Sasso of INFN, Italy, searches for neutrinoless double beta ($0\nu\beta\beta$) decay of ^{76}Ge. The GERDA experiment completed a first phase in 2013 and a lower limit on the half-life of the $0\nu\beta\beta$ decay for ^{76}Ge was derived: $T^{0\nu}_{1/2} > 2.1 \cdot 10^{25}$ yr (90% C.L.). Other results include an improved value for the two-neutrino double beta decay half-life $T^{2\nu}_{1/2} = 1.926 \pm 0.095 \cdot 10^{21}$ yr and a limit for Majoron accompanied double beta decay $T^{0\nu\chi}_{1/2} > 4.2 \cdot 10^{23}$ yr (90% C.L.). Currently, GERDA is upgrading to the second phase which allows to achieve a factor of 5-10 better sensitivity with respect to Phase I. In this report, the main results obtained from GERDA Phase I and the status of Phase II preparations are discussed.

1 Introduction

The GERmanium Detector Array, Gerda, searches for neutrinoless double beta decay of ^{76}Ge. The detection principle of Gerda is based on bare high-purity germanium (HPGe) detectors made from isotopically enriched material (86% of ^{76}Ge), immersed in liquid argon (LAr). Neutrinoless double beta decay of atomic nuclei (A, Z) $\rightarrow$ (A, Z+2) + 2e$^-$ is a forbidden process in the Standard Model (SM) of particle physics because it violates lepton number conservation by two units. The observation of such a decay would demonstrate that neutrinos have a Majorana component.

In Gerda Phase I, an exposure of 21.6 kg·yr has been collected with a background index (BI) of the order of BI$\simeq 10^{-2}$ cts/(keV·kg·yr). No excess of events from $0\nu\beta\beta$ decay has been detected in the region of interest and a lower limit on the half-life of the decay has been determined: $T^{0\nu}_{1/2} > 2.1 \cdot 10^{25}$ yr (90% C.L.). The data have been used to search also for other ^{76}Ge decay modes like different Majoron accompanied decays.

In Gerda Phase II, the total mass of ^{76}Ge will be increased to about 35 kg and the background will be reduced by a factor of ten by the detection of liquid argon scintillation light as veto in combination with an improved pulse-shape discrimination performance. The sensitivity goal on half-life is $1.5 \cdot 10^{26}$ yr with a background index of 10^{-3} cts/(keV·kg·yr) and an exposure of 100 kg·yr.

2 The Phase I setup

The Gerda experiment employs germanium diodes made from material enriched to about 86% in ^{76}Ge (^{enr}Ge) and in strings of eight detectors in a cryostat filled with liquid argon. An artist view of the detector is shown in Fig. 1. The LAr acts as both the cooling medium for the semiconductors and as shield against external background. The internal side of the stainless steel cryostat vessel is covered with a copper lining to reduce gamma radiation from the cryostat walls. The cryostat is surrounded by a large tank (8.5 m height and 10 m diameter) filled with 590 m^3 of ultra-pure water. The water tank is instrumented with 66 PMTs to detect Cherenkov light produced by muons. Muon detection is also achieved by an array of 36 plastic scintillator panels placed on the roof of the cleanroom. A class 7 clean room and a two-arm lock are installed on the top of the Gerda building to insert the detectors into the cryostat. For further details about the Gerda experimental setup see Ref. [1].

Gerda Phase I started in November 2011 with 8 p-type ^{enr}Ge semi-coaxial (HPGe) detectors (17.7 kg total mass), five of them from the previous Heidelberg-Moscow (HdM) experiment and three from the IGEX experiment, and one with natural isotope composition from the GENIUS-Test-Facility (3 kg). In July 2012, five diodes (Broad Energy Germanium detectors, BEGe), with total mass of 3.6 kg, were added to test them in the real Gerda environment. Signal read out from the diodes is made by charge sensitive amplifiers located about 30 cm above the detectors. Signals are digitized by 100 MHz Flash ADCs. Digital filters reconstruct the physical parameters of interest like the energy and the rise time of the event [2]. The energy calibration is made with ^{228}Th sources on a weekly basis. The exposure-weighted average energy resolution (FWHM) at $Q_{\beta\beta}$ is (4.8±0.2) keV for semi-coaxial detectors and (3.2±0.2) keV for BEGe detectors. Phase I data were split into three sets; one containing the BEGe data (labelled "BEGe"), one (labelled "Silver") containing semi-coaxial data taken in the short period when the BEGe detectors were deployed (a higher background index was observed) and the third containing the rest of the data from semi-coaxial detectors (labelled "golden"). Events in the region of interest (in the interval $Q_{\beta\beta}\pm 20$ keV) were kept "blinded", *i.e.* not processed, until the calibration was finalized

Figure 1: An artist's view of the GERDA detector. The array of Ge detectors is not to scale. (1): the array of germanium detector string; (2): the stainless steel cryostat; (3): copper lining; (4): the water tank; (5): the clean room; (6): the lock. Plot from Ref. [1].

and all the selection cuts and analyses were fixed. The energy spectrum from semi-coaxial and BEGe detectors was fitted to a background model in the range between 570 and 7500 keV (for further details see Ref. [3]): the background is mainly due to sources close to the detectors or on the detector surface and the background is expected to be flat in the region of interest. Excluding ±5 keV around the expected position of the single escape peak from ^{208}Tl (2104 keV) and of the γ line from ^{214}Bi (2119 keV), the interpolated value for the background index (BI) in the region of interest was BI=$1.75^{+0.26}_{-0.24}\times10^{-2}$ cts/(keV·kg·yr) for semi-coaxial detectors and BI=$3.6^{+1.3}_{-1.0}\times10^{-2}$ cts/(keV·kg·yr) for BEGe detectors. The characteristic pulse shape of $0\nu\beta\beta$ events was used to discriminate signal events from background ones. Different methods for Pulse Shape Discrimination (PSD) were developed for semi-coaxial and BEGe detectors due to the characteristics of the pulses and electric field distributions for the two types [4]. For a review of the GERDA experiment see also Ref. [6].

3 Results from GERDA Phase I

In the following sections the results obtained from GERDA Phase I data are discussed. An analysis on the search for neutrinoless double beta decay to excited states from GERDA Phase I is still ongoing.

3.1 Limit on the half-life of $0\nu\beta\beta$ decay of ^{76}Ge

With a total collected exposure of Phase I of 21.6 kg·yr, a limit on the half-life of $0\nu\beta\beta$ decay of ^{76}Ge was derived (see Refs. [5] and [6]). After the analysis cuts and methods were fixed, the region around $Q_{\beta\beta}\pm5$ keV was unblinded. In this energy region seven events were observed while

5.1±0.5 were expected from background. The PSD cut rejected three of the six events from the semi-coaxial detectors and the one from the BEGe detector. The Background Index after Pulse Shape Discrimination on "golden" data was 10^{-2} cts/(keV·kg·yr). No excess of events above the background expectation was observed. To derive the limit on signal counts $N^{0\nu}$ and a frequentist coverage interval, a profile likelihood fit of the three data sets was performed. The fitted function contained a constant term for the background and a Gaussian peak for the signal with mean at $Q_{\beta\beta}$ and standard deviation σ_E. The fit had four free parameters: the backgrounds of the three data sets and $1/T^{0\nu}_{1/2}$, which relates to the peak integral. The likelihood ratio was evaluated only for the physically allowed region $T^{0\nu}_{1/2} > 0$. The systematic uncertainties due to the detector parameters, selection efficiency, energy resolution and energy scale were folded in with a Monte Carlo approach which takes correlations into account. The best fit value obtained was $N^{0\nu} = 0$ and the 90% C.L. limit $N^{0\nu}$ <3.5 which converts to

$$T^{0\nu}_{1/2} > 2.1 \cdot 10^{25} \text{ yr (90\% C.L.)}, \tag{1}$$

including systematic uncertainties. Given the background levels and the efficiencies, the median sensitivity for the 90 % C.L. limit was 2.4 $\cdot 10^{25}$ yr.

In Fig. 2 the spectrum before and after PSD is shown together with the likelihood fit (solid blue curve) and the expectation based on the claim (dashed red curve from Ref. [7]). Taking $T^{0\nu}_{1/2}$ from Ref. [7] at its face value 5.9±1.4 decays are expected in $\Delta E = \pm 2\sigma_E$ and 2.0±0.3 background events after the PSD cuts (red dotted curve in Fig. 2). This can be compared with three events detected after PSD cuts, none of them within $Q_{\beta\beta} \pm \sigma_E$. The model ($H_1$), which includes the $0\nu\beta\beta$ signal calculated above, gives in fact a worse fit to the data than the background-only model (H_0): the Bayes factor, namely the ratio of the probabilities of the two models, is $P(H_1)/P(H_0)$ =0.024. Assuming the model H_1, the probability to obtain $N^{0\nu}$ =0 as the best fit from the profile likelihood analysis is P($N^{0\nu} = 0|H_1$)=0.01. The GERDA result is consistent though stronger with the limits by the previous HdM [8] and IGEX [9] experiments. The profile likelihood fit is extended to include the energy spectra from HdM and IGEX. Constant backgrounds for each of the five data sets and Gaussian peaks for the signal with common $1/T^{0\nu}_{1/2}$ are assumed. Experimental parameters (exposure, energy resolution, efficiency factors) are obtained from the original references or, when not available, extrapolated from the values used in GERDA. The best fit yields $N^{0\nu} = 0$ and a limit of

$$T^{0\nu}_{1/2} > 3.0 \cdot 10^{25} \text{ yr (90\% C.L.)}. \tag{2}$$

The Bayes factor is $P(H_1)/P(H_0) = 2 \cdot 10^{-4}$; the claimed $0\nu\beta\beta$ signal is hence strongly disfavored. The combined half-life limit corresponds to an upper limits on the effective neutrino mass between 0.2 and 0.4 eV using different nuclear matrix element calculations.

3.2 Results on $\beta\beta$ decay with emission of two neutrinos or Majorons in ^{76}Ge from GERDA Phase I

The GERDA collaboration has completed two more analyses: a new measurement of the half-life of the $2\nu\beta\beta$ process and the search for neutrinoless double beta decay of ^{76}Ge with Majoron emission. The paper describing both analyses was submitted to EPJC [12]. The new measurement of $T^{2\nu}_{1/2}$ of the $2\nu\beta\beta$ decay of ^{76}Ge is obtained using the golden data set (17.9 kg·yr) with the coaxial detectors:

$$\begin{aligned} T^{2\nu}_{1/2} &= \left(1.926\,^{+0.025}_{-0.022\,\text{stat}}\,^{+0.092}_{-0.092\,\text{syst}}\right) \cdot 10^{21}\,\text{yr} \\ &= (1.926 \pm 0.095) \cdot 10^{21}\,\text{yr}. \end{aligned} \tag{3}$$

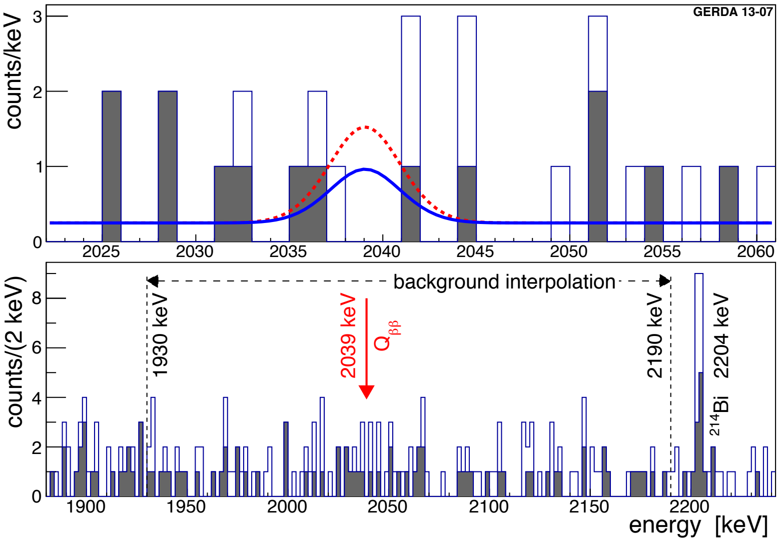

Figure 2: Energy spectrum from all ^{enr}Ge detectors with (filled) and without (open) PSD selection. In the upper panel, the expectation based on the central value of the half-life predicted by Ref. [7] is also shown (red), together with the 90% C.L. limit (blue). In the lower panel the energy window used for the background interpolation is indicated. Plot from Ref. [5].

with the latter combining in quadrature the statistical and systematic uncertainties. The largest contribution to the systematic uncertainties comes from the uncertainty on the active masses of the coaxial detectors used in the analysis (4%). In this analysis, the background model uncertainty ($^{+1.4\%}_{-1.2\%}$) has been significantly reduced compared to the analysis of the first 5 kg·yr of Phase I data reported in Ref. [13] where the systematic uncertainty due to the background model was $^{+5.7\%}_{-2.1\%}$. The new result is in good agreement with the previous one. The background level achieved in GERDA Phase I is about one order of magnitude lower with respect to predecessor ^{76}Ge experiments and has allowed the measurement of $T^{2\nu}_{1/2}$ with a signal-to-background ratio of 3:1 in the 570–2039 keV interval, or 4:1 in the smaller interval of 600–1800 keV. These ratios are much better than for any past experiment which studied $2\nu\beta\beta$ decay of ^{76}Ge.

Although the main focus of experimental efforts lies on the detection of $0\nu\beta\beta$ decay, there are also other proposed mechanisms which are being searched for. Some models predict $0\nu\beta\beta$ decays proceeding through the emission of a massless Goldstone boson, called Majoron (χ) [14, 15, 16]. In other models, the Majoron carries leptonic charge and cannot be a Goldstone boson [17, 18] or the $0\nu\beta\beta$ decay proceeds through the emission of two Majorons [19]. All these models predict different distributions of the summed energy K of the emitted electrons. The spectral shapes are essentially defined by the phase space G of the emitted particles:

$$\frac{dN}{dK} \sim G \sim (Q_{\beta\beta} - K)^n \tag{4}$$

where n is the spectral index of the model. Single Majoron emitting $\beta\beta$ decays can be divided into three classes, $n = 1$, $n = 2$, and $n = 3$. Double Majoron emitting decays can have either $n = 3$ or $n = 7$. Their characteristic spectral shapes differ from that of two-neutrino $\beta\beta$ decay ($2\nu\beta\beta$) with $n = 5$. Majoron emission processes ($0\nu\beta\beta\chi$) were searched for in the energy spectra with exposure of 20.3 kg·yr using both coaxial and BEGe detectors. The analysis was performed for all four possibilities of the spectral index n. No indication for a contribution of $0\nu\beta\beta\chi$ was

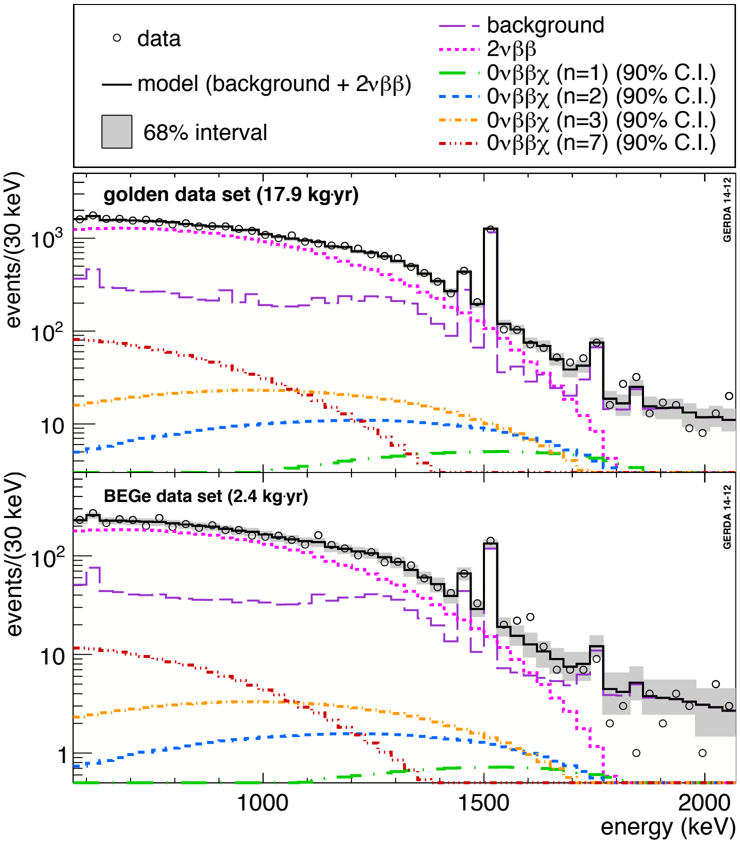

Figure 3: Best-fit model and data energy spectrum for the coaxial and the BEGe data sets. The contributions from $2\nu\beta\beta$ decay and the background contributions are shown separately. The best-fit model does not contain contributions from $0\nu\beta\beta\chi$. The smallest interval of 68% probability for the model expectation is indicated in grey. Also shown is the upper limit for $0\nu\beta\beta\chi$ decay with $n = 1$ as determined from the 90% quantile of the marginalized posterior probability for $1/T^{0\nu\chi}_{1/2}$. For illustrative purpose, also the upper limits at 90% C.I. of the other three spectral indices $n = 2, 3, 7$ are reported. Plot from Ref. [12].

found in any of the cases. Lower limits on the half-lives $T^{0\nu\chi}_{1/2}$ were determined from the quantiles of 90% probability of the marginalized posterior probability distributions. The results constitute the most stringent limits on $T^{0\nu\chi}_{1/2}$ of ^{76}Ge obtained to date. For the standard mode ($n = 1$), the lower limit is determined to be:

$$T^{0\nu\chi}_{1/2} > 4.2 \cdot 10^{23} \text{ yr}. \tag{5}$$

From the lower limit of Eq. 5, an upper limit on the effective neutrino-Majoron coupling constant, $\langle g \rangle$, can be inferred:

$$\langle g \rangle < (3.4 - 8.7) \cdot 10^{-5}. \tag{6}$$

The global model together with the energy spectra for both the coaxial and the BEGe data sets is shown in Fig. 3. The contributions from the background components, from the $2\nu\beta\beta$ decay only and the combined spectra from both contributions are drawn separately. For illustrative purpose, also the upper limits at 90% C.I. of the other three spectral indices $n = 2, 3, 7$ are reported.

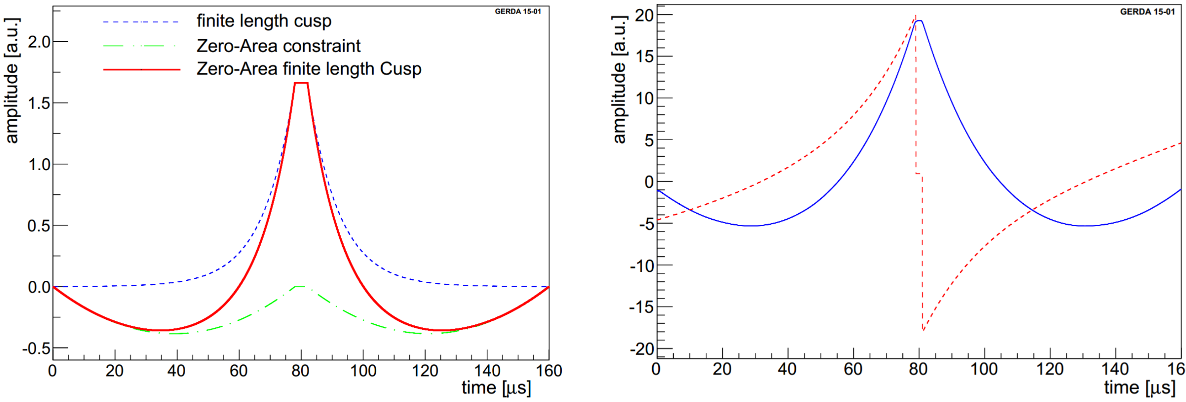

Figure 4: Left: Zero Area Cusp filter response (red full line) for a short current pulse. It is composed of the finite-length cusp (blue dashed) from which two parabolas are subtracted on the cusp sides (green dash-dotted). Right: ZAC filter after the convolution with the inverse amplifier response function (red dashed) and a typical waveform after the convolution with it (full blue).

3.3 Reprocessing of GERDA Phase I Data with the ZAC Filter

One of the crucial experimental parameters in the search for $0\nu\beta\beta$ decay is energy resolution. The sensitivity to find a Gaussian peak over a flat background depends on the Full Width at Half Maximum (FWHM) at $Q_{\beta\beta}$ (2039 keV in the case of ^{76}Ge) as:

$$T^{0\nu}_{1/2} \propto \frac{1}{\sqrt{\mathrm{FWHM}(Q_{\beta\beta})}} \tag{7}$$

where $T^{0\nu}_{1/2}$ is the sensitivity to give a limit for the $0\nu\beta\beta$ half-life at a given confidence level. During Phase I, the resolution was deteriorated due to low-frequency noise. A digital shaping filter with enhanced low-frequency rejection properties has been developed and tested as an alternative to the standard Gaussian shaping for energy reconstruction. The new filter consists of a cusp filter, which is known to be the optimum for series and parallel noise [20], with the condition of having zero area for reducing low-frequency noise [21] and with a central flat-top for the correction of ballistic deficit. The current signal deformation induced by the amplifier integration and the resistive discharge is corrected via a deconvolution. The construction of this Zero-Area finite-length Cusp filter (referred to as “ZAC filter”) is depicted in Fig. 4

The signal shaping is performed via a convolution of each recorded waveform with this filter and the energy is deduced from the maximum of the shaped signal. The filter parameters have been tuned for each detector separately in order to fully exploit the available information. All Phase I calibration and physics data have been reprocessed. The average resolution improvement is 0.3 keV for the calibration data at $Q_{\beta\beta}$ and about 0.5 keV for the combined physics data. The impact of this resolution improvement in the physics reach of GERDA Phase I is $\sim 5\%$ in median sensitivity. For this reason, the same filter optimization technique is going to be used from the beginning of Phase II. A GERDA Collaboration paper describing the algorithm and the reprocessing of Phase I data has been submitted for publication [22].

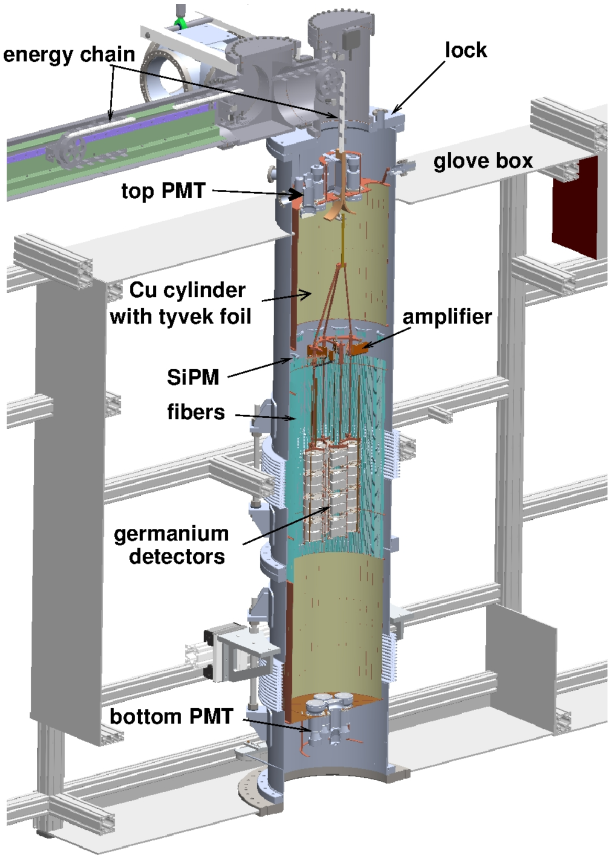

Figure 5: Design of the Phase II lock with the internal instrumentation.

4 Preparations for Phase II

In 2014, the main effort of GERDA has been the transition to the second phase of the experiment. The motivation for the upgrade is an expected improvement in sensitivity by a factor of 5-10 by doubling the detector mass and measurement time and by reducing the background level by an order of magnitude. The latter is achieved by the detection of liquid argon scintillation light produced by ^{208}Tl or ^{214}Bi decays and by improved pulse shape performance of the new detector type (BEGe detectors) which allows to discriminate surface events and multiple energy depositions in a detector effectively.

The transition of the hardware from GERDA Phase I to Phase II affects all components of the experiment except the cryostat and the muon veto. The development and construction of all items started during Phase I and most items were installed in 2014. Fig. 5 shows a cross section of the glove box (for detector handling in nitrogen atmosphere) and the lock with the detectors, readout electronics, liquid argon veto and the energy chain. In the following, the different components will be discussed briefly.

Lock and energy chain

The number of cables needed for the readout of the germanium detectors and the argon veto increases by a factor of five compared to Phase I and accordingly the number of feedthroughs. Consequently, the energy chain, which contains all cables and is the support for detectors and

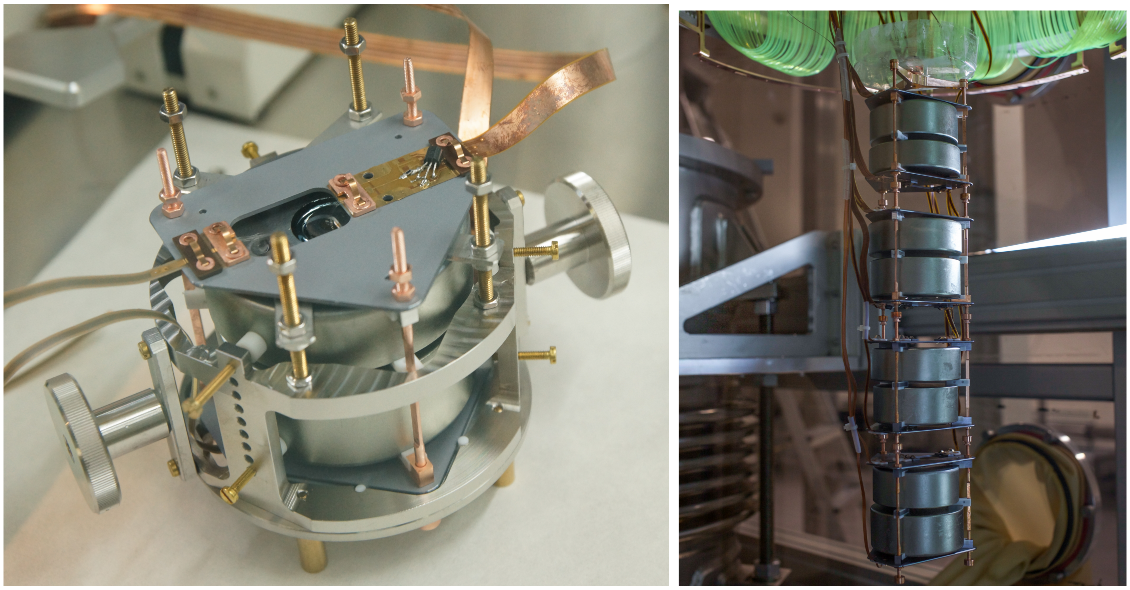

Figure 6: Left: BEGe pair in Phase II mount and the stainless steel jig for handling. Right: mounted detector string with 4 pairs.

veto, was enlarged in cross section and material thickness. The total radioactivity of the cables in the chain is similar compared to Phase I since the specific radioactivity is reduced due to a custom production.

Instead of the two locks of Phase I, now only one lock with increased diameter houses the argon veto and the detector strings.

The mechanics was assembled and tested together with the PLC operating the energy chain, vacuum pumps and shutter. Radon emanation of 13 ± 4 mBq from the cables and the lock was measured with our 1 m^3 electrostatic radon monitor. This value is small compared to the emanation of the cryostat and the cryogenic infrastructure of 54 mBq.

Germanium detectors, support and contacting

To double the detector mass, 30 BEGe type diodes made from material with ^{76}Ge fraction enriched to about 87% have been produced. Aluminum pads have been deposited on the detectors for electrical contacting by wire bonding. All detectors were characterized in a vacuum cryostat [23] and are ready for deployment.

In Phase I, each detector was mounted in a copper frame (80 g) with PTFE spacers for insulation of the outer surface (11 g). In Phase II (see Fig. 6) this mass is reduced to about 26 g Cu and 2 g PTFE for a BEGe pair. In addition, we use about 40 g of mono-cryostaline silicon. The latter is expected to be radio pure [24] and radon emanation measurements show no signs of surface contamination. The first detectors were deployed in the GERDA cryostat soon after the new lock was installed and one entire string at the end of 2014 (see Fig. 6). The detector support and the handling and assembly procedures were tested and proved to be adequate.

Germanium detector readout

The charge sensitive amplifiers for the readout of germanium detectors should contribute little to the total background. The solution chosen for Phase I was to place the electronics about 30 cm

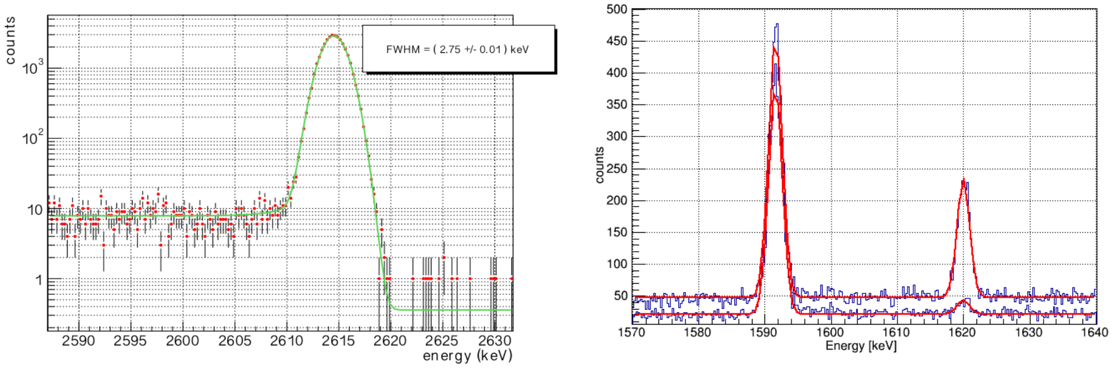

Figure 7: Left: ^{228}Th calibration spectrum at 2.6 MeV. Right: same spectrum around 1.6 MeV with and without PSD.

above the top detector. The long cables connecting the detectors to the amplifiers contribute to the capacitance at the input - and hence to the noise - and are responsible for an increased sensitivity to microphonic noise [22].

To reduce both effects while complying with the radioactivity constrain, the amplifier can be split into two parts: the input JFET and the feedback components are placed close to the detector and the remaining parts consisting of commercial components are about 40 cm above the top detector.

Flexible printed circuit cables made on Kapton or Cuflon (copper on PTFE) are used for the connection between the JFET and the rest of the amplifier and for the high voltage contact of the germanium detector (see Fig. 6). The detector is bonded to the cables. The small value feedback and test pulse capacitors are implemented between top and bottom traces on the cable. Kapton is a standard material available also in full length of 80 cm required for the longest connection of the bottom detector in a string. Cuflon is typically an order of magnitude less radioactive and hence the preferred material. Recently, several processing steps may add radium contaminations on the final cable. Especially, the additional deposition of copper and the gold finish could be identified as main contributors. Consequently, the production process has to be adjusted (e.g. only partial deposition) to limit additional contaminations while still keeping the required mechanical specifications. The final cable production is pending.

The energy resolution and PSD results from the string test data taking are shown in Fig. 7 for ^{228}Th calibration data. The performance is similar to what was achieved before in other test benches: FWHM at 2.6 MeV is 2.8 keV and for a double escape peak acceptance of 90% about 13% of the ^{212}Bi peak events at 1621 keV survive.

Argon scintillation light readout

The argon veto is assembled as a cylinder of 47 cm diameter and 2.2 m height. The germanium detector array with about 30 cm diameter and 40 cm height is inside. For the argon scintillation light detection a hybrid solution was chosen. Sixteen 3” PMTs (Hamamatsu R11065-20) are mounted at the top and bottom plates such that the minimal distance to the germanium detectors is 80 cm (see Fig. 5).

Scintillating fibers (Bicron BCF-91A) cover the central meter of the veto cylinder. The light at the fiber ends is read out by silicon photo multipliers (SiPM from Ketek). Fig. 8 shows two views of the argon veto system.

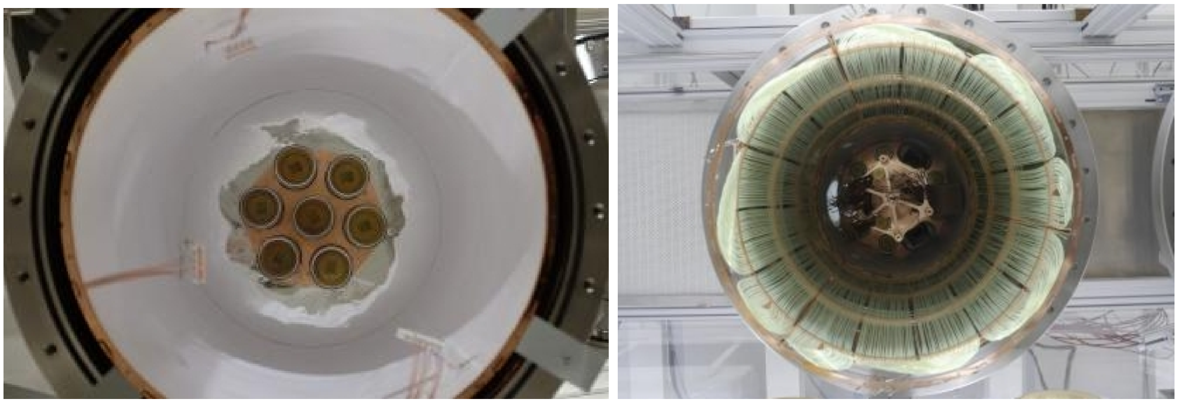

Figure 8: Pictures from the liquid argon veto instrumentation. Left: view inside the copper cylinder covered with Tyvek and the bottom PMTs. Right: central view of the fiber curtain, part of the detector suspension mechanics in the middle and the top PMT plate.

To shift the 128 nm scintillation light to about 400 nm where the quantum efficiency of the PMTs and SiPMs peak, the fibers are covered with TPB in a custom-made vacuum evaporation oven, the PMTs are brushed with a TPB polystyrene solution - like the nylon cylinders around the individual detector strings - and the cylindrical surfaces are lined with Tyvek foil, which was dip-coated with TPB [27].

Fig. 9 shows a spectrum of a ^{228}Th calibration source with and without the argon veto and pulse shape selection of events with single interactions in the crystal for a test run based on the A/E parameter [4]. The total suppression factor is about 50 for the veto alone and 90 for the combined selection. Note that these are preliminary results since only half of the SiPM channels worked properly in the first installation. Recently, all broken channels have been replaced with working ones with better quantum efficiency.

^{42}Ar background

At the start of Phase I an unexpected large background from ^{42}K (progeny of ^{42}Ar) was observed which could be reduced to an acceptable level by encapsulating each detector string in a copper cylinder. This shroud will be replaced in Phase II by a transparent nylon foil [25] covered with tetra-phenyl-buthadiene (TPB) to shift the 128 nm argon scintillation light to about 400 nm for the detection with PMTs and SiPM (see below).

The effect of the nylon foil and PSD for ^{42}K surface β decays is shown in Fig. 10. The data are from a measurement in the LArGe cryostat [26] filled with argon enriched in ^{42}Ar. Depending on the PSD performance, the Phase II background is expected to be dominated at a level close to 0.001 cts/(keV·kg·yr) from this source.

Other activities

Other hardware upgrades include new computers for slow control and data acquisition, a scaler system for the measurement of the PMT rate, new ^{228}Th calibration sources with improved mechanics and additional channels for the amplification and digitization of the argon veto channels and germanium detectors. Software upgrades include new slow control clients like for ramping of PMT and germanium detector high voltages, monitoring during data taking and for the analysis of the argon veto data.

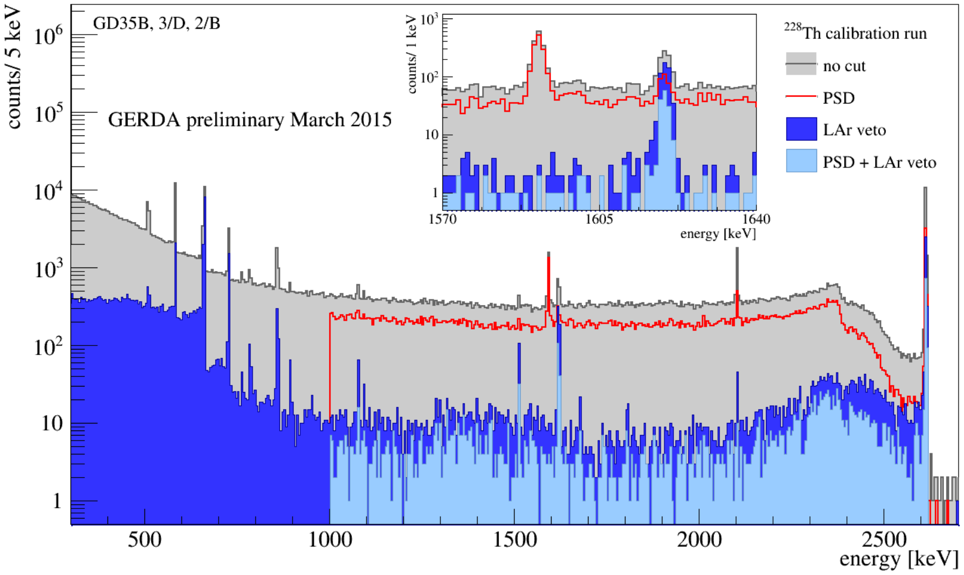

Figure 9: ^{228}Th calibration spectrum (filled grey histogram) after pulse shape discrimination (PSD, red curve), after the liquid argon veto is applied (LAr veto, filled dark blue histogram) and the combination (PSD + LAr veto, filled light blue histogram). The insert shows the double escape peak at 1592 keV which is only rejected by the LAr veto and the ^{212}Bi line at 1621 keV which is mainly suppressed by PSD (by the LAr veto only due to random coincidences of two decays).

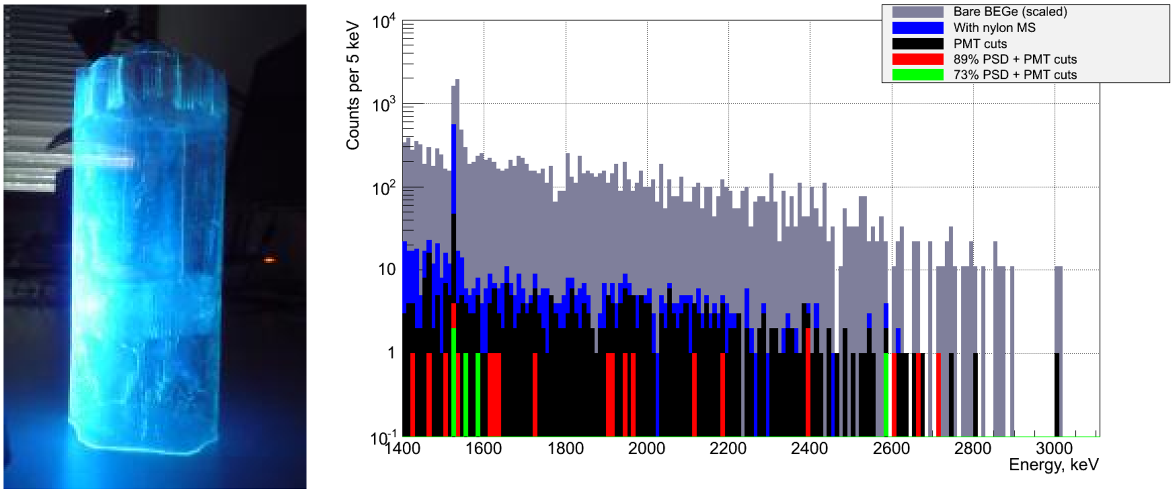

Figure 10: Left: Nylon foil covered with TPB; illuminated with a UV lamp. Right: ^{42}K background suppression studies in LArGe: without suppression (grey), with nylon shroud (blue), with additional LAr veto (black), with additional pulse shape discrimination PSD (red and green).

5 Conclusions

The Gerda experiment has completed Phase I in 2013 with an exposure of 21.6 kg·yr and a background level of BI$\simeq 10^{-2}$ cts/(keV·kg·yr) after Pulse Shape Discrimination. A 90% C.L. limit on the half-life of $0\nu\beta\beta$ decay of ^{76}Ge was derived: $T^{0\nu}_{1/2} > 2.1 \cdot 10^{25}$yr.
The installation of the Gerda Phase II upgrade is currently ongoing. The new lock and argon veto were installed in 2014 and first commissioning data show adequate performance. Phase II is expected to start in 2015.

6 List of Publications

1. *The background in the neutrinoless double beta decay experiment* Gerda,
   the Gerda collaboration, M. Agostini *et al.*.
   Eur. Phys. J. C **74** (2014) 2764.

2. *Determination of dead-layer variation in HPGe detectors*,
   E. Andreotti, M. Hult, G. Marissens, G. Lutter, A. Garfagnini, S. Hemmer, and K. von Sturm,
   Applied Radiation and Isotopes **87** (2014) 331.

3. *Search for neutrinoless double beta decay with the* Gerda *experiment*,
   C. Macolino for the Gerda collaboration,
   Mod. Phys. Lett. A **29** (2014) 1430001.

4. *Status of double beta decay experiments using isotopes other than* ^{136}*Xe*,
   Luciano Pandola.
   Phys. Dark Univ. **4** (2014) 17.

5. *Phase II Upgrade of the GERDA Experiment for the Search of Neutrinoless Double Beta Decay*,
   B. Majorovits for the Gerda collaboration.
   Physics Procedia. Proceeding of the 13th International Conference on Topics in Astroparticle and Underground Physics **61** (2015) 254.

6. *Improvement of the GERDA Ge Detectors Energy Resolution by an Optimized Digital Signal Processing*,
   G. Benato et al.
   Physics Procedia. Proceeding of the 13th International Conference on Topics in Astroparticle and Underground Physics **61** (2015) 673.

7. *Upgrade of the GERDA Experiment*,
   K. T. Knöpfle for the Gerda collaboration.
   Proceedings of Science (TIPP2014) (2014) 109.

8. *The GERDA experiment: results and perspectives*
   C. Macolino for the GERDA collaboration.
   J. Phys. Conf. Ser. **556** (2014) 012063.

9. *Neutrinoless double beta decay in GERDA Phase II*,
   Carla Macolino for the GERDA collaboration. Nuovo Cim. C **037** (2014) 04.

10. *The GERDA experiment at Gran Sasso: search for neutrinoless double beta decay in ^{76}Ge*,
A. Garfagnini for the Gerda collaboration.
Nuovo Cim. C **037** (2014) 01.

11. *GERDA: Recent results and future plans* ,
B. Lehnert for the Gerda collaboration.
Nucl. Instrum. Meth. A **742** (2014) 254.

References

[1] The Gerda collaboration, *Eur. Phys. J. C* **73**, 2330 (2013).

[2] M. Agostini et al., *J. Instrum.* **6**, P08013 (2011).

[3] The Gerda collaboration, *Eur. Phys. J. C* **74**, 276 (2014).

[4] The Gerda collaboration, *Eur. Phys. J. C* **73**, 2583 (2013).

[5] The Gerda collaboration, *Phys. Rev. Lett.* **111**, 122503 (2013).

[6] C. Macolino on behalf of the Gerda collaboration, *Mod. Phys. Lett. A* **29**, 1430001 (2014).

[7] H.V. Klapdor-Kleingrothaus et al., *Phys. Lett. B* **586**, 198 (2004).

[8] H.V. Klapdor-Kleingrothaus et al., *Eur. Phys. J. A* **12**, 147 (2001).

[9] C.E. Alseth et al., *Phys. Rev. D* **65**, 092007 (2002).

[10] A. Gando et al., *Phys. Rev. Lett.* **110**, 062502 (2013).

[11] J. B. Albert et al., *Nature* **510** 229 (2014).

[12] The Gerda collaboration, arXiv:1501.02345, submitted to *Eur. J. Phys. C.*.

[13] The Gerda collaboration, *J. Phys. G: Nucl. Part. Phys.* **40**, 035110 (2013).

[14] Y. Chikashige, R. H. Mohapatra and R. D. Peccei, *Phys. Rev. Lett.* **45**, 1926 (1980).

[15] R. Santamaria and J. W. F. Valle, *Phys. Rev. Lett.* **60**, 397 (1988).

[16] G. B. Gelmini and M. Roncadelli, *Phys. Lett. B* **99**, 411 (1981).

[17] C. P. Burgess and J. M. Cline, *Phys. Lett. B* **298**, 141 (1993).

[18] C. P. Burgess and J. M. Cline, *Phys. Rev. D* **49**, 5925 (1994).

[19] P. Bamert, C. P. Burgess and R. N. Mohapatra, *Nucl. Phys. B* **449**, 25 (1995).

[20] M. O. Deighton, *IEEE Trans. Nucl. Sci.* **16** 68 (1969).

[21] A. Geraci et al., *Nucl. Instrum. Methods A* **482** 441 (2002).

[22] The Gerda collaboration, arXiv:1502.04392, accepted for publication in *Eur. Phys. J. C.*

[23] The Gerda collaboration, *Eur. Phys J* **C75** 39 (2015).

[24] T. Goldbrunner, Dissertation *Technische Universtät München*, 1997.

[25] L. Cadonati et al, *Int. J. Mod. Phys. A* **29** 1442004 (2014).

[26] M. Agostini et al, arXiv:1501.05762.

[27] L. Baudis et al, arXiv:1503.05349, sumitted to JINST.

GINGER/G-GranSasso-RD
Annual Report 2014

J. Belfi[a], N. Beverini[a,b], F. Bosi[a], B. Bouhadef[a], G. Carelli[a,b], G. Cella[a]
A. Di Virgilio[a], E. Maccioni[a,b], R. Santagata[a,c], A. Simonelli[a,b], and G. Terreni[a]
A. Beghi[d], D. Cuccato[d,e], and A. Ortolan[e]
G. Passeggio[f], A. Porzio[f,g]
M.L. Ruggiero[h,i] and A. Tartaglia[h,i]
C. Zarra[l]

[a] INFN-Pisa- Italy
[b] University of Pisa-Italy
[c] University of Siena-Italy
[d] DEI, University of Padova-Italy
[e] LNL -INFN Padova-Italy
[f] INFN-Napoli-Italy
[g] CNR-SPIN Napoli-Italy
[h] Politecnico di Torino-Italy
[i] INFN-Torino-Italy
[l] Laboratorio Nazionale del GranSasso, Assergi-Italy

Abstract

Large ring laser gyroscopes (with a perimeter of several meters) are capable to measure angular rotations with precision better that a fraction of $prad/s$, not far from what is necessary for General Relativity tests (about 10^{-14} rad/s). GINGERino, installed at LNGS at the end of September 2014, is a 3.6 m side square ring laser. The instrument has been tailored to be the largest possible fitting the area assigned by the laboratory, since large rings have higher sensitivity. Its main objective is to measure the very low frequency rotational motions inside LNGS, in order to show if this is a suitable location for very low noise measurements and General Relativity tests. At the same time it will provide interesting informations for geodesy and geophysics. At the end of the year 2014 the largest part of the apparatus has been installed and the first laser light of the GINGERino ring has been observed. Since then the commissioning of the apparatus has started: in order to provide suitable data it will be necessary to improve the experimental set up of the instrument, complete the installation with reference signals from GPS, data acquisition and other instruments as tilt meters and seismometers.

1 Introduction

Ring laser gyroscopes are, at present, the most precise sensors of absolute angular velocity. They are essential in estimating rotation rates relative to the local inertial frame in many contexts

ranging from inertial guidance to angle metrology, from geodesy to geophysics, as well to fundamental physics. In the near future, their application is foreseen to provide ground based tests of General Relativity. GINGER (Gyroscopes IN GEneral Relativity) is a proposal to measure the gravito-magnetic (Lense- Thirring) effect of the rotating Earth by means of an array of high sensitivity and accuracy ring lasers. In a ground-based laboratory, this effect amounts to 1 part in a billion of the Earth rotational rate, thus requiring an unprecedented sensitivity of the apparatus. An array of at least three ring lasers would allow us to measure the angular velocity vector and, having at disposal the time series of the daily estimate of Earth rotation vector from the International Earth Rotation and Reference System Service (http://www.iers.org), it would be possible to isolate the Geodetic and Lense-Thirring contributions. An underground location, far from external disturbances as rain, wind etc., is essential for this challenging experiment, and LNGS may be a suitable location.
G-GranSasso-RD (INFN Commission II) is aiming at the planning, installation and operation of GINGER. The key points of GINGER are the mechanical structure, the control of the geometry of each ring laser, and the monitoring of the relative angles between different rings of the array. G-GranSasso has developed two ring laser prototypes (GP2 and G-Pisa), and in 2014 GEMS (GINGER External Metrology System) prototype metrology has been proposed to measure the position of each mirror with nm accuracy. GP2 prototype is dedicated to study the control of the ring geometry; it was installed in 2014 in S.Piero, but at the time of writing has been moved to the INFN Section in Pisa. G-Pisa, a square ring with side length of 1.35 m, was our first prototype. It was a transportable device, which has been installed in different locations, with different orientations (horizontal, vertical, or aligned with the Earth rotational axis). In 2013 it has been transferred inside LNGS, providing a set of measurements (see our LNGS Report 2013 for details). This first set of measurements suggested a new improved installation, that was recently realised. This new installation has been located inside LNGS, approximately 11 m (South) far from node B, in a place isolated from human activity, starting at the end of September 2014. The apparatus, named GINGERino, uses the mechanics of G-Pisa, but the dimension of the perimeter has been increased up to 14.4 m, which should provide a factor 7 improvement in sensitivity, and a large suppression of laser systematic effects (backscattering and frequency pulling). The sensitivity of GINGERino is expected to be about $5 \times 10^{-10}\ rad/s/\sqrt{Hz}$, assuming mirrors with total losses of about 15 ppm, similar to the best set of mirrors we have had so far.

2 An Overview of the Apparatus of GINGERino

GINGERino is a small apparatus compared to the average size of the LNGS experiments, nevertheless it is composed of several parts and other high sensitivity instruments are co-located, as tilt meters with nrad resolution and high performance seismometers These two instruments will improve the knowledge of the behaviour of the location, and will be very helpful in the interpretation of geophysical data. In the following the different components will be described. The implementation of data acquisition and analysis will be described as well.

2.1 The Ringlaser

GINGERino uses the mechanics of the prototype G-Pisa, which is made up of 4 mirror boxes connected by vacuum pipes, see Fig. 1. This mechanical structure is an evolution of the design (called GEOSENSOR) developed by U. Schreiber for seismological applications; each box is equipped with mechanical tools to tilt and align the four mirrors of the square optical cavity. Two piezoelectric translators are used to stabilize the perimeter in order to compensate for the

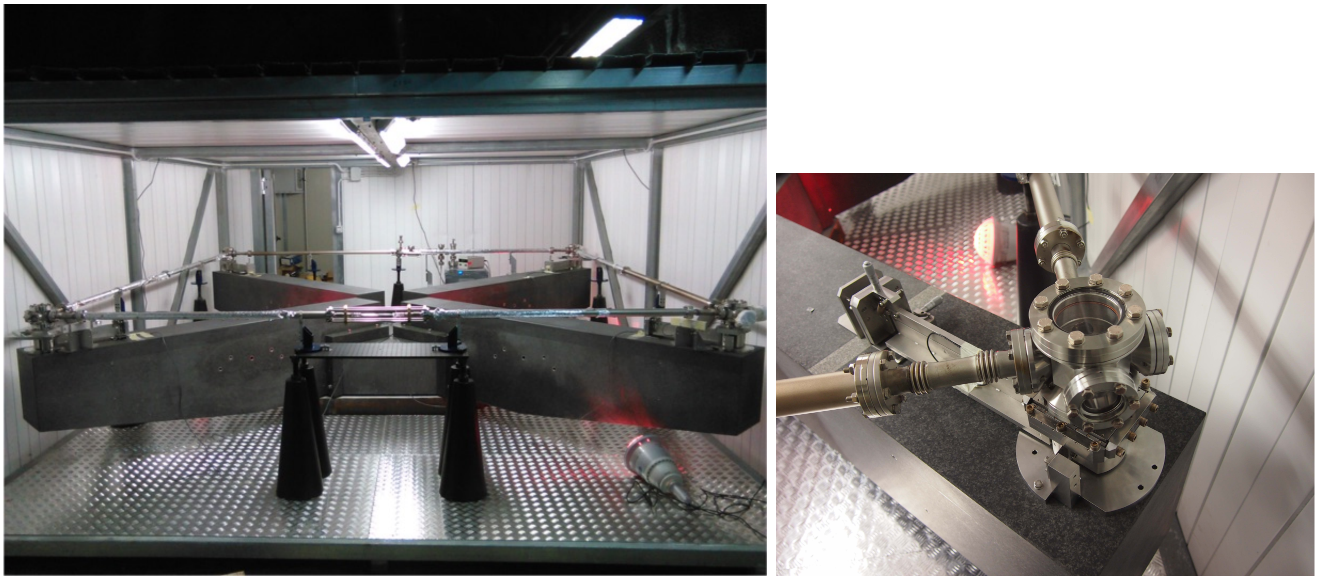

Figure 1: **Left: The main structure of GINGERino is shown, it is composed of the G-Pisa mechanical structure with longer vacuum tubes, attached to a granite cross, which is attached to the bedrock with a concrete solid structure. Right: Detail of one of the four mirror boxes, the two output viewports and the micrometrical system to tilt the mirrors are well visible.**

thermal expansion of the cavity. This avoids mode jumps of the laser, allowing the device to run continuously. To build GINGERino, a new set of vacuum pipes has been manufactured; its size is the maximum for a square ring in the present location. Fig. 1 shows GINGERino in December 2014. The ringlaser is attached to a cross granite structure, composed by a central octagonal massive block of granite, and four arms on lightened granite. The granite structure is screwed to a reinforced concrete block integral to the underneath bedrock, that has been installed at the beginning of May 2014. The black granite of Africa can be machined with high precision and has a good thermal expansion coefficient (7×10^{-6} $/degree$). This 5 parts structure has been designed having in mind that a crane is not present there. The installation was carefully prepared, developing several tools to handle such heavy structures (the octagonal central piece is about 3 tons in weight and each arm is about 800 kg).

A box protects the whole installation in order to reduce the external acoustic disturbances and the very high local value of the humidity. A first simple solution to the humidity problem was to warm up the box with infrared lamps. So far, this system has been running for several months, and has shown that it keeps the GINGERino area at a temperature around 18 degrees Celsius. We will investigate later if this system needs to be improved and attached to servo system.

2.2 Data Analysis, Diagnostics and Calibration

To improve both long term stability and accuracy of ring laser gyros, it is of paramount importance to model the details of the stimulated emission process of the laser active medium (typically $He-Ne$ isotopic mixture) in non-ideal optical cavities. In fact, systematic errors in the estimate of the rotation rate are mainly related to interactions of light with the optical

Figure 2: **May 2014: the different phases of the installation of the reinforced concrete solid structure. The interface to attach the granite structure is well visible, this interface is immersed in the concrete, several rigid rods have been inserted in the underneath bedrock and in the concrete in order to well attach this structure to the bedrock itself.**

Figure 3: **September 2014: the central granite block prepared for the installation phase; the weight of this central block is approximately 3 tons.**

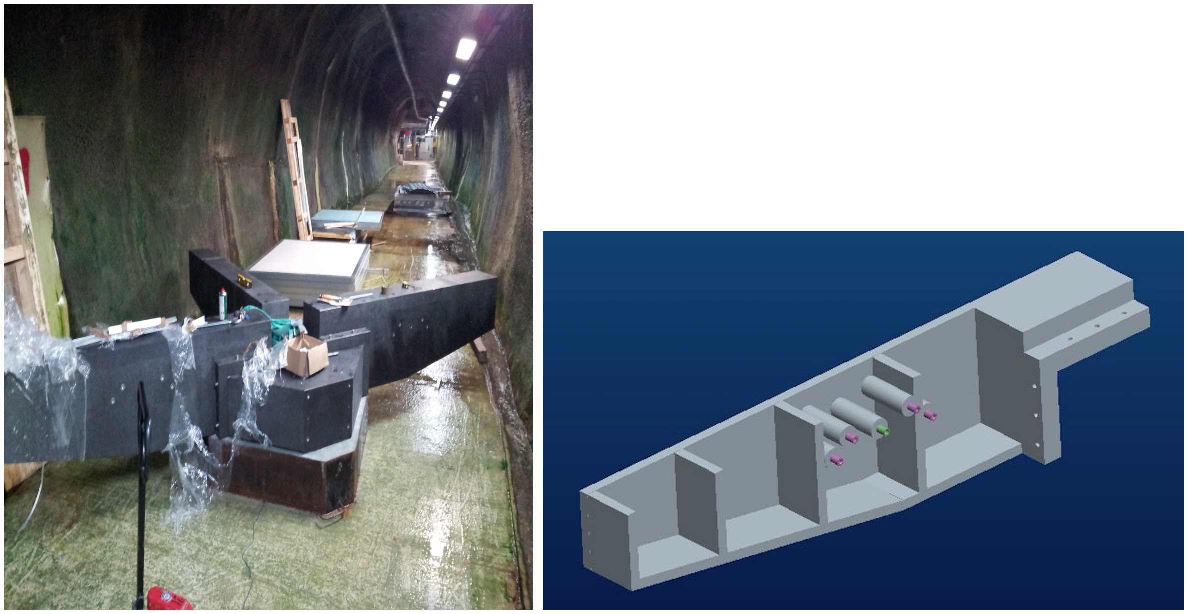

Figure 4: **Left: September 2014, the central block is attached to the concrete interface, and three arms are in place. Right: a drawing which shows the inner part of the granite arms, made by lightened granite, i.e. slices of granite glued together and machined; several reinforcements are visible around the center of mass of the whole structure, this is necessary in order to handle the arm in its center of mass**

Figure 5: **Left: Early phase of the installation of the box, Right: the box is complete**

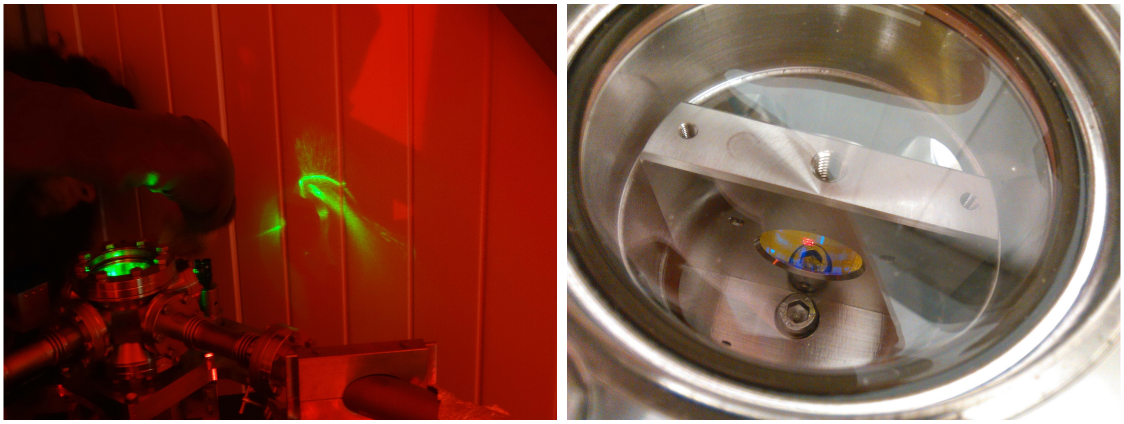

Figure 6: **Left: A shot taken during the alignment of the cavity injecting green light. Right: GINGERino is lasering! The red Helium Neon light is visible on one of the mirrors.**

medium (non-linear laser dynamics), dissipative and parasite processes taking place during light scattering on mirrors, and cavity deformations due to mirror displacements. We have developed a very detailed model which accounts for the non-linear ring laser dynamics and the optical cavity geometry [5]. The model depends on a set of parameters that can be either measured once per run, or continuously estimated during the operation of the ring laser. As some parameters are related to the active medium and others to the cavity dissipations, they are classified as active or passive parameters, respectively. The schematic flow of data analysis is presented in Fig.7.

At the start of each run, some active laser parameters are estimated by a calibration procedure (CLB) that evaluates the calibration coefficients of single pass gain and light intensities, and produces the INIT_DATA file. During the run the DAQ system digitizes the ring laser output signals (interferogram, light intensities and fluorescence monitor of laser gain) and some auxiliary channels (seismometers, titlmeters, hygrometers, pressure and temperature sensors). The resulting time series (RLG_DATA and AUX_DATA) are stored on local hard disks in hourly files. Then the main data analysis routines (Loop 1 in Fig.7) run with a delay of 1 hour. The main analysis is divided into two parts: 1) the identification of the ring laser dynamics for the unbiased estimation of the Earth rotation rate; and 2) the robust filtering of the Sagnac frequency (DGN procedure) for diagnostic purposes, for monitoring the local rotations (earthquakes or teleseisms), and for time-frequency analysis [6]. The output data from the main analysis are produced at the rate of 1 Hz for geodesy applications (Earth rotation) and at the rate of 50 Hz for geophysical applications (local rotations). One can perform also offline interactive analyses of the ring laser dynamics (e.g. the monitor of loss and scattering processes), and of the instantaneous Sagnac frequency (e.g. time-frequency analysis). In order to discard malfunctioning time spans of the ring laser, the QLT procedure, which assesses the quality of each hour of data taking, can be run daily (Loop 2). The ID_EST procedure collects RLG_DATA samples which are processed to remove electronic noises and select the frequency bands of interest. The ID_FIT procedure estimates the passive parameters of the ring laser dynamics. The EKF procedure apply an Extended Kalman filter routine for the subtraction of the systematic errors. Finally, the RR_EST procedure converts the unbiased Sagnac frequency into the Earth rotation rate. The procedures of the data analysis and their physical motivations are detailed in the following paragraphs.

Ring laser parameters The set of equations describing the ring laser dynamics for the complex

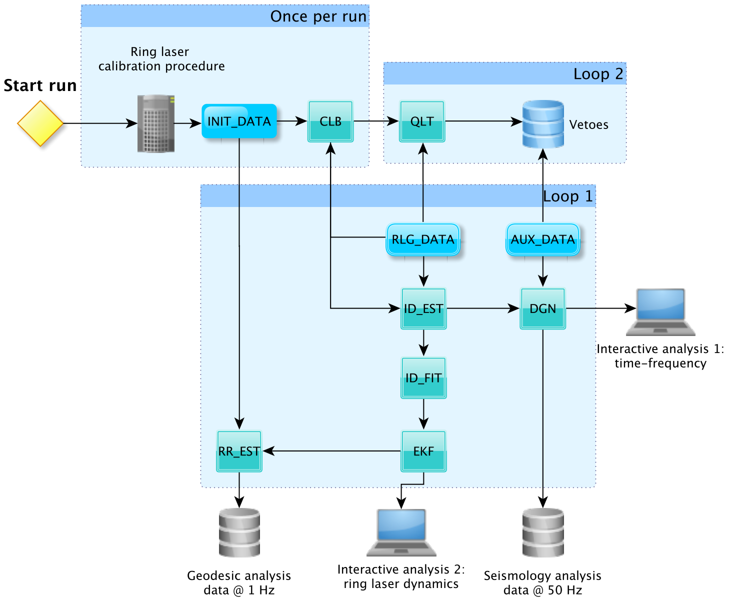

Figure 7: **Schematic flow of the ring laser data analysis.**

valued functions $\mathbf{E}(t) = (E_1, E_2)^T$ representing the electric fields inside the optical cavity. The subscripts 1 and 2 refer respectively to the clockwise and counter-clockwise intra-cavity radiation fields. It, derived elsewhere [3, 4, 5], reads

$$\dot{\mathbf{E}} = \Big[\mathbf{A} - \mathscr{D}(\mathbf{E}).\mathbf{B}.\mathscr{D}(\mathbf{E}^*)\Big]\,\mathbf{E}\,, \tag{1}$$

where the matrices $\mathbf{A}$ and $\mathbf{B}$ account for the linear and quadratic interactions, and $\mathscr{D}(\mathbf{E}) = \mathrm{diag}(E_1, E_2)$. $\mathbf{A}$ and $\mathbf{B}$ depend on turn on the free spectral range c/L (L is the cavity length), the Sagnac frequency ω_s, the backscattering angles $\varepsilon_{1,2}$ and on the excess gain minus losses $\alpha_{1,2}$, the self saturation $\beta_{1,2}$, the cross saturation $\theta_{12,21}$, the frequency error $\sigma_{1,2}$, the null shift error $\tau_{12,21}$ and the backscattering amplitude $r_{1,2}$ coefficients [3, 4].

To implement the data analysis, we divided the parameters in two sets: cold cavity parameters associated to dissipative and parasite scattering effects, and active medium parameters associated to atomic polarizability. Correspondingly, the matrices can be written as [1, 5]

$$\mathbf{A} \equiv \frac{c}{L}\mathbf{P^{(0)}} - \mathbf{M} \quad , \mathbf{B} \equiv \frac{c}{L}\mathbf{P^{(2)}} \tag{2}$$

where $\mathbf{P^{(0)}}$ and $\mathbf{P^{(2)}}$ are the 0-th and 2-nd order contributions to the gas mixture polarizability and $\mathbf{M}$ is the dissipative linear coupling matrix [1].

Ring laser data (RLG_DATA) The most important measured signal for ring lasers is the interferogram, i.e. the signal obtained combining on a photo-diode the two counter propagating beams transmitted throught one of the ring mirrors. The intensities of both beams are also separately acquired by photo-diodes faced on another mirror [5]. The vector collecting all the outputs of the system at the time intervals kT_S reads

$$\mathbf{y}(k) = \begin{pmatrix} c_1 I_1(kT_s) \\ c_2 I_2(kT_s) \\ c_3 S(kT_s) \end{pmatrix} + \mathbf{w}(kT_s)\ , \tag{3}$$

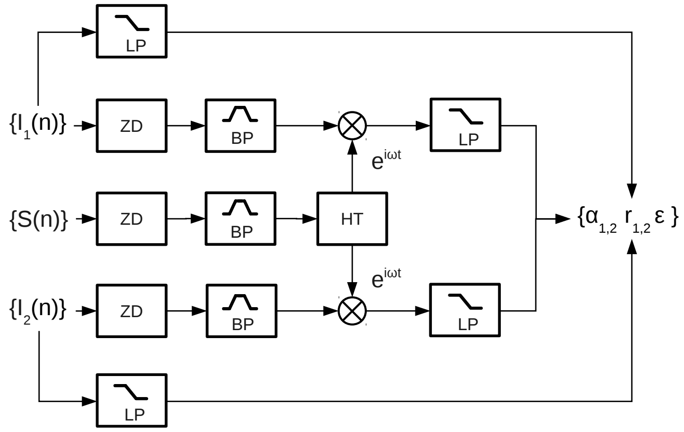

Figure 8: **Schematic of the parameter estimation procedure, where *LP* → lowpass *Butterworth* filter, *BP* → bandpass *Butterworth* filter, *ZD* → Zoom and Decimation routine, *HT* → *Hilbert* transform (see text).**

where T_S is the sampling time, the vector $\mathbf{w}$ represents a white noise stochastic process, and the constants c_i are real numbers which account for photodetectors characteristics. The interferogram signal $S(kT_s)$ can be recast as $S(k) = c_3 h_1^2 I_1(kT_s){+}c_3 h_2^2 I_2\; 2c_3 h_1 h_2 \sqrt{I_1(kT_s) I_2(kT_s)} \cos\left(\psi(kT_s)\right)$. The steady state intensities $I_{1,2}$ are usually in the form of constant signals plus small modulations, so the phase information in the interferogram is, at a first approximation, introduced only by $\psi(kT_s)$. For this reason the interferogram signal is regarded as the most important signal in the estimation of rotation rates.

Data conditioning procedure (ID_EST) Data are acquired at a sampling frequency of $5\,kHz$ ($T_s = 200\ \mu s$). To remove the oscillating component, intensity signals are low-pass filtered with a first order *Butterworth* filter with $1\,Hz$ cutoff frequency. The quantities $I_{1,2}$ are estimated by averaging the decimated intensities over a time interval of 10 s (i.e. 5×10^4 samples). On the other side, to calculate the modulation $i_{1,2}$ and phases $\phi_{1,2}$, the intensities are first band-passed around the fundamental *Sagnac* band [95÷125] Hz by means of a *Butterworth* filter, and decimated by a factor 2. The decimation procedure has been carried out by the tail recursive routine "Zoom and Decimation of a factor 2^n (ZD(n)), where each iteration step is composed of a half band filter stage with discrete transfer function $H(z) = \left(\frac{z^3 + 2z^2 + 2z + 2}{4z^3 + 2z}\right)^5$, followed by a downsampling by 2. The ZD(n) procedure ensures a linear phase filter response at least for $n = 3$ iterations, as no appreciable phase distortion was observed in simulated sinusoidal signals. The resulting data are then demodulated with a digital lock-in using as reference signal the discrete *Hilbert* transform of the interferogram, and setting the integration time to 10 s. A schematic of the parameter estimation procedure is reported in Fig.8. In addition, the phase of the two monobeam oscillating components is determined by the discrete *Hilbert* transform, and their difference is estimated by unwrapping the phase angle and taking its average over 10 s. As a concluding remark on the parameter estimation procedure, we mention that the problem of filtering very long time series has been solved by the *"overlap and save"* method, which is an efficient algorithm for avoiding the boundary transients due to finite length of digital filters.

.

Dissipative Identification Procedure In [2] we demonstrated that the ring laser dynamics has asymptotic solutions periodic with period $T = 2\pi/\omega$, where ω is the Sagnac frequency. This greatly simplify the steady state analysis. In fact, we can construct the likelihood functional

[2, 5] and search for its minimum value to derive a statistics of parameters estimation. The perturbative solutions of the steady state reads [2, 5]

$$\begin{cases} I_1(t) & = I_1 + i_1 \sin(\omega t + \phi_1) \\ I_2(t) & = I_2 + i_2 \sin(\omega t + \phi_2) \\ X(t) & = \frac{1}{2} \log\left[\frac{I_1(t)}{I_2(t)}\right] + i\omega t \end{cases} . \tag{4}$$

where $I_{1,2}$, $i_{1,2}$, and $\phi_{1,2}$ are the intensity offsets, monobeam modulation amplitudes and phases, which can be readily measured from ring laser outputs. The backscattering phase differences are estimated by $\widehat{\varepsilon}_{1,2} = \phi_{1,2}$. We found that the cavity loss parameters $\mu_{1,2}$ and $r_{1,2}$ are estimated by

$$\begin{cases} \hat{\mu}_{1,2} & = \alpha_0 - \beta\left(I_{1,2} + \frac{i_{1,2}^2}{I_{1,2}}\right) - \frac{i_1 i_2 I_{2,1}(L\omega/c)\cos\widehat{\epsilon}}{4I_{1,2}^2} - \\ & -\theta\left(\frac{i_{2,1}^2 + 4I_{2,1}^2}{4I_{1,2}} - \frac{i_{1,2}^2 I_{2,1}^2}{2I_{1,2}^3} + \frac{i_1 i_2 I_{2,1}\cos\widehat{\epsilon}}{I_{1,2}^2} + \frac{i_{2,1}^2 \cos 2\widehat{\epsilon}}{4I_{1,2}}\right), \\ \hat{r}_{1,2} & = \frac{i_{2,1}(L\omega/c)}{2\sqrt{I_1 I_2}} \mp i_{1,2}\sqrt{\frac{I_{1,2}}{I_{2,1}}}\theta \sin\widehat{\epsilon} \end{cases} \tag{5}$$

where $\widehat{\epsilon} = \widehat{\epsilon}_1 - \widehat{\epsilon}_2$, and α_0 is the mean excess gain for zero losses [1, 5].

Calibration Procedure (CLB) In the following we will discuss the monitoring signals acquisition and their application to calibration procedures.

Ring Down time measurement The spectroscopic technique known as *"Ring Down Time measurement" (RDT)* allows us to estimate mirror losses from the impulse response of a linear system. The experimental procedure is performed by recording with a fast detector, (photomultiplier *Hamamatsu H7827012*) loaded on a 1 kΩ impedance, after a rapid switch off of the radio-frequency discharge. In our setup we obtain a sufficiently rapid switch off by grounding one of the two electrodes of the radio-frequency discharge by means of a mechanical switch. A validation of this technique is obtained by measuring the decay time of the plasma fluorescence which results to be of the order of few microseconds. Finally, we performed an exponential fit of the collected data.

Calibration of Intensities in Lamb units To get accurate estimates of the *Sagnac* frequency, the light intensities input of the *EKF* must be calibrated in *Lamb* units. An accurate experimental method consists in the generation of additional longitudinal mode to the two fundamental cavity modes. This dynamical change is known as "multimode transition". The multimode transition can be achieved by increasing the laser output power and the laser single pass gain until new modes appear. The value of the mean light intensity for the multimode transition expressed in lamb units I_{th}, is commonly defined multimode threshold [1]. The threshold condition for multimode transition can be calculated from the stability analysis of the ring laser system. In ref.[1, 5] we derive a threshold condition for the multimode operation considering the dynamics of 2 counterpropagating laser modes. The resulting value I_{th} provides the calibration of the voltages $\{V_{1,2}(n)\}$, acquired by photodetectors to the intensities $\{I_{1,2}(n)\}$ in *Lamb* units. We have also derived an estimate of G_{th} that will be used as the initial value of the gain monitor.

Population Inversion Monitor The intensity of the plasma fluorescence line at 632.8 nm provides a good observable for monitoring the relative variations of the atomic population in the upper laser level. In order to perform an on-line measurement of the laser gain, we coupled part of the plasma fluorescence to a multi-fiber bundle. The collected light containing all the spectral contribution of the $He-Ne$ discharge, is filtered by a line filter 1 nm wide around 632.8 nm and detected with a photodiode. The photocurrent is amplified with a transimpedance stage with a gain of 1 GΩ. The voltage V_p of the photodiode is used as an optical monitor of the laser gain by recording the dependence of the output powers I_1 and I_2 on V_p, after losses have been estimated. The calibration of the monitor signal is obtained by performing intensity steps in the neighborhood of the monomode working regime of the ring laser [1].

Spectroscopic probe of the gain medium Essential information about the gain medium can be extracted by observing the *Doppler* absorption of the plasma at 640.2 *nm* using a tunable laser. This is a closed Neon transition and can be easily interrogated by probing the $He-Ne$ plasma. We setup a frequency tunable *ECDL* (Extended Cavity Diode Laser) crossing the $He-Ne$ plasma through the pyrex capillary . From this measurement one can get a precise estimation of the *Doppler* broadening, as well as of the isotopic composition of the gas. An example of this measurement is given in Ref.[1], where a standard $He-Ne$ gas mixture has been studied by injecting a scanning laser frequency around 640.2 nm.

Extended Kalman Filter procedure (EKF) The knowledge of the *Lamb* parameters $\widehat{\alpha}_{1,2}$,$\widehat{r}_{1,2}$ and $\widehat{\varepsilon}$ by means of the identification routine, together with the active medium parameters experimentally measured, and the monitor of the gain G, allow us to set up an *EKF* for an efficient and unbiased estimation of the rotation rate $\widehat{\omega}_s$. The *EKF* state variables are the $\mathbb{R}^3$ vector $\mathbf{X}(t) \equiv [I_1(t),\ I_2(t),\ \psi(t)]^T$. The dynamics model is given by Eqs.1, with the addition of the model error as a zero mean, white, stochastic vector field $\mathbf{v}(t)$ with variance $\mathrm{Var}[\mathbf{v}(t)] \equiv Q$, where Q is a 3×3 covariance matrix that accounts for the effects of unmodeled dynamics, for instance, identified parameter errors, calibration errors, and numerical integration inaccuracies. The *EKF* prediction step, which corresponds to the integration of Eqs.(1) over the time interval T_s, is carried out using the *RK4 Runge-Kutta* routine. In the discrete time domain, the model of the measurement process reads $\{\mathbf{y}(n)\} = \{\mathbf{X}(n)\} + \{\mathbf{w}(n)\}$, where $\mathbf{w}(n)$ is zero mean, white, stochastic vector field (observation noise) with variance $Var[\mathbf{w}(n)] \equiv R$, and R is a 3×3 covariance matrix. In the standard experimental set up of ring lasers $[I_1(t),\ I_2(t),\ \psi(t)]$ are measured by independent sensors, and so we can assume that R is diagonal, with diagonal elements the observation noise variances $\sigma^2_{I_1}$, $\sigma^2_{I_2}$, σ^2_{ψ} which can be conveniently calculated through the level of white noise in the power spectrum of $\{\mathbf{y}(n)\}$.

The backscattering frequency is estimated from the filtered channels $\widehat{I}_{1,2}(n)$, $\widehat{\psi}(n)$, the identified parameters $\widehat{\alpha}_{1,2}$, $\widehat{r}_{1,2}$, $\widehat{\varepsilon}$, and the exogenous parameter β as

$$\widehat{\omega}_{BS} = \frac{c}{L}\left[\widehat{r}_1\sqrt{\frac{\widehat{I}_1}{\widehat{I}_2}}\sin(\widehat{\psi}-\widehat{\varepsilon}) + \widehat{r}_2\sqrt{\frac{\widehat{I}_2}{\widehat{I}_1}}\sin(\widehat{\psi}+\widehat{\varepsilon})\right]$$

where, for simplicity, we have dropped the index (n) from time series. The *Sagnac* frequency is then estimated from the difference $\widehat{\omega}_s = \dot{\widehat{\psi}} - \widehat{\omega}_{BS}$, where the numerical derivative of $\widehat{\psi}$ has been computed by the "5 *point method*" [5] designed to reject the derivative amplification of the noise.

Diagnostic procedure (DGN) This procedure monitors the operation of the ring laser and also provides useful data for rotational seismology. The routine saves files, on hourly basis, containing time series downsampled at 50 Hz sampling rate. The time series are: the derivatives of the acquired beat signal $S(k)$; an estimation of the Sagnac frequency by means of the Hilbert transform of $S(k)$; the sum and the difference of the light intensities $I_1(k) + I_2(k)$, and $I_1(k) - I_2(k)$; the phase difference between the the two intensities ε; and a row estimate of the backscattering pulling in the Sagnac frequency [3].

2.3 DAQ system, Online and Control

Our instrumentation run unattended, in order to minimize vibrations and temperature changes. Through the DAQ not only the data to be analysed off-line are acquired, but as well the status of the apparatus can be monitored, the mirrors can be moved by means of the piezo actuators, and, if necessary, the control loops can be opened. Sometimes it is necessary to move remotely one of the mirrors to bring the apparatus close to a different position, for example when the ring-laser is working in split mode (i.e. the two modes have different longitudinal order and the beat-note is higher than the free spectral range of the ring, about 20 MHz). The DAQ system itself is remote-controlled and transfers the data from INFN-LNGS to INFN-Pisa. The hardware has been selected in order to be transportable; its main features can be listed as follows:

- analog to digital conversion and storage of the optical signals produced by the ring laser, with 5 kHz sampling rate (the Sagnac and the two mono/beams);
- analog to digital conversion and storage of environmental signals (temperature, humidity, pressure), laser parameters (plasma intensity, average intensities, piezoelectric transducers driving voltage) and local tiltmeters (nano-rad precision), with 1 Hz sampling rate;
- analog to digital conversion and storage of seismic channels (seismometers/accelerometers) at 100 Hz sample rate;
- real-time processing of experimental parameters connected to laser gain, backscattering phase, actuators signals.
- digital to analog generation of the signals driving the laser, necessary for some of the controls of the apparatus.
- the DAQ acquisition rate is conditioned with GPS, this is necessary to well identify the very low frequency signals of geodetic origin. As well the time stamp, with the precision of milliseconds, is required to record the arrival time of tele seismic events.

DAQ hardware is based on a modular PXI system. A PXI system is composed of three parts: the chassis, the controller and one or more modules. The acquisition system of GINGERino is based on components by National Instruments.

Acquisition Software The operative system running on the PXI-8106 controller is LabView-RT, a real-time system provided by National Instruments. The development environment chosen for the implementation of the DAQ is LabVIEW graphical programming language by National Instruments. Software development occurs on a host Windows PC and subsequently is transferred on the PXI controller via ethernet communication and finally executed under LabView real-time. The program of acquisition first waits to receive a signal from a sufficiently precise PPS reference, then starts acquiring signals continuously from the different boards. Acquired data are written in the PXI local hard-disk: for every hour of the day a file is generated and stored in the internal memory of PXI, the files are named time sampled and overwrite the previous days. Each hour acquisition creates a file of about 300 Mb.

Acquisition Timing Both frequency and time accuracy are important since the former affects the estimation of the Sagnac frequency and the latter introduces errors in the time localization of seismic events. In the LNGS underground area we receive a GPS-synchronized PPS (pulse per second) signal and we are connected to the local NTP server (ntp0.lngs.infn.it) in order to obtain a time stamp with an error of few ms. The frequency accuracy is obtained by disciplining the clock PXI-6653 board to the PPS via the PXI-6682. The error on the time stamp is on the other

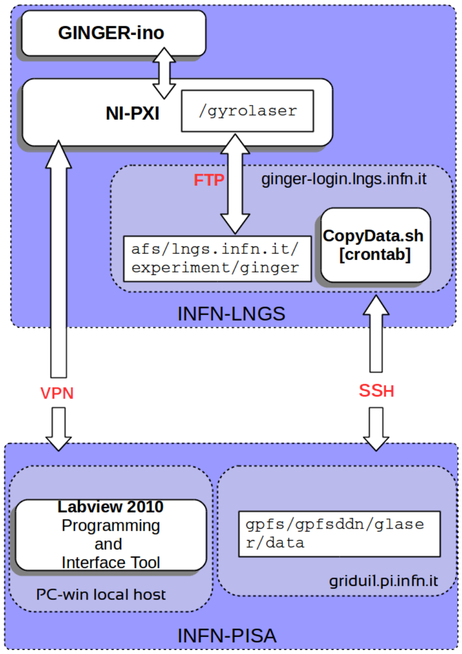

Figure 9: **Schematics of the connections for the data transfer between INFN-LNGS and INFN-Pisa: VPN and SSH protocols are used for security reasons.**

hand limited by the uncertainty on the NTP. The time vector t of the acquired data is then given by $t = t_0 + n * dt$ where t_0 is the time-stamp from NTP, n is the sample number, $dt = 1/f_{sampling}$ is the time sampling time interval obtained from the GPS referenced PPS signal.

Data transfer and storage The data acquired by the PXI are written on its local hard-disk in a directory containing 1 day of data which is updated hourly in FIFO mode. In this way a buffer of the last 23 hours of acquired data is present on the hard-disk for data recovery purposes. The scheme of the internet connections linking LNGS to Pisa is shown in figure 9. The data written on the PXI hard-disk are copied via FTP (the only viable solution for the Labview-RT OS) into a dedicated directory on the virtual machine named 'ginger-login.lngs.infn.it' that can be accessed from the internet via authorized SSH-account. The file content of the directory in 'ginger-login.lngs.infn.it' named /afs/lngs.infn.it/experiment/ginger/ is then copied into the 'gridui1.pi.infn.it'. The data copy service is a cronjob script running every hour on the ginger-login virtual machine. It makes the following operations:

- compares the file content of the data storage directory /gyrolaser on the PXI with the content of the destination directory on /gpfs/ddn/glaser/data/ on gridui1.pi.infn.it (data transfer destination);
- copies via FTP the missing data files from the PXI to the directory /afs/lngs.infn.it/experiment/ginger/ on 'ginger-login.lngs.infn.it';
- transfer via SCP from /afs/lngs.infn.it/experiment/ginger to /gpfs/ddn/glaser/data/ on 'gridui1.pi.infn.it'.

At the end of the process, the data from the PXI are transferred to Pisa, and an image of the PXI buffer is updated hourly on 'ginger-login.lngs.infn.it'.

3 Future Plan and Conclusions

The apparatus of GINGERino has been constructed and at the moment is in the commissioning phase. The ringlaser has shown the first light, and a bringdown time of 250 μsec has been measured; but improvements are necessary in order to maximise the output light power. The first data are expected before next summer. We do not foresee big changes in the plant, but several tests will be done with different sets of mirrors and different size of the discharge. The main objective will be to improve the shot noise level and increase the stability of the whole apparatus. At the beginning the instrument will be free running, without perimeter control. This will be eventually installed at the end of 2015, we don't have the necessary iodine stabilised laser source for LNGS, but we expect to borrow the absolute reference laser from our colleagues in Germany. The 2015 plan will depend on how the ring laser behaves, our effort will be concentrated on identifying noise sources and applying the routines to study and subtract the systematic of the instrument. The apparatus should be able to see daily and sub daily polar motions, and tele seismic events relevant for seismology (GINGERino is an experiment of common interest between INFN and INGV).

4 Acknowledgement

The construction of GINGERino has been a very tough job, which has been possible for the big effort of several colleagues of Pisa, Naples and LNGS. For that we are grateful to: A. Soldani, G. Petragnani, G. Balestri, M. Garzella, A. Sardelli and F. Francesconi of Pisa, and G. Bucciarelli, Lorenzo Marrelli and Nicola Massimiani (Servizio Esercizio e Manutenzione) and Francesco Esposito, Luca Faccia, Giustino D?Alfonso, Stefano Giusti e Luigi Rossi of 'Servizio Facchinaggio' at LNGS. We have to thank as well the Computing and Network teams of LNGS and Pisa Section for its continuous assistance.

5 List of Publications 2014

1. D Cuccato, A Beghi, J Belfi, N Beverini, A Ortolan, A Di Virgilio: Controlling the nonlinear intra-cavity dynamics of large He-Ne laser gyroscopes, Metrologia 51 97-107 (2014) doi:10.1088/0026-1394/51/1/97

2. N Beverini, M Allegrini, A Beghi, J Belfi, B. Bouhadef, M Calamai, G Carelli, D Cuccato, A Di Virgilio, E Maccioni, A Ortolan, A Porzio, R Santagata, S Solimeno, A Tartaglia: Measuring general relativity effects in a terrestrial lab by means of laser gyroscopes, Laser Phys. 74 074005 (2014) doi:10.1088/1054-660X/24/7/074005

3. J Belfi, N Beverini, G Carelli, D Cuccato, A Di Virgilio, E Maccioni, A Ortolan, R Santagata, Interferometric length metrology for the dimensional control of ultra-stable Ring Laser Gyroscopes, Class. Quantum Grav. 31 225003 (2014)

4. A. Di Virgilio, M. Allegrini, A. Beghi, J. Belfi, N. Beverini, F. Bosi, B. Bouhadef, M. Calamai, G. Carelli, D. Cuccato, E. Maccioni, A. Ortolan, G. Passeggio, A. Porzio, M.L. Ruggiero, R. Santagata, A. Tartaglia: A ring lasers array for fundamental physics, C. R. Physique 15, 866874 (2014)

References

[1] D. Cuccato et. al. “Controlling the non-linear intra-cavity dynamics of large $He-Ne$ laser gyroscopes”, Metrologia, 51, 1, (2014).

[2] A. Beghi et. al. “Compensation of the laser parameter fluctuations in large ring-laser gyros: a Kalman filter approach”, Applied Optics, 51, 31, (2012).

[3] F. Aronowitz. Theory of a travelling wave optical maser. Physical Review, 139(3A), A635-A645, December 1965.

[4] Jr. W. E. Lamb. Theory of an optical maser. Physical Review, 134(6A):1429-1450, June 1964.

[5] D. Cuccato, Modeling, estimation and control of ring Laser Gyroscopes for the accurate estimation of the Earth rotation, Ph.D. thesis, University of Padova (2015).

[6] we use the time-frequency browser baudline, url:”http://www.baudline.com/”.

The ICARUS Experiment

The ICARUS Collaboration

M. Antonello[a], B. Baiboussinov[b], P. Benetti[c], F. Boffelli[c], A. Bubak[m], E. Calligarich[c], S. Centro[b],
A. Cesana[e], K. Cieślik[f], D.B. Cline[g], A.G. Cocco[d], A. Dabrowska[f], A. Dermenev[h], R. Dolfini[c†], A. Falcone[c],
C. Farnese[b], A. Fava[b], A. Ferrari[i], G. Fiorillo[d], D. Gibin[b], S. Gninenko[h], A. Guglielmi[b], M. Haranczyk[f],
J. Holeczek[m], M. Kirsanow[h], J. Kisiel[m], I. Kochanek[m], J. Lagoda[l], S. Mania[m], A. Menegolli[c], G. Meng[b],
C. Montanari[c], S. Otwinowski[g], P. Picchi[n], F. Pietropaolo[b], P. Plonski[o], A. Rappoldi[c], G.L. Raselli[c],
M. Rossella[c], C. Rubbia[1,a,i], P.R. Sala[e], A. Scaramelli[e], E. Segreto[a], F. Sergiampietri[p], D. Stefan[a], R. Sulej[a,l],
M. Szarska[f], M. Terrani[e], M. Torti[c], F. Varanini[b], S. Ventura[b], C. Vignoli[a], H.G. Wang[g], X. Yang[g],
A. Zalewska[f], A. Zani[c] K. Zaremba[o],

[a]INFN - Laboratori Nazionali del Gran Sasso, Assergi, Italy
[b]Università di Padova e INFN, Padova, Italy
[c]Università di Pavia e INFN, Pavia, Italy
[d]Università Federico II di Napoli e INFN, Napoli, Italy
[e]Politecnico di Milano e INFN, Milano, Italy
[f]H.Niewodniczański Institute of Nuclear Physics, Kraków, Poland
[g]Department of Physics, UCLA, Los Angeles, USA
[h]Institute for Nuclear Research of the Russian Academy of Sciences, Moscow, Russia
[i]CERN, Geneva, Switzerland
[l]Nuclear Center for Nuclear Research, Warszawa, Poland
[m]Institute of Physics, University of Silesia, Katowice, Poland
[n]INFN Laboratori Nazionali di Frascati, Frascati, Italy
[o]Institute for Radioelectronics, Warsaw Univ. of Technology, Warsaw, Poland
[p]Università di Pisa e INFN, Pisa, Italy

Abstract

In 1977 C.Rubbia [1] conceived the idea of a LAr-TPC (Liquid Argon Time Projection Chamber). The ICARUS T600 cryogenic detector is the largest LAr-TPC ever built and operated. Installed in the Gran Sasso underground laboratory and exposed to the CNGS neutrino beam, on June 26th 2013 ICARUS has completed 3 years of data taking collecting about 3000 CNGS neutrino events but also cosmic rays, and showing optimal performances. The data analysis is still going on. In this report the observation of a extremely high value of the electron lifetime exceeding 15 ms, and results of the muon momentum measurement with the Coulomb multiple scattering method will be presented. The future perspectives for the ICARUS T600 detector, i.e. detector overhauling within the CERN WA104 experiment, and far station for the Short Baseline Neutrino Fermilab program will be also shortly described.

---

[1] Spokesman of the ICARUS Collaboration

1 ICARUS T600 Detector

The ICARUS T600 detector is the largest Liquid Argon Time Projection Chamber (LAr-TPC) ever built and operated. The detector consists of a large cryostat split into two identical, adjacent half-modules with internal dimensions 3.6×3.9×19.6 m^3 and filled with a total of 760 tons of ultra-pure LAr. Each half-module houses two TPCs separated by a common cathode, with a drift length of 1.5 m. Ionization electrons, produced by charged particles along their path, are drifted under uniform electric field (E_D = 500 V/cm) towards the TPC anode made of three parallel wire planes, facing the drift volume. A total of 54000 wires are deployed, with a 3 mm pitch, oriented on each plane at different angles (0^0, + 60^0, - 60^0) with respect to the horizontal direction. The drift time of each ionization charge signal, combined with the electron drift velocity information (v_D = 1.55 mm/s), provides the position of the track along the drift coordinate. Combining the wire coordinate on each plane at a given drift time, a three-dimensional image of the ionizing event can be reconstructed. The absolute time of the ionizing event is provided by the prompt ultra-violet scintillation light emitted in LAr and detected through an array of 74 Photo Multiplier Tubes (PMTs), installed in LAr behind the wire planes, which are also used for triggering purposes. The detector is completed by a cryogenic plant made of a liquid Nitrogen cooling circuit which keeps Argon in liquid phase and guarantees high LAr thermal stability (within 1K). The LAr purity is a key issue for the detector imaging capability and for a correct estimation of the ionization charge of events at any depth along the drift path. A system of LAr purifiers, operating both in gas and in liquid phase, keep the LAr purity under control.

The ICARUS T600 detector performances can be summarized as follows: 1 mm^3 precision in event topology, e/γ separation with 2% X_0 sampling, electromagnetic showers energy resolution $\sigma(E)/E = 0.03/\sqrt{E(GeV)} \oplus 0.01$, low energy electrons resolution $\sigma(E)/E = 0.11/\sqrt{E(GeV)} \oplus 0.02$ and hadronic showers resolution $\sigma(E)/E = 0.30/\sqrt{E(GeV)}$.

During 2013, after the definitive CNGS beam stop on December 3^{rd} 2012, the ICARUS T600 detector continued its data taking with cosmic rays untill June 26^{th}, when the detector decommissioning started. The decommissioning procedure lasted in almost entire 2014 and resulted in transportation of both ICARUS cryostats to CERN in December 2014.

The analysis of the collected data sample is still progressing. This report will focus on the following items: (1) observation of extremely high value of the ionization electrons lifetime, and (2) the validation of the Coulomb multiple scattering algorithm for the measurement of muon momentum in the few GeV energy range.

2 Observation of an extremely high electron lifetime

One of the most important issues in the LAr TPC detection technique is extremely low level of electronegative impurities, which is required to transport ionization electron over macroscopic distances with small signal attenuation. The electron lifetime τ_{ele} in the ICARUS T600 LAr TPC has been measured using the attenuation $\lambda = 1/\tau_{ele}$ of the charge signal, produced by cosmic-ray muon tracks traversing the detector volume, as a function of the electron drift distance. The charge signal was measured in the Collection plane removing noisy channels for selected clean (no assocaited electromagnetic showers, no large number of delta electrons) and sufficiently long muon tracks with $>$ 100 wires and $>$ 94 cm length along the drift coordinate. The area of the signal above the local baseline represents the ionization signal (see fig. 1). The truncation method, described in details in [P2], applied to the asymmetric Landau tail of the dE/dx depositions was used on each track, splitted into short segments in which the attenuation is negligible compared to the Landau fluctuactions. A sample of about 3100 through going cosmic rays collected every day has been used to determine the electron lifetime in the ICARUS T600 detector. The LAr purity trend in the T600 East module is shown in fig. 2. Each data point was obtained averaging over about 100 muon tracks collected in about half a day.

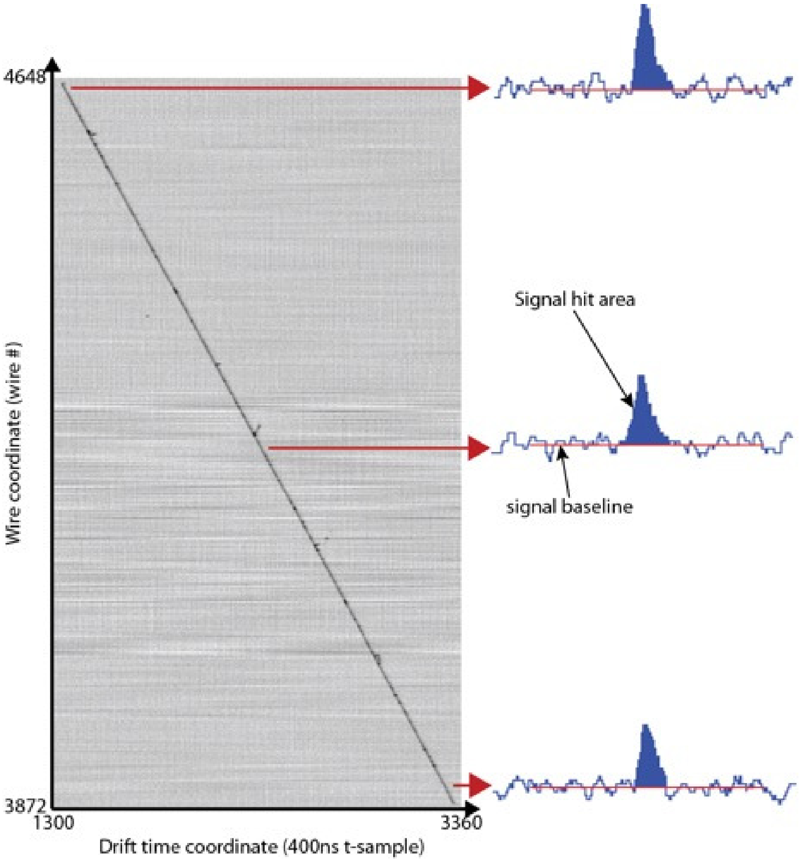

Figure 1: Example of a track used for purity measurement extending over 776 wires and 2060 t-samples, corresponding to a drift time of 824 μs. Signals of three different hits are also shown.

In April 2013 the ACD CRYO pump used during the first 2 years of data taking was replaced with a new Barber Nichols BNCP-32C-000 pump with an external motor similar to those used in the liquid nitrogen recirculation. The τ_{ele} decreased rapidly to the values below 1 ms during the two weeks period of pump replacement. With the Barber Nichols pump installed, τ_{ele} started to increase very fast reaching the value of $16.1^{+1.3}_{-1.1}$ corresponding to the maximum signal attenuation of 6% for the maximum drift distance of 1.5 m. It should be noticed that at the end of the ICARUS T600 data taking the τ_{ele} was still rising. The uniformity of the electron lifetime over the large ICARUS detector volume was also verified with the use of about 1000 almost vertical cosmic muon tracks traversing the East cryostat. The tracks have been automatically reconstructed in three dimensions in order to determine their position along the detector, which has been divided in nine 2 m long regions for the left and the right chamber. The $\delta\lambda$ parameter which is the difference between the attenuation λ_T associated to the track and λ obtained in the considered period was calculated. From the distribution of the $\delta\lambda$ the mean value for the tracks inside the selected 2 m region was extracted. The trend of the $\delta\lambda$ is plotted in fig. 3 showing a uniformity of the LAr impurities. The free electron lifetime greater than 15 ms corresponds

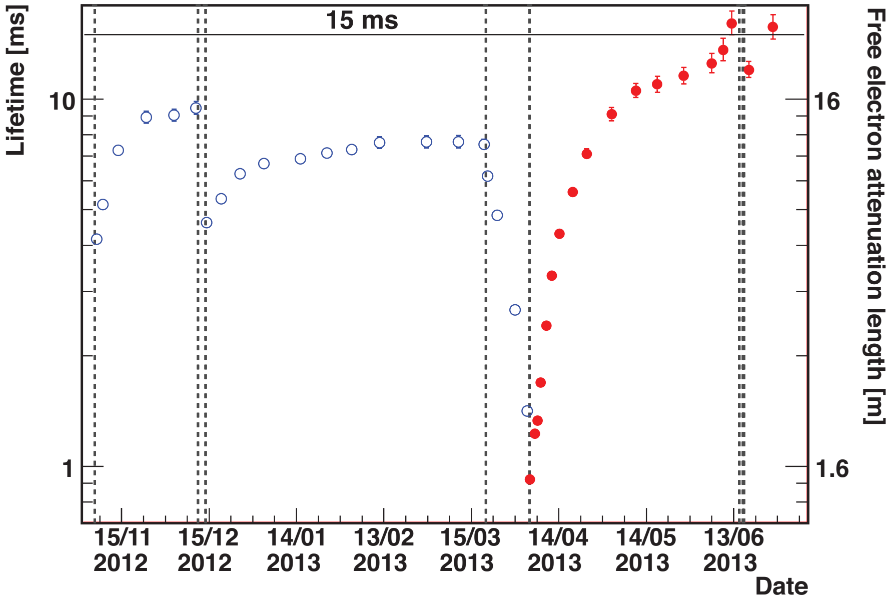

Figure 2: Electron lifetime τ of the East module for the last part of the ICARUS data taking: in red full points the measurements with the new pump with external motor are shown. The dashed vertical lines represent the stops and restart of the LAr recirculation; during this period the GAr recirculation system continued to operate.

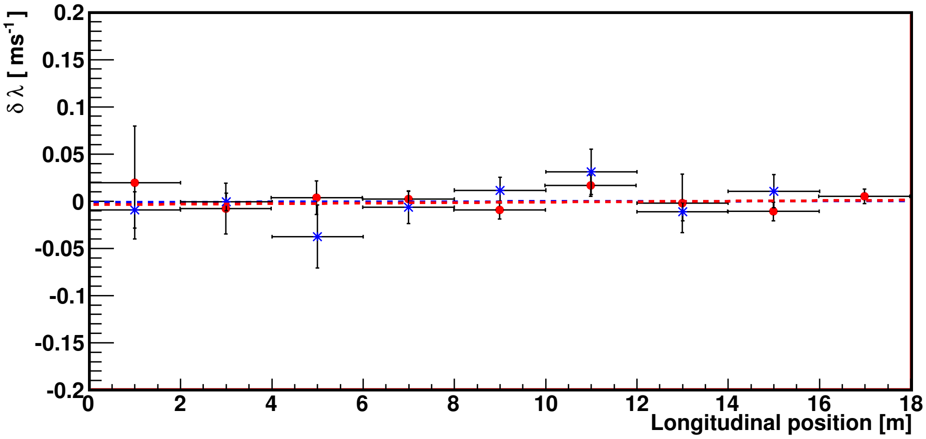

Figure 3: The measured variation of the level of impurities in the East cryostat along the longitudinal direction. Red circles refer to the left chamber, blu stars to the right one. The dashed lines are the linear fits in both chambers. The fit results are amply compatible with a uniform LAr purity across the length of the whole detector: slope for the left chamber $(8.8 \pm 90) \cdot 10^{-5}$ ms^{-1}m^{-1}, slope for the right chamber $(2.7 \pm 11) \cdot 10^{-4}$ ms^{-1}m^{-1}.

to a mean attenuation length of about 25 meters, the value of great importance for the next generation of LAr TPC detectors.

3 Muon momentum from multiple scattering

There is no magnetic field in the active volume of the ICARUS T600 LAr TPC. Therefore, the measurement of the muon momentum, required for the reconstruction of ν_μ charged current (CC) events, has to be performed with the use of the Multiple Coulomb Scattering (MCS) method. For the presented analysis 415 single muon events, with minimum track length of 2.5 m, produced by the CNGS ν_μ interactions with the T600 upstream rock were selected. The produced hadrons were fully absorbed in the rock, while muons stopped in the LAr volume. The distribution of analyzed stopping muons as a function of their kinetic energy (obtained from the calorimetric measurement) and track length is presented in fig. 4. The final meter of each muon track was not used for the MCS measurement, in order to avoid bias from the knowledge of the muon range. The outlier hits, originating mainly from the δ-rays, have been removed from the track.

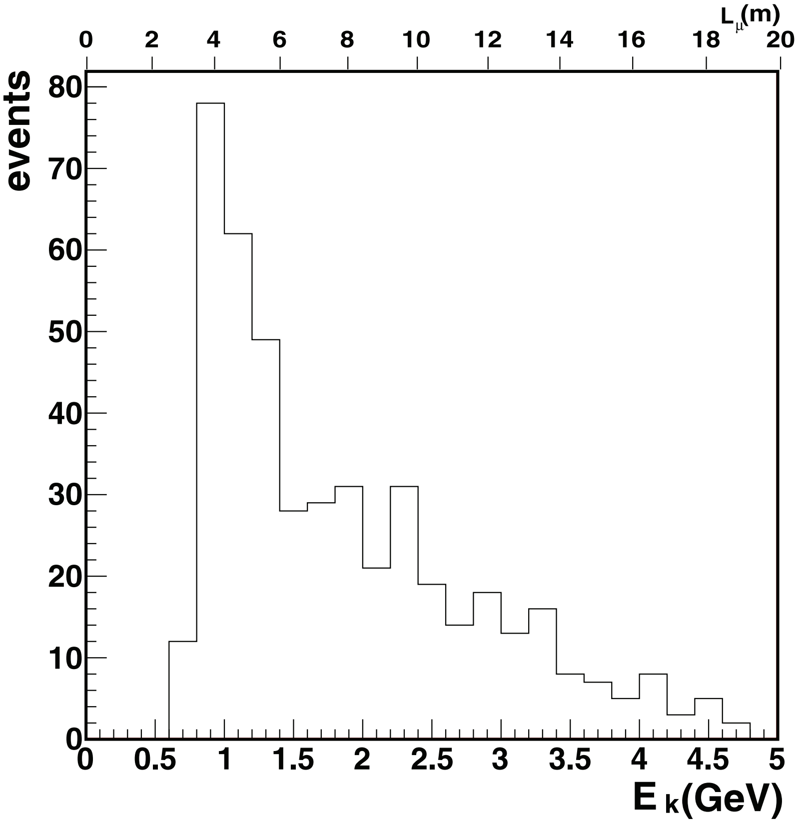

Figure 4: The distribution of stopping muons analyzed in this work, as a function of their kinetic energy (bottom axis) and corresponding muon length (top axis).

The MCS measurement was performed on the muon track projection on the two-dimensional Collection plane. A precise and unbiased estimation of all measurement errors is necessary, in order to disentangle the MCS effects from the apparent track deflections due to positional uncertainty. The coordinates of each 2D point are given by the wire position (known with precision better than 0.01 mm) and drift time, which is the main source of uncertainty of the hit position measurement. This presents a single-hit contribution, which was estimated by measuring the dispersion of the drift coordinate with respect to a sufficiently short (three consecutive hits) part of the track, to minimize the MCS contribution. The average value of hit position uncertainty, found according to this procedure, was about 0.7 mm. A term due to the non-synchronization of electronic boards was also present.

The measurement of the RMS multiple scattering angle ϕ_{MCS} over a track segment L allows to determine muon momentum p according to the following formula, which describes the Gaussian part of the angle distribution, i.e. large values of scattering angle are neglected,

$$\phi_{MCS} = \frac{13.6MeV/c}{p}\sqrt{\frac{L}{X_0}}(1 + 0.038ln\frac{L}{X_0}), \tag{1}$$

where X_0 is the radiation length in LAr. The muon track has been divided into segments of length of about 19.2 cm (hits from two consecutive electronic boards) with average number of 57 hits. The deflection angles between consecutive segments along the muon track were measured, and from their distribution muon momentum can be extracted. The observed deflection angles contain, in addition to MCS, also contributions from the single point space resolution, and from the board to board synchronization, which are equal to 2 mrad and 1 mrad, respectively, and are momentum independent.

The performance of the MCS momentum measurement can be verified by comparison with the calorimetric measurement of the stopping muons. For this purpose a sample of 415 stopping muons has been analyzed. The comparison is presented in fig.5.

The measured MCS momentum p_{MCS} is in agreement with the corresponding calorimetric measurement p_{CAL}. A momentum resolution $\delta p/p$ of about 16% for muon tracks of length of 4m has been approximately estimated from a Gaussian fit to the p_{MCS}/p_{CAL} distribution. The p_{MCS}/p_{CAL} ratio decreases for larger values of the muon momentum and depends on the track distance from the cathode (see fig. 6), suggesting a non-perfect planarity of the cathode. This hypothesis has been checked by introducing in the MC simulation a sinusoidal, with amplitude value of 2.5 cm and λ 4m, deformation of the cathode. The obtained p_{MCS}/p_{CAL} ratio is similar to the one observed in real data, confirming the influence of the cathode deformation on the muon MCS momentum measurement. The details of the analysis will be given in the publication which is presently under collaboration review[2].

4 Future perspectives

The successful, underground, continuous, long therm operation of the ICARUS T600 detector has conclusively demonstrated that the LAr-TPC is the leading technology for the future short and long baseline accelerator driven neutrino physics.

During 2014 the detector has been decommissioned and moved out of the underground laboratory. At the end of November 2014 INFN and CERN have signed a MOU for the transportation and overhauling of the T600 at CERN. The transfer of the two T600 TPCs to CERN has been completed: after the positioning of the first module into its transport vessel, the first cargo has arrived to CERN at the middle of November 2014. Movement operations at LNGS proceeded smoothly, with 4 to 6 people continuously involved for three weeks during October 2014. After

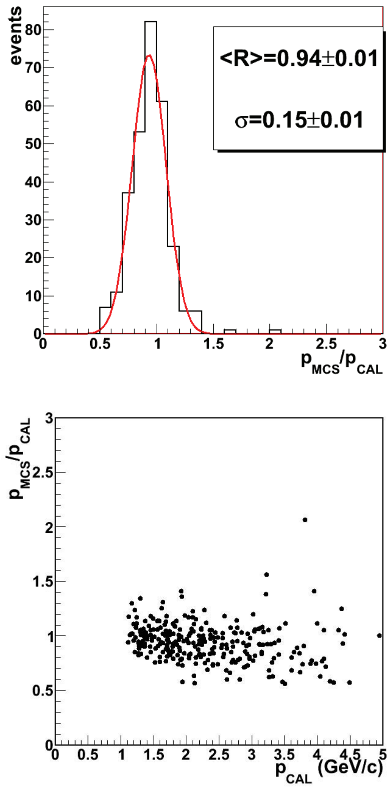

Figure 5: The distribution of p_{MCS}/p_{CAL} ratio for the stopping muon sample (left) and p_{MCS}/p_{CAL} ratio vs. p_{CAL} (right) for L_{μ}= 4 m. The FWHM width of the p_{MCS}/p_{CAL} ratio is $\tilde{3}3\%$.

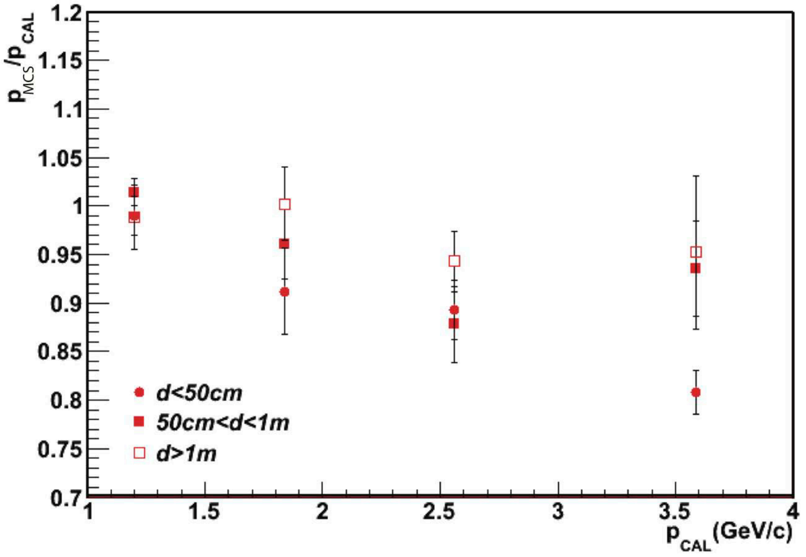

Figure 6: The dependency of p_{MCS}/p_{CAL} ratio vs. p_{CAL} (right) for L_{μ}= 4 m. Data have been subdivided in 3 bins of distance from the cathode ($\tilde{5}0$ cm each) spanning the full drift path in the TPCs.

the arrival of the second transport vessel at LNGS in November 2014, also the second T600 TPC was moved to CERN, being on site at the middle of December 2014.

The WA104/ICARUS programme is now firmly established through a Memorandum of Understanding between CERN and INFN. This project is devoted at "Improving the ICARUS T600 Liquid Argon Time Projection Chamber (LAr TPC) in order to prepare for its operation at shallow neutrino depths", on a two years time schedule to be completed by end of 2016.

The detector will then be transferred to Fermilab to search for sterile neutrinos at the eV mass scale through both appearance and disappearance channels at FNAL Booster Neutrino Beam exploiting three LAr-TPC detectors at different distances from the proton target: LAr1-ND at 110 m, MicroBooNE at 470 m and ICARUS-T600 at 600 m. The proposed SBN experiment will investigate the presence of sterile neutrinos as hinted by neutrino anomalies observed at accelerator neutrino beams, nuclear reactors and radioactive Mega sources in solar neutrino experiments. In three years of data taking the experiment will explore the ν_μ to ν_e appearance signal with 5 sigma sensitivity the parameter region indicated by the LSND experiment and measure independently the ν_μ disappearance with a sensitivity exceeding an order of magnitude the present experimental limits. In the framework of additional sterile neutrinos the ν_e appearance and ν_μ disappearance are mutually related through the relation $sin^2 2\theta_{e\mu} \sim 0.25 sin^2 2\theta_{ee} sin^2 2\theta_{\mu\mu}$. Therefore the intrinsic ν_e events with a disappearance signal (if confirmed by reactors experiments) may result in the reduction of a superimposed LSND-like ν_e signal in the present experiment. These two effects could be disentangled by running with a different intrinsic ν_e beam contamination adopting different beam line optics (horn and decay tunnel length). The ability to perform search for oscillation signals in multiple channels is a major advantage for the FNAL SBN oscillation physics program. A simultaneous analysis of ν_eCC and ν_μCC events will be a very powerful way to explore oscillations and untangle the effects of $\nu_\mu \to \nu_e$, $\nu_\mu \to \nu_X$ and $\nu_e \to \nu_X$ transitions.

On a longer time scale the overhauled ICARUS T600 detector could also provide a convenient near detector in LBNE.

List of Publications Year 2014

[P1] M. Antonello et al. [ICARUS Coll.], The trigger system of the ICARUS experiment for the CNGS beam, JINST, 9:P08003 (2014).

[P2] M. Antonello et al. (ICARUS Collaboration), Experimental observation of an extremely high lifetime with the ICARUS T600 LAr TPC, JINST, 9:P12006 (2014).

References

[1] C.Rubbia, CERN-EP/77-08 (1977).

[2] M.Antonello et al., Momentum measurement in ICARUS-T600 via multiple Coulomb scattering analysis in the few-GeV range, *in preparation.*

LUNA: Laboratory for Underground Nuclear Astrophysics

M. Aliotta[a], M. Anders[b], D. Bemmerer[b], A. Best[c], A. Boeltzig[d], C. Broggini[e], C. Bruno[a], A. Caciolli[f], F. Cavanna[g], P. Corvisiero[g], T. Davinson[a], R. Depalo[f], A. Di Leva[h], Z. Elekes[i], F. Ferraro[g], A. Formicola[c], Zs. Fülöp[i], S. Gazzana[c], G. Gervino[j], A. Guglielmetti[k], C. Gustavino[l], Gy. Gyürky[i], G. Imbriani[h], L. Leonzi[c], M. Junker[c], I. Kochanek[c], R. Menegazzo[e], P. Prati[g], D. Scott[a], E. Somorjai[i], O. Straniero[m], F. Strieder[n], T. Szucs[b], M. Takacs[b], D. Trezzi[k]

SPOKESPERSON: A. GUGLIELMETTI

[a]University of Edinburgh, Edinburgh, United Kingdom
[b]Helmholtz-Zentrum Dresden-Rossendorf, Dresden, Germany
[c]INFN, Laboratori Nazionali del Gran Sasso (LNGS), Assergi (AQ), Italy
[d]Gran Sasso Science Institute (GSSI), L'Aquila, Italy
[e]INFN, Padova, Italy
[f]Università degli Studi di Padova and INFN, Padova, Italy
[g]Università degli Studi di Genova and INFN, Genova, Italy
[h]Università degli Studi di Napoli "Federico II", and INFN, Napoli, Italy
[i]Institute for Nuclear Research (MTA ATOMKI), Debrecen, Hungary
[j]Università degli Studi di Torino and INFN, Torino, Italy
[k]Università degli Studi di Milano and INFN, Milano, Italy
[l]INFN, Roma, Italy
[m]Osservatorio Astronomico di Collurania, Teramo, and INFN Napoli, Italy
[n]Institut für Experimentalphysik III, Ruhr-Universität Bochum, Bochum, Germany

Abstract

Aim of the LUNA experiment is the direct measurement of the cross section of nuclear reactions relevant for stellar and primordial nucleosynthesis. The year 2014 was dedicated to the completion of the data taking for the ^{17}O(p,α)^{14}N reaction and to the measurement of the ^{22}Ne(p,γ)^{23}Na and ^{18}O(p,α)^{15}N reactions. The two reactions on oxygen isotopes were studied using solid targets and an array of silicon detectors while the (p,γ) reaction on ^{22}Ne required a windowless gas target and two HPGe detectors. Moreover, a feasibility test of the ^{2}H(p,γ)^{3}He reaction was performed, again with a gas target and an HPGe detector. The LUNA MV project was pursued in parallel to the LUNA activities and new developments were obtained.

1 The ^{17}O$(p,\alpha)^{14}$N reaction

The ^{17}O$(p,\alpha)^{14}$N reaction (Q = 1.2 MeV), is one of the reactions of the CNO cycle and it plays a key role in giant branch stars. ^{17}O is a stable oxygen isotope that is especially suited to

trace mixing processes in quiescent stars. These processes could explain the anomalous isotopic enrichments found in some pre-solar grains. An improved knowledge of the expected abundance of ^{17}O in these grains could improve the precision of current stellar models [1, 2]
The ^{17}O$(p, \alpha)^{14}$N reaction was studied in detail at the underground 400kV LUNA accelerator. At temperatures of astrophysical interest (0.03-0.4 GK), the reaction S-factor is dominated by two narrow resonances at roughly E_p = 70 and 193 keV in the laboratory frame. The latter is reasonably well-known [3, 4], but direct information on the 70 keV resonance is incomplete because of its extreme weakness [5]. Indirect methods have also been used [6], because of the challenges of performing a direct measurement. Such direct measurement was the final objective of a recently-completed experimental campaign at LUNA. The reduction in natural background afforded by the underground environment was expected to be decisive for the success of this campaign.

The E_p = 70 keV resonance (expected resonance strength of neV) was measured in thick-target yield conditions. We used solid Ta_2 O_5 targets, 95% enriched in ^{17} O and roughly 5 keV thick for 200 keV protons, produced as described in [7].
Protons were accelerated by the LUNA 400kV machine at typical beam currents of 100 μA and alpha particles produced by the reaction at E_{alpha}= 1 MeV were detected with an array of eight silicon detectors mounted in an hemi-spherical configuration as shown in Fig.1 (top). A small lead shielding was mounted around the setup, as show in Fig 1 (bottom) in order to further suppress the natural background.
In order to protect the detectors from the intense flux of elastically scattered protons, we mounted aluminised mylar foils, nominally 2.4 μm thick, in front of each detector.

The commissioning of the setup has been completed by studying the resonance strength of the 151 keV resonance in $^{18}O(p, \alpha)^{15}$N and of the 193 keV resonance in $^{17}O(p, \alpha)^{14}$N. Using the alpha peaks from these two resonances, we calibrated the detectors and measured very precisely the thickness of the foils.
The setup was indipendently simulated using two GEANT4-based simulations, with the primary aim of obtaining the efficiency. Both simulations highlighted the presence of a geometric shadow effect that reduced the efficiency of the four detectors mounted at 102.5^0 by 20% roughly. The overall efficiency of the setup was estimated to be around 15%.

Data acquisition for the 70 keV resonance in $^{17}O(p, \alpha)^{14}$N took several months of beamtime and hundreds of coulombs of charge on target.
We acquired data in three different conditions. We measured on-resonance (71.5 keV), where we expected the resonance signal to appear; off-resonance (65 keV), where we expected the signal from the reaction to be negligible but beam-induced background to be still present; and without beam to study natural background. We expected a very challenging experimental campaign since the overall rate had been estimated at a few alpha particles per hour and the detected energy (after the foils) at just 200 keV. Because of the difficulty in detecting a clear alpha peak, the constraints on the region of interest obtained from the measurement of the 193 keV resonance in the same reaction were extremely useful.

Data taking is complete: The signal from the 70 keV resonance in $^{17}O(p, \alpha)^{14}$N has been observed with an high statistical significance, but the status of the analysis is still preliminary to give a final result.

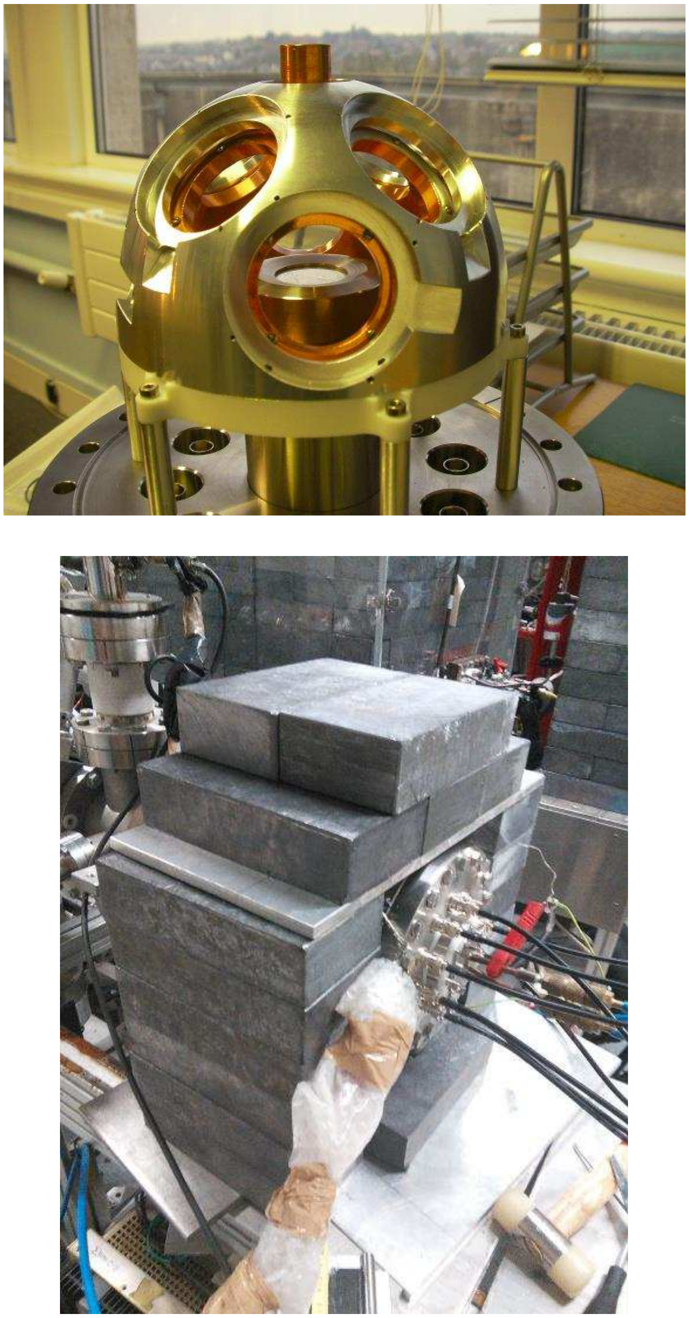

Figure 1: (top) A picture of the scattering chamber before mounting the detectors. The proton beam enters from the copper tube on the top. (bottom) The chamber mounted horizontally on the beamline and shielded with lead.

2 The ^{18}O$(p, \alpha)^{15}$N reaction

The ^{18}O$(p, \alpha)^{15}$N reaction (Q=3.98 MeV) plays a key role in giant branch stars for reasons that are very similar to those of the $^{17}O(p, \alpha)^{14}N$. ^{18}O, like ^{17}O, is especially suited to trace mixing processes in quiescent stars.[1, 2].
At temperatures of astrophysical interest, the ^{18}O$(p, \alpha)^{15}$N reaction is dominated by three resonances at $E_p = 20$, 151 and 650 keV in the laboratory frame [8]. The first of these resonances is extremely weak (resonance strength $\omega\gamma \sim 10^{-18}$ eV), and a direct investigation is beyond the current technical capabilities, even in an underground laboratory. The second, at E_p=151 keV, has already been investigated in detail during the ^{17}O$(p, \alpha)^{14}$N campaign and the last one, at E_p=650 keV is out of the reach of the LUNA-400kV accelerator.

There are, however, still a few open questions about this reaction. First of all there is a resonance at E_p=96 keV which has been considered of secondary astrophysical importance until now. A recent paper [9] highlighted some inconsistencies between the partial widths measured for this resonance in ^{18}O$(p, \alpha)^{15}$N and ^{18}O$(p, \gamma)^{19}$F. Some of the proposed solutions to these inconsistencies, including a different resonant energy, could potentially translate into a significantly higher astrophysical impact.
Secondly, the current claim in the literature [10, 11] is that the non-resonant process of this reaction is completely negligible at all energies. While this is true at energies above 100 keV, where precise, direct data exist, it might not be correct below the 96 keV resonance where the uncertainties are significantly higher. If the non-resonant process neglected in R-matrix fits until now did play a significant role, the ^{18}O$(p, \alpha)^{15}$N reaction rate could be enhanced at temperatures of astrophysical interest.
Finally, there are no direct data at all below E_p=70 keV while they could be extremely useful to constrain extrapolations from higher energies down to the astrophysically relevant energy region.

The campaign was carried out using the same setup and techniques previously employed for the ^{17}O$(p, \alpha)^{14}$N measurement, in order to capitalise on the experience gained during that campaign. The only significant difference in the setup was that the aluminised Mylar foils used to shield the silicon detectors from the elastically scattered protons were 5.5 μm thick instead of 2.2 μm. This change allowed us to reach proton energies of 360 keV without damaging the fragile detectors.
Data taking has already been completed, but data analysis is still at a preliminary stage. We measured the excitation function of the ^{18}O$(p, \alpha)^{15}$N reaction from $E_p = 60$ to 360 keV in 5 keV steps and observed the resonances at $E_p = 96$, 151, 217 and 334 keV reported in the literature [8]. All resonances were investigated in detail using a fine step size in thick-target yield conditions.

The next step in the data analysis process will be to extract a cross-section value for all measured energies and compare our direct data with extrapolations performed from higher energies [10, 11]. We also intend to carry out an R-matrix fit of our data to extrapolate our results to lower energies and improve the precision of the reaction rate in the astrophysically relevant region.

3 Study of the ^{22}Ne(p,γ)^{23}Na reaction

3.1 Science case

The ^{22}Ne(p,γ)^{23}Na reaction is included in the hydrogen burning neon-sodium (NeNa) cycle. This cycle affects the nucleosynthesis of neon and sodium isotopes, and it plays a key role in the study of the surface composition of Red Giant Branch stars (Gamow peak 30-100 keV), the composition of the ejecta from Asymptotic Giant Branch Stars and classical novae (Gamow peak 100-600 keV) [12] and possibly in the simmering phase prior to the explosion of a type Ia supernova [13].

The ^{22}Ne(p,γ)^{23}Na is the NeNa cycle reaction with the most uncertain cross section. In the energy range relevant for astrophysics, the ^{22}Ne(p,γ)^{23}Na reaction rate is poorly known because of the contribution of a large number of resonances, many of which have never been observed directly [14, 15]. The mere existence of several of these energy levels, e.g. the ones corresponding to the $E_p = 215$ and 104 keV resonances, is even doubted [16].

The lowest-energy resonance with a directly measured strength is the one at $E_p = 436$ keV [5]. For the resonances below that energy, only upper limits are reported in the literature [18, 19]. An experimental campaign structured in two phases is currently underway at LUNA in order to address this astrophysically relevant energy range.

3.2 Phase I (HPGe): Study of selected resonances with a HPGe detector

First phase of the data taking of the ^{22}Ne(p,γ)^{23}Na reaction with enriched neon-22 gas was concluded in fall 2014. Immediately afterwards, the setup was removed to make space for phase II. Several resonances have been observed for the first time during phase I of the experiment (fig. 2). Detailed branching schemes have been developed for several of the new resonances, and in two cases, even a coincidence analysis of the two HPGe detectors was possible. The comparison of the new LUNA data with previous, surface-based direct and indirect results impressively confirms the validity of the LUNA approach of direct, low-energy cross section measurements deep underground.

The final data analysis is still in progress, in view of a publication in 2015. The development of the setup and the study of several systematic effects have been published in a regular article in the European Physical Journal A [20].

3.3 Phase II (BGO): Direct capture and low-energy resonances with a BGO detector

In phase II of the experiment, a high-luminosity BGO borehole detector will be used in order to address several low-energy resonances and the direct capture component, as well (fig. 2). The typical γ-ray detection efficiency of 70% of this detector [21] will enable either a positive confirmation or a severe upper limit for the low-energy resonances that make up much of the discrepancy between the Iliadis and NACRE reaction rates (fig. 2).

Some systematic checks have already been completed for phase II. The pressure (fig. 3) and temperature profiles have been studied with neon gas in the new setup. For the first time, the pressure drop in the 4 cm long collimator where the beam enters the target chamber has been measured experimentally. The data confirm the previous assumption of a linear pressure drop but remove an uncertainty when computing the effective target thickness.

The data taking for phase II is expected to start in spring 2015.

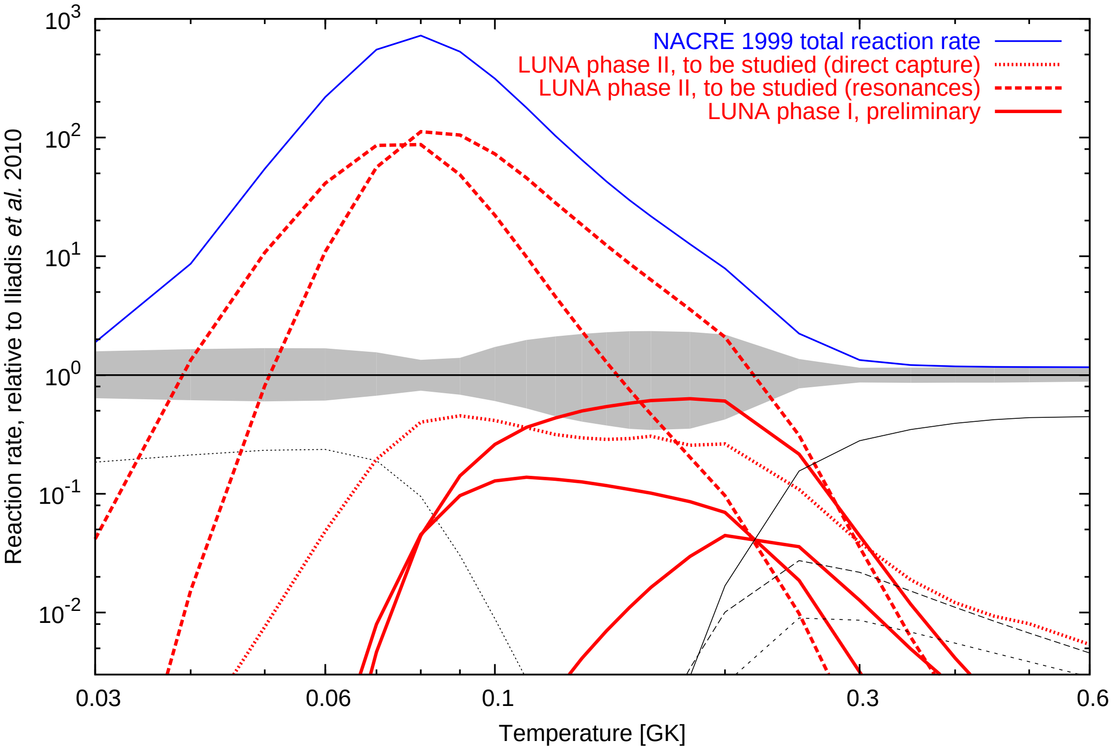

Figure 2: Thermonuclear reaction rate for the ^{22}Ne(p,γ)^{23}Na reaction, relative to the published rate by Iliadis *et al.* [15]. The reaction rate contributions of several of the new resonances discovered in phase I are plotted in red full lines. The contributions of some resonances to be studied in phase II is given in red dashed lines, direct capture as red dotted line. The previous rate of the NACRE compilation [14], which differs by up to a factor 1000 from Iliadis, is shown as blue line.

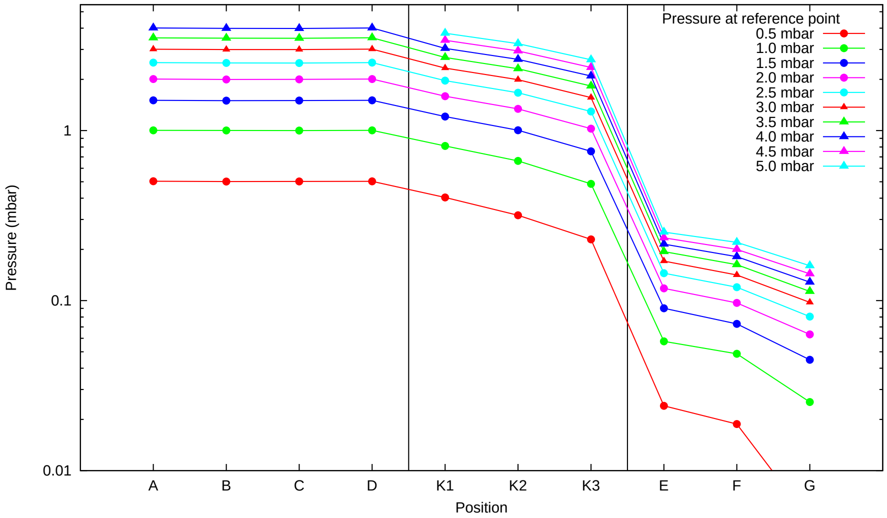

Figure 3: Pressure profile in the setup for phase II of the ^{22}Ne(p,γ)^{23}Na experiment. Positions A-D are inside the target chamber proper, K1-K3 inside the collimator tube at the target chamber entrance, and E-G in the tube connecting the target chamber to the first stage of the differential pumping system.

4 The ^{2}H(p,γ)^{3}He reaction

4.1 Introduction

Standard Big Bang Nucleosynthesis (BBN) started when the Universe was cold enough to allow deuterium nuclei to survive to photo-disintegration. The total amount of deuterium produced in the Universe during the first minutes depends on the cosmological parameters and on nuclear cross sections of the reactions involved. The former is independently inferred from Cosmic Microwave Background (CMB) power spectrum, recently measured by Planck [22], while the latter are measured by nuclear physics experiments [23]. For what concerns the deuterium abundance estimation, the main source of uncertainty comes from the ^{2}H(p,γ)^{3}He cross section [24]. The present experimental status was reviewed in [25], where a 6-10% uncertainty on the astrophysical S-factor in the BBN energy range is reported (see figure 4).

Starting from this value a primordial deuterium abundance of ^{2}H/H = $(2.65 \pm 0.07)\times 10^{-5}$ is obtained [24]. This one is in little tension with the value ^{2}H/H = $(2.53 \pm 0.04)\times 10^{-5}$, recently obtained analysing all the known astronomical deuterium absorption-line systems [31]. Comparing BBN calculation and astronomical observation it's clear that the first one is the more uncertain and a new precise measurement of the ^{2}H(p,γ)^{3}He cross section in the BBN energy range is thus necessary, as suggested by many authors [22],[24],[32],[33]. Moreover there is a disagreement of about 10% between the experimental S-factor [25] and the one obtained starting from ab-initio calculations [30][32][34][35]. In order to clarify the actual scenario, a measurement of the ^{2}H(p,γ)^{3}He cross section at the 3% level in the [40-400] keV energy range is planned at LUNA for the end of 2015 and the beginning of 2016. A preliminary investigation of the reaction has been done in October 2014, using a setup similar to the one used in the ^{22}Ne(p,γ)^{23}Na measurement campaign [36]. The ^{2}H(p,γ)^{3}He feasibility test results are discussed in the next paragraph.

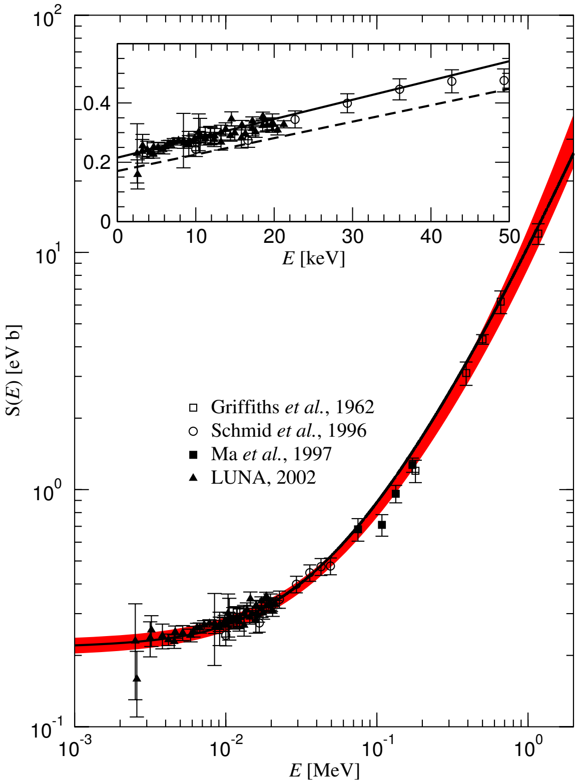

Figure 4: The astrophysical S-factor experimental data [26][27][28][29] together with theoretical ab-initio calculations [30] (solid line). The band represents the 68% lower and upper limits of the adopted quadratic best fit [25]

4.2 Feasibility test results

The experimental setup consists in a windowless gas target filled with deuterium at 0.3 mbar without recirculation. The gas target pressure, monitored with a Labview application, was maintained constant thanks to an analog feedback system. The beam current has been measured with a calibrated constant temperature gradient beam calorimeter. An oxygen-free copper endcap was mounted on the calorimeter in order to reduce possible contaminants present on the calorimeter surface. A 136% High Purity Germanium detector (HPGe) at 90° with respect to the beam direction detects the γ-rays emitted. Its efficiency has been measured with a ^{60}Co (1173, 1333 keV gamma peak energies) and ^{137}Cs (662 keV) radioactive sources. Unfortunately, no data point had been taken at higher energies (using for example the ^{14}N(p,γ)^{15}O reaction) due to problems with the LUNA 400 kV accelerator. This did not allow to obtain an experimental estimation of the total efficiency for the ^{2}H(p,γ)^{3}He reaction, where the γ-ray Region of Interest (RoI) is around 5.5 MeV. No lead castle and anti-radon box were present. The natural background has been found stable within 17% and completely negligible in the ^{2}H(p,γ)^{3}He RoI. We measured the ^{2}H(p,γ)^{3}He reaction at five different proton beam energies: 112.5 keV, 199.5 keV, 259.5 keV, 340.0 keV and 380.0 keV with an average current of about 150 μA (see figure 5).

The only contaminants found during the feasibility test are ^{19}F and ^{12}C. The first one gives the main contribution, expecially at high energy where the strong resonance of the ^{19}F(p,$\alpha\gamma$)^{16}O

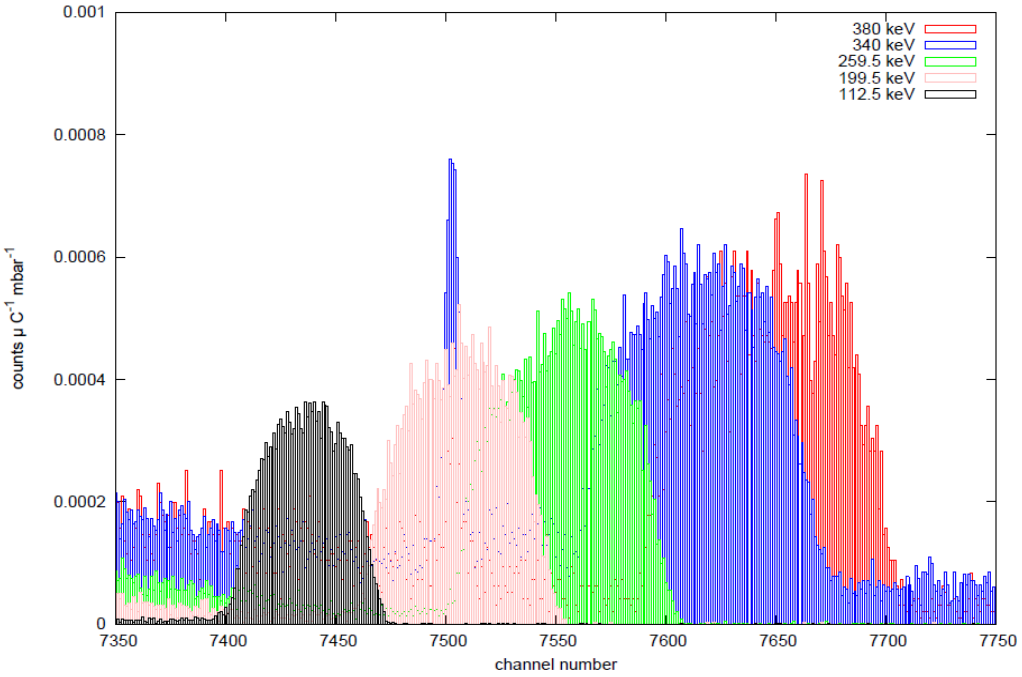

Figure 5: The ^{2}H(p,γ)^{3}He counting rate taken at LUNA during the 2014 feasibility test phase. The ^{2}H(p,γ)^{3}He peak is broad due to the Doppler effect of the emitted gammas and the recoil of the ^{3}He nuclei. Its width depends on the setup geometry. The narrow peak at 6.1 MeV for the 380 keV run is due to the ^{19}F(p,$\alpha\gamma$)^{16}O reaction on fluorine contaminant.

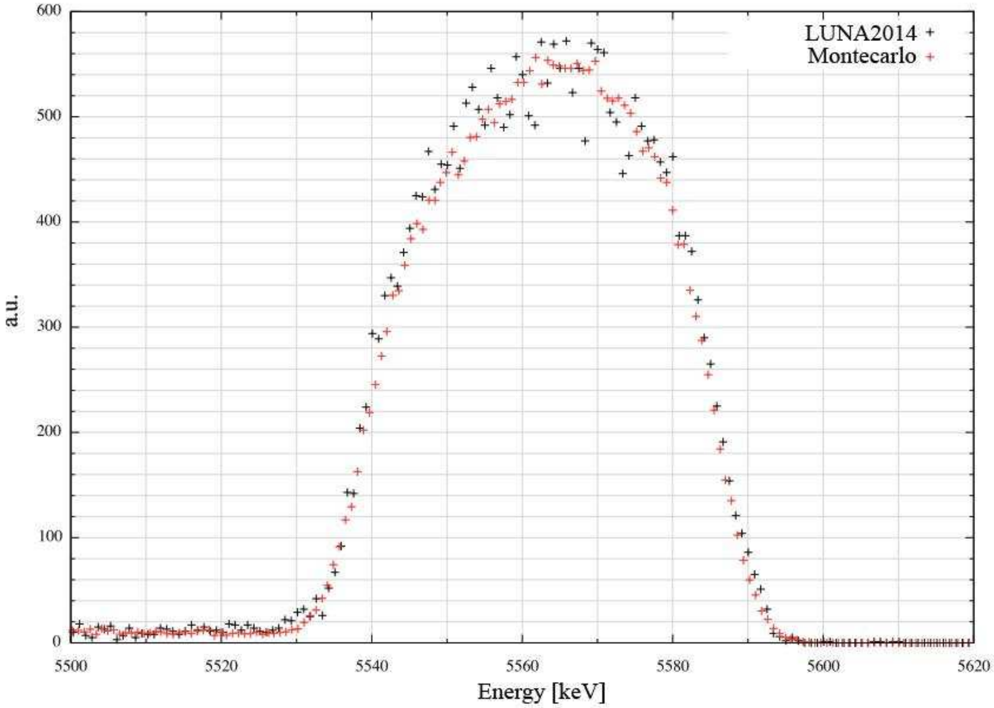

Figure 6: Overlap between the Montecarlo simulation of the ^{2}H(p,γ)^{3}He signal based on the ab-initio calculations of the differential cross section at 112.5 keV beam energy (red) and experimental data (black).

reaction at 380 keV is present. No deuterium implantation on the gas target inner surface has been found during the measurement campaign. The shape of the ^{2}H(p,γ)^{3}He has been found in agreement with the one calculated by Montecarlo simulations and reported in figure 6.

4.3 Conclusions

The feasibility test shows that a precise measurement of the ^{2}H(p,γ)^{3}He cross section is possible at LUNA. Moreover, most of the systematics have been considered and checked. Thanks to the results obtained we are now able to proceed in the design of the new setups that will be used for the 2015-2016 measurement campaigns.

5 LUNA-MV

The LUNA-MV project foresees the realization of a worldwide unique facility inside the underground Gran Sasso Laboratory centered on a 3.5 MV single-ended accelerator able to provide intense proton, alpha and carbon beams. Two different beam lines are foreseen, devoted to solid and gas target experiments, respectively. This will allow us to study key reactions of the Hydrogen, Helium and Carbon burning and the so-called neutron source reactions, which provide the neutron flux necessary for the slow neutron capture process. The project has been financed in the framework of the "Progetti Premiali" calls of the Italian Research Ministry (years 2011 and 2012) with a total budget of about 5.3 millions of euros. In the year 2014, the precise location of the LUNA MV accelerator inside LNGS was established: it will occupy the South part of Hall C, where presently the OPERA experiment is sitting. The characteristics of the accelerator have been studied in detail and the documentation for tendering has been recently submitted to the INFN central administration. Meanwhile, the design of the infrastructure is going on. The present preliminary schedule foresees the installation of the accelerator at LNGS by summer 2018.

References

[1] M. Lugaro et al., A&A 461 (2007) 657

[2] S. Palmerini et al., ApJ. 764 (2013) 128

[3] A. Chafa et al., Phys. Rev. Lett. 95 (2005) 031101

[4] B.H. Moazen, Pys. Rev. C 75 (2007) 065801

[5] C. Angulo et al., Nucl. Phys. A 656 (1999) 3-183 [9]

[6] M.L. Sergi et al., Phys. Rev. C 82 (2010) 032881

[7] A. Caciolli et al., Eur. Phys. J. A 48 (2012) 144

[8] H. Lorenz-Wirzba et al., Nuc. Phys. A 313 (1979) 346

[9] T. Fortune, Phys. Rev. C 88 (2013) 015801

[10] C. Iliadis et al., Nuc. Phys. A 841 (2010) 31-250

[11] M. La Cognata et al., ApJ. 723 (2010) 1512

[12] C. Iliadis, A. Champagne, J. José, S. Starrfield, and P. Tupper, Astrophys. J. Suppl. Ser. **142**, 105 (2002).

[13] D. A. Chamulak, E. F. Brown, F. X. Timmes, and K. Dupczak, Astrophys. J. **677**, 160 (2008), 0801.1643.

[14] C. Angulo *et al.*, Nucl. Phys. A **656**, 3 (1999).

[15] C. Iliadis, R. Longland, A. E. Champagne, and A. Coc, Nucl. Phys. A **841**, 251 (2010).

[16] R. B. Firestone, Nucl. Data Sheets **108**, 1 (2007).

[17] R. Longland *et al.*, Phys. Rev. C **81**, 055804 (2010).

[18] J. Görres, C. Rolfs, P. Schmalbrock, H. P. Trautvetter, and J. Keinonen, Nucl. Phys. A **385**, 57 (1982).

[19] J. Görres *et al.*, Nucl. Phys. A **408**, 372 (1983).

[20] F. Cavanna *et al.*, Eur. Phys. J. A **50**, 179 (2014), 1411.2888.

[21] C. Casella *et al.*, Nucl. Inst. Meth. A **489**, 160 (2002).

[22] P. A. R. Ade et al. (Planck collaboration), arXiv:1502.01589v2 [astro-ph.CO] (2015)

[23] P. D. Serpico et al., JCAP12 (2004) 010

[24] E. Di Valentino et al., Phys. Rev. D 90 (2014) 023543

[25] E. G. Adelberger et al., Rev. Mod. Phys. 83 (2011) 195

[26] Griffiths et al., Can. J. Phys. 40 (1962) 402

[27] G. J. Schmid et al., Phys. Rev. Lett. 76 (1996) 3088

[28] L. Ma et al., Phys. Rev. C 55 (1997) 588

[29] C. Casella et al., Nucl. Phys. A706 (2002) 203

[30] L. E. Marcucci et al., Phys. Rev. C 72 (2005) 014001

[31] R. Cooke et al., Astrophys. J. 781, 31 (2014)

[32] K. M. Nollett and G.P. Holder, arXiv:1112.2683v1 [astro-ph.CO] (2011)

[33] N. Saviano et al., Phys. Rev. D 90 (2014) 113009

[34] M. Viviani et al., Phys. Rev. C 61 (2000) 064001

[35] L. E. Marcucci et al., Nucl. Phys. A777 (2006) 111

[36] M. Aliotta et al. (LUNA collaboration), LNGS Annual Report 2013

6 List of Publications

- *"Underground study of the $^{17}O(p,\gamma)^{18}F$ reaction relevant for explosive hydrogen burning"*, A. Di Leva, D. A. Scott, A. Caciolli, A. Formicola, F. Strieder, M. Aliotta, M. Anders, D. Bemmerer, C. Broggini, P. Corvisiero, Z. Elekes, Zs. Fulop, G. Gervino, A. Guglielmetti, C. Gustavino, Gy. Gyurky, G. Imbriani, J. Jose, M. Junker, M. Laubenstein, R. Menegazzo, E. Napolitani, P. Prati, V. Rigato, V. Roca, E. Somorjai, C. Salvo, O. Straniero, T. Szucs, F. Terrasi, and D. Trezzi
  Phys. Rev. C 89 (2014) 015803

- *"First Direct Measurement of the $^{2}H(\alpha,\gamma)^{6}Li$ Cross Section at Big Bang Energies and the Primordial Lithium Problem"*,
  M. Anders, D. Trezzi, R. Menegazzo, M. Aliotta, A. Bellini, D. Bemmerer, C. Broggini, A. Caciolli, P. Corvisiero, H. Costantini, T. Davinson, Z. Elekes1, M. Erhard, A. Formicola, Zs. Fulop, G. Gervino, A. Guglielmetti, C. Gustavino1a, Gy. Gyurky, M. Junker, A. Lemut, M. Marta, C. Mazzocchi, P. Prati, C. Rossi Alvarez, D. A. Scott, E. Somorjai, O. Straniero, and T. Szucs
  Phys. Rev. Lett. 113 (2014) 042501

- *"A new study of the $^{22}Ne(p,\gamma)^{23}Na$ reaction deep underground: Feasibility, setup, and first observation of the 186 keV resonance"*,
  F. Cavanna, R. Depalo, M. -L. Menzel, M. Aliotta, M. Anders, D. Bemmerer, C. Broggini, C. G. Bruno, A. Caciolli, P. Corvisiero, T. Davinson, A. di Leva, Z. Elekes, F. Ferraro, A. Formicola, Zs. Fulop, G. Gervino, A. Guglielmetti, C. Gustavino, Gy. Gyurky, G. Imbriani, M. Junker, R. Menegazzo, P. Prati, C. Rossi Alvarez, D. A. Scott, E. Somorjai, O. Straniero, F. Strieder, T. Szucs, D. Trezzi
  Eur. Phys. J. A 50 (2014) 179

- *"Underground study of the $^{17}O(p,\gamma)^{18}F$ reaction at Gamow energies for classical novae"*
  D. Scott
  PhD thesis, The University of Edinburgh

- *"First test on the $^{22}Ne(p,\gamma)^{23}Na$ reaction at LUNA"*
  F. Cavanna
  EPJ Web of Conferences 66 (2014) 07004

- *"Cross-section measurements at astrophysically relevant energies: The LUNA experiment"*
  A. Formicola et al.
  NIM A 258 (2014) 742

- *"Exploring the $^{22}Ne(p,\gamma)^{23}Na$ reaction at LUNA and at HZDR"*
  F. Cavanna
  AIP Conf. Proc., 1595 (2014) 251

- *"Low-energy resonances in the $^{22}Ne(p,\gamma)^{23}Na$ reaction directly observed at LUNA"*
  F. Cavanna and R. Depalo
  submitted to EPJ Web of Conferences

- *"Low-energy resonances in the $^{22}Ne(p,\gamma)^{23}Na$ reaction directly observed at LUNA"*
  R. Depalo
  submitted to Proceedings of Science (NIC XIII) 087

- *"Studying stars by going underground. The LUNA experiment at Gran Sasso Laboratory"*
  A. Caciolli
  Acta Physica Polonica B 45 (2014) 137

- *"Origin and Status of LUNA at Gran Sasso"*
  C. Broggini
  Proceedings of the International Symposium on Subnuclear Physics: Past, Present and Future, Pontificiae Academiae Scientiarum Scripta Varia 119, Vatican City 2014

- *"LUNA: Nuclear Astrophysics Underground"*
  A. Best
  Exotic Nuclei and Nuclear Particle Astrophysics (V). From Nuclei to Stars, 2014

- *"A direct underground measurement of the $^{17}O(p,\alpha)^{14}N$ reaction cross-section at energies of astrophysical interest"*
  C. Bruno
  AIP Conference Proceedings 258 (2014) 1595

- *"The LUNA experiment at Gran Sasso Laboratory"*
  A. Guglielmetti
  EPJ web of conference 78 (2014) 07001

- *"The LUNA-MV Project at Gran Sasso Underground Laboratory"*
  A. Guglielmetti
  Nuclear Physics News 24:1 (2014) 40

- *"Nuclear astrophysics and underground accelerators"*
  A. Guglielmetti
  Physics of the Dark Universe 4 (2014) 10

- *"Studying stars by going underground: the LUNA experiment at Gran Sasso Laboratory"*
  A. Guglielmetti
  EPJ web of conference 66 (2014), 07007

- *"Neutrinos, BBN and Nuclear Astrophysics"*
  C. Gustavino
  Proceedings of Science (Bormio 2014) 050

- *"Neutrinos and Nuclear Astrophysics at LUNA"*
  C. Gustavino
  to be published in Nuclear Physics B - Proceedings Supplements

- *"BBN, neutrinos and Nuclear Astrophysics"*
  C. Gustavino
  Frascati Physics Series Vol. 58 (2014)

- *"The $^{2}H(\alpha,\gamma)^{6}Li$ experiment at LUNA"*
  C. Gustavino
  EPJ web of conference 66 (2014), 07009

- *"Probing nuclear rates with Planck and BICEP2"*
  E. Di Valentino, C. Gustavino, J. Lesgourgues, G. Mangano, A. Melchiorri, G. Miele, and

O. Pisanti
Phys.Rev. D 90 (2014) 023543

- *"First direct measurement of the $^{2}H(\alpha,\gamma)^{6}Li$ cross section at Big Bang energies*
  D. Trezzi
  Proceedings of Science (Bormio 2014) 020

7 Conference and seminar contributions

- F. Cavanna,"Exploring the ^{22}Ne(p,γ)^{23}Na reaction at LUNA and at HZDR", talk at 11th Russbach School on Nuclear Astrophysics, Russbach (Austria) 09-15.03.2014
- F. Cavanna,"Low-energy resonances in the ^{22}Ne(p,γ)^{23}Na reaction directly observed at LUNA", talk at Fifteenth International Symposium on Capture Gamma-Ray Spectroscopy and Related Topics (CGS15), Dresden (Germany) 25-29.08.2014
- R. Depalo,"Low-energy resonances in the ^{22}Ne(p,γ)^{23}Na reaction directly observed at LUNA", poster at International Conference on Nuclei in the Cosmos XIII, Debrecen (Hungary) 07-11.07.2014 - EPL prize winner
- R. Depalo,"Low-energy resonances in the ^{22}Ne(p,γ)^{23}Na reaction directly observed at LUNA", talk at International School of Nuclear Physics, Erice (Italy) 16-24.09.2014
- R. Depalo,"Low-energy resonances in the ^{22}Ne(p,γ)^{23}Na reaction directly observed at LUNA", invited seminar at Dipartimento di Fisica e Astronomia dell'Università degli Studi di Padova, Padua (Italy) 22.10.2014
- C. Broggini,"LUNA: from Sun to Novae and beyond", invited talk at Vulcano Workshop 2014-Frontier Objects in Astrophysics and Particle Physics, Vulcano (Italy) 18-24.05.2014
- C. Broggini,"LUNA: from the sun to novae and beyond", invited talk at International School of Nuclear Physics, Erice (Italy) 16-24.09.2014
- M. Aliotta,"Underground Laboratories for Nuclear Astrophysics: Present Status and Future Opportunities", invited talk at International Conference on Nuclei in the Cosmos XIII, Debrecen (Hungary) 07-11.07.2014
- T. Szucs,"Underground nuclear astrophysics", invited lecture at Helmholtz International Summer School nuclear theory and astrophysical applications, Dubna (Russia) 21.07-01.08-2014
- A. Best,"LUNA: Nuclear Astrophysics Underground", invited talk at Carpathian Summer School of Physics 2014, Sinaia (Romania) 13-26.07.2014
- C. Bruno,"Direct measurement of the ^{17}O(p,α)^{14}N reaction at energies of astrophysical interest", talk at International Conference on Nuclei in the Cosmos XIII, Debrecen (Hungary) 07-11.07.2014
- C. Bruno,"A direct underground study of the ^{17}O(p,α)^{14}N reaction at energies of astrophysical interest", talk at 11th Russbach School on Nuclear Astrophysics, Russbach (Austria) 09-15.03.2014

- A. Guglielmetti,“The LUNA experiment at Gran Sasso Laboratory: studying stars by going underground”, invited seminar at University of Edinburgh, Edinburgh (UK) 17.10.2014

- A. Guglielmetti,“L’esperimento LUNA ai Laboratori del Gran Sasso: studiare le stelle da sotto una montagna”, invited seminar at Università degli Studi di Bari, Bari (Italy) 02.12.2014

- R. Menegazzo,“The Luna-MV project, an underground facility for nuclear astrophysics measurements”, seminar at CSNSM, Orsay (France) 08.07.2014

- R. Menegazzo,“The LUNA - MV project at the Gran Sasso Laboratory”, invited lecture at 3rd Andromde Workshop, IPN, Orsay (France) 09.07.2014

- A. Caciolli,“Future study of ^{13}C(α,n)^{16}O and ^{22}Ne(α,n)^{25}Mg at LUNA”, talk at NEDENSAA NuPNET Collaboration Meeting 2014, Istanbul (Turkye) 10-12.09.2014

- A. Caciolli,“Underground nuclear astrophysics”, talk at LEA COLLIGA and LEA COPIGAL workshop, Paris (France) 07-10.01.2014

- A. Caciolli,“^{18}O hydrogen burning at the energies of classical nova at LUNA”, talk at International Conference on Nuclei in the Cosmos XIII, Debrecen (Hungary) 07-11.07.2014

- A. Di Leva,“Astrophysical S-factor for the ^{17}O(p,γ)^{18}F reaction at Nova energy”, invited talk at “Classical Novae in the Cosmos” workshop, Debrecen (Hungary) 05-06.07.2014

- A. Formicola,“Underground cross section measurements of stellar reactions at astrophysically relevant energies”, invited talk at Fifteenth International Symposium on Capture Gamma-Ray Spectroscopy and Related Topics (CGS15), Dresden (Germany) 25-29.08.2014

- M. Junker,“The Future of Nuclear Astrophysics at LUNA”, invited talk at Fifteenth International Symposium on Capture Gamma-Ray Spectroscopy and Related Topics (CGS15), Dresden (Germany) 25-29.08.2014

- G. Imbriani,“Stellar burning phases: experiments - Overview”, invited talk at ATHENA Brussels Workshop on Astrophysics, Brussels (Belgium) 27-28.01.2014

- C. Gustavino,“Neutrinos, BBN and Nuclear Astrophysics”, talk at 52nd International Winter Meeting on Nuclear Physics, Bormio (Italy) 26-30.01.2014

- C. Gustavino,“LUNA results at BBN energies”, invited talk at Electron-Nucleus Scattering XIII, Marciana Marina (Italy) 23-27.06.2014

- C. Gustavino,“Neutrinos and Nuclear Astrophysics at LUNA”, talk at 37th International Conference on High Energy Physics (ICHEP), Valencia (Spain) 02-09.07.2014

- C. Gustavino,“BBN, neutrinos and Nuclear Astrophysics”, invited talk at “Frontier Objects in Astrophysics and Particle Physics”, Vulcano (Italy) 18-24.05.2014

- C. Gustavino,“LUNA400 e LUNA-MV”, talk at What Next LNGS: Prospettive per il ruolo scientifico dei LNGS, L’Aquila (Italy) 15-16.10.2014

- D. Trezzi,“Is the second lithium problem still unsolved?” invited talk at Unsolved Problems in Astrophysics and Cosmology, Budapest (Hungary) 29.06-05.07.2014

- D. Trezzi,“First direct measurement of the ^{2}H(α,γ)^{6}Li cross section at Big Bang energies”, poster at 52nd International Winter Meeting on Nuclear Physics, Bormio (Italy) 27-31.01.2014 - Best poster prize winner
- D. Trezzi,“First direct measurement of the ^{2}H(α,γ)^{6}Li cross section at Big Bang energies at LUNA”, poster at International Conference on Nuclei in the Cosmos XIII, Debrecen (Hungary), 7-11.07.2014
- D. Bemmerer, “Underground nuclear astrophysics in Europe: a status update”, group report at Frühjahrstagung der Deutschen Physikalischen Gesellschaft, Frankfurt am Main (Germany) 17-21.03.2014

2014 LVD STATUS REPORT

The LVD Collaboration

N.Yu.Agafonova[7], M.Aglietta[8], P.Antonioli[1], V.V.Ashikhmin[7], G.Badino[8], G.Bari[1], R.Bertoni[8], E.Bressan[1], G.Bruno[5], V.L.Dadykin[7], E.A.Dobrynina[7], R.I.Enikeev[7], W.Fulgione[8], P.Galeotti[8], M.Garbini[1], P.L.Ghia[2], P.Giusti[1], F.Gomez[8], E.Kemp[3], V.B.Korchaguin[7], A.S.Mal'gin[7], B.Miguez[3], A.Molinario[8], R.Persiani[1], I.A.Pless[6], A.Romero[8], V.G.Ryasny[7], O.G.Ryazhskaya[7], O.Saavedra[8], G.Sartorelli[1], M.Selvi[1], I.R.Shakiryanova[7], G.C.Trinchero[8], M.Ventura[4], C.Vigorito[8], V.F.Yakushev[7], A.Zichichi[1]

[1] *University of Bologna and INFN-Bologna, Italy*
[2] *CNRS-IN2P3, Paris, France*
[3] *University of Campinas, Campinas, Brazil*
[4] *INFN-LNF, Frascati, Italy*
[5] *INFN-LNGS, Assergi, Italy*
[6] *Massachusetts Institute of Technology, Cambridge, USA*
[7] *Institute for Nuclear Research, Russian Academy of Sciences, Moscow, Russia*
[8] *INFN-Torino, INAF-OATO, Torino and University of Torino, Italy*

Abstract

The Large Volume Detector (LVD) in the INFN Gran Sasso National Laboratory, Italy, is a neutrino observatory designed to study low energy neutrinos from core collapse supernovae. The experiment has been monitoring the Galaxy since June 1992, under increasing larger configurations, in January 2001 it has reached its present active mass $M = 1$ kt. Since July 2005 has been member of the Supernovae Early Warning System (SNEWS) project, the network of neutrino observatories whose aim is to provide the astronomical community with a prompt ad confident alert of the occurrence of a galactic supernova event.

Since 2006 LVD has been acting as a far-monitor of the CNGS project, the high energy, wide band ν_μ beam, set up at Cern and sent towards the INFN Gran Sasso National Laboratory, for the observation of the ν_τ appearance, through neutrino flavor oscillation. In 2012 LVD gave a primary contribution to establish the inconsistency of the OPERA result of a superluminal neutrino velocity and furthermore confirmed that the neutrino speed is compatible with c.

No neutrino burst candidate has been found over 7700 days of live-time, the resulting 90% C.L. upper limit to the rate of gravitational stellar collapses in the Galaxy ($D \leq 25$ kpc) is 0.109 yr^{-1}.

1 Introduction

The detection of neutrinos from SN1987A, first observation of neutrinos from extrasolar origin, marked the beginning of the experimental phase of neutrino astrophysics [Hirata et al.(1987), Bionta et al.(1987), Alekseev et al.(1987)] and [Aglietta et al.(1987)]. Core collapse supernovae are the known most powerful neutrino emitters. While the observation of neutrinos from SN1987A was guided by the optical observation, currently running ν detectors must be able to identify a neutrino burst even in the absence of an electromagnetic counterpart. Neutrinos can actually travel across our Galaxy and reach the Earth were they can be identified, while light gets partially or totally absorbed by dust in the Galactic plane. As the great part (~ 80 %) of core collapse supernovae in our Galaxy are not visible through their light emission, neutrino detection is in many cases the only possibility to detect and study these events.

Neutrino detectors are also sensitive to collapsing objects that fail to explode becoming black holes (so-called failed supernovae), as those are expected to emit a neutrino signal even stronger, although shorter in time, than core collapse supernovae [Nakazato et al.(2008)].

In the presence of an electromagnetic counterpart, on the other hand, the prompt identification of the neutrino signal could alert the worldwide network of observatories [Antonioli et al.(2004)] allowing to study many aspects of the rare event from its onset.

Previous direct searches of supernova neutrino bursts from our Galaxy have given null results [Dye et al.(1989)]; [Ahrens et al.(2002)]; [Alekseev & Alexeyeva (2002)]; [Ambrosio et al.(2004)]; [Novoseltseva et al.(2011)]. The Super-Kamiokande Collaboration set an upper limit at 90% c.l. for the supernova explosion rate out to 100 kpc of 0.32 per year [Ikeda et al.(2007)].

The Large Volume Detector (LVD), in the INFN Gran Sasso National Laboratory (Italy), at the depth of 3600 m of water equivalent, is a one kiloton liquid scintillator detector [Aglietta et al.(1992)]. It consists of an array of 840 scintillator counters, 1.5 m^3 each, viewed from the top by three photomultipliers (PMTs), 2520 in total, arranged in 105 modules hosting clusters of 8 counters. The whole array is divided in three identical towers with independent power supplies, trigger, absolute clock and data acquisition, DAQ.

LVD started the commissioning phase in February 1992 for five months till June 1992, mainly dedicated to stabilize the DAQ system. Since June 6^{th} 1992, with the first tower completely built, the detector started the first science run. The experiment has been running under increasing larger configurations since then and in January 2001, with the completion of the last tower, it reached its final layout: the scintillator mass of one kton. Thanks to its modularity and dedicated DAQ system LVD allows a very high duty cycle. It can be serviced during data taking and in case of failures, the neutrino observatory automatically remove the not properly working region and reconfigures itself at lower mass. The effect is to adjust dynamically the LVD active mass, M_{act}.

Neutrinos can be detected in LVD through charged current (CC) and neutral current (NC) interactions on proton, Carbon nuclei and electrons of the liquid scintillator. The iron support structure of the detector, whose total mass is about 0.85 kt can also act as a target for neutrinos and antineutrinos, with a certain probability that the product of the interaction may reach the liquid scintillator and be detected [Agafonova et al.(2007-a)]. The total LVD target consists of:
free protons - 8.313×10^{31}
C nuclei - 4.267×10^{31}
Fe nuclei - 9.7×10^{30}
electrons - 3.393×10^{32}
Neutrino interaction channels, relevant to the detector, are reported here:

$$\bar{\nu}_{\mathrm{e}} + \mathrm{p} \rightarrow \mathrm{e}^{+} + \mathrm{n} \qquad (1.8\ \mathrm{MeV}) \quad (88\%) \tag{1}$$

$$\nu_{\mathrm{e}} +^{12}\mathrm{C} \rightarrow^{12}\mathrm{N} + e^{-} \qquad (17.3\ \mathrm{MeV}) \quad (1.5\%) \tag{2}$$

$$\bar{\nu}_{\mathrm{e}} +^{12}\mathrm{C} \rightarrow^{12}\mathrm{B} + e^{+} \qquad (14.4\ \mathrm{MeV}) \quad (1.0\%) \tag{3}$$

$$\nu_{\mathrm{i}} +^{12}\mathrm{C} \rightarrow \nu_{\mathrm{i}} +^{12}\mathrm{C}^{*} + \gamma \qquad (15.1\ \mathrm{MeV}) \quad (2.0\%) \tag{4}$$

$$\nu_{\mathrm{i}} + e^{-} \rightarrow \nu_{\mathrm{i}} + e^{-} \qquad (-) \quad (3.0\%) \tag{5}$$

$$\nu_{\mathrm{e}} +^{56}\mathrm{Fe} \rightarrow^{56}\mathrm{Co}^{*} + e^{-} \qquad (10.\ \mathrm{MeV}) \quad (3.0\%) \tag{6}$$

$$\bar{\nu}_{\mathrm{e}} +^{56}\mathrm{Fe} \rightarrow^{56}\mathrm{Mn} + e^{+} \qquad (12.5\ \mathrm{MeV}) \quad (0.5\%) \tag{7}$$

$$\nu_{\mathrm{i}} +^{56}\mathrm{Fe} \rightarrow \nu_{\mathrm{i}} +^{56}\mathrm{Fe}^{*} + \gamma \qquad (15.\ \mathrm{MeV}) \quad (2.0\%) \tag{8}$$

Cross sections of different interactions are obtained referring to [Strumia & Vissani(2010)] for interaction 1, [Fukugita et al.(1988)] for interactions 2 and 4, [Bahcall et al.(1995)] for interaction 5 and [Kolbe & Langanke(2001)] and [Toivanen et al.(2001)] for interactions 6 and 8.
The main neutrino reaction in hydrogenate targets, at the typical energy of neutrino from gravitational stellar collapses (GSC), is the inverse beta decay, IBD, (1) which gives two detectable signals: the prompt one due to the e^{+} (visible energy $E_{\mathrm{vis}} \simeq E_{\bar{\nu}_{\mathrm{e}}} - 1.8$ MeV + 2 $\mathrm{m_e c^2}$) followed by the signal from the $\mathrm{np} \rightarrow \mathrm{d}\gamma$ capture ($E_{\gamma} = 2.2$ MeV, mean capture time $\simeq 185\ \mu$s).

At present a universally accepted model of neutrino emission associated with GSC does not exist. This is due to the great complexity of the problem, in which all known forces interplay with each other in extreme physical conditions. The critical role of neutrinos for the energy transport, as first suggested in [Colgate & White(1966)], is however generally accepted. A few other points are nowadays well established. The total energy of the collapse, the binding energy of the future neutron star, is between 2 and 3 $\cdot 10^{53}$ erg, and 99% of this is delivered by neutrino emission. The formation of a region where neutrinos are trapped determines the time scale of this emission, as confirmed by the observation of neutrino from SN1987A, of the order of ten seconds.

There has been a wide discussion whether SN1987A data show an hint of the presence of an accretion phase, which would occur in the first stage of neutrino emission. Important reference in this discussion is the paper by Loredo and Lamb [Loredo & Lamb(2002)] where it is argued that the SN1987A observations can be used to claim for an evidence of the accretion phase.

The neutrino-driven mechanism [Bethe & Wilson(1985)], or delayed scenario for the explosion, has been the most studied so far. In this scenario the explosion of the massive star receives crucial assistance from the energy deposition due to an initial, intense neutrino luminosity. Simulations based on this model have given different estimations of mean energies and luminosity of neutrino emission. In particular early one-dimensional simulations gave quite different results for the mean energies of various neutrino flavors (10-12 MeV for ν_e, 11-17 MeV for $\bar{\nu}_e$, 15-24 MeV for ν_μ,$\bar{\nu}_\mu$, ν_τ,$\bar{\nu}_\tau$, hereafter ν_x) [Totani et al.(1998)]. However, recent studies [Tamborra et al.(2012)], [Janka(2012)] show a tendency towards lower values for the mean energies as well as a smaller spread among them. It should be noted though that models, assuming a quite different scenario, have been proposed enlarging the theoretical panorama [Imshennik & Ryazhskaya(2004)].

A parallel approach to this problem is the attempt to parameterize the neutrino emission, of which a remarkable example can be found in [Keil et al.(2003)]. Another work [Pagliaroli et al.(2009)] considers the microscopic processes of the collapse to build a parameterization of the neutrino emission, which comprehends both an accretion and a cooling phase. The free parameters are then determined with a maximum likelihood procedure on the data from SN1987A.

We refer to this study for an estimation of the neutrino signal from a GSC in LVD. MSW effect while crossing the matter of the collapsing star [Wolfenstein(1978)], [Mikheev & Smirnov(1985)] is taken into account, while ν-ν interactions are neglected. The normal mass hierarchy scenario has been assumed together with the most recent values of θ_{12} and mass squared differences Δm^2_{12} and Δm^2_{23}. In this scenario the recent discovery of a non null value for θ_{13} mixing angle [An et al.(2012)] has no significant impact on the expected neutrino signal. We find that a total of about 300 events would be detected in LVD (1kt) for a GSC at 10 kpc from the Earth. They would be shared among the possible interaction channels as shown in the previous table. Focusing on the Inverse Beta Decay (IBD) interaction (1), it results that 250 of these signals would be recorded (and recognized) in LVD, which is quite on the conservative side. The neutrino signal is expected to develop on a time scale of 20 s, being 90% (50%) the fraction of detected events in the first 10s (1s).

The LVD neutrino burst sensitivity for different selection algorithms and energy cuts, E_{cut}, has been exhaustively discussed in [Agafonova et al.(2008)] for real background conditions. The highest sensitivity can be achieved, in LVD, for E_{cut} = 10MeV, Δt=10 seconds and without any additional selection criterium based on the expected neutrino flavor content. Different choices on the duration of the time interval Δt, based on model predictions, and supported by the SN1987A data, increase the model dependence of the search without introducing an important improvement in sensitivity.

LVD working stand alone, with an imitation frequency threshold, F_{im}, of one fake event every 100 years, reaches the sensitivity shown in figure 1, calculated for $E_{cut} = 10$ MeV and for $300 \leq M_{act} \leq 1000$ ton. Even in this very conservative panorama, LVD results to be observing, with full efficiency, a region of space centered in the Earth with radius 25 kpc as long as its active mass remains greater than 300 tons.

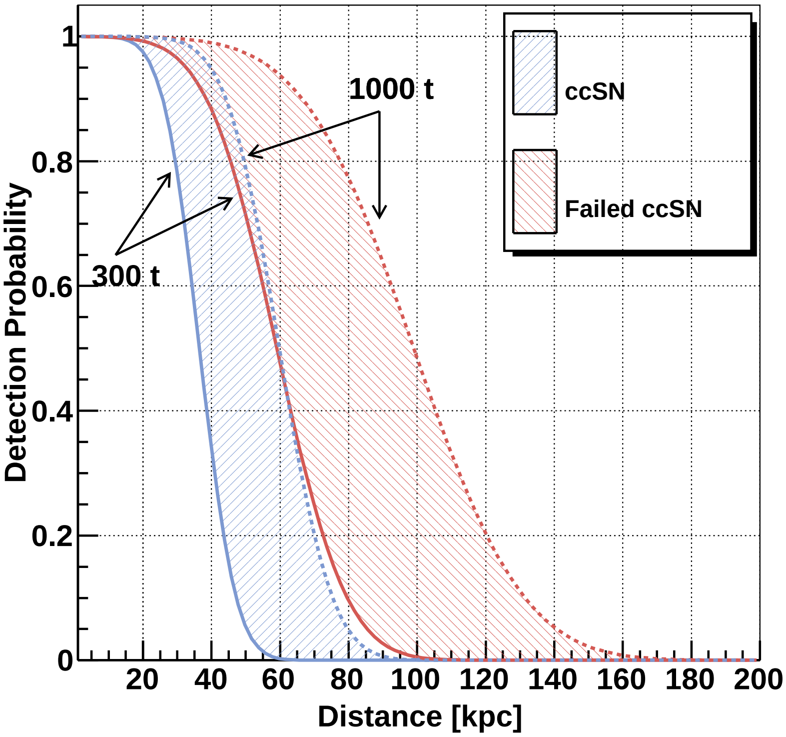

Figure 1: LVD detection probability versus source distance for the imitation frequency of 1/100 y^{-1} (see text). The blue and red bands correspond to the case of standard core collapse (ccSN) and failed supernovae, respectively. The solid (dashed) line represents an active mass of 300 (1000) t.

2 Core Collapse SN Monitor

2.1 Data set

The whole LVD data taking can be devided in 2 periods according to slightly different values of the trigger threshold. In the first period, from June 6^{th}, 1992, to December, 31^{st}, 2003, the hardware trigger energy threshold was set to $\mathcal{E}_H \simeq 5$ MeV, for the core counters, i.e., counters not directly exposed to the rock radioactivity which represent 47% of the total, and $\mathcal{E}_H \simeq 7$ MeV, for external ones. In the second period, from January 1^{st}, 2004 up to now, the trigger energy threshold of the array was set uniformly to $\mathcal{E}_H \simeq 4$ MeV. A secondary energy threshold, $\mathcal{E}_L \simeq 0.5$ MeV, to detect gammas from n-captures, is enabled during 1 ms after the occurrence of each trigger and remained unchanged during both periods. Duty cycle of the detector, averaged over 10 days windows, is shown in figure 2.

Fluctuations on the duty cycle, after the construction period, are mainly due to maintenance activity. The duty cycle of the whole data set achieves 96.1% (93.4% at $M_{\rm act} > 300$ t).

The detector active mass, $M_{\rm act}$, is dynamically adjusted. $M_{\rm act}$ is continuously monitored through the atmospheric muon flux. The muon rate observed by the whole LVD array is 0.097 ± 0.01 muons per second, while each counter detects, on average, 1.8 muons per hour. The detector active mass is updated every 8 hours by considering the counters that detected at least one muon in this period. Quality cuts on single counters are applied at this level to determine the reliable active mass of the detector:

- The response to atmospheric muons is used to identify and discard bad working counters, problems that are mainly due to electronic failures.
- Counters with a background rate $R(E \geq 7MeV) \geq 3 \cdot 10^{-3} s^{-1}$ [Agafonova et al.(2008)] are rejected as noisy. On average this problem regards less than 2% of the counters.

LVD active mass, M_{act}, as a function of time is shown in figure 2. From June 9^{th} 1992 to December 31^{st} 2014 M_{act} remained greater than 300 t during 7700 days.

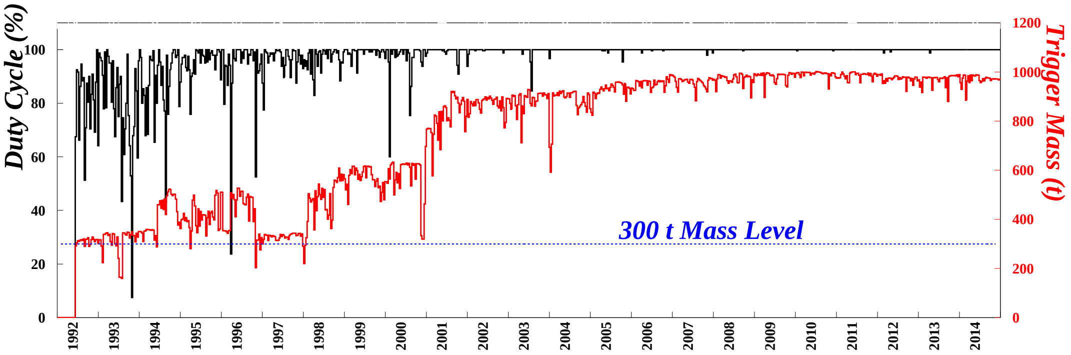

Figure 2: *LVD duty cycle and active mass as a function of time.* $M_{\rm act}$ *remained greater than the 300 t limit during 7700 days, from June* 9^{th} *1992 to December* 31^{st} *2014.*

2.2 Selection criteria

Most accredited model and numerical experiments predict that in core collapse supernovae neutrinos emission occur in three main phases:

- ν_e are emitted in shock breakout, when ν_e produced in electron captures (neutronization) are freed by the passage of the shock wave trough the neutrino sphere, duration few milliseconds;

- ν_e and $\bar{\nu}_e$ are emitted during the accretion phase, whose duration, around 500 ms, will determine the future evolution of the collapse;

- neutrinos and antineutrinos, ν_i and $\bar{\nu}_i$, of all flavors are emitted during the thermal cooling, duration few tents of seconds.

Average energy of emitted neutrinos ranges between 10 and 25 MeV, energy spectra are approximately thermal. On the bases of these expectations the data set dedicated to the search for neutrino burst must be free from the atmospheric muon component and limited to a convenient energy window to cut most of the background due to radioactivity. For these reasons the following cuts on single events are applied:

- coincident events in 2 or more counters within 200 ns, are rejected as muon candidates. To avoid the contamination of any signal associated with muon interactions inside the detector or in the surrounding rock, a dead time of 1 ms is applied after each muon event. This cut introduces a dead time, $t_{dead} \leq 0.01\%$, corresponding to less than 1 hour per year. The possibility that the product of a neutrino interaction involves more than one counter (and for this reason is rejected) has been evaluated in [Antonioli et al.(1991)]. Convolving this probability with the expected energy spectra we obtain that about 3% of neutrino interactions will be excluded from the following burst candidate selection process because of this cut. In case of a positive detection, i.e., the burst identification, these events will be recovered.
- According to the expected signal, the energy of the trigger events are selected in the range $E_{cut} \leq E_{trigger} \leq 100\ MeV$. Two energy ranges are considered with $E_{cut} = 7\ MeV$ and 10 MeV. Radioactivity background is highly suppressed at these energies, while the impact on the expected signal is negligible because of the energy dependence of the cross sections.

Moreover applying these two filters, in particular the second one, the rate becomes almost independent from the local hardware configuration and the effect due to the threshold change is negligible.

The core of the algorithm for the neutrino bursts candidate on-line selection consists in the search for a cluster of signals within a fixed time window, Δt. The burst candidate is simply characterized by its multiplicity m, i.e., the number of events detected during Δt and Δt itself. All the other characteristics of the cluster, as its topological distribution inside the detector, the detailed time structure, energy spectrum and ν flavor content, are left to a subsequent independent analysis (consistency check). A set of dedicated cuts are introduced in the process of burst candidate selection. They are occasionally applied to disentangle and reject local fluctuations of the trigger rate due to temporary failures, electric noise or human activities in the experiment. They can involve single counters (S-Cut) or sets of counters which are in some way connected as modules (M-Cut) or groups (G-Cut).

All these cuts are based on the simple requirement that events belonging to the cluster are due to low energy neutrinos that, because of their huge mean free path, are expected to interact uniformly inside an array made by elements with same detection efficiency. After applying the cut, the cluster is reanalyzed with the new multiplicity $m' = m - m_i$ and new background rate, f'_{bk}. We refer to these cuts as *topological cuts*. Their effects are carefully monitored along data taking and processing. For clusters that, before applying topological cuts, had an imitation frequency lower than 1 per month, an individual inspection is performed. The majority of these downgraded clusters are due to electronics failures, in particular TDC failures impacting muon rejection. It is not rare to see that the increasing of the number of downgraded clusters is correlated with a decreased number of recognized muons.

2.3 Results

At the end of the data selection and after applying topological cuts, the LVD background data behaves as a stochastic series well described by the Poisson statistic independently from the local hardware configuration.

In the search for a cluster of events within a fixed time window, Δt, each data period, T, is scanned through a "sliding window" with duration Δt=20s, that is, it is divided into N=$\frac{T}{\Delta t}$ intervals. This process has been repeated twice, where the Δt windows are relatively shifted of Δt/2. In this way the unbiased time window is 10s. The expected frequency of clusters of duration 20s and multiplicity $\geq m$, due to background, is:

$$F_{im}(m, f_{\mathrm{bk}}) = C \cdot \sum_{\mathrm{k \geq m}} P(k; 20 \cdot f_{\mathrm{bk}})\ ev \cdot day^{-1} \tag{9}$$

where $\mathrm{f_{bk}}$ is the background counting rate of the detector for visible energy, $\mathrm{E_{vis}} \geq \mathrm{E_{cut}}$ (E_{cut} = 10MeV in this analysis), $P(k; f_{\mathrm{bk}}\Delta t)$ is the Poisson probability to have clusters of multiplicity k if $f_{\mathrm{bk}}\Delta t$ is the average background multiplicity, and C = $86400/(2 \cdot \Delta t)$ is the number of trials per day.

Indeed, a candidate burst is defined by its multiplicity to which, for a known background rate, an imitation frequency is associated (through eq.9). F_{im}^{-1} thus represents the significance of the detected cluster defined as the average time you have to wait for a fake event originated by the Poissonian background [Agafonova et al.(2008)].

To check the performance of the selection procedure and to validate the reliability of the algorithm to reproduce background fluctuations, a number of test had been performed in the past and are periodically repeated. We simulate clusters of events in a subset of counters equipped with a LED system. We test, and online continuously monitor, the cluster selection criteria at low thresholds, i.e., with $\mathrm{F}_{im} \leq 1 \cdot \mathrm{day}^{-1}$, $1 \cdot \mathrm{week}^{-1}$, $1 \cdot \mathrm{month}^{-1}$. The comparison between expected and detected clusters at different significance allows us to keep the detector behavior and the reliability of the method used in the search for neutrino burst candidates.

While for LVD working standalone a detected cluster is considered a candidate neutrino burst only if its significance is higher than 100 years. This request is relaxed to 1 month when working in coincidence with other detectors in the SNEWS project [Antonioli et al.(2004)]. Furthermore, in case of detection, the neutrino burst candidate will be sent to a second level analysis, which aims at studying the consistency of these clusters with the features of a real neutrino burst. This second level analysis is called consistency check[1].

LVD has been observing the Galaxy searching for neutrino bursts from core collapse SN since June 1992. The detector is considered active only if its active mass, $\mathrm{M_{act}}$, was at least 300 t, being, in this way, fully sensitive to core collapse SN occurring at a distance D $\leq$ 25 kpc from the Earth. No neutrino burst candidate has been detected during 7700 days, from June 9th 1992 to December 31st 2014. The corresponding upper limit on the rate of gravitational stellar

---

[1] In the SNEWS project, the required coincidence with other detectors is considered, by LVD, the main instrument to confirm the reliability of the alarm. No additional test on the detected cluster is performed in this case before sending the alarm to the central server if the cluster has $\mathrm{F}_{im} \leq 1$/month.

collapse at 90% C.L. is: 0.109 year^{-1}. This is the most stringent limit to date achieved by the direct observation of the entire Galaxy searching for neutrino bursts.

In addition to the on-line analysis, described in this section, LVD make an off-line search of neutrino burst. In this analysis all the clusters with duration up to 100 seconds are studied. The results of this analysis applied to the data set from June 1992 up to the end of 2013 has been recently published [Agafonova et al.(2015)].

References

[Agafonova et al.(2007-a)] Agafonova N.Yu. et al., 2007, Astroparticle Physics, 27, 254-270; [hep-ph/069305].

[Agafonova et al.(2007-b)] Agafonova N.Yu. et al., 2007, Eur. Phys. J. C 52, 849-855 (2007).

[Agafonova et al.(2008)] Agafonova N.Yu. et al., 2008, Astroparticle Physics, 28, 516

[Agafonova et al.(2012-a)] Agafonova N.Yu. et al., 2012, Eur. Phys. J. Plus, 127-6, 71 (2012)

[Agafonova et al.(2012-b)] Agafonova N.Yu. et al., 2012, Phys. Rev. Lett., 109-7, 070801 (2012). [arXiv:1208.1392v2]

[Agafonova et al.(2015)] The Astrophysical Journal, 802:47, 2015 March 20

[Aglietta et al.(1987)] Aglietta, M. et al., 1987, Europhys. Letters, 3, 1315

[Aglietta et al.(1992)] Aglietta, M. et al., 1992, Il Nuovo Cimento A, 105, 1793

[Aglietta et al.(2004)] Aglietta M. et al., Nuclear Instruments and Methods in Physics Research A 516, 96 (2004).

[Ahrens et al.(2002)] Ahrens, J., et al. 2002, Astropart. Phys., 16, 345

[Alekseev et al.(1987)] Alekseev, E. N., et al., 1987, J. Exp. Theor. Phys. Lett., 45, 589

[Alekseev & Alexeyeva (2002)] Alekseev, E. N., & Alexeyeva, L. N. 2002, J. Exp. Theor. Phys, 95, 10

[Ambrosio et al.(2004)] Ambrosio, M., et al. 2004, Eur. Phys. J. C, 37, 265

[An et al.(2012)] An, F. P., et al., 2012, Phys. Rev. Lett., 108, 171803

[Antonioli et al.(2004)] Antonioli, P., et al., 2004, New J.Phys., 6, 114

[Antonioli et al.(1991)] P. Antonioli, W. Fulgione, P. Galeotti and L. Panaro, NIM A **309** (1991) 569.

[Bahcall et al.(1995)] Bahcall, J.N., Kamionkowski, M., Sirlin, A., 1995, Phys. Rev. D 51, 6146

[Bethe & Wilson(1985)] Bethe H.A., Wilson J.R., 1985, Astrophys.J.,295, 14

[Bionta et al.(1987)] Bionta, R. M., et al. (IMB collaboration). 1987, Phys. Rev. Lett., 58, 1494

[Colgate & White(1966)] S.A. Colgate, R.H. White, Astrophys. J. 143 (1966) 626

[Dye et al.(1989)] Dye, S. T., et al., 1989, Phys. Rev. Lett., 62, 2069

[Fukugita et al.(1988)] Fukugita M., Kohyama Y., Kubodera K., 1988, Physics Letters B, 212, 139

[Hirata et al.(1987)] Hirata, K., et al., 1987, Phys. Rev. Lett., 58, 1490

[Ikeda et al.(2007)] Ikeda, M., et al., 2007, The Astrophysical Journal, 669,519

[Imshennik & Ryazhskaya(2004)] Imshennik, V.S. & Ryazhskaya, O., 2004, Astronomy Letters, 30, 14

[Janka(2012)] H. T. Janka, Annual Review of Nuclear and Particle Science, 62, (2012), 407-451 arXiv:1206.2503v1

[Loredo & Lamb(2002)] T.J. Loredo, D.Q. Lamb, Phys. Rev. D 65 (2002) 063002

[Keil et al.(2003)] M. T. Keil, G. G. Raffelt, and H.-T. Janka, Astrophys. J. 590, 971 (2003)

[Kolbe & Langanke(2001)] Kolbe E., Langanke K., 2001, Phys. Rev. C, 63, 025802

[Mikheev & Smirnov(1985)] Mikheev, S.P. & Smirnov, A.Yu., 1985, Sov.J.Nucl.Phys., 42

[Nakazato et al.(2008)] Nakazato, K., Sumiyoshi, K., Suzuki, H., & Yamada, S., 2008, PhRvD, 78, 083014

[Novoseltseva et al.(2011)] Novoseltseva et. al., Bulletin of the Russian Academy of Sciences: Physics, vol 75, issue 3, (2011) pp. 419 - 422

[Pagliaroli et al.(2009)] Pagliaroli G., Vissani F., Costantini M.L., Ianni A., 2009, Astroparticle Physics 31, 163

[Strumia & Vissani(2003)] Strumia A., Vissani F., 2003, Physics Letters B, 564

[Strumia & Vissani(2010)] Strumia, A. & Vissani, F., arXiv:hep-ph/0606054v3

[Tamborra et al.(2012)] [4] I. Tamborra, B. Muller, L. Hudepohl, H. T. Janka, G.Raffelt, Phys. Rev. D 86, 125031 (2012)

[Toivanen et al.(2001)] Toivanen J., Kolbe E., Langanke K., Martinez-Pinedo G., Vogel P., 2001, Nuclear Physics A, 694, 395

[Totani et al.(1998)] Totani, T. et al., 1998, Astrophys. J., 496, 216

[Wilson(1985)] Wilson, J.R., 1985, Numerical Astrophysics, ed. J. M. Centrella, J. M. LeBlanc and R. L. Bowers, Jones and Bartlett Boston, 422

[Wolfenstein(1978)] Wolfenstein, L., 1978, Phys.Rev. D, 17

OPERA

N. Agafonova[1], A. Aleksandrov[2], O. Altinok[3], A. Anokhina[4], S. Aoki[5], A. Ariga[6], T. Ariga[6], D. Autiero[7], A. Badertscher[8], A. Bagulya[9], A. Bendhabi[10], A. Bertolin[11,*], C. Bozza[12], T. Brugière[7], R. Brugnera[13,11], F. Brunet[14], G. Brunetti[15,16,7], S. Buontempo[2], A. Cazes[7], L. Chaussard[7], M. Chernyavskiy[9], V. Chiarella[17], A. Chukanov[18], N. D'Ambrosio[19], F. Dal Corso[11], G. De Lellis[20,2], P. del Amo Sanchez[14], Y. Déclais[7], M. De Serio[21], F. Di Capua[2], A. Di Crescenzo[20,2], D. Di Ferdinando[16], N. Di Marco[22,a], S. Dmitrievski[18], M. Dracos[23], D. Duchesneau[14], S. Dusini[11], T. Dzhatdoev[4], J. Ebert[24], O. Egorov[25], R. Enikeev[1], A. Ereditato[6], L. S. Esposito[8], J. Favier[14], T. Ferber[24], R. A. Fini[21], D. Frekers[26], T. Fukuda[27], A. Garfagnini[13,11], G. Giacomelli[15,16 †], M. Giorgini[15,16,b], C. Göllnitz[24], J. Goldberg[28], D. Golubkov[25], L. Goncharova[9], Y. Gornushkin[18], G. Grella[12], F. Grianti[29,17], A. M. Guler[3], C. Gustavino[39], C. Hagner[24], K. Hamada[27], T. Hara[5], M. Hierholzer[24], A. Hollnagel[24], K. Hoshino[27], M. Ieva[21], H. Ishida[30], K. Jakovcic[31], C. Jollet[23,*], F. Juget[6], M. Kamiscioglu[3], K. Kazuyama[27], S. H. Kim[32,d], M. Kimura[30], N. Kitagawa[27], B. Klicek[31], J. Knuesel[6], K. Kodama[33], M. Komatsu[27], U. Kose[13,11], I. Kreslo[6], H. Kubota[27], C. Lazzaro[8], J. Lenkeit[24], I. Lippi[11], A. Ljubicic[31], A. Longhin[13,11,e], P. Loverre[34,39], G. Lutter[6], A. Malgin[1], G. Mandrioli[16], K. Mannai[10], J. Marteau[7], T. Matsuo[30], V. Matveev[1], N. Mauri[15,16,e], E. Medinaceli[16], F. Meisel[6], A. Meregaglia[23,*], P. Migliozzi[2], S. Mikado[30], S. Miyamoto[27], P. Monacelli[39], K. Morishima[27], U. Moser[6], M. T. Muciaccia[35,21], N. Naganawa[27], T. Naka[27], M. Nakamura[27], T. Nakano[27], D. Naumov[18], V. Nikitina[4], K. Niwa[27], Y. Nonoyama[27], S. Ogawa[30], N. Okateva[9], A. Olchevski[18], M. Paniccia[17], A. Paoloni[17], B. D. Park[32,f], I. G. Park[32], A. Pastore[35,21], L. Patrizi[16], E. Pennacchio[7], H. Pessard[14], K. Pretzl[6], V. Pilipenko[26], C. Pistillo[6], N. Polukhina[9], M. Pozzato[15,16], F. Pupilli[22], R. Rescigno[12], T. Roganova[4], H. Rokujo[5], G. Romano[12], G. Rosa[34,39], I. Rostovtseva[25], A. Rubbia[8], A. Russo[20,2], V. Ryasny[1], O. Ryazhskaya[1], O. Sato[27], Y. Sato[36], A. Schembri[19], W. Schmidt-Parzefall[24], H. Schroeder[37], L. Scotto Lavina[20,2,g], A. Sheshukov[18], H. Shibuya[30], G. Shoziyeov[4], S. Simone[35,21], M. Sioli[15.16], C. Sirignano[13,11], G. Sirri[16], J. S. Song[32], M. Spinetti[17], L. Stanco[11], N. Starkov[9], M. Stipcevic[31], T. Strauss[8,h], P. Strolin[20,2], S. Takahashi[27], M. Tenti[15,16], F. Terranova[17], I. Tezuka[36], V. Tioukov[2], P. Tolun[3], A. Trabelsi[10], T. Tran[7], S. Tufanli[3,h], P. Vilain[38], M. Vladimirov[9], L. Votano[17], J. L. Vuilleumier[6], G. Wilquet[38], B. Wonsak[24] V. Yakushev[1], C. S. Yoon[32], T. Yoshioka[27], J. Yoshida[27], Y. Zaitsev[25], S. Zemskova[18], A. Zghiche[14] and R. Zimmermann[24].

1. INR-Institute for Nuclear Research of the Russian Academy of Sciences, RUS-117312 Moscow, Russia
2. INFN Sezione di Napoli, I-80125 Napoli, Italy
3. METU-Middle East Technical University, TR-06531 Ankara, Turkey
4. SINP MSU-Skobeltsyn Institute of Nuclear Physics of Moscow State University, RUS-119992 Moscow, Russia
5. Kobe University, J-657-8501 Kobe, Japan
6. Albert Einstein Center for Fundamental Physics, Laboratory for High Energy Physics (LHEP), University of Bern, CH-3012 Bern, Switzerland

---

[†] deceased

7. IPNL, Université Claude Bernard Lyon 1, CNRS/IN2P3, F-69622 Villeurbanne, France
8. ETH Zurich, Institute for Particle Physics, CH-8093 Zurich, Switzerland
9. LPI-Lebedev Physical Institute of the Russian Academy of Sciences, RUS-117924 Moscow, Russia
10. Unité de Physique Nucléaire et des Hautes Energies (UPNHE), Tunis, Tunisia
11. INFN Sezione di Padova, I-35131 Padova, Italy
12. Dipartimento di Fisica dell'Università di Salerno and INFN, I-84084 Fisciano, Salerno, Italy
13. Dipartimento di Fisica dell'Università di Padova, I-35131 Padova, Italy
14. LAPP, Université de Savoie, CNRS/IN2P3, F-74941 Annecy-le-Vieux, France
15. Dipartimento di Fisica dell'Università di Bologna, I-40127 Bologna, Italy
16. INFN Sezione di Bologna, I-40127 Bologna, Italy
17. INFN - Laboratori Nazionali di Frascati dell'INFN, I-00044 Frascati (Roma), Italy
18. JINR-Joint Institute for Nuclear Research, RUS-141980 Dubna, Russia
19. INFN - Laboratori Nazionali del Gran Sasso, I-67010 Assergi (L'Aquila), Italy
20. Dipartimento di Scienze Fisiche dell'Università Federico II di Napoli, I-80125 Napoli, Italy
21. INFN Sezione di Bari, I-70126 Bari, Italy
22. Dipartimento di Fisica dell'Università dell'Aquila and INFN, I-67100 L'Aquila, Italy
23. IPHC, Université de Strasbourg, CNRS/IN2P3, F-67037 Strasbourg, France
24. Hamburg University, D-22761 Hamburg, Germany
25. ITEP-Institute for Theoretical and Experimental Physics, RUS-117259 Moscow, Russia
26. University of Münster, D-48149 Münster, Germany
27. Nagoya University, J-464-8602 Nagoya, Japan
28. Department of Physics, Technion, IL-32000 Haifa, Israel
29. Università degli Studi di Urbino "Carlo Bo", I-61029 Urbino, Italy
30. Toho University, J-274-8510 Funabashi, Japan
31. IRB-Rudjer Boskovic Institute, HR-10002 Zagreb, Croatia
32. Gyeongsang National University, ROK-900 Gazwa-dong, Jinju 660-300, Korea
33. Aichi University of Education, J-448-8542 Kariya (Aichi-Ken), Japan
34. Dipartimento di Fisica dell'Università di Roma "La Sapienza" and INFN, I-00185 Roma, Italy
35. Dipartimento di Fisica dell'Università di Bari, I-70126 Bari, Italy
36. Utsunomiya University, J-321-8505 Tochigi-Ken, Utsunomiya, Japan
37. Fachbereich Physik der Universität Rostock, D-18051 Rostock, Germany
38. IIHE, Université Libre de Bruxelles, B-1050 Brussels, Belgium
39. INFN Sezione di Roma1, I-00185 Roma, Italy
a. Now at INFN - Laboratori Nazionali del Gran Sasso, I-67010 Assergi (L'Aquila), Italy
b. Now at INAF/IASF, Sezione di Milano, I-20133 Milano, Italy
c. Now at Dipartimento di Fisica dell'Università di Roma "La Sapienza" and INFN, I-00185 Roma, Italy
d. Now at Pusan National University, Geumjeong-Gu Busan 609-735, Korea
e. Now at INFN - Laboratori Nazionali di Frascati dell'INFN, I-00044 Frascati (Roma), Italy
f. Now at Asan Medical Center, 388-1 Pungnap-2 Dong, Songpa-Gu, Seoul 138-736, Korea
g. Now at SUBATECH, CNRS/IN2P3, F-44307 Nantes, France
h. Now at Albert Einstein Center for Fundamental Physics, Laboratory for High Energy Physics (LHEP), University of Bern, CH-3012 Bern, Switzerland

Abstract

The OPERA neutrino detector at the underground Gran Sasso Laboratory (LNGS) was designed to perform the first detection of neutrino oscillations in appearance mode through the study of $\nu_\mu \to \nu_\tau$ oscillations. The apparatus consists of a lead/emulsion-film target complemented by electronic detectors. It is placed in the high-energy long-baseline CERN to LNGS beam (CNGS) 730 km away from the neutrino source. Runs with CNGS neutrinos were successfully conducted in 2008, 2009, 2010, 2011 and 2012 for a total luminosity of 18×10^{19} p.o.t. (*proton on target*). In November 2012 the CNGS run has been stopped and subsequently the beam line has been dismounted. The emulsion analysis has continued during 2013 and 2014 and will presumably continue for the whole 2015. At the beginning of 2015 the decommissioning of the OPERA detector has started. After a brief description of the beam and of the experimental apparatus we report on the data and related analysis results.

1 Introduction

The solution of the long-standing solar and atmospheric neutrino puzzles has come from the hypothesis of neutrino oscillations. This implies that neutrinos have non vanishing and non-degenerate mass eigenstates, and that their flavor eigenstates involved in weak interaction processes are a superposition of the mass eigenstates. Several experiments carried on in the last decades with solar and reactor neutrinos, as well as with atmospheric and accelerator neutrinos, contributed to build-up our present understanding of neutrino mixing. Atmospheric neutrino oscillations have been studied mainly by the Kamiokande, MACRO, Super-Kamiokande and SOUDAN2 experiments. Long baseline experiments with accelerator neutrinos (K2K and MINOS) confirmed the oscillation scenario first pointed out by the Super-Kamiokande experiment supporting the $\nu_\mu \to \nu_\tau$ oscillation channel for atmospheric neutrinos, while the CHOOZ and Palo Verde reactor experiments excluded the $\nu_\mu \to \nu_e$ channel as the dominant one. However, the direct appearance of a different neutrino flavor is still an important open issue. This is the main goal of the OPERA experiment [1] that uses the long baseline (L=730 km) CNGS neutrino beam from CERN to LNGS. The challenge of the experiment is to measure the appearance of ν_τ from ν_μ oscillations in an almost pure muon-neutrino beam. This requires the detection of the short-lived τ lepton ($c\tau = 87.11$ μm) produced in the charged-current interaction of a ν_τ. This sets two conflicting requirements: a large target mass needed to have sufficient statistics and an extremely high accuracy detector technique to observe the short-lived τ lepton. The τ is identified by the detection of its characteristic decay topologies either in one prong (electron, muon or hadron) or in three prongs. The τ track is measured with a large-mass active target made of 1 mm thick lead plates (target mass and absorber material) inter-spaced with thin nuclear emulsion films (high-accuracy tracking devices). This detector is historically called Emulsion Cloud Chamber (ECC). Among past applications it was successfully used in the DONUT experiment for the first direct observation of the ν_τ.

The OPERA detector [2] is made of two identical Super Modules (SM) each consisting of a target section of about 625 tons made of lead/emulsion-film ECC modules (hereafter called "bricks"), of a scintillator tracker detector (TT) needed to trigger the read-out and pre-localize neutrino interactions within the target, and of a muon spectrometer (Figure 1). A single SM has longitudinal dimensions of about 10 m. The detector is equipped with an automatic machine (the Brick Manipulator System, BMS) that allows the on-line removal of bricks from the detector. Ancillary facilities exist for the handling, the development and the scanning of the emulsion films. The film scanning is performed with two independent types of scanning microscopes: the European Scanning System (ESS) in Europe and the S-UTS in Japan.

A target brick consists of 56 lead plates of 1 mm thickness interleaved with 57 emulsion films [3]. The plate material is a lead alloy with a small calcium content to improve its mechanical properties [4]. The transverse dimensions of a brick are 12.8 × 10.2 cm^2 and the thickness along the beam direction is 7.9 cm (about 10 radiation lengths). The construction of more than 150,000 bricks for the neutrino target has been accomplished by an automatic machine, the Brick Assembly Machine (BAM) operating underground in order to minimize the number of background tracks from cosmic-rays and environmental radiation. The bricks have been inserted in the detector target by the BMS and housed in a light support structure placed between consecutive TT walls. The support structure has been designed with the requirement of minimizing the material along the neutrino beam direction in order to reduce to the 0.1% level the number of interactions in regions not instrumented with emulsion films or scintillators. In order to reduce the emulsion scanning load the use of Changeable Sheets (CS) [5], successfully applied in the CHORUS experiment, was extended to OPERA. Tightly packed doublets of

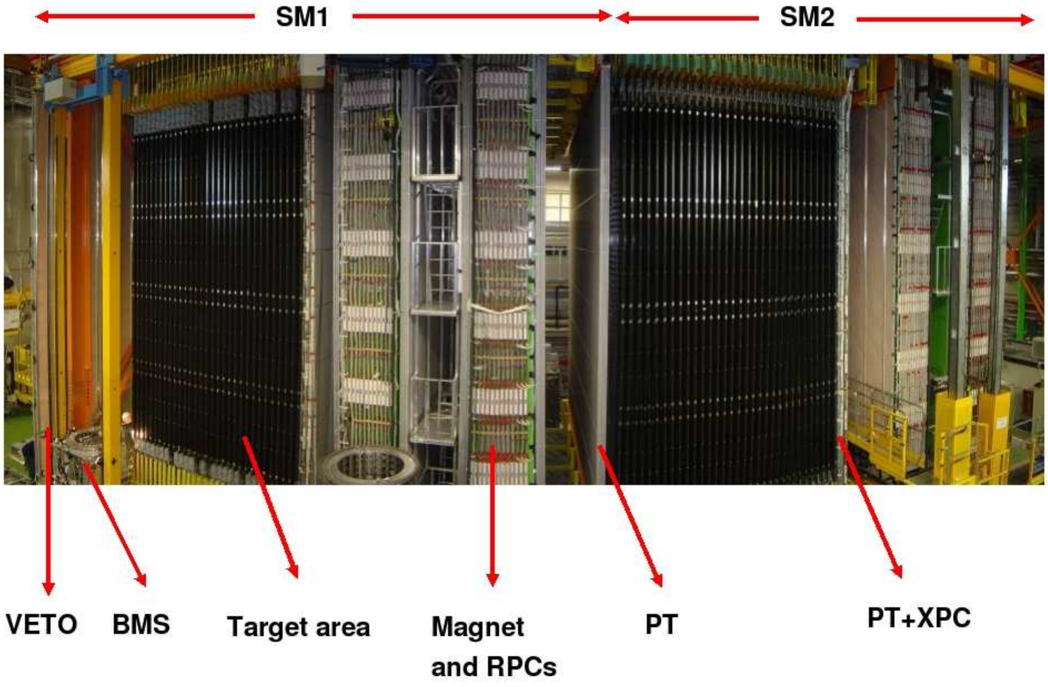

Figure 1: Fish-eye view of the OPERA detector. The upper horizontal lines indicate the position of the two identical supermodules (SM1 and SM2). The "target area" is made of walls filled with ECC bricks interleaved with planes of plastic scintillators (TT). Arrows also show the position of the VETO planes, the drift tubes (PT), the RPC with diagonal strips (XPC), the magnets and the RPC installed between the magnet iron slabs. The Brick Manipulator System (BMS) is also visible. See [2] for more details.

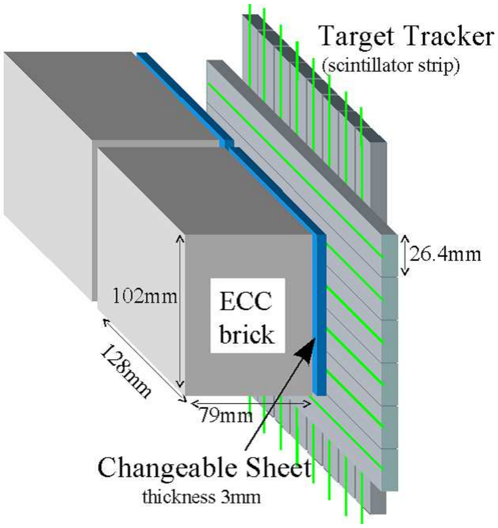

Figure 2: Schematic view of two bricks with their Changeable Sheet and target tracker planes.

emulsion films are attached to the downstream face of each brick and can be removed without opening the brick. Charged particles from a neutrino interaction in the brick cross the CS and produce signals in the TT scintillators. Following these signals the brick is extracted and the CS developed underground and analyzed in the scanning facilities at LNGS and in Nagoya. The information of the CS is used for a precise prediction of the position of the tracks in the most downstream films of the brick, hence guiding the so-called *scan-back* vertex finding procedure. The brick, CS and TT layout [5] is schematically shown in Figure 2.

2 Evidence of $\nu_\mu \to \nu_\tau$ appearance in the CNGS beam with direct τ detection

The CNGS neutrino beam was designed and optimized for the study of $\nu_\mu \to \nu_\tau$ oscillations in appearance mode, by maximizing the number of charged current (CC) ν_τ interactions at the LNGS site. For a detailed description of the CNGS beam we refer to [2].

After the beam commissioning run in 2006, the CNGS run started on September 2007 at rather low intensity. The first event inside the OPERA target was observed on October 3^{rd}.Longer runs took place in 2008, 2009, 2010, 2011 and 2012. On December 2012 the last CNGS neutrinos were delivered to LNGS. A long shutdown took place at CERN in 2013 and 2014 for the upgrade of LHC, and the CNGS beam has been decommissioned. The decommissioning of the OPERA detector has started at the beginning of 2015. A first ν_τ interaction candidate with a one-prong topology was found in 2010 [6].

A second ν_τ interaction candidate was found in 2011 with a three-prong topology and presented in 2012 [8] (Fig.4).

A third ν_τ interaction candidate was found in 2012 in the muonic decay channel and officially presented in 2013 [9] (Fig.5).

A fourth ν_τ interaction candidate was found in 2014 with a one prong decay topology [11] (Fig.6).

The four candidate events found, together with a conservative background estimation, mostly

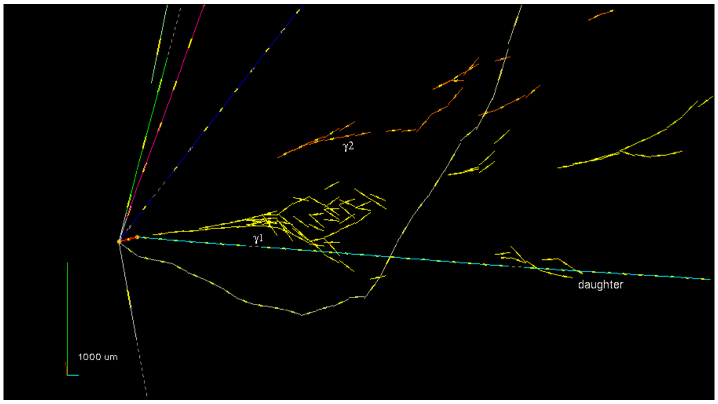

Figure 3: The first OPERA tau candidate (see [6] for details).

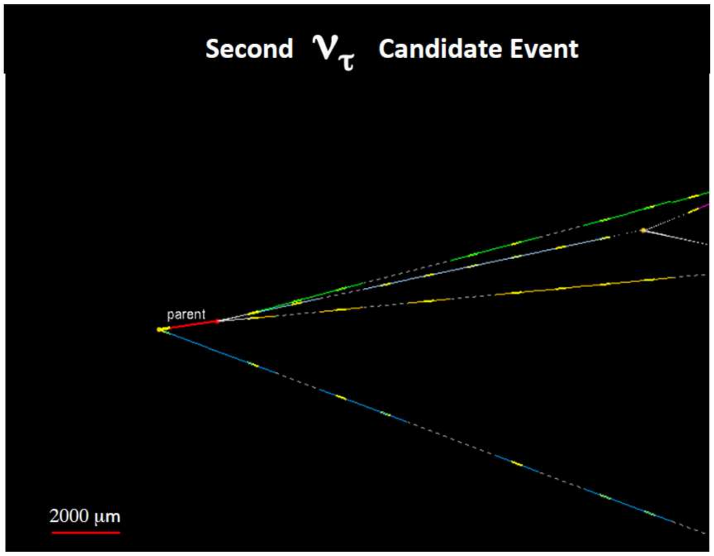

Figure 4: The second OPERA tau candidate; in this candidate event the tau decays into three prongs (see [8] for details).

due to charm candidates with undetected muon, give a significance of 4.2 sigma for the direct detection of $\nu_\mu \to \nu_\tau$ oscillations [9] [11] .

3 Status of the event analysis and plan for 2015

(Fig.7) shows the history of the data analysis as a function of time, from the beginning of data taking (2008 run) up to now. The upmost line shows the number of events reconstructed in the target with the Target Tracker detectors (TT), then the number of events with at least one brick extracted is shown, and subsequently the number of events with at least one pair of CS scanned interactions. The next line shows the number of events with positive result in the CS an subsequently the number of events with at least one brick scanned is shown.The last two

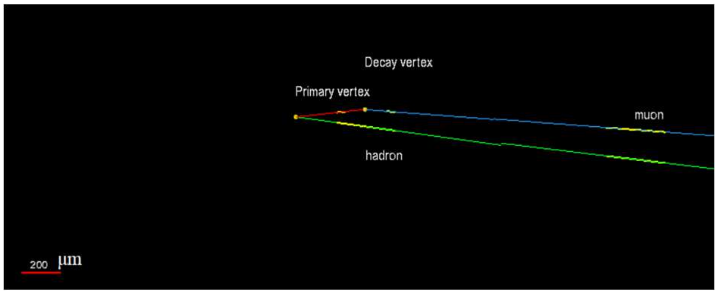

Figure 5: The third OPERA tau candidate; in this candidate event the short track is seen to decay leptonically into one muon which stops in the spectrometer.

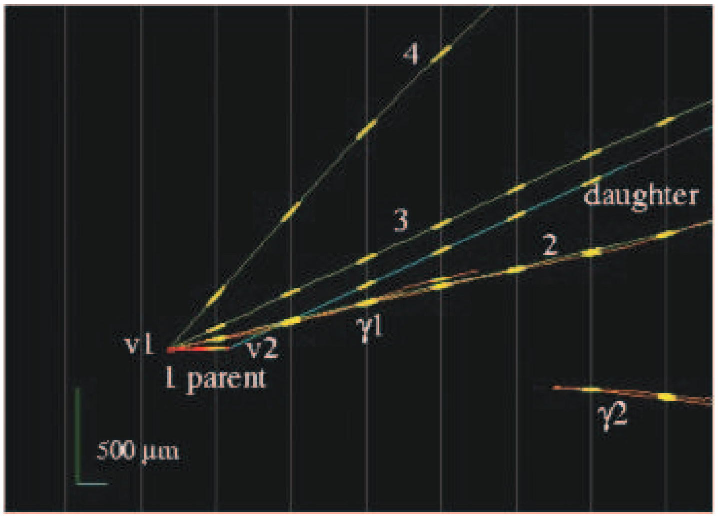

Figure 6: The fourth OPERA tau candidate event. In this event the short parent track is seen to decay into a daughter particle which is consistent to be a hadron, from momentum/range measurements. None of the tracks originating from the primary vertex is consistent with being a muon.

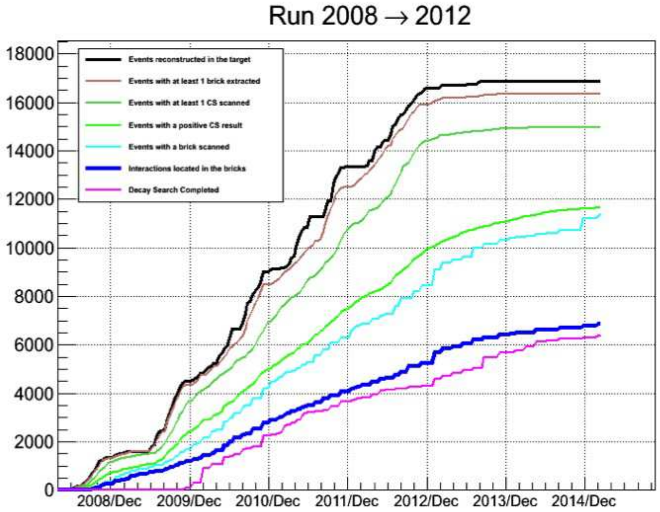

Figure 7: OPERA data analysis as function of time.The upmost line shows the number of events reconstructed in the target, then the number of events with at least one extracted brick is shown and the number of events with at least one CS pair scanned. The next two curves indicate the number of events with positive signal found in the CS and the number of events with at least one brick scanned. The lowest two lines indicate the number of events with the neutrino interaction found in the brick and the number of events whith the decay search completed.

lines show the number of interacts found and measured in the bricks and the number of events with the decay search completed. As can bee seen there is an important fraction of the events which has not been located in the bricks, and this fraction can be reduced measuring also the bricks adjacent to those which have been indicated by the TT to be the most probable bricks to contain the interaction vertex

The scanning and analysis of the extracted bricks, will continue during 2015 in order to complete the search for ν_τ events collected in the last years and not yet found. All the most probable event bricks and the second probable bricks have been measured and analyzed. During the year 2015 the remaining third and fourth most probable bricks (for those events which have not been confirmed in the first and second brick) will be developed and analyzed.The extraction will continue during the decommissioning phase in order to keep apart the bricks which could contain events to be measured.

References and list of publications

[1] M. Guler *et al.*, OPERA proposal, CERN/SPSC 2000-028, SPSC/P318, LNGS P25/2000.

[2] R. Acquafredda *et al.* [OPERA Collaboration] ”The OPERA experiment in the CERN to Gran Sasso neutrino beam”, JINST 4:P04018,2009.

[3] T. Nakamura *et al.*, ”The Opera Film: New Nuclear Emulsion For Large-Scale, High-Precision Experiments,” Nucl. Instrum. Meth. A **556** (2006) 80.

[4] A. Anokhina *et al.* [OPERA Collaboration], "Study of the effects induced by lead on the emulsion films of the OPERA experiment," JINST **3** P07002 (2008).

[5] A. Anokhina *et al.* [OPERA Collaboration], "Emulsion sheet doublets as interface trackers for the OPERA experiment," JINST **3** (2008) P07005

[6] N. Agafonova *et al.* [OPERA Collaboration], "Observation of a first ν_τ candidate in the OPERA experiment in the CNGS beam," Phys. Lett. *B691* , 138 (2010).

[7] N. Agafonova *et al.* [OPERA Collaboration], "Search for ν_μ -ν_e oscillation with the OPERA experiment in the CNGS beam." JHEP *1301* 1307 (2013) 004, Addendum-ibid 1307 (2013) 085

[8] N. Agafonova *et al.* [OPERA Collaboration], New result on $\nu_\mu \to \nu_\tau$ appearance with the OPERA Experiment in the CNGS beam." JHEP11 *1301* , 036 (2013)

[9] N. Agafonova *et al.*[OPERA Collaboration],"Evidence for $\nu_\mu \to \nu_\tau$ appearance in the CNGS neutrino beam with the OPERA experiment." Phys.Rew. D 89 051102(R),(2014)

[10] N. Agafonova *et al.* [OPERA Collaboration]"Measurement of TeV atmospheric muon charge ratio with the full OPERA data." Eur.Phys. J. C 74, 2933 (2014)

[11] N. Agafonova *et al.*[OPERA Collaboration],"Observation of tau neutrino appearance in the CNGS beam with the OPERA experiment." PTEP 2014, no. 10, 101C01 (2014)

[12] N. Agafonova *et al.*[OPERA Collaboration],"Procedure for short-lived particle detection in the OPERA experiment and its application to charm decays Eur.Phys.J.C 74, no. 8,2986 (2014)

THEORY GROUP

The LNGS theory group is organized in the following five working subgroups (or IS, from *Iniziative Specifiche*): Astrofisica delle alte energie (AAE), Inflation, dark matter and the large-scale structure of the universe (INDARK), Non-Perturbative quantum chromodynamics (NPQCD), Nuclear matter and compact stellar objects (NUMAT), Theoretical astroparticle physics (TASP). The local coordinators are indicated in bold face in the members list. The research topics concern five main areas: astroparticle physics (mainly TASP); compact stellar objects and dense hadronic matter (NUMAT); cosmology, large scale structures and dark matter (INDARK); computer simulations of gauge theories (NPQCD); particle physics phenomenology and beyond standar model physics (mainly AAE). There is a tradition of collaboration between the LNGS theory group and several experimental groups. In this report, we briefly describe the activities of the theory group in 2014.

Members of the group: A. Addazi, R. Aloisio, L. Ambrogi, Z. Berezhiani, V. Berezinsky, R. Biondi, P. Blasi, D. Boncioli, M. Crisostomi, M. D'Angelo, G. Di Carlo, G. Di Panfilo, D. Ejlli, A. Esmaili, P. Giammaria, **M. Mannarelli**, A. Palladino, G. Pagliaroli, A. Parisi, L. Pilo, S. Recchia, F. Tonelli, F.L. Villante, F. Vissani.

More information can be found at: `http://theory.lngs.infn.it/index.html`

NPQCD

Member: **G. Di Carlo**.
– Collaboration with V. Azcoiti, E. Follana, E. Royo (Universidad de Zaragoza, Spain) and A. Vaquero (INFN-MiB).

Scientific work

Our main interest is the study of lattice theories with sign problem, in particular Lattice QCD at non-zero baryon density; we are also working on a class of possible new geometric algorithms for simulating fermion models. Another field of interest are abelian and non abelian gauge theories with theta term in the action.

During 2014 we have finalized the analysis of the spectral flow for the operator introduced by D.H.Adams for the staggered fermion formulation on realistic (quenched) gauge configurations. The result of this analysis is reported in [1]. We started the study of the effects of the theta term in the (one flavour) Schwinger model, in particular trying to reproduce the Coleman prediction on the phase structure at $\theta = \pi$.

AAE

Members: A. Addazi, **Z. Berezhiani**, R. Biondi, G. Di Panfilo, D. Ejlli
– Collaboration with A. D. Dolgov (Univ. Ferrara), O. Benhar (Univ. Roma I), Y. Kamyshkov (Univ. Tennessee, USA)

Scientific work

The research activity has been focused on the following topics:

- Baryon number violation and neutron oscillations.
  We worked on different models of baryon number violation and neutron oscillations, with special attention to $\Delta B = 2$ processes leading to neutron-antineutron oscillation and $\Delta B = 1$ ones leading to neutron-mirror neutron oscillations. The cases of spontaneous baryon violation and its relations with the lepton number violation was studied. Extended report on the neutron oscillations is submitted to Phys. Reports for publication [2] which summarize the theoretical motivations and the experimental efforts to search for baryon number violation, focussing on nucleon decay and neutron-antineutron oscillations. Present and future nucleon decay search experiments using large underground detectors, as well as planned experiments with free high intensity neutron beams at ESS were highlighted. Also, some exotic instantons were discussed as a source of neutron-antineitron oscillation [3].
- Lepton number violation and neutrinoless 2β decay.
  The nuclear matrix element of neutrinoless double-β decay were calculated with taking into account the short-range correlation effects: nucleon-nucleon correlations in both physical and spin-space, which led to about 20 % decrease of nuclear matrix elements with respect previous calculations [4].
- Axion physics and cosmology.
  Cosmological limits on the axions and other light pseudo-scalars were studied from the spectral distortion of the cosmic microwave background radiation (CMB) due to the photon oscillation into axions in intergalactic magnetic fields [5, 6].

INDARK

Members: M. Crisostomi, **L. Pilo** and F.L. Villante.
– Collaboration with E. Babichev (LPT-Orsay), D. Comelli (INFN-Ferrara), K. Koyama, (ICG-Portsmouth), F. Nesti, (Boskovic Institue-Zagreb), M. Pinsonneault (Ohio State Univ.), A. Serenelli (UAM-Barcellona), A. Riotto (University of Ginevra), G. Tasinato(Swansea Univ.)

Scientific work

The research activity has been focused on the following topics:

- Study of FRW cosmology of the most general ghost free massive gravity with five propagating degrees of freedom. This large class of theories includes both the case with a residual Lorentz invariance as the cases with simpler rotational invariance. We find that the existence of a nontrivial homogeneous FRW background, in addition to selecting the Lorentz-breaking case, implies in general that perturbations around strict Minkowski or dS space are strongly coupled. The result is that dark energy can be naturally accounted for in massive gravity but its equation of state w_{eff} has to deviate from -1. We find indeed a relation between the strong coupling scale of perturbations and the deviation of w_{eff} from -1. Taking into account current limits on w_{eff} and sub-millimeter tests of the Newton's law as a limit on the possible strong coupling regime, we find that it is still possible to have a weakly coupled theory in a quasi dS background. Future experimental improvements may be used to predict w_{eff} in a weakly coupled massive gravity theory

- Classification and study of non-derivative modified gravity. Theories of gravity modified by a generic non-derivative potential built from the metric, under the minimal requirement of unbroken spatial rotations can be studied in a systematic way by using canonical analysis. The deforming potentials V are classified according to the number of degrees of freedom (DoF) that propagate at the non-perturbative level. A generic V implies 6 propagating DoF at the non-perturbative level, with a ghost on Minkowski background. There exist potentials which propagate 5 DoF; no V with unbroken rotational invariance admitting 4 DoF is found. Theories with 3 DoF turn out to be strongly coupled on Minkowski background. Finally, potentials with only the 2 DoF of a massive graviton exist. Their effect on cosmology is simply equivalent to a cosmological constant.

- Gravitational and electromagnetic properties of quark starts The crystalline color superconducting phase is believed to be the ground state of deconfined quark matter for sufficiently large values of the strange quark mass. This phase can sustain large shear stresses, supporting torsional oscillations of large amplitude. The torsional oscillations could lead to observable electromagnetic signals if strange stars have a crystalline color superconducting crust. When a torsional oscillation is excited, for instance by a stellar glitch, the positive charge oscillates with typical kHz frequencies, for a crust thickness of about one-tenth of the stellar radius, to hundreds of Hz, for a crust thickness of about nine-tenths of the stellar radius. Higher frequencies, of the order of few GHz, can be reached if the star crust is of the order of a few centimeters thick. The estimated emitted power can be quite large, of the order of 1045 erg/s for a thin crust. The associated relaxation times are very uncertain, with values ranging between microseconds and minutes, depending on the crust thickness. The radiated photons will be in part absorbed by the electronic atmosphere, but a sizable fraction of them should be emitted by the star.

- FRW Cosmological Perturbations in Massive bigravity Cosmological perturbations of FRW solutions in ghost free massive bigravity, including also a second matter sector, are studied in detail. At early time, we find that sub-horizon exponential instabilities are unavoidable and they lead to a premature departure from the perturbative regime of cosmological perturbations.

- Limits to the properties of non standard weakly interacting particles (axions and hidden photons) from solar data global fits. We presented a new statistical analysis that combines helioseismology (sound speed, surface helium and convective radius) and solar neutrino observations (boron and beryllium fluxes) to place upper limits to the properties of non standard weakly interacting particles. We obtained a 3σ upper limit on the axion-photon coupling constant $g_{a\gamma} < 4 \cdot 10^{-10}\text{GeV}^{-1}$. For hidden photons, we obtained the most restrictive upper limit for the product of the kinetic mixing and mass of $\chi m < 1.8 \cdot 10^{-12}\text{eV}$ at 3σ.

TASP

Members: R. Aloisio, L. Ambrogi V. Berezinsky, P. Blasi, D. Boncioli, M. D'angelo, A. Esmaili, P. Giammaria, A. Palladino, S. Recchia, **F.L. Villante**, F. Vissani
– Collaboration with F. Aharonian (Dublin Institute for Advanced Studies, Irlanda), V. Dokuchaev (INR, Moscow), Yu. Eroshenko (INR, Moscow), S.K. Kang (Seoul National University of Science and Technology, Corea del Sud), P. Serpico (Laboratoire de Physique Thorique d'Annecy-le-Vieux, Francia), O. Peres, M. Guzzo (UNICAMP, Brasile).

Scientific work

The research activity has been focused on the following topics:

- Neutrino physics and astronomy.
  Studies of the possible sources and of the characteristic signatures of a cosmic population of very high energy neutrinos; Analysis and interpretation of the high-energy IceCUBE data; Phenomenology of kev-sterile neutrinos as potential dark matter candidates. Determination of the galaxy structure in scenarios with fermionic warm dark matter; Study of the spectrum of supernova neutrinos in ultra-pure scintillators, in particular, in connection to the possibility to observe neutral current events; Study of new expectations and uncertainties on neutrinoless double beta decay, in particular in view of the renormalisation of the couplings of the nucleons in nuclear medium; Quantitative study of the solar composition problem. Analysis of the role of a future CNO solar neutrino measurement. Limits to the properties of non standard weakly interacting particles from solar data global fits.
- Cosmic ray physics
  Study of the propagation of very high energy cosmic ray in extragalactic environment; comparison between different numerical simulations; Analysis and interpretation of Pierre Auger Observatory experimental data (energy spectrum and observables related to chemical composition; Non linear effects in cosmic ray physics; Effects of intergalactic magnetic fields in the physics of ultra high energy cosmic rays; Dark matter models and indirect detection of dark matter.

Numat

Members: M. Mannarelli, A. Parisi, **G. Pagliaroli**, F. Tonelli and F. Vissani.
– Collaboration with C. Lujan-Peschard, S. Dell'Oro, S. Marcocci, R. Anglani (CNR-Bari), R. Casalbuoni (University of Florence and INFN), M. Ciminale (University of Bari), N. Ippolito(University of Bari), R. Gatto (University of Geneve), M. Ruggieri (University of Catania).

Scientific work

The research activity has been focused on the following topics:

- Properties of neutrinos.
  We have studied the Majorana Effective Mass, i. e. the crucial parameter that regulates the rate of the neutrinoless double beta decay due to light neutrino exchange. We have updated the previous estimations of this parameter and we have evaluated the impact of the quenching in the nuclear medium of the axial vector coupling constant, as discussed by Iachello and collaborators [14]. Concerning astrophysical neutrinos we have investigated the possibility to study core collapse supernovae (SN) by observing, for the first time, neutral-current reactions due to SN neutrinos. We have studied the entire expected energy spectrum in the Borexino, KamLAND and SNO+ detectors, quantifying the effect of confusion, due to the different components of the energy spectrum overlapped [15].

- Matter in extreme conditions.
  Regarding the properties of ultra-dense matter, we have studied inhomogeneous color superconductors in detail and in particular crystalline color superconductors. We have also reviewed the possible astrophysical signatures associated with the presence of Crystalline Color SuperConducting (CCSC) phases within the core of compact stars [27]. In particular, the CCSC phase can sustain large shear stresses, supporting torsional oscillations of large amplitude. We have studied the electromagnetic signals produced by torsional oscillations of strange stars with a crystalline color superconducting crust. We have estimated that the emitted EM power could be quite large for frequency in the GHz band, and both frequency that power depend on the crust thickness [28].

- Gravitational waves
  A large collaboration involving gravitational waves detectors, i.e. Ligo and Virgo, and neutrinos detectors, i.e. LVD, Borexino and IceCube, we started developing techniques and strategies for joint analysis of Neutrinos and Gravitational Waves emitted by Core Collapse Supernovae. This is the Phase 1 of a structured proposal submitted and accepted by several detectors (neutrino detectors and GW detectors) to increase the detection probability for these complex astrophysical events.

Publications in journals, proceedings and preprints

[1] V. Azcoiti, G. Di Carlo, E. Follana and A. Vaquero, Phys. Lett. B **744**, 303 (2015) [arXiv:1410.5733 [hep-lat]].

[2] D. G. Phillips, W. M. Snow, K. Babu, S. Banerjee, D. V. Baxter, Z. Berezhiani *et al.*, “Neutron-Antineutron Oscillations: Theoretical Status and Experimental Prospects,” [arXiv:1410.1100 [hep-ex]]; Phys.Reports (in press)

[3] A. Addazi and M. Bianchi, “Neutron Majorana mass from exotic instantons,” JHEP **1412**, 089 (2014)

[4] O. Benhar, R. Biondi and E. Speranza, “Short-range correlation effects on the nuclear matrix element of neutrinoless double-β decay,” Phys. Rev. C **90**, no. 6, 065504 (2014)

[5] D. Ejlli and A. D. Dolgov, "CMB constraints on mass and coupling constant of light pseudoscalar particles," Phys. Rev. D **90**, no. 6, 063514 (2014)

[6] D. Ejlli, "Bounds on QCD axion mass and primordial magnetic field from CMB μ-distortion," Phys. Rev. D **90**, no. 12, 123527 (2014)

[7] D. Comelli, F. Nesti and L. Pilo, JCAP **1411**, no. 11, 018 (2014) [arXiv:1407.4991 [hep-th]].

[8] D. Comelli, M. Crisostomi and L. Pilo, Phys. Rev. D **90**, 084003 (2014) [arXiv:1403.5679 [hep-th]].

[9] M. Mannarelli, G. Pagliaroli, A. Parisi, L. Pilo and F. Tonelli, arXiv:1504.07402 [astro-ph.SR].

[10] D. Comelli, F. Nesti and L. Pilo, JCAP **1405**, 036 (2014) [arXiv:1307.8329 [hep-th]].

[11] F. L. Villante, A. M. Serenelli, F. Delahaye and M. H. Pinsonneault, Astrophys. J. **787**, 13 (2014) [arXiv:1312.3885 [astro-ph.SR]].

[12] G. Bellini, L. Ludhova, G. Ranucci and F. L. Villante, Adv. High Energy Phys. **2014**, 191960 (2014) [arXiv:1310.7858 [hep-ph]].

[13] E. Babichev and M. Crisostomi, Phys. Rev. D **88**, no. 8, 084002 (2013) [arXiv:1307.3640].

[14] S. Dell'Oro, S. Marcocci and F. Vissani, Phys. Rev. D **90**, no. 3, 033005 (2014) [arXiv:1404.2616 [hep-ph]].

[15] C. Lujan-Peschard, G. Pagliaroli and F. Vissani, JCAP **1407**, 051 (2014) [arXiv:1402.6953 [astro-ph.SR]].

[16] R. Aloisio, V. Berezinsky and P. Blasi, JCAP **1410**, no. 10, 020 (2014) [arXiv:1312.7459 [astro-ph.HE]].

[17] V. S. Berezinsky, V. I. Dokuchaev and Y. N. Eroshenko, Phys. Usp. **57**, 1 (2014) [Usp. Fiz. Nauk **184**, 3 (2014)] [arXiv:1405.2204 [astro-ph.HE]].

[18] V. Berezinsky, Astropart. Phys. **53**, 120 (2014) [arXiv:1301.0914 [astro-ph.HE]].

[19] P. Blasi, Nucl. Phys. Proc. Suppl. B **256-257**, 36 (2014) [arXiv:1412.8430 [astro-ph.HE]].

[20] A. Aab *et al.* [Pierre Auger Collaboration], Astrophys. J. **789**, 160 (2014) [arXiv:1406.2912 [astro-ph.HE]].

[21] A. Aab *et al.* [Pierre Auger Collaboration], Astrophys. J. **789**, L34 (2014) [arXiv:1406.4038 [astro-ph.HE]].

[22] P. Blasi, Comptes Rendus Physique **15**, 329 (2014) [arXiv:1403.2967 [astro-ph.HE]].

[23] D. Boncioli [Pierre Auger Collaboration], Nucl. Instrum. Meth. A **742**, 22 (2014).

[24] A. Aab *et al.* [Pierre Auger Collaboration], Phys. Rev. D **89**, no. 5, 052002 (2014) [arXiv:1402.3677 [astro-ph.HE]].

[25] A. Aab *et al.* [Pierre Auger Collaboration], JCAP **1408**, no. 08, 019 (2014) [arXiv:1407.3214 [astro-ph.HE]].

[26] A. Aab *et al.* [Telescope Array and Pierre Auger Collaboration], Astrophys. J. **794**, no. 2, 172 (2014) [arXiv:1409.3128 [astro-ph.HE]].

[27] R. Anglani, R. Casalbuoni, M. Ciminale, N. Ippolito, R. Gatto, M. Mannarelli and M. Ruggieri, Rev. Mod. Phys. **86**, 509 (2014) [arXiv:1302.4264 [hep-ph]].

[28] M. Mannarelli, G. Pagliaroli, A. Parisi and L. Pilo, Phys. Rev. D **89**, no. 10, 103014 (2014) [arXiv:1403.0128 [hep-ph]].

[29] M. Mannarelli, EPJ Web Conf. **80**, 00039 (2014) [arXiv:1409.3667 [astro-ph.HE]].

[30] M. Mannarelli, arXiv:1401.7551 [hep-ph].

Conferences, seminars and other activities

Quantum gravitational spectroscopy with ultracold systems, Les Houches, France, 2014; (Talk, Z. Berezhiani)

“The Structure and Signals of Neutron Stars, from Birth to Death”, GGI, Florence, 2014, (Seminar talk, Z. Berezhiani)

“IFAE 2014 - Incontri di Fisica delle Alte Energie”, L’Aquila, Italy, 2014; (Talk, R. Biondi)

“NNbar@ESS first workshop”, CERN, Geneve, Switzerland, 12 – 13 June 2014; (Seminar, Z. Berezhiani)

“NOW 2014: Neutrino Oscillation Workshop”, Conca Specchiulla, Otranto, Lecce, Italy 2013 (Talk, Z. Berezhiani)

“Multiple Messengers and Challenges in Astroparticle Physics”, October 6-17, GSSI L’Aquila, Italy 2014 (Seminar, L. Pilo)

“New Frontiers in Theoretical Physics”, Cortona, Italy, 2014 (Talk, L. Pilo)

“Cosmology and Astroparticle Physics”, University of Geneva, 2014 (Invited seminar, L. Pilo)

Dipartimento di Fisica Univ. Milano, Italy, 2014 (Invited seminar, L. Pilo)

“The Structure and Signals of Neutron Stars, from Birth to Death” GGI, Florence, 2014 (Talk, Pagliaroli)

“Multiple Messengers and Challenges in Astroparticle Physics”, 2014 (Talk, Pagliaroli)

“SIGRAV XXI Conference”, Alessandria, 2014 (Talk, Pagliaroli)

What Next 2014, “Neutrino Oscillations”, Padova (Talk, Pagliaroli)

IFAE 2014 ”Incontri di fisica delle Alte Energie. L’Aquila 9-11 Aprile 2014 (Poster, Parisi)

Int. Workshop, “The Structure and Signals of Neutron Stars, from Birth to Death” GGI, Florence, 2014 (Lecture, Mannarelli)

“QCD@work”, Giovinazzo, Bari, 2014 (Talk, Mannarelli)

“Incontro Nazionale di Fisica Nucleare”, Padova, Italy, 2014 (Invited talk, Mannarelli)

“CSQCD IV”, Prerow, Germany, 2014 (Talk, Mannarelli)

Activity in INFN and International organizations

R. Aloisio is a member of the GSSI Scientific Board.

Z. Berezhiani organizes the Int. Workshop “Hot Topics in Modern Cosmology” in Cargese, is coordinator of the L’Aquila unit of PRIN biennal grant 20084ZCK5J-004 “Astroparticle Physics”, is scientific Coordinator of the Russian Science and Education Ministry biennial Grant N. 14.U02.21.0913 ”Physics of solar, reactor and geo-neutrinos” at JINR, Dubna (2012-2013).

V. Berezinsky is a member of Councel ”Cosmic Ray Research” (Russia), a member of Int. Advisory Board of JEM-EUSO, a member of Int. Scientific Advisory Committee of Gigaton Volume Detector of High Energy Neutrinos.

M. Mannarelli is the scientific secretary of the LNGS. Coordinator of the CFA and co-organizer of the LNGS seminars.

L. Pilo is member of the Doctorate Collegium of the Physics Dept. and of the Doctorate Commission, University of L’Aquila and teaches Weak and Strong Interactions I at the University of L’Aquila.

F.L. Villante is a member of the Scientific Board of the Center for Astroparticle Physics (”Sapere e Crescita”) at LNGS.

F. Vissani is the physics area coordinator and Chair of the GSSI Astroparticle Physics PhD Committee, co-organizer of the LNGS seminars, observer in Comm.II on behalf of Comm.IV, referee for the INFN National Permanent Committees II on non-accelerator physics and IV on theoretical physics, LNGS representative in the Italian Physics Society, INFN representative in the Scientific Advisory Committee of ApPEC/ASPERA, member of the scientific committee for the ICRANet-INFN agreement, member of the scientific council of the Groupement de Recherche Neutrino (CEA and IN2P3), coordinator of the CFA, lecturer of two PhD neutrino courses, one at the University of Milan and one at the University of Catania.

The XENON experiments

E. Aprile[a,*], F. Agostini[b,c], M. Alfonsi[d,e], L. Arazi[f], K. Arisaka[g], F. Arneodo[h],
M. Auger[i], C. Balan[j], P. Barrow[i], L. Baudis[i], B. Bauermeister[e], A. Behrens[i],
A. Brown[k], E. Brown[l,m], S. Bruenner[n], G. Bruno[l], R. Budnik[f], L. Butikofer[o],
J. M. R. Cardoso[j], M. Cervantes[k], D. Coderre[o], A. P. Colijn[d], H. Contreras[a],
J. P. Cussonneau[p], M. P. Decowski[d], A. Di Giovanni[h], E. Duchovni[f], S. Fattori[e],
A. D. Ferella[b], A. Fieguth[l], W. Fulgione[b], M. Garbini[c], C. Geis[e], L. W. Goetzke[a],
C. Grignon[e], E. Gross[f], W. Hampel[n], R. Itay[f], F. Kaether[n], B. Kaminsky[o],
G. Kessler[i], A. Kish[i], H. Landsman[f], R. F. Lang[k], M. Le Calloch[p], D. Lellouch[f],
L. Levinston[f], C. Levy[l,m], S. Lindemann[n], M. Lindner[n], J. A. M. Lopes[j],
A. Lyashenko[g], S. Macmullin[k], T. Marrodán Undagoitia[n], J. Masbou[p],
F. V. Massoli[c], D. Mayani Paras[i], A. J. Melgarejo Fernandez[a], Y. Meng[g],
M. Messina[a], B. Miguez[q], A. Molinario[q], M. Murra[l], J. Naganoma[r],
U. Oberlack[e], S. E. A. Orrigo[j,†], P. Pakarha[i], E. Pantic[g], R. Persiani[c],
F. Piastra[i], J. Pienaar[k], G. Plante[a], N. Priel[f], L. Rauch[n], S. Reichard[k],
C. Reuter[k], A. Rizzo[a], S. Rosendahl[l], J. M. F. dos Santos[j], G. Sartorelli[c],
S. Shindler[e], J. Schreiner[n], M. Schumann[o], L. Scotto Lavina[p], M. Selvi[c],
P. Shagin[r], H. Simgen[n], A. Teymourian[g], D. Thers[p], A. Tiseni[d], G. Trinchero[q],
C. Tunnell[d], O. Vitells[f], R. Wall[r], H. Wang[g], M. Weber[n,a] and C. Weinheimer[l]
(The XENON Collaboration)

---

[*] Spokesperson

[†] Present address: IFIC, CSIC-Universidad de Valencia, Valencia, Spain

[a] Physics Department, Columbia University, New York, NY, USA
[b] INFN-Laboratori Nazionali del Gran Sasso and Gran Sasso Science Institute, L'Aquila, Italy
[c] Department of Physics and Astrophysics, University of Bologna and INFN-Bologna, Bologna, Italy
[d] Nikhef and the University of Amsterdam, Science Park, Amsterdam, Netherlands
[e] Institut für Physik & Exzellenzcluster PRISMA, Johannes Gutenberg-Universität Mainz, Mainz, Germany
[f] Department of Particle Physics and Astrophysics, Weizmann Institute of Science, Rehovot, Israel
[g] Physics & Astronomy Department, University of California, Los Angeles, CA, USA
[h] New York University in Abu Dhabi, Abu Dhabi, United Arab Emirates
[i] Physics Institute, University of Zürich, Zürich, Switzerland
[j] Department of Physics, University of Coimbra, Coimbra, Portugal
[k] Department of Physics and Astronomy, Purdue University, West Lafayette, IN, USA
[l] Institut für Kernphysik, Wilhelms-Universität Münster, Münster, Germany
[m] Department of Physics, Applied Physics and Astronomy, Rensselaer Polytechnic Institute, Troy, NY, USA
[n] Max-Planck-Institut für Kernphysik, Heidelberg, Germany
[o] Albert Einstein Center for Fundamental Physics, University of Bern, Bern, Switzerland
[p] SUBATECH, Ecole des Mines de Nantes, CNRS/In2p3, Université de Nantes, Nantes, France
[q] INFN-Torino and Osservatorio Astrofisico di Torino, Torino, Italy
[r] Department of Physics and Astronomy, Rice University, Houston, TX, USA

Abstract

Year 2014 has represented a very important milestone for the XENON collaboration. While operating, analyzing and publishing data from the running XENON100 experiment, performing novel NR and ER calibrations, and testing new purifications and data acquisition tools, the construction of the XENON1T experiment run at full steam in all the various subsystem. This experiment, sited in Hall B of LNGS, will be two orders of magnitude more sensitive than XENON100. XENON1T installation will be completed during 2015 and we will start collecting data by the end of that year.

1 Introduction

The XENON collaboration operates a series of direct detection experiments at LNGS to search for dark matter particles in our Milky Way. The experiments use dual-phase liquid xenon time-projection chambers (TPCs) which are particularly well-suited to search for one of the most compelling dark matter candidate particle, the Weakly Interacting Massive Particle (WIMP), over a broad range of parameters. Starting with the XENON10 experiment more than a decade ago, the collaboration has successively built larger and more sensitive detectors. The XENON100 experiment was the world's most sensitive direct detection dark matter experiment for a number of years, until late 2013. The collaboration is currently constructing the next experiment, XENON1T, which itself will be two orders of magnitude more sensitive than XENON100, with a sensitivity goal of $2 \times 10^{-47}\,\mathrm{cm}^2$; we expect to get the first signals from the detector by the end of 2015. Most of the infrastructure and detector design for XENON1T is such that it can be reused for an even larger upgrade in the future, with 7 t of liquid xenon inside, to gain another order of magnitude in sensitivity.

2 XENON100

2.1 Operation status

A new dark matter search run was started in April 2013 and ended in January 2014, with more than 150 days of data collected. These data were complemented with a dedicated ^{241}AmBe neutron calibration run and regular calibrations using gamma sources.

The data of this run are now in final stages towards unblinding: they will complete more than two years for annual modulations study, and will improve the sensitivity of the experiment to WIMPs when combined with the already published data.

During 2014 the XENON100 run was dedicated mainly to take calibration data with a new source, ^{88}YBe, which allows to get a deeper insight into the sensitivity for low mass WIMPs. This source provides nuclear recoils similar to those of a few-GeV WIMP, and it is the first time that this kind of measurement is performed in a liquid xenon detector.

XENON100 continues to run healthy and to provide science data: in the coming months it will be used to test a novel system for inline ^{222}Rn removal by cryogenic distillation, to calibrate the response of the detector to ER with a ^{83m}Kr source, and for DAQ tests relevant for the XENON1T system.

2.2 Published Data

The XENON collaboration continued to analyze and publish results based on the same 225 day data-set used in Ref. [1].

The ultra-low background of XENON100 has enabled to study interactions different from the WIMP-nucleus ones, even without ER background rejection. A sensitive search for the interactions of solar axion and galactic axion-like particles with electrons has been carried out and published in [2]. A summary of the work is presented in the next subsection.

2.2.1 First Axion Results from the XENON100 Experiment

Axions and Axion-Like Particles (ALPs) can be detected through their different electromagnetic couplings with photons ($g_{A\gamma}$), electrons (g_{Ae}) and nuclei (g_{AN}). The g_{Ae} coupling can be tested looking for scatterings off the electrons of the Xe atoms through the axio-electric effect. Thus, for this analysis, all the events in the ER band has been considered after the application of all the quality cuts: they are shown in figure 1.

The energy deposited by each interaction is obtained using the observed $S1$ signal. The keV - PE conversion is performed using the NEST model (v0.98) [3]. This takes into account the scintillation efficiency $R(E)$ relative to the 32.1 keV transition of ^{83m}Kr at zero electric field (as chosen by [4] and [5]) and the quenching factor $Q(E)$ for a non-zero electric field (measured by [5] for values close to the field applied in XENON100). The model agrees with the direct measurements at zero field [4, 5], as well as the measurements with a non-zero field [6, 5]. The uncertainty on $R(E) \times Q(E)$ is taken from NEST and assumed to be Gaussian. This reflects the intrinsic uncertainty of the model (4%) as well as the spread in the measured data points, particularly relevant at low energies. The conversion from the energy deposition, E, to the observed signal in photoelectrons (pe), n^{exp}, is thus given by:

$$n^{exp}(E) = R(E) \times Q(E) \times f \times E \equiv L_Y(E) \times E.$$

The event rate with a given number of detected photons, n, is obtained by applying Poisson

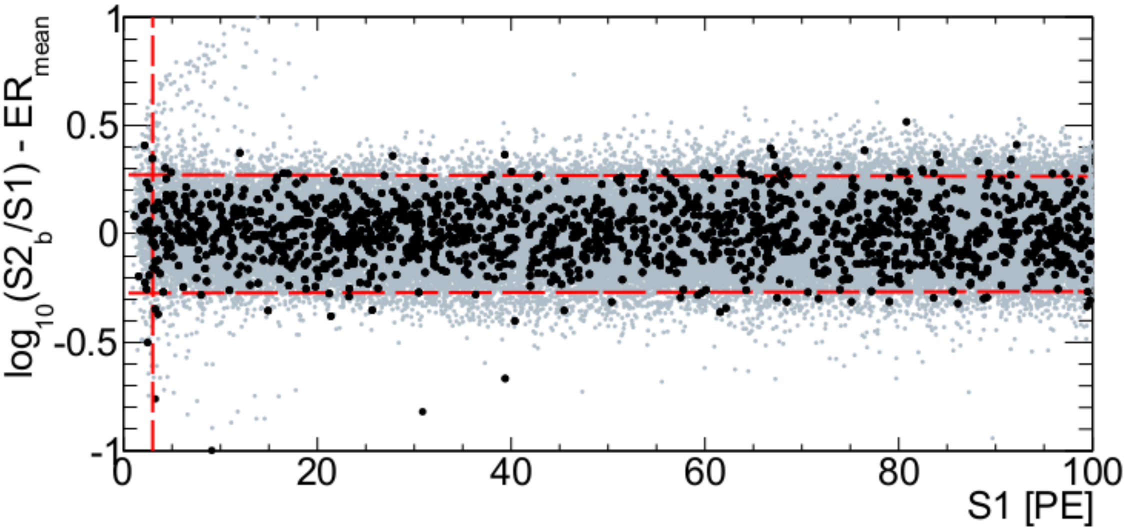

Figure 1: Event distribution in the flattened $\log_{10}(S2_b/S1)$ vs. $S1$ space for science data (black points) and calibration (grey points). Straight dashed lines show the selection cut on the flattened $\log_{10}(S2_b/S1)$ (horizontal red lines) and the 3 PE threshold cut (red vertical line).

smearing to the predicted energy spectrum dR/dE,

$$\frac{dR}{dn} = \int_0^\infty \frac{dR}{dE} \times \text{Poiss}\left(n|n^{exp}(E)\right) dE.$$

The spectrum of the 393 events, between 3 and 30 PE and after all the selection cuts, are shown in Fig. 2 (left) as a function of $S1$. The solid grey line shows the background model. The expected $S1$ spectrum for solar axions, lighter than 1 keV/c^2, is shown as a blue dashed line for g_{Ae}= 2×10^{-11}, *i.e.* the best limit so far, reported by the EDELWEISS-II collaboration [7]. The data are compatible with the background model, and no excess is observed for the background only hypothesis.

Fig. 2 (right) shows the XENON100 exclusion limit on g_{Ae} at 90% CL. The sensitivity is shown by the green/yellow band ($1\sigma/2\sigma$). As we used the most recent and accurate calculation for solar axion flux from [8], which is valid only for light axions, we restrict the search to $m_A < 1$ keV/c^2. For comparison, we also present other recent experimental constraints [7, 9, 10]. Astrophysical bounds [11, 12, 13] and theoretical benchmark models [14, 15, 16, 17] are also shown. For solar axions with masses below 1 keV/c^2 XENON100 is able to set the strongest constraint on the coupling to electrons, excluding values of g_{Ae} larger than 7.7×10^{-12} (90% CL).

For a specific axion model the limit on the dimensionless coupling g_{Ae} can be translated to a limit on the axion mass. Within the DFSZ and KSVZ models [14, 15, 16, 17] XENON100 excludes axion masses above 0.3 eV/c^2 and 80 eV/c^2, respectively. For comparison, the CAST experiment, testing the coupling to photons, $g_{A\gamma}$, has excluded axions within the KSVZ model in the mass range between 0.64 - 1.17 eV/c^2 [18, 19].

In Fig. 3 (left) we show the XENON100 data after the selection cuts in the larger energy region of interest used for the search for non-relativistic galactic ALPs (1422 surviving events), along with their statistical errors. Also shown is the expected signal for different ALP masses, assuming a coupling of g_{Ae}= 4×10^{-12} and that ALPs constitute all of the galactic dark matter.

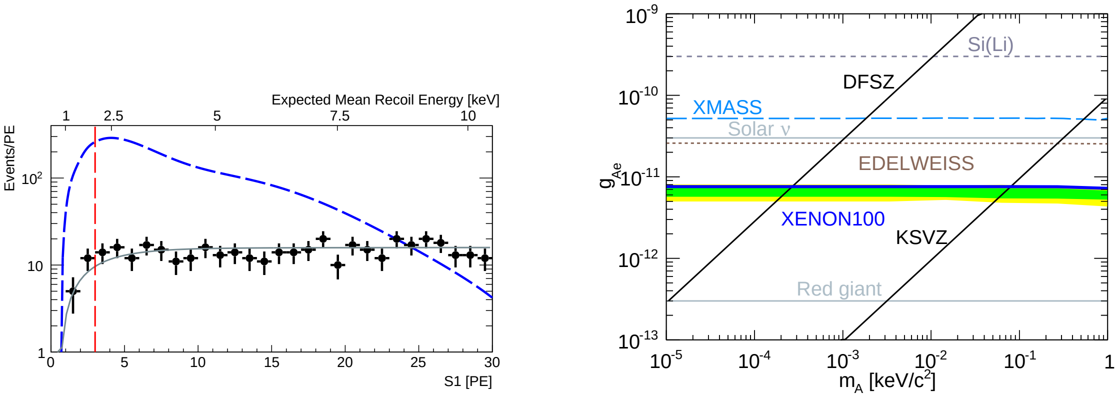

Figure 2: *Left*: Event distribution of the data (black dots), and background model (grey) of the solar axion search. The expected signal for solar axions with $m_A < 1$ keV/c^2 is shown by the dashed blue line, assuming g_{Ae}= 2×10^{-11}, the current best limit, from EDELWEISS-II [7]. The vertical dashed red line indicates the low $S1$ threshold, set at 3 PE. The top axis indicates the expected mean energy for electronic recoils as derived from the S1 signal. *Right*: The XENON100 limits (90% CL) on solar axions is indicated by the blue line. The expected sensitivity, based on the background hypothesis, is shown by the green/yellow bands ($1\sigma/2\sigma$). See text for the legenda of the other lines.

The width of the monoenergetic signal is given by the energy resolution of the detector at the relevant $S1$ signal size [22]. As for the solar axion search, the data is compatible with the background hypothesis, and no excess is observed for the background-only hypothesis for the various ALP masses.

The XENON100 90% CL exclusion limit for galactic ALPs is shown in Fig. 3 (right), together with other experimental constraints [20, 21, 7]. Astrophysical bounds [11, 12, 13] and the KSVZ benchmark model [16, 17] are also presented. The expected sensitivity is shown by the green/yellow bands ($1\sigma/2\sigma$). In the 5 - 10 keV/c^2 mass range, XENON100 sets the best upper limit, excluding an axion-electron coupling $g_{Ae} > 1 \times 10^{-12}$ at the 90% CL, assuming that ALPs constitute all of the galactic dark matter.

2.2.2 Other ongoing analysis

Several data analysis are underway in different phases of completion or close to submission, including: full lifetime limit of the experiment in both SI and SD interaction models, annual modulation, low mass WIMP analysis using S2 only data, inelastic NR analysis and exclusion limits for various interaction models (leptophylic, asymmetric and others) based of ER data. We expect several of these analyses to be concluded and submitted in the first months of 2015.

3 XENON1T

XENON1T is the successor to the XENON100 experiment and 2014 was an important year for this phase of the XENON-series of experiments. With a design sensitivity two orders of magnitude better than XENON100, over a broad range of WIMP masses and interaction types, this first LXe TPC experiment at the tonne-scale will have significant discovery potential. In designing the experiment, we have built-in the possibility for a rapid sensitivity scale-up by

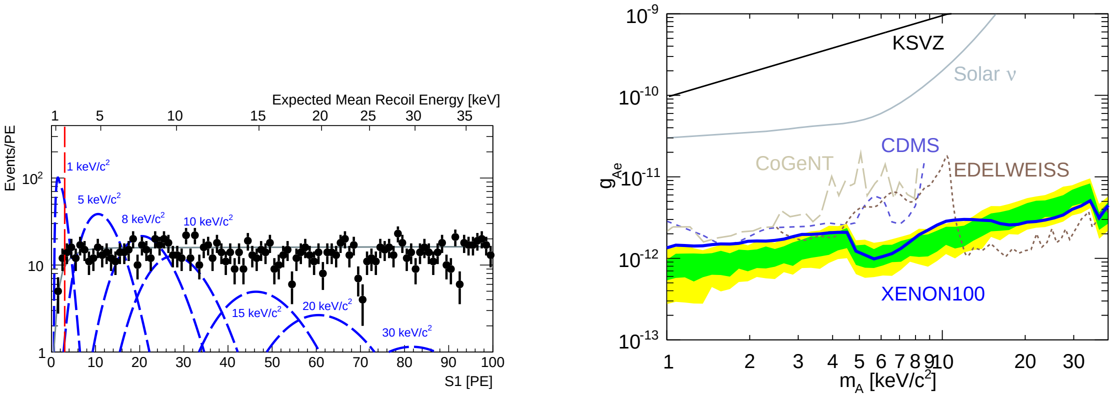

Figure 3: *Left*: Event distribution in the galactic ALPs search region between 3 and 100 PE (black dots). The grey line shows the background model used for the profile likelihood function. The red dashed line indicates the $S1$ threshold. The expected signal in XENON100 for various ALP masses, assuming $g_{Ae} = 4 \times 10^{-12}$, is shown as blue dashed lines. The top axis indicates the expected mean energy for electronic recoils as derived from the observed $S1$ signal. *Right*: The XENON100 limit (90% CL) on ALP coupling to electrons as a function of the mass, under the assumption that ALPs constitute all the dark matter in our galaxy (blue line). The expected sensitivity is shown by the green/yellow bands ($1\sigma/2\sigma$). See text for the meaning of the other lines.

another order of magnitude, by enabling a ∼ 2× larger LXe detector to fit into the same cryostat while re-using most of the other systems developed for XENON1T. XENON1T is in full steam of commissioning phase, with expected full operation by the end of 2015. Below we detail the progress and plans of all subsystems, leading to this goal.

Water Tank and Muon Veto

The Water Tank (WT) for XENON1T, to be filled with 700 m^3 of ultra pure water and instrumented with PMTs for an active Cherenkov Muon Veto, is a stainless steel cylinder, 9.6 m diameter and 9 m high, with a conical roof rising an additional 3.2 m. It was completed at the end of 2013 and, in order to test the mechanical stability of the tank and identify possible water leaks, an hydrostatic test was done at the beginning of 2014 after the required approvals and discharge line were provided by the LNGS technical staff. The tank was slowly filled with water (total filling time was 26 hours) while the shell displacement was measured. After a period of 12 hours during which no leaks were identified, the water was removed. The inspection of the tank showed no damage.

The muon veto installation progressed well during 2014. All the PMTs for the Muon Veto (MV) system have been tested both in air (in Bologna and Mainz) and in water (at LNGS) together with the electronics to be used (HV power supply, digitizers and trigger card). Two different calibration systems have been tested and the reflective foil has been characterized. The PMTs mounting structures have been constructed and tested. In autumn, after construction of a scaffold along the inside wall of the water tank, the installation of reflective foil on the side walls has been completed, together with the installation of PMTs at the top and side of the water tank. Stainless steel cable trays have been fixed in their positions, then the PMT cables and the fibers for optical calibrations have being routed through flanges on the top of the tank

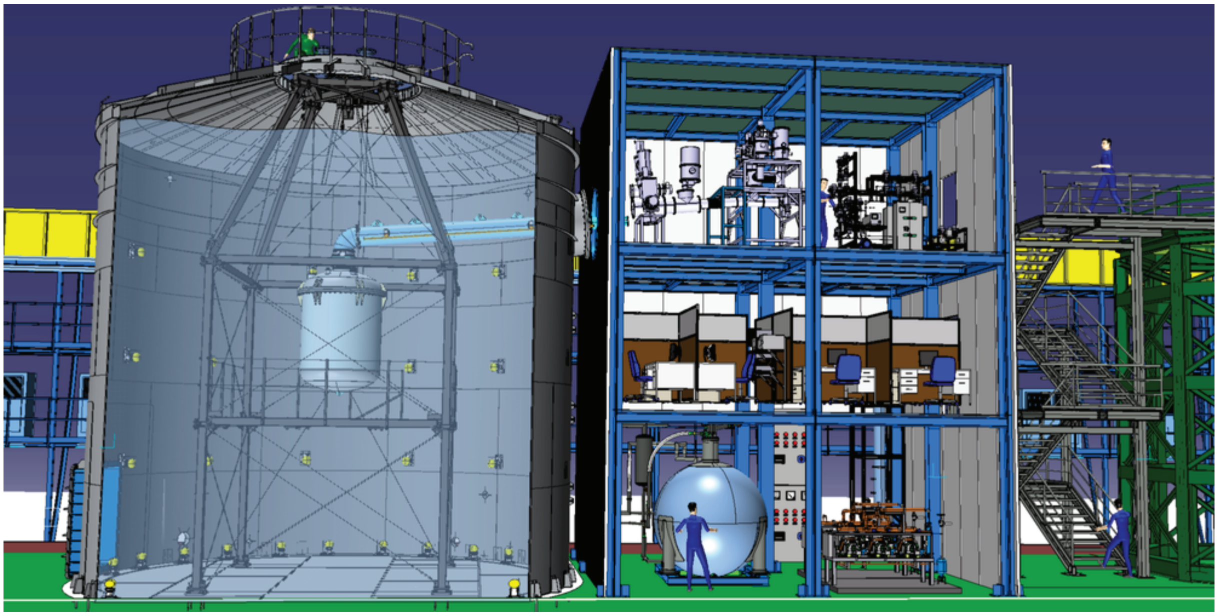

Figure 4: 3D rendering of XENON1T. The cryostat housing the dual-phase xenon TPC is hanging in the middle of the water tank (left). The service building with all equipment to support running the experiment, has three, fully packed, floors.

to the roof. Looking further, cable routing on the roof is in preparation, and cable trays from the side of the water tank down to the data acquisition room in the support building are already in place.

At the end of 2014 we published the design study of the muon veto system: the performances are very good, we obtain a detection efficiency $> 99.5\%$ for muons crossing the WT and $> 70\%$ for showers of secondary particles from muon interactions in the rock. This allows to keep the background produced by muon-induced neutrons down to a negligible level, less than 0.01 events per year in the 1 ton fiducial volume [24].

Service building

The construction of the service building has been completed with floors, doors, glass panels walls and external stairs. The electrical plant (with open network and tel distribution and external fiber connection) has been completed. The internal Slow Control network will be completed in early 2015. The study of the remaining service and safety plants is started. This includes: conditioning of the electronics room; fire system; oxygen detectors; and ventilation and exhaust. The tender procedure is also started, the work should be completed in mid 2015. The water plant is progressing as well, LNGS staff (Ing. Balata and Ing. Gallese) is designing the system (mechanics and controls).

Cryostat and support

The production of the support structure was finished at VDL company (http://www.vdlsystems.nl). After an on-site assembly test at VDL the structure was delivered at LNGS. In May 2014 the support structure with the temporary working platform was successfully assembled. In spring 2015 the last components of the cryostat leveling mechanism will be installed on top of the water

Figure 5: *Left:* The cryostat of XENON1T with its umbilical pipe, installed on the support structure; the outer thermal insulation vessel is not mounted. The Muon Veto PMTs are also visible, attached to the Water Tank, together with the reflective foil. *Right:* The service building: on the ground floor the ReStoX and Distillation systems, at floor 1 the DAQ room and at floor 2 the Purification and Cryogenic systems.

tank.

The construction of the Cryostat, consisting of a double walled superinsulated vessel and cryogenic/cables pipe, was completed in July at the ALCA Technology Company, near Vicenza. The key requirements for this system are the low heat-load (50 W) and the low background level. The forming of the two cylindrical shells for the inner and outer vessels and that of the end caps has been realized with the goal of minimizing the welds, a known source of Rn emanation. The stainless steel plates used have been selected after a long screening campaign to identify materials with activity in U, Th, Co and K, low enough for the background constrains of the experiment. The design of the pipes needed to connect the cryostat to the cooling and DAQ systems, outside of the water tank, was largely simplified resulting in a single pipe carrying multiple lines and cables. The signal and HV cables were installed prior to delivery to LNGS, and were tested for Rn emanation. The overall installation procedure of the system inside the tank has been worked out. Finally, the design reflects the requirement for a future upgrade of the detector with a Xe mass increased to about 7 tonnes, by replacing the current inner vessel with a new one of larger diameter.

The Cryogenic pipe with temporary end caps was installed first and successfully fastened to the roof of the water tank, positioned with five degrees angle as from design. Subsequently the inner vessel with its dome and also the dome of the outer vessel were connected to the leveling system. The outer vessel was not installed to allow for the leak test of the inner vessel. Presently, the inner volume of the Cryostat is under test and a vacuum of few 10^{-7} mbar has been achieved. The metal sealing (Helicoflex) of the inner vessel has been tested and a leak rate less than 10^{-9} mbar l/s has been measured.

Cryogenics

The cryogenic system of XENON1T was shipped to LNGS in 2014, arrived safely, and has been installed in the top floor of the building. At the end of 2014 it was very close to be ready for first operation on the experiment; it is coupled with the purification, ReStoX and cryostat. The system was screened for ^{222}Rn emanation, and will next be attached to the umbilical tube and the cryostat.

Purification system

The purification system was delivered to LNGS on July 2nd 2014, and was installed in the service building in its final location. Its installation at the end of 2014 is at an advanced stage, with all of the sensors, actuators, getters and the HALO water monitor mounted on the system and operational. The system has been leak checked with a He leak detector and is leak tight at the level of 10^{-10} mbar l/s. The connections to ReStoX and Cryogenics has been completed. The Construction of two QDrive circulation pumps is completed, which includes a new epoxy coating on the magnets to reduce the Rn emanation.

Distillation system

The commissioning of the cryogenic distillation column phase 2 (3m package, 5m total height) has been successfully completed off site. Some measurements have been taken to allow stable operation with rather dirty input gas. The phase 2 distillation column for XENON1T completely fulfills the requirements of XENON1T and all our measurements confirmed or surpassed the results obtained during the distillation column phase 1. The design through-put of 3 kg/h was confirmed, stable distillation was tested up to about 7 kg/h. By using a RGA behind a LN_2 cryotrap the krypton-in-xenon concentration could be measured online down to 200 ppt. For high krypton dopings the design separation factor of 10^5 was confirmed by measurements. For low krypton dopings of the input gas the krypton-in-xenon concentration of the output gas was below the detection limit. Pipettes with distilled xenon were sent to MPIK Heidelberg and to Columbia University, which possess ultra-sensitive krypton-in-xenon measurement devices. The confirmation of krypton-in-xenon concentrations at the ppq level like for the phase 1 distillation column is expected. A 60 MBq ^{83}Rb generator has been used to inject the fast decaying isomer ^{83m}Kr into the input gas and to study the dynamics of the distillation process by several ^{83m}Kr-decay detectors in detail. A paper on this novel ^{83m}Kr tracer method has been published in JINST [23]. Dirty xenon gas from an air leak at XENON100 has been successfully distilled.

The column has been downgraded to phase 1 (1.2 m package, 3 m total height) for better transportation and for another distillation test at XENON100: Radon is expected to be the most important source of background for XENON1T. We want to test experimentally whether a continuous distillation of the xenon gas from XENON1T will reduce the radon-in-xenon concentration when run in opposite direction (at the temperature of liquid xenon, krypton has a 10 times higher vapor pressure w.r.t. xenon but radon has a 10 times lower vapor pressure w.r.t. xenon). For this test the XENON100 detector will be used as radon source and radon detector.

ReStoX

The Xe recovery and storage (ReStoX) system has been successfully built by the Italian company Costruzioni Generali, and installed in the ground floor of the service building on Aug. 13th. Then the commissioning phase started.

The ReStoX system, based on a 2.1 m diameter spherical double walled stainless steel pressure vessel, is able to store 7.6 tonnes both in supercritical, liquid or even solid state. Such a capacity will enable ReStoX to serve also for the upgraded XENON1T detector. The cooling system is based on two nitrogen-based systems: a 3 kW condenser, made of copper mounted inside the sphere, enables ReStoX to keep the xenon in liquid state for filling into the TPC; a system of cooling lines surrounding the inner sphere is powerful enough to enable ReStoX to efficiently and rapidly recover the LXe from the detector, in case of emergency. All cryogenic valves connecting ReStoX to the cryogenic system have been carefully selected for ultra-low internal and external leak rates. All ReStoX components that will be in contact with xenon have been electro-polished.

The construction at the company has been followed closely also by a cryogenic expert, hired by the Collaboration to follow the commissioning of ReStoX. The system has been connected with the external nitrogen dewars and with other XENON1T subsystems, namely the cryogenic and purification. We reached already a ultra-low vacuum in the insulation jacket (required for the insulation) and in the internal sphere (prerequisite to fill it with xenon). The first cooling of the sphere is foreseen in early 2015, after that we will start filling ReStoX from xenon bottles.

The Collaboration is also progressing on the collection of all xenon bottles from different sites to LNGS. Prior to transferring the Xe gas into ReStoX, each bottle will be sampled for a quick analysis of impurities content. The gas bottles manifold and the gas analytics tools needed for this phase is ready.

TPC

The TPC working group is approaching the important step of the critical TPC design review by engineers and the collaboration. Only minor design details, such as the treatment of the PTFE reflector walls, the final thickness of the cathode electrode and levelmeters, are still to be finalized and awaiting the results from ongoing tests and analyses. The main emphasis is now on material identification (together with the screening WG) and procurement. All required stainless steel raw material is already at hand. The OFHC copper and PTFE for the PMT arrays have been identified and we are actively searching for the raw material for the PTFE reflectors and field shaping rings. The latter are connected by two chains of resistors, which have already been selected among many options, in order to fulfill the requirements in terms of lowest radioactive contamination. Tests on the soldering procedure are ongoing to ensure that the electrical contacts will withstand the mechanical stress due to the cold temperature. As all parts of the TPC have to fit together, the machining of any piece will only start after the entire design has been frozen after the review. Due to the distributed production at all participating institutions or at external companies we expect a production within schedule. At the end of 2014 we were finalizing the details of the assembly procedures for all sub-systems (TPC field cage, top and bottom PMT arrays, TPC electrode stack) and of the full TPC in the above ground cleanroom. The entire TPC will be transported into the LNGS tunnel by truck and will be installed in one piece inside the watertank in hall B, using the same lifting devices which have been successfully used to lift and close the cryostat. The connection of the PMTs to the signal and high voltage cables, which have already been installed inside the pipe connecting to the XENON building, is performed efficiently via of custom-made low-background connectors.

PMTs

A total of 255 R11410-21 PMTs have been ordered for XENON1T. Out of these, 166 R11410-21 PMTs have been already delivered by the Hamamatsu company. The rest will be delivered by the end of February 2015. We continuously screen the tubes using low-background germanium spectrometers at LNGS to assess their radioactive contamination. After the screening at LNGS, the tubes undergo measurements at room temperature and at -100°C. By the end of 2014 113 tubes have been tested. Each tube is cooled down at least three times to test robustness to thermal contractions/expansions. The cooling and warming-up rates are slow, in order to fulfill the Hamamatsu upper limit of 2 K/min. As previously reported, the tubes show a very good separation of the single photo-electron (SPE) from the noise, a low after-pulse rate and a low dark count rate at -100°C, of several tens of Hz. A subset of 12 tubes are operated directly in a dedicated LXe detector, in 2-3 cool down cycles. The performance of these tubes is comparable with the previous results. The voltage divider (base) for the tube has been screened with the final components and the radioactivity results fulfill the requirements for XENON1T. A few final base prototypes have been successfully tested for their electrical performance at room temperature and at -100°C in two setups. The final measurement of the radon emanation from the base is ongoing. Afterwards the Cirlex substrates for all the bases will be ordered, and the bases will be manufactured and tested. We are currently preparing the installation of the tubes into their support structures. Once installed, the tubes will be tested one more time to confirm proper connection and performance with the final bases and cables. This operation is planed for March/April of next year.

DAQ

The data acquisition (DAQ) system for XENON1T is in progress. The main readout chain is operational and basically ready for installation at LNGS. It is based on a novel trigger-less, continuous operation of sampling digitizers followed by a fully digital event builder in order to select valid events which are eventually stored to disk. The front-end electronics (DaqReader and veto system) are fully developed and are waiting for first XENON1T data for further optimization of operation parameters. The data acquisition software, as well as the event builder are almost finalized, the latter is currently being optimized for speed on realistic computer infrastructure. We have made the first important development steps towards the data processor for XENON1T (which also needs to be tuned on real data) and have defined the layout of the underground counting room. The DAQ computing and networking hardware will be ready for installation in early 2015. We will perform a full end-to-end test of the new DAQ system on the XENON100 detector initially. The XENON100 ADCs will be reused in the XENON1T detector and their firmware has to be upgraded for the new DAQ. Using the XENON100 detector will allow us to test the full readout chain, with realistic signals and noise levels.

Slow Control

The XENON1T Slow Control system is based on a networked architecture of controller units with a central Supervisory Control and Data Acquisition system (SCADA). The controllers, their IO modules and the SCADA software are purchased from General Electric. During 2014 the Slow Control group purchased the infrastructure (PLC modules, SCADA servers, Cimplicity software) and began the installation and commissioning of the core sub-systems (cryogenics infrastructure, xenon recovery or ReStoX, Xenon purification hub and the water loop circuit of the muon veto water shield). In the software development, progress was made in the parsers interface code of the PLCs along with the new development of "guarded operation" code modules to assure that no operation can jeopardize pre-identified experiment states or compromise safety rules. Also a central database for all the instrumentation and logical entities included in the XENON1T Slow Control was built and is being populated as the systems are installed. This database is used to define the hundreds of variables and alarms, and their properties, consistently in the various hardware and software modules. All the central computers for the redundant SCADA systems, the Historian database, the web server for remote interaction, data display and analysis, the operator console and the development station have been delivered and are being deployed. The operation modes for the Slow Control of the overall experiment were identified in several joint meetings with the leaders of the core systems. Eighteen distinct operation modes were identified and for each mode the state of all valves and main parameters were defined. A detailed study of the transitions between operation states was initiated and is ongoing, with the aim of protecting from human error as much as possible. With respect to the installation process a realistic calendar was established with three levels of increasing functionality for each sub-system defined for the commissioning process.

Computing

The design of XENON1T computing system during 2014 was in a continuous development phase. The network system for Slow Control and Data/DAQ has been recently fixed and we started purchasing the required hardware.

The maximum data flow required for the DAQ system will happen during calibration, with a rate of about 300 MB/s. A local facility able to withstand for few days the burden of data processing alone is planned to ensure the normal operations even in case of temporary absence of connectivity. For the operations of XENON100 the Collaboration already purchased a series of disks for a total of about 170 TB and 64 cores, most of them mounted and maintained by the LNGS IT department (some CPUs are integrated in the LNGS U-LITE system). The extension of this facility is a natural candidate for our local facility, together with machines that will be handled by the Collaboration directly. The purchasing of the hardware will be done the latest in order to profit of the best ones present in the market.

We are also investing on the development of off-site facilities connected with high bandwidth, for year-long runs, profiting on the GRID technology. The GRID is a powerful and reliable resource for two key points. The first one is the run of Monte Carlo simulations, required for the background estimation of rare events and for the determination of the detector performances. The second one is the processing and the re-processing of large amounts of raw data. The GRID sites joining the XENON Virtual Organization (VO) created two years ago are increasing in number, with 4 sites today. For that reason we are closely following the future upgrades of the LNGS-GARR connection.

Calibration

During 2014 we worked closely with the LNGS dedicated office to obtain the necessary licenses and permissions for all required calibration sources. For the electronic recoil calibration using Rn-220, we have procured multiple Th-228 sources from PTB, Germany, and are subjecting these to a variety of tests to establish their suitability in terms of both licensing and physical suitability, so far with very promising results. The single-photoelectron calibration system, based on LEDs and optical fibers like in XENON100, has been finalized. Integration of the external source positioning system with the XENON1T slow control is well on its way for deployment in early 2015.

Screening

During 2014 the following samples were measured with the Gator HPGe spectrometer at LNGS: 41 3-inch R11410-21 PMTs, 44 kg of PTFE of the field cage of the TPC, a sample from a stainless steel pipe to be used in the cryostat, as well as MMCX connectors and D-Sub pins that are employed in the PMT signal and HV connectors, respectively. Small samples from the same PTFE will also be measured via ICP-MS at LNGS. Gator will be busy screening PMTs, in batches of 15, until March 2015. To cross-check the PMT results from Gator, 4 PMTs were measured for a longer period with a highly sensitive GeMPI Ge spectrometer at LNGS. No relevant discrepancies were detected. Hamamatsu also needed additional material for the PMT production. The GeMPIs measured these materials before they went to the production line.

Radon screening: In the second half of 2014 we studied the ^{222}Rn emanation of the following samples: stainless steel batches from different suppliers have been measured for their emanation rate before and after adding several meters of weld seam. Afterwards sub-samples thereof have been individually treated by etching, electropolishing as well as the combination of etching and electropolishing and finally remeasured for their ^{222}Rn emanation. Further two stainless steel heat exchangers for XENON1T, that have been measured untreated before, have now been thoroughly etched and remeasured. The excellent result achieved confirms the gained knowledge on ^{226}Ra removal from stainless steel surfaces. 29 3-inch PMTs have been investigated for their ^{222}Rn emanation. A previous measurement of a sample consisting of only 6 R11410 PMTs resulted in an upper limit on the emanation rate of a single PMT. That limit successfully was lowered by this 5 times larger sample. We studied the ^{222}Rn emanation of the cryogenic infrastructure of XENON1T. The emanation of the inner vessel, the cryogenic system as well as the cryogenic pipes that connect inner vessel and cryogenic system have been assayed both individually and after assembly in Hall B. In order to avoid ^{222}Rn emanation of the QDrive recirculation pumps as much as possible, we studied radon emanation of all the individual parts as well as suited alternatives thereof. Based on these studies a modified version of the QDrive was designed that is under investigation right now.

Monte Carlo and Sensitivity

The electromagnetic (ER) and neutron backgrounds (NR) from all detector components have been evaluated using a GEANT4 simulation and the measured radioactive contaminations. Assuming realistic concentrations after gas purification, the intrinsic background from ^{85}Kr and ^{222}Rn has been calculated, as well as the background produced by solar neutrino scattering off electrons and the double-beta decay of ^{136}Xe. Simulations of the light collection efficiency have been performed in order to convert the energy deposited in the detector into the S1 observable. The work towards the full simulation of the waveforms from prompt and proportional scintillation signals in the TPC is ongoing. S2 signal simulations were used to train and test position reconstruction algorithms.

Considering 1 t fiducial volume and 1 year of data acquisition, an S1 range of 3-70 PE (4-50 $\mathrm{keV_{nr}}$) and assuming an ER discrimination level of 99.75% at 40% NR acceptance (XENON100 performance), we expect 0.3 background events from ERs and 0.2 events from radiogenic neutrons. We also investigated the impact of the coherent scattering of neutrinos (mostly solar ^{8}B) producing NR events: with the same assumptions we expect 0.5 events very close to threshold. With this background, we calculated the XENON1T sensitivity using a Profile Likelihood method, leading to a spin-independent WIMP-nucleon cross section of below $2 \times 10^{-47}\,\mathrm{cm}^2$ for $m_\chi = 50\,\mathrm{GeV}/c^2$, after 2 t×year of exposure, at the 90% CL.

4 Conclusions

The construction of XENON1T, which started in 2013, had a strong boost during 2014 in all the subsystems, in order to be on schedule to deliver first data by the end of 2015. The LNGS laboratory support has been invaluable and exemplary during this time, from providing the engineering support and integration of various sub-systems, from water tank, support building and muon veto to support structure and cryostat up to the installation of the cryogenic-purification-RestoX system, to maintain the safety of construction and operations.

While the construction of XENON1T was ongoing, the XENON collaboration has also operated and analyzed data from XENON100, reported in several publications. We expect to still release a number of important publications based on data from this experiment in the coming years.

5 List of Publications

The XENON Collaboration published the following papers during 2014:

- "Analysis of the XENON100 Dark Matter Search Data", E. Aprile *et al.* [XENON Collaboration], Astropart.Phys. **54** (2014) 11-24.
- "Observation and applications of single-electron charge signals in the XENON100 experiment", E. Aprile *et al.* [XENON Collaboration], J.Phys. **G41** (2014) 6, 035201.
- "First Axion Results from the XENON100 Experiment", E. Aprile *et al.* [XENON Collaboration], Phys.Rev. **D90** (2014) 6, 062009.
- "Conceptual design and simulation of a water Cherenkov muon veto for the XENON1T experiment", E. Aprile *et al.* [XENON Collaboration], JINST **9** (2014) 11006.

References

[1] E. Aprile *et al.* [XENON Collaboration], Phys. Rev. Lett. **109**, 181301 (2012) [arXiv:1207.5988 [astro-ph.CO]].

[2] E. Aprile *et al.* [XENON Collaboration], Phys.Rev. **D90** (2014) 6, 062009. [arXiv:1404.1455v2 [astro-ph.CO]].

[3] M. Szydagis, N. Barry, K. Kazkaz, J. Mock, D. Stolp, M. Sweany, M. Tripathi, S. Uvarov, N. Walsh, and M. Woods, JINST 6, P10002 (2011).

[4] E. Aprile et al. Phys. Rev. D 86, 112004 (2012).

[5] L. Baudis, H. Dujmovic, C. Geis, A. James, A. Kish, A. Manalaysay, T. Marrodn Undagoitia, and M. Schumann Phys. Rev. D 87, 115015 (2013).

[6] A. Manalaysay et al., Rev. Sci. Instrum. 81, 073303 (2010).

[7] E. Armengaud *et al.* [EDELWEISS-II Collaboration], J. Cosmol. Astropart. Phys. **11** (2013) 067.

[8] J. Redondo, J. Cosmol. Astropart. Phys. 12 (2013) 008.

[9] K. Abe et al. (XMASS Collaboration), Phys. Lett. B 724, 46 (2013).

[10] A. V. Derbin, I. S. Drachnev, A. S. Kayunov, and V. N. Muratova, JETP Lett. 95, 339 (2012).

[11] P. Gondolo and G. G. Raffelt, Phys. Rev. D 79, 107301 (2009).

[12] G. G. Raffelt, Lect. Notes Phys. 741, 51 (2008).

[13] N. Viaux, M. Catelan, P. B. Stetson, G. G. Raffelt, J. Redondo, A. A. R. Valcarce, and A. Weiss, Phys. Rev. Lett. 111, 231301 (2013).

[14] M. Dine, W. Fischler, and M. Srednicki, Phys. Lett. 104B, 199 (1981).

[15] A. R. Zhitnitsky, Sov. J. Nucl. Phys. 31, 260 (1980).

[16] J. E. Kim, Phys. Rev. Lett. 43, 103 (1979).

[17] M. A. Shifman, A. I. Vainshtein, and V. I. Zakharov, Nucl. Phys. B166, 493 (1980).

[18] M. Arik et al. (CAST Collaboration), Phys. Rev. Lett. 112, 091302 (2014).

[19] K. Barth et al. (CAST Collaboration), J. Cosmol. Astropart. Phys. 05 (2013) 010.

[20] C. E. Aalseth et al. (CoGeNT Collaboration), Phys. Rev. Lett. 101, 251301 (2008).

[21] Z. Ahmed et al. (CDMS Collaboration), Phys. Rev. Lett. 103, 141802 (2009).

[22] E. Aprile *et al.* [XENON Collaboration], Astropart. Phys. 35 (2012), 573-590 [arXiv:1107.2155 [astro-ph.CO]].

[23] S. Rosendahl et al., JINST 9 (2014) 10010.

[24] E. Aprile *et al.* [XENON Collaboration], JINST **9** (2014) 11006.

Cosmic Silence

E. Fratini[a,b], M.F. Fischietti[a,c], G. Simone[a], E. Bortolin[b], G. Esposito[b], P. Fattibene[b], C. Nuccetelli[b], M. A. Tabocchini[a,b,*], E. Alesse[c], A. Tessitore[c], F. Zazzeroni[c], M. Balata[d], L. Ioannuci[d], Esposito[e], M. Chiti[e], L. Satta[a,e,*]

[a]Museo Storico della Fisica e Centro Studi e Ricerche Enrico Fermi
[b]Istituto Superiore di Sanit, Technology and Health Department, and INFN-Roma1
Gr. coll. Sanit, 00161 Roma, Italy
[c]LAquila University, Department of Biotechnological and Applied Clinical Sciences
[d]INFN - Gran Sasso National Laboratory
[e]INFN - Frascati National Laboratory
(*) Spokespersons

Abstract

The influence of the environmental radiation on the metabolism and the response to genotoxic stress capability has been investigated in A11 cells grown underground at the Laboratori Nazionali del Gran Sasso (LNGS-INFN), where the radiation background is negligible, and in a reference laboratory located at the Istituto Superiore di Sanit (ISS), Rome. Expression analysis of proteins relevant in the control of apoptosis, proliferation and antioxidant activity has shown that cells grown in reduced radiation environment are less capable to cope with the endogenous stress than those grown in reference conditions, suggesting that the environmental radiation might work as trigger of cellular defense mechanisms Moreover, a characterization of the radiation field in the different experimental sites is in progress.

1 Introduction

Life has evolved on Earth for 3 billion years in the presence of environmental ionizing radiation, and this constant very small daily stimulus has been incorporated in the biology of living organisms during evolution. Very little is known about this influence on living matter. In principle, important information can be acquired by analyzing possible differences between parallel biological systems, one kept in a reference radiation environment (RRE) and one in a low radiation environment (LRE).

The underground Gran Sasso National Laboratory (LNGS) of the Italian Institute of Nuclear Physics (INFN), thanks to its very low-radiation environmental conditions, was constructed to boost underground physics, and, more generally, to study quite rare events such as proton decay or solar neutrino detection. In this underground laboratory, shielded by at least 1400 m of rock overburden, cosmic radiation is almost absent [1] and, given the scarce Uranium and Thorium content in the dolomite rocks of the mountain, the neutron flux is reduced by a factor of 10^3 with respect to external values [2,3]. In addition, being the mountain of sedimentary origin, the natural occurrence of γ and μ radiation is minimal, and further reduced by the low-activity concrete lining of the laboratory walls. Radon concentration is kept at a very low level by an efficient ventilation system that pumps low-radon-concentration air from the outside into the laboratory.

Thanks to these features, underground LNGS represents a unique opportunity to explore an environment where the presence of radiation is strongly reduced.

Our previous works [4-8] on the influence of different environmental radiation on biological systems of different origin (yeast, mouse and human) have indicated that cell cultures maintained under low radiation environment (LRE) developed a different biochemical behavior, compared to the cultures in reference radiation environment (RRE). In particular, cells cultured in the LNGS underground laboratory are less preserved from DNA damage, induced by chemical and physical agents, and show a reduced Reactive Oxygen Species (ROS) scavenging power than cells cultured in the external laboratory set up at the Istituto Superiore di Sanit (ISS), Rome.

The Cosmic Silence Project aims to study the biochemical behavior of living organisms in a reduced radiation environment by means of very sensitive biological *in vitro* and *in vivo* models, kindly donated by Prof. Pamela Sykes, Flinders University, Adelaide, Australia: A11 hybridoma cells derived from transgenic pKZ1 mouse model and pKZ1 mice.

The reported data are obtained with the hybridoma cell line A11, obtained from pKZ1 mouse splenocytes harboring the pKZ1 inversion cassette [9] and myeloma cells. A11 cells were cultured for 4 weeks in both LRE (underground at LNGS) and RRE (at the Istituto Superiore di Sanit, ISS, in Rome). Expression analysis of proteins relevant in the control of apoptosis and proliferation (poly (ADP-ribose) polymerase-1, Parp-1), as well as of proteins related to antioxidant activity (i.e., superoxide dismutase, SOD; catalase, CAT; glutathione peroxidase 1 and 4, GPX1 and GPX4), have been investigated in the different radiation environments. Moreover, at the end of the 4^{th} week, the cells cultured underground were grown for 2 further weeks, in parallel with the external cultures, at the ISS reference laboratory. The overall results have shown that cells grown in reduced radiation environment are less capable to cope with the endogenous stress than those grown in reference conditions, suggesting that the environmental radiation might work as trigger of cellular defense mechanisms.

In the framework of the Cosmic Silence Project, an animal housing facility, satellite of the facility already existing at LAquila University, has also been designed for *in vivo* studies. The first step will be to use *Drosophila melanogaster* and eventually, once the license from the competent Authorities will be obtained, the pKZ1 mouse model.

For an accurate interpretation of the biological *in vitro* and *in vivo* results, the characterization of the different components of the radiation environment is in progress in the different experimental sites.

2 Characterization of the radiation field in the different experimental sites

The Cosmic Silence project requires a characterization of the radiation field in the environments where the in vitro and the in vivo experiments will be carried out. To this purpose measurements have been planned in the different sites of interest, namely in the underground laboratories of Gran Sasso (INFN) and in the ground laboratories at LAquila University and at ISS.

Concerning the dose measurements, first of all, a preliminary check of the dosimetric characteristics of the thermoluminescence dosimeters (TLD 700H) selected for the study was carried out. In particular, the following characteristics were investigated: batch variability, radiation sensitivity, fading behavior and re-use effect. Successively, sets of 5 TLDs were used to monitor the different sites previously identified. Specifically, at LNGS underground laboratories three cell incubators with different characteristics, were monitored for 73 and 98 days: one located inside a 5 cm thick iron shield, one without shielding and a third one, containing tablets of radioactive KCl to enhance the gamma rays contribution to radiation background. A set of dosimeters of the same type was also placed on the top of one of the three incubators to monitor the laboratory.

At the ISS, one incubator was monitored for 28 and 55 days. In the ground laboratories at LAquila University, sets of 5 TLDs were kept inside and outside of a cage for mice, for 38 and 98 days. The calibration of the dosimeters and the analysis of the data are in progress.

Further measurements were planned for analyzing the gamma radiation energy spectrum, and the activity concentration of gamma radiation emitting radionuclides by gamma spectroscopy with an HpGe. Moreover, neutron dose will be assessed by BF3 high sensitive detector and a tentative neutron spectrometry will be carried out by an extended range multi-spheres system. Radon activity concentration in air will

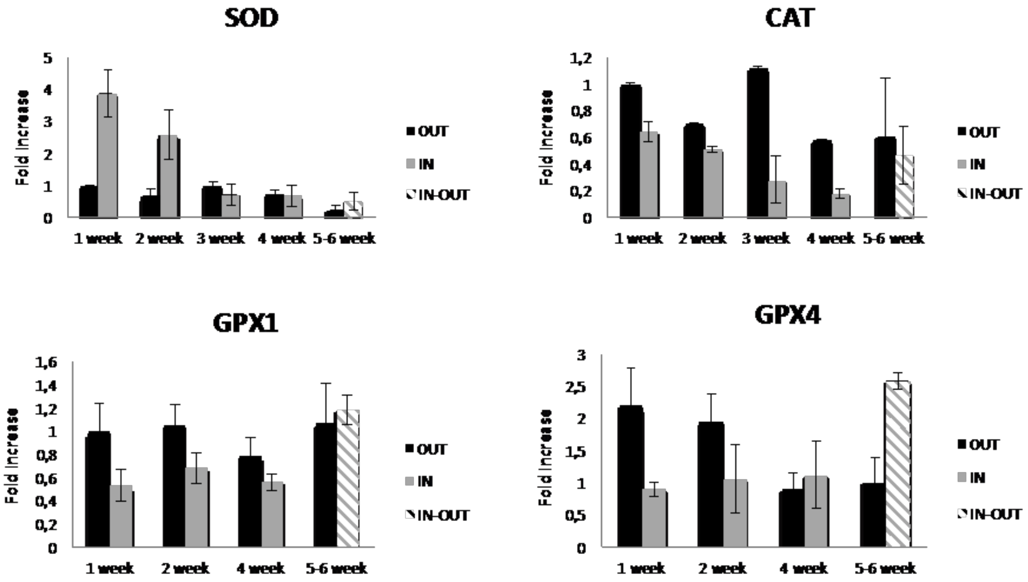

Figure 1: Gene expression of Catalase (CAT), Superoxide dismutase (SOD), Glutathione peroxidase (GPX1 and GPX4) evaluated by qPCR and normalized with respect to A11 cells at time 0.

be measured and monitored using an Alfaguard instrument.

3 Experimental results on in vitro cell cultures

The hybridoma cell line (A11) was kindly donated by Prof. Pamela Sykes, Flinders University, Adelaide, Australia. Four A11 cell cultures (A, B, C, D) were grown in parallel for up to 4 weeks at the ISS (RRE) and at the LNGS underground cell culture laboratory (LRE), in the presence or in the absence of 5 cm Fe shield. Afterwards, A11 cells grown at LRE were brought to RRE laboratory and cultured for additional 2 weeks, together with the 4 weeks-old RRE culture.

To evaluate gene expression of enzymes such as catalase (CAT), superoxide dismutase (SOD), and glutathione peroxidase (GPX), all of them involved in quenching the damage produced by Reactive Oxygen Species (ROS), mRNA was extracted weekly from the A11 parallel cultures. CAT catalyzes the decomposition of hydrogen peroxide to water and oxygen and SOD catalyze the dismutation of superoxide into oxygen and hydrogen peroxide. GPX (with his 4 isoforms) has several functions. In particular, GPX1 is a scavenger of intracellular hydrogen peroxide and GPX4 is a phospholipid hydroperoxidase that protects cells against membrane lipid peroxidation. Analysis of gene expression of antioxidant enzymes was performed with real time quantitative PCR analysis (RT-qPCR), and relative quantification was carried out with the $\Delta\Delta$CT method [10].

Gene expression analysis of ROS-scavenger genes (Fig. 1) showed that the two *Gpx* mRNA isoforms (*Gpx1* and *Gpx4*) as well as *CAT* are less expressed in A11 cells grown at LRE with respect to cells maintained at RRE as soon as after 1 week of culture, confirming the trend toward repression of GPX isoforms and CAT gene in LRE condition. This under expression is maintained for up to 4 weeks of culture. The expression of these genes is re-induced in cells brought back to RRE after 4 weeks at LRE (5th and 6th week).

Together with gene expression analysis of ROS-scavenger genes, protein expression of poly (ADP-ribose) polymerase-1 (PARP-1), a key protein in DNA repair as well as physiological and pathological functions, from cell survival control to several forms of cell death, was further evaluated. The obtained results confirmed the previous finding: i) A11 cells grown at LRE showed less protein modulation respect

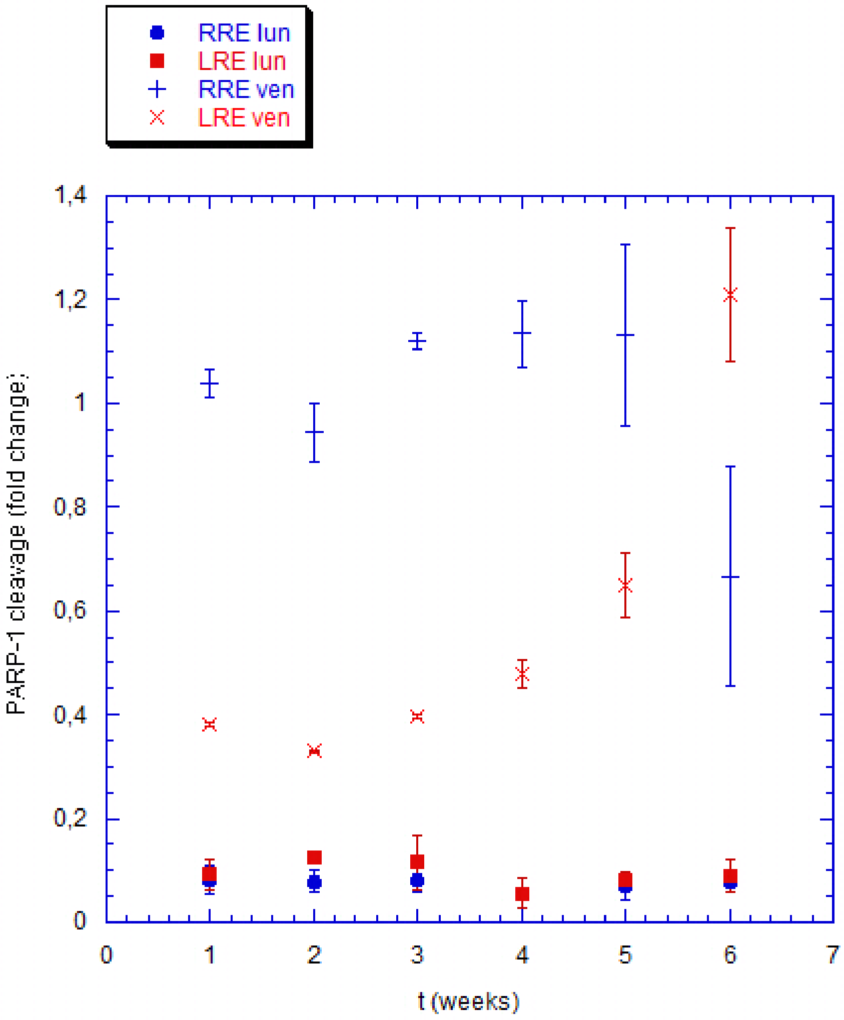

Figure 2: Hybridoma cell line 9198 A11 were grown in RRE or in LRE. Cells were subjected to passage twice a week. After 3 days of culture, both RRE (•) and LRE (■) cells show a low level of Poly [ADP-ribose] polymerase-1 cleaved protein (Parp-1). After 4 days of culture, cells at LRE (x) show a lower level of PARP-1 cleavage than cells cultured at RRE (+).

to cells grown at RRE during the 4 weeks of culture; ii) when A11 cells grown at LRE were brought to RRE laboratory and cultured for additional 2 weeks, together with the 4 weeks-old RRE culture, the protein modulation increases and showed an inversion between the two cultures. Moreover, we found that in A11 cells, PARP-1 begins to be cleaved after 3 days of exponential growth, probably as a result of stress, due to high cell concentration and/or serum starvation. After 3 days, both RRE and LRE cultures have low level of PARP-1 cleavage. However, after 4 days of exponential growth, cells cultured at LRE show a significantly lower level of PARP-1 cleavage than cells cultured at RRE; moreover, this trend reverses when LRE cultured cells are brought back to RRE (Fig. 2).

These results complement the previous finding obtained at longer culture time, opening a new scenario on the interaction between radiation environment and individual genotype, either on the incidence

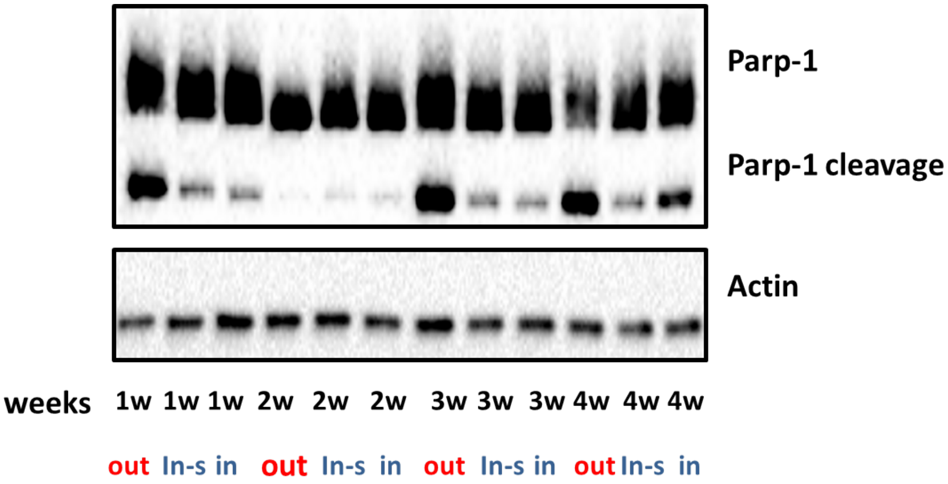

Figure 2: Expression level of PARP-1 protein in A11 cells grown for 4 weeks in 3 different environmental radiation conditions: at RRE, at the ISS (out), and at LRE at the LNGS with 5 cm Fe shield (In-s) and without the shield (in). 1-3 and 4w samples have been collected after 4 days of exponential culture; the 2w samples have been collected after 3 days of exponential culture (no PARP-1 cleavage is expected).

of DNA damage related diseases or on life span. Actually, literature data show a correlation among lifespan and PARP-1 modulated DNA repair [11-14]. Besides PARP-1, gene expression analysis of heat shock protein (HSP70) and tumor-suppressor gene TP53, both involved in cellular stress response, have been also performed. While HSP70 did not show any difference in modulation by comparing A11 cells grown at RRE or at LRE, preliminary results have shown a modulation for p53. It is well known that p53 is involved in the cellular response to DNA damage and plays a critical role in regulating apoptosis and G1/S cell cycle arrest. On the other hand, p53 can be involved in the transcriptional induction/repression of genes involved in keeping a correct cellular metabolism.

All the above LRE results refer to cell cultures grown in an incubator with a Fe shield (able to reduce the gamma component of the radiation spectrum by a factor of about 10). Preliminary experiments on gene expression conducted on cells grown at LRE without this Fe shield did not show difference between the two experimental conditions (with and without shielding). This finding indicates that a gamma component increase of the environmental radiation does not significantly influence the biological response.

The overall *in vitro* data until now obtained corroborate the hypothesis that environmental radiation contributes to the development and maintenance of defence mechanisms in organisms living today. The Cosmic Silence Project will continue the *in vitro* investigation on the A11 cell line with the aim to identify the biological mechanisms that are triggered by different environmental radiation. To this purpose, besides the tests on modulation of the protein involved on DNA repair and on expression of genes involved in ROS detoxification, experiments will be performed to gain information on changes in the methylation profiles. The purpose of these experiments is to achieve the most complete information on the way cells perceive the environmental radiation and, consequently, adapt to the environment.

Although the *in vitro* experiments are a fundamental tool to understand the biological effects of low-very low doses of ionizing radiation, for a more comprehensive knowledge *in vivo* studies are essential. It is well know that not all the damage has a local origin and that part of the biological response is due to non-cell-autonomous physiological mechanism that point to studies at organism level.

Conceivably, the evolution of the *in vitro* investigations is to verify whether effects caused by extremely low-doses of environmental ionizing radiation, including cosmic radiation, exist *in vivo.* To this purpose, a facility for housing living organisms of different complexity in the phylogenetic tree, satellite of that installed at the LAquila University, will be set up underground at LNGS. The transgenic pKZ1 mouse model, with its exceptional sensitivity in detecting intra-chromosomal inversion induced by ultra-low doses of ionizing radiation, is the gold standard for these experiments. However, authorization procedures requiring long time to be completed are needed for mice. For this reason, in the meanwhile, experiments are proposed using *Drosophila melanogaster* as a model organism to be maintained in different radiation environments (low and reference). *Drosophila melanogaster* is indeed a well-established model for genetic analyses on development, aging as well as DNA damage response. This organism shows several advantages in laboratory practice, due to its relatively short reproduction time (ten-day generation time), high fertility with many progeny. Finally, a large number of developmental processes are conserved between fruit fly and vertebrates, thus making *Drosophila* a great candidate as complementary organism for the Cosmic Silence experiment.

Acknowledgements

We are indebted with Dr. M. Belli for the interesting discussions and suggestions and to Prof. P. Sykes, Flinder University, Australia, for sending us the pKZ1 cells and mice to be used in the framework of the Cosmic Silence collaboration. We also thank Dr. G. Cenci for the fruitful discussions and suggestions aimed at planning *Drosophila melanogaster* collaborative experiments.

References

[1] The MACRO Collaboration (1990) Study of penetrating cosmic ray muons and search for large scale anisotropies at the Gran Sasso Laboratory. Phys Lett B 249:149 156

[2] Rindi A, Celani F, Lindozzi M, Miozzi S. *Underground neutron flux measurement.* Nucl Inst Meth A (1998)272:871-874

[3] Belli P, Bernabei R, DAngelo S, De Pascale M, Paoluzi L, Santonico R, Taborgna NIN, Villoresi G *Deep underground neutron flux measurement with large BF3 counters.* Rivista del Nuovo Cimento A (1989) 101:959-966

[4] Satta L, Augusti-Tocco G, Ceccarelli R, Esposito A, Fiore M, Paggi P, Poggesi I, Ricordy R, Scarsella G, Cundari E Low environmental radiation background impairs biological defence of the yeast Saccharomyces cerevisiae to chemical radiomimetic agents. Mutat Res (1995) 347(3-4):129-33

[5] Satta L, Antonelli F, Belli M, Sapora O, Simone G, Sorrentino E, Tabocchini M A, Amicarelli F, Ara C, Cer MP, Colafarina S, Conti Devirgiliis L, De Marco A, Balata M, Falgiani A, Nisi S. Influence of a low background radiation environment on biochemical and biological responses in V79 cells. Radiat Environ Biophys (2002) 41 (3):217-24

[6] Carbone M C, Pinto M, Antonelli F, Amicarelli F, Balata M, Belli M, Conti Devirgiliis L, Ioannucci L, Nisi S, Sapora O, et al (2009) The Cosmic Silence Experiment: on the putative adaptive role of environmental ionizing radiation. Radiat. Environ. Biophys. 48:189-196

[7] Carbone M C, Pinto M, Antonelli F, Amicarelli F, Balata M, Belli M, Conti Devirgiliis L, Sapora O, Simone G, Sorrentino E, Tabocchini M A, Satta L (2010) Effects of deprivation of background environmental radiation on cultured human cells. Il Nuovo Cimento 4:469-477

[8] Fratini E., Carbone C., Capece D., Esposito G., Simone G., Tabocchini M.A., Tomasi M., Belli M., Satta L. (2015) Jan 31 [Epub ahead of print]. Low-radiation environment affects the development of protection mechanisms in V79 cells. Radiat. Environ. Biophys. DOI 10.1007/s00411-015-0587-4

[9] Hooker A M, Home R, Morley A A, Sykes P J, (2002) Dose-dependent increase or decrease of somatic intrachromosomal recombination produced by etoposide. Mut. Res. 500, 117-124.

[10] Livak K J and Schmittgen T D (2001) Analysis of Relative Gene Expression Data Using Real-Time Quantitative PCR and the 2-[Delta][Delta]CT Method. Methods, 25(4):402-408

[11] Grube K., Brkle A. Poly(ADP-ribose) polymerase activity in mononuclear leukocytes of 13 mammalian species correlates with species-specific life span. Proc. Natl. Acad. Sci. U.S.A. (1992) 89 (24): 1175963. doi:10.1073/pnas.89.24.11759

[12] Muiras M.L., Mller M., Schchter F., Brkle A. Increased poly(ADP-ribose) polymerase activity in lymphoblastoid cell lines from centenarians. J. Mol. Med. (1998) 76 (5): 34654. doi:10.1007/s001090050226

[13] Lebel M., Lavoie J., Gaudreault I., Bronsard M., Drouin R. Genetic cooperation between the Werner syndrome protein and poly(ADP-ribose) polymerase-1 in preventing chromatid breaks, complex chromosomal rearrangements, and cancer in mice. Am. J. Pathol. (2003) 162 (5): 155969. doi:10.1016/S0002-9440(10)64290-3

[14] Bernstein H., Payne C.M., Bernstein C., Garewal H., Dvorak K. Cancer and aging as consequences of un-repaired DNA damage. (2008) Kimura H, Suzuki A, ed. New York: Nova Science Publishers, Inc. pp.147

ERMES
Atmospheric transport modelling of ^{133}Xe: a case study of the emissions from the isotope production facility ANSTO, Australia

Michael Schöppner[a], Wolfango Plastino[b,c], Nikolaus Hermanspahn[d],
Emmy Hoffmann[e], Martin Kalinowski[f], Blake Orr[g], Rick Tinker[g]

[a] Princeton University, Woodrow Wilson School, United States of America
[b] Roma Tre University, Department of Physics, Italy
[c] National Institute of Nuclear Physics (INFN), Section of Roma Tre, Italy
[d] National Radiation Laboratory, ESR Science Centre, New Zealand
[e] Australian Nuclear Science and Technology Organisation, Australia
[f] Comprehensive Nuclear Test-Ban-Treaty Organization, Austria
[g] Australian Radiation Protection and Nuclear Safety Agency, Australia

Abstract

Historic source terms of ^{133}Xe emissions from the isotope production facility at ANSTO, Sydney, Australia, have been made available in a daily resolution. Based on these high resolution data, different source term sets with weekly, monthly and yearly time resolution have been compiled. These different sets are then applied together with atmospheric transport modelling (ATM) to predict the concentration time series at two radioxenon monitoring stations. The results are compared with each other in order to examine the improvement of the prediction capability depending on the used time resolution of the most dominant source term in the region.

1 Introduction

Over 400 reactors at Nuclear Power Plants (NPPs) are currently in operation worldwide [1], while only five Isotope Production Facilities (IPFs) are considered to be continuously emitting relevant activity levels. Nevertheless, the emission strengths of typical nuclear power reactors are below the emission strengths of these IPFs; a typical IPF usually emits radioxenon in the order of magnitude or above the total of all operational NPPs together [2]. Therefore, the long-term global radioxenon background is a result of many weak and a few strong sources. However, batch emissions can make also an NPP acting like a strong source on a shorter time scale. Operators of IPFs generally do not publish their day-to-day emission reports. It is assumed that knowledge about the time-dependent source terms of these few, but strong, sources would improve the prediction capability of radioxenon concentrations based on atmospheric transport modelling (ATM) with forecast or analysed meteorological data.
For this work daily ^{133}Xe emission data from ANSTO, an IPF near Sydney, Australia, has

been used to compile data sets with various time resolutions. Previous detections of radioxenon near Melbourne have been attributed to ANSTO [3](Tinker et al., 2010). It is the aim to show how different time resolutions of emission reports from regionally dominant radioxenon sources would impact the prediction capability of ATM-based methods. This quantification could also be used to demonstrate to IPF operators the usefulness of releasing emission data of a certain time resolution.

2 Results and discussion

The presented research is based on historic daily emission data of ^{133}Xe from ANSTO, an Australian IPF near Sydney. Releases from the ANSTO IPF are measured continuously using a NaI gamma spectrometer monitoring a flow-through sampling cell. A bypass feed from the IPF active ventilation extract duct is passed through the sampling cell. The emissions are ducted to the main discharge stack where they are diluted by other flows and released to the atmosphere. The source term varies over about four orders of magnitude and often has day-to-day variations of one order of magnitude. In any case the resulting doses are significantly below the 1 mSv annual limit for public exposure [3]. The provided data have been used to compile further emission data sets with various time resolutions: weekly, monthly and yearly emissions have been determined based on the original report. Besides these emissions also other known radioxenon sources have been included in the simulations. Due to the meteorological patterns sources in the southern hemisphere have a higher chance of contributing to the radioxenon concentrations in Australia and New Zealand. Another IPF is located in Pelindaba, South Africa, and only a few other NPPs exist in South Africa and South America. The available emission data of these background sources are annual estimations, where constant discharge rates have to be assumed for the simulations. Another prospective IPF with irregular and low, but basically unknown emissions at the time is located in Indonesia [4]. However, the emissions from this IPF could not have been included in the simulations.

In the frame of this research data from one Australian and one New Zealand station were used. The source-receptor sensitivity (SRS) fields were calculated according to the collection times of these two IMS stations. The Australian CTBTO-IMS (Comprehensive Nuclear-Test-Ban Treaty Organization-International Monitoring System) station AUX04 near Melbourne is located about 700 kmin a southwest direction from the ANSTO facility near Sydney. The New Zealand CTBTO-IMS station NZX46 on Chatham Islands is about 3000 km in an east south-east direction from the ANSTO facility. It has been shown that the ATM-based predictions for AUX04 and NZX46 concentrations of ^{133}Xe are generally well-predicted with a tendency to under-prediction. For both stations the prediction quality of the overall time series improve with increased time resolution of the regionally dominant source term. In any case the daily resolved source term data yields the best results and clearly improves the correlation between experimental and simulated data. The particular structure in the AUX04 can be explained by the share of ANSTO-related ^{133}Xe in each sample. The statistical analysis suggests that the prediction quality is not only dependent on the source term time resolution, but also on the share of ANSTO related ^{133}Xe in the detected concentration.

3 Conclusion

The ANSTO source term has been provided for this research directly from the plant operator and is taken to be accurate, though regulated operators tend to overestimate their emissions to be on the safe side of the governmental issued release limits. Since only the ^{133}Xe emissions were reported, the influence of parent decay products can only be estimated. For this ^{133m}Xe and ^{133}I are believed to be the most important precursors [5](Saey et al., 2010); the emissions of these from the ANSTO facility are below significance. A possible emitting, but unaccounted source of radioxenon (and radioiodine) in this region could be found e.g. in Indonesia, a country with access to nuclear technology and intentions to produce medical isotopes [4]. The emissions are not exactly known, but it can be assumed that they are on average lower than the ANSTO emissions by a factor of around five [6].

The fact that the samples with the highest shares of ANSTO related ^{133}Xe are simulated with a high correlation and a fractional bias close to zero suggests that the ANSTO source term can indeed be taken as accurate.

Further studies could include even higher time resolution of up to three hours, which would equal the time resolution of the used meteorological fields in this study. It is believed that also for other regions with a high background from legitimate sources, such as Europe and North America, the availability of emission data of dominant sources, such as IPFs, can contribute to the operational understanding of the daily samples. In these regions the background may be a few orders of magnitudes higher than in Australia, but also their respective dominant source of radioxenon usually emits more than the ANSTO facility due to higher production rates of isotopes.

References

[1] PRIS, 2012. Power Reactor Information System of the IAEA. http://pris.iaea.org/public/.

[2] Wotawa, G., Becker, A., Kalinowski, M.B., Saey, P., Tuma, M., Zhringer, M., 2010. Computation and analysis of the global distribution of the radioxenon isotope ^{133}Xe based on emissions from nuclear power plants and radioisotope production facilities and its relevance for the verification of the nuclear-Test-Ban Treaty. Pure and Applied Geophysics 167, 541-557.

[3] Tinker, R., Orr, B., Grzechnik, M., Hoffmann, E., Saey, P., Solomon, S., 2010. Evaluation of radioxenon releases in Australia using atmospheric dispersion modelling tools. Journal of Environmental Radioactivity 101, 353-361.

[4] Imardjoko, Y., 2012. Status of radioisotope production of ^{99}Mo from FPM using LEU Target and ^{131}I; current and increased production capacity in the near future. In: Presentation at the Workshop on the Signatures of Medical and Industrial Isotope Production (WOSMIP) on 20 June 2012.

[5] Saey, P., Bowyer, T., Ringbom, A., 2010. Isotopic noble gas signatures released from medical isotope production facilitiesdSimulations and measurements. Applied Radiation and Isotopes 68, 1846-1854.

[6] Hoffmann, E., 2012. Personal communication on 9 November 2012.

THE VIP EXPERIMENT

S. Bartalucci[a], S. Bertolucci[b], M. Bragadireanu[a,c]
M. Cargnelli[d], A. Clozza[a], C. Curceanu[a],
S. Di Matteo[e], J-P. Egger[f], C. Guaraldo[a], M. Iliescu[a],
M. Laubenstein[g], J. Marton[d], E. Milotti[h], A. Pichler[d], D. Pietreanu[a,c],
K. Piscicchia[a], M. Poli Lener[a], T. Ponta[c], A. Romero Vidal[a],
A. Scordo[a], H. Shi[a], D.L. Sirghi[a,c], F. Sirghi[a,c], L. Sperandio[a],
O. Vazquez Doce[i], E. Widmann[d], J. Zmeskal[d]

[a] INFN, Laboratori Nazionali di Frascati, CP 13, Via E. Fermi 40, I-00044,
Frascati (Roma)-Italy
[b] CERN, CH-1211, Geneva 23-Switzerland
[c] "Horia Hulubei" National Institute of Physics and Nuclear Engineering,
Str. Atomistilor no. 407, P.O. Box MG-6, Bucharest - Magurele-Romania
[d] The Stefan Meyer Institute for Subatomic Physics, Boltzmanngasse 3,
A-1090 Vienna-Austria
[e] Institut de Physique UMR CNRS-UR1 6251, Université de Rennes1,
F-35042 Rennes-France
[f] Institut de Physique, Université de Neuchâtel, 1 rue A.-L. Breguet,
CH-2000 Neuchâtel-Switzerland
[g] INFN, Laboratori Nazionali del Gran Sasso, S.S. 17/bis, I-67010 Assergi (AQ)-Italy
[h] Dipartimento di Fisica, Università di Trieste and INFN– Sezione di Trieste,
Via Valerio, 2, I-34127 Trieste-Italy
[i] Excellence Cluster Universe, Technische Universität München, Garching, Germany

Abstract

The Pauli exclusion principle (PEP) and, more generally, the spin-statistics connection, stays at the very basis of our understanding of matter and the Universe. The PEP spurs, presently, a lively debate on its possible limits, deeply rooted in the very foundations of Quantum Mechanics and Quantum Field Theory. There are theories, starting from the quon-theory, which might allow for a tiny violation of PEP. Therefore, it is extremely important to experimentally test the limits of its validity. The VIP collaboration is testing the validity of PEP for electrons. VIP is considering, as well, the possibility to extend its scientific program towards the study of spontaneously emitted x-ray radiation, a phenomena experimentaly predicted in the framework of collapse models.

1 Introduction

The Pauli Exclusion Principle (PEP), which plays a fundamental role in our understanding of many physical and chemical phenomena, from the periodic table of elements, to the electric conductivity in metals and to the degeneracy pressure which makes white dwarfs and neutron stars stable, is a direct consequence of the spin-statistics connection [1]. Although the principle has been spectacularly confirmed by the huge number and accuracy of its predictions, its foundation lies deep in the structure of quantum field theory and has defied all attempts to produce a simple proof [2]. Given its basic standing in quantum theory, it is not only appropriate, but as well necessary, to carry out precise tests of the PEP validity and, indeed, mainly in the last 20 years, several experiments have been performed to search for possible small violations [3, 4, 5, 6, 7, 8, 9, 10, 11, 12]. Many (if not all) of these experiments are using methods which are not obeying to the so-called Messiah-Greenberg superselection rule [13]. The indistinguishability and the symmetrization (or antisymmetrization) of the wave-function should be checked independently for each particle, and accurate tests were and are being done.

The VIP (VIolation of the Pauli Exclusion Principle) experiment has the goal to dramatically improve the limit on the probability of the violation of the PEP for electrons, ($P < 1.7 \times 10^{-26}$ established by E. Ramberg e G. A. Snow: *Experimental limit on a small violation of the Pauli principle*, Phys. Lett. **B 238** (1990) 438), exploring a region where new theories might allow for PEP violation.

The experimental method, originally described in [14], consists in the introduction of electrons into a copper strip, by circulating a current, and in the search for X rays resulting from the forbidden radiative transition that would occur if some of the "new" electrons are captured by copper atoms and cascade down to the 1s state already filled by two electrons with opposite spins. The energy of the *2p* → *1s* transition would differ from the normal K_α transition by about 300 eV (7.729 keV instead of 8.040 keV) [15] providing an unambiguous signal of the PEP violation. The measurement alternates periods without current in the copper strip, in order to evaluate the X-ray background in conditions where no PEP violating transitions are expected to occur, with periods in which current flows in the conductor, thus providing "new" electrons, which might violate PEP.

The experiment is being performed at the LNGS underground Laboratories, where the X-ray background, generated by cosmic rays, is reduced.

Presently, the group is considering the extension of its scientific program to the study of the collapse models, by the measurements of the spontaneously emitted radiation (X rays), predicted by these models. Very encouraging preliminary results were already obtained.

2 The VIP experimental setup

The first VIP setup was realized in 2005, using Charge Coupled Devices (CCD) as X-ray detectors [16, 17, 18, 19, 20], and consisted as main elements of a copper cylinder, were current was circulated, 4.5 cm in radius, 50 μm thick, 8.8 cm high, surrounded by 16 equally spaced CCDs of type 55.

The CCDs were placed at a distance of 2.3 cm from the copper cylinder, grouped in units of two chips vertically positioned. The setup was enclosed in a vacuum chamber, and the CCDs were cooled to about 165 K by the use of a cryogenic system. A schematic drawing of this setup is shown in Fig. 1. The setup was surrounded by layers of copper and lead (as seen in the picture) to shield it against the residual background present inside the LNGS laboratory, see Fig. 2.

The DAQ alternated periods in which a 40 A current was circulated inside the copper target with periods without current, referred as background.

This apparatus was installed at the LNGS Laboratory in Spring 2006 and was taking data in this configuration until Summer 2010.

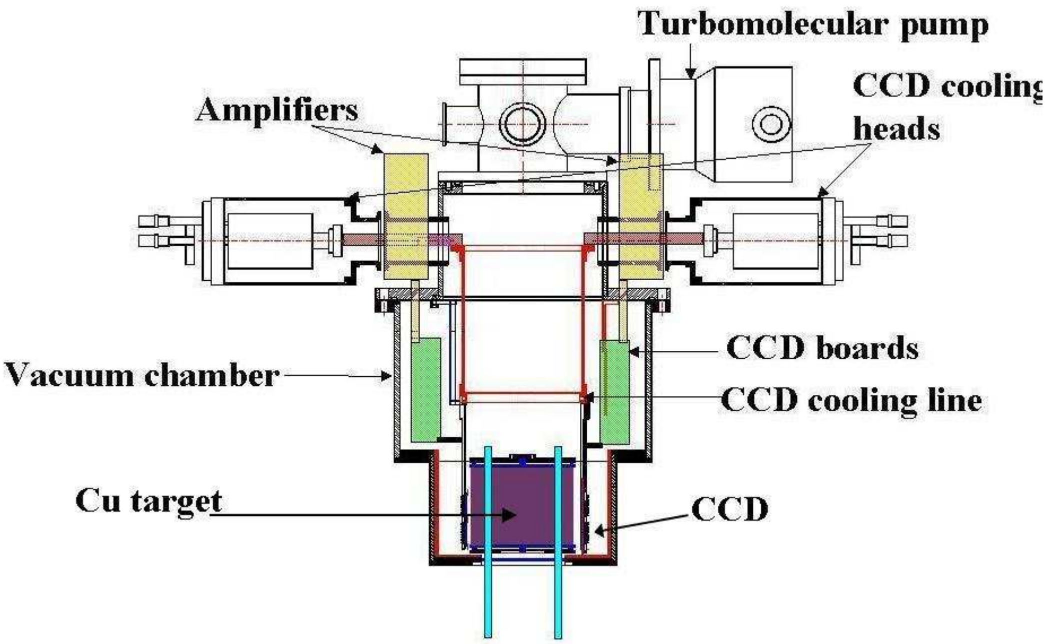

Figure 1: *The VIP setup. All elements af the setup are identified in the figure.*

Presently, we are building a new setup, VIP2, which will allow to gain other two orders of magnitude in the limit of the PEP violation probability.

3 The VIP results

3.1 VIP results on the probability of PEP violation

Until summer 2010 the VIP experiment was in data taking, alternating periods of "signal" (I=40 A) with periods without signal (I=0 A) at LNGS.

Data analyses were performed (energy calibration, sum of spectra, subtraction of background) and the probability of violation of PEP for electrons obtained in 2014 after a refined re-analysis of the data, involving charge transport correction for CCDs, is:

$$\frac{\beta^2}{2} < 3 \times 10^{-29} \tag{1}$$

3.2 Discussion of the results

We are attempting an interpretation of our results in the framework of quon-theory, which turned out to be a consistent theory of *small* violations of PEP. The basic idea of quon theory [21] is that (anti)commutators, are replaced by weighted sums

$$\frac{1-q}{2}\left[a_i, a_j^+\right]_+ + \frac{1+q}{2}\left[a_i, a_j^+\right]_- = a_i a_j^+ - q a_j^+ a_i = \delta_{i,j} \tag{2}$$

where $q = -1$ ($q = 1$) gives back the usual fermion (boson) commutators. The statistical mixture in equation (2) also shows that the PEP violation probability is just $(1+q)/2$ and thus

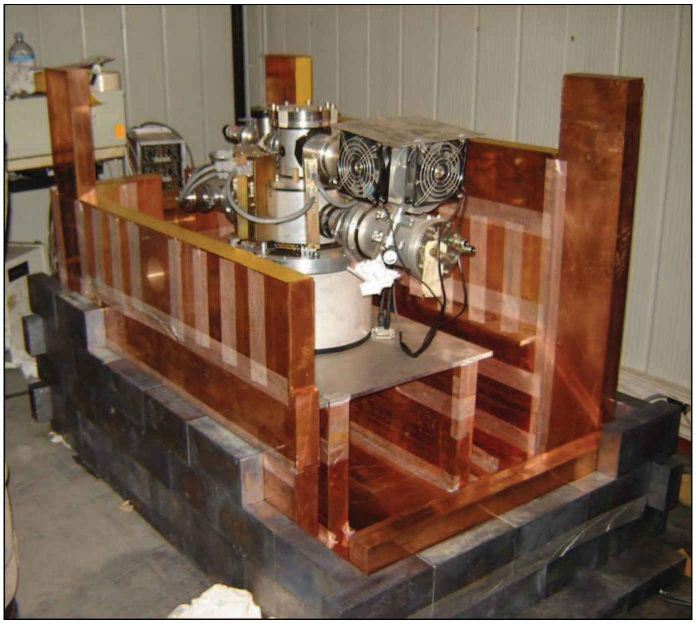

Figure 2: The VIP setup at the LNGS laboratory during the installation procedure.

our final experimental bound on q is

$$\frac{1+q}{2} < 3 \times 10^{-29} \tag{3}$$

We are in close contacts with theoreticians and philosophers, looking for implications of the possible small violation of the PEP in physics, cosmology and philosophy.

4 VIP2, a high sensitivity setup and future perspectives

The VIP setup used CCD detectors, which are excellent X-ray detectors, but slow. We are using a new type of detectors for precision X-rays measurements, the triggerable Silicon Drift Detectors (SSD) which have a fast readout time ($\simeq 1\mu$s) and large collection area (100 mm^2) in the framework of VIP2, a new high sensitivity setup. These detectors were successfully used in the SIDDHARTA experiment at LNF-INFN for measurements of the kaonic atoms transitions at the DAΦNE accelerator of LNF-INFN [22]; using a proper trigger system a background rejection factor of the order of 10^{-4} was achieved in SIDDHARTA. We built a new setup, much more compact, with higher current circulating and with a veto system against background coming from outside. A picture of the new setup is shown in Fig. 3.

In 2014 the setup was under assembly and tests at LNF-INFN and SMI-Vienna, where a series of preliminary measurements were done. In 2015 the setup will be transported, installed and debugged at LNGS.

We then expect to gain about 2 orders of magnitude in the limit of PEP violation in a data taking of 3-4 years.

We are, as well, extending the scientific program towards studies of limits on the parameters of the collapse model (as a solution of the measurement problem, put initially forward by

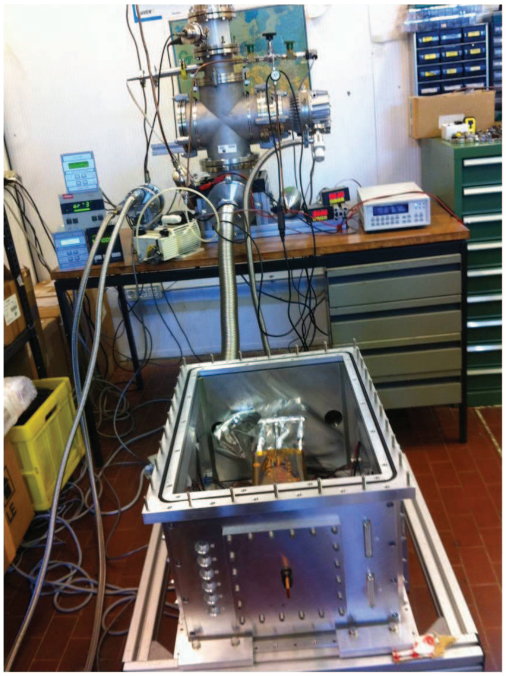

Figure 3: The VIP2 setup using SDD detectors and an external veto-system under test in in LNF-INFN laboratory

Ghirardi, Rimini and Weber) by measurements of the X rays spontaneously emitted and which are predicted by the continuous spontaneous localization (CSL) models [23], [24].

Our preliminary results are very encouraging and show that this method is the most powerful one, presently, in setting limits on the collapse models (see List of Publications).

5 Acknowledgements

The VIP Collaboration thanks all the LNGS laboratory staff for the precious help and assistance during all phases of preparation, installation and data taking. The supports from Museo Storico della Fisica e Centro Studi e Ricerche Enrico Fermi, Roma, the HadronPhysics FP6, HadronPhysics2 and HadronPhysics3 FP7 and from the EU COST 1006 Action projects are acknowledged.

6 List of Publications in 2014-2015

1. C. Curceanu *et al.*, *Quantum explorations from the waltz of the Pauli exclusion Principle to the rock of the spontaneous collapse*, Phys. Scr. **90** (2015) 028003.
2. C. Curceanu *et al.*, *X-rays help to unfuzzy the concept of measurement*, e-Print: arXiv:1502.05961, to appear in Journal of Advanced Physics.
3. K. Piscicchia *et al.*, *Beyond quantum mechanics? Hunting the "impossible " atoms (Pauli Exclusion Principle violation and spontaneous collapse of the wave function at test)*, Acta Physics Polonica, **B46** (2015) 147.

4. C. Curceanu *et al.*, *Experimental Tests of Quantum Mechanics: Pauli Exclusion Principle and Spontaneous Collapse Models*, Springer Proc. Phys. **145** (2014) 181.
5. H. Shi *et al.*, *Testing the Pauli Exclusion Principle for electrons at LNGS*, e-Print: arXiv:1405.1634.

References

[1] W. Pauli, *Phys. Rev.* **58**, (1940), 716.

[2] R. P. Feynman, R. B. Leighton and M. Sands *The Feynman Lectures on Physics*, Addison-Wesley, Reading, MA (1963).

[3] R. Arnold, *et al.*, *Eur. Phys. J. A***6** (1999) 361.

[4] H.O. Back, *et al.*, *Eur. Phys. J. C***37** (2004) 421.

[5] A. Barabash, *Found. of Phys.* **40** (2010) 703.

[6] A.S. Barabash,*et al.*, *JETP Lett.* **68** (1998) 112.

[7] P. Belli, *et al.*, **460** (1999) 236.

[8] G. Bellini, *et al.*, *Phys. Rev. C* **81** (2010) 034.

[9] R. Bernabei, *et al.*, *Phys. Lett. B* **408** (1997) 439.

[10] R. Bernabei, *et al.*, *Eur. Phys. J. C* **62** (2009) 327.

[11] Y. Suzuki, *et al.*, *Phys. Lett. B* **311** (1993) 357.

[12] S. R. Elliott *et al.*, *Found. Phys.* **42** (2012) 1015.

[13] A.M.L. Messiah, O.W. Greenberg, *Phys. Rev.* **136** (1964) B248.

[14] E. Ramberg and G. A. Snow, *Phys. Lett. B* **238** (1990) 438.

[15] C. Curceanu *et al.* Evaluation of the X-ray transition energies for the Pauli-Principle-violating atomic transitions in several elements by using the Dirac-Fock method, LNF preprint, INFN-13-21/LNF, 21-11-2013.

[16] J. L. Culhane, *Nucl. Instrum. Methods A* **310** (1990) 1.

[17] J.-P. Egger, D. Chatellard and E. Jeannet, *Particle World* **3**, (1993) 139.

[18] G. Fiorucci, *et al. Nucl. Instrum. Methods A* **292** (1990) 141.

[19] D. Varidel, *et al.Nucl. Instrum. Methods A* **292** (1990) 147

[20] R. P. Kraft, *et al.Nucl. Instrum. Methods A* **372** (1995) 372.

[21] O. W. Greenberg *Phys. Rev. Lett.* **64** (1990) 705.

[22] C. Curceanu *et al. Eur Phys* **J A31** (2007) 537-539; M. Bazzi *et al. Phys. Lett.* **B681** (2009) 310; M. Bazzi *et al. Phys. Lett.* **B704** (2011) 113; Bazzi *et al. Phys. Lett.* **B697** (2011) 199; Bazzi *et al. Phys. Lett.* **B714** (2012) 40.

[23] Q. Fu *Phys. Rev* **A56** (1997) 1806.

[24] G.C. Ghirardi, A. Rimini and T. Weber *Phys. Rev.* **D34** (1986) 470: ibid. (1987) 3287: *Found. Phys.* **18** (1988) 1.

THE PIERRE AUGER OBSERVATORY

D. Boncioli[a], A. di Matteo[b], A.F. Grillo[a], S. Petrera[b,c], V. Rizi[b]
for the Pierre Auger Collaboration

[a] INFN Laboratori Nazionali del Gran Sasso, Assergi (Aq), Italy
[b] INFN and Department of Physical and Chemical Sciences,
University of L'Aquila, L'Aquila, Italy
[c] GSSI, Gran Sasso Science Institute, L'Aquila, Italy

Abstract

The Pierre Auger Project is an international Collaboration involving over 400 scientists from 17 countries, with the objective of studying the highest energy cosmic rays. Recent results from the Collaboration as well as further developments in the detector are presented in this report.

1 Introduction

Ultra-high energy cosmic rays are of intrinsic interest as their origin and nature are un- known. It is quite unclear where and how particles as energetic as $\approx 10^{20}$ eV are accelerated. Over 40 years ago it was pointed out that if the highest energy particles are protons then a fall in the flux above an energy of about 4×10^{19} eV is expected because of energy losses by the protons as they propagate from distant sources through the CMB radiation. At the highest energies the key process is photo-pion production in which the proton loses part of its energy in each creation of a Δ resonance. This is the Greisen–Zatsepin–Kuzmin (GZK) effect. It follows that at 10^{20} eV any proton observed must have come from within about 50 Mpc and on this distance scale the deflections by intervening magnetic fields in the galaxy and intergalactic space are expected to be so small that point sources should be observed. Despite immense efforts in the period since the prediction, the experimental situation remains unclear. The main problem in examining whether or not the spectrum steepens is the low rate of events which, above 10^{20} eV, is less than 1 per km^2 per century so that the particles are only detectable through the giant air showers that they create.

These showers have particle footprints on the ground of ≈ 20 km^2 and suitably distributed detectors can be used to observe them. Also the showers excite molecules of atmospheric nitrogen and the resulting faint fluorescence radiation, which is emitted isotropically, can be detected from distances of several tens of kilometers.

The Pierre Auger Observatory has been developed by a team of over 400 scientists from 17 countries. The Observatory comprises about 1600 10 m^2 $\times$ 1.2m water-Cherenkov detectors deployed over 3000 km^2 on a 1500 m hexagonal grid, plus a sub array, the Infill, with 71 water Cherenkov detectors on a denser grid of 750 m covering nearly 30 km^2. This part of the Observatory (the surface detector, SD) is over-looked by 24 fluorescence telescopes in 4 clusters located on four hills around the SD area which is extremely flat. The surface detectors contain 12 tonnes of clear water viewed by $3 \times 9''$ hemispherical photomultipliers. The fluorescence detectors (FD) are designed to record the faint ultra-violet light emitted as the shower traverses the atmosphere. Each telescope images a portion of the sky of 30° in azimuth and 1°–30° in elevation using a spherical mirror of 3 m^2 effective area to focus light on to a camera of 440×18 cm^2 hexagonal pixels, made of photomultipliers complemented with light collectors, each with a field of view of 1.5° diameter. 3 High Elevation Auger Telescopes (HEAT) located at one of the fluorescence sites are dedicated to the fluorescence observation of lower energy showers. The Observatory also comprises a sub array of 124 radio sensors (AERA, Auger Engineering Radio Array) working in the MHz range and covering 6 km^2, a sub Array of 61 radio sensors (EASIER, Extensive Air Shower Identification with Electron Radiometer) working in the GHz range and covering 100 km^2, and two GHz imaging radio telescopes AMBER and MIDAS with respectively $14° \times 14°$ and $10° \times 20°$ field of views.

An important feature of the design of the Observatory was the introduction of the hybrid technique as a new tool to study airshowers. It is used here for the first time. The hybrid technique is the term chosen to describe the method of recording fluorescence data coincident with the timing information from at least one surface detector. Employing these two complementary observation methods provides the Auger Observatory with high quality information about angular reconstruction, determination of the core position of the shower and of the types of particles in the primary cosmic rays. Comparing results from the different types of detectors also helps scientists reconcile the two sets of data and produce the most accurate results about the energy of primary cosmic rays.

2 Recent results from the Pierre Auger Observatory

2.1 The Energy Spectrum

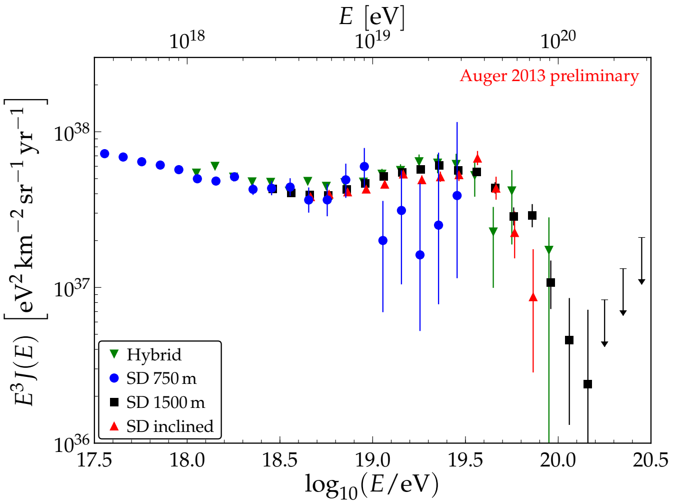

Figure 1: Comparison of the four spectra obtained with the Auger Observatory. The spectrum obtained with the SD for events with $\theta < 60°$ is shown with black squares, the inclined spectrum ($62° < \theta < 80°$) is plotted with red upright triangles and that obtained in the 750 array is indicated with blue circles. The spectrum obtained with hybrid data is indicated with green triangles. Only statistical uncertainties are indicated with the error bars [1, 2].

The energy spectrum of ultra-high energy cosmic rays at energies greater than 3×10^{17} eV

has been derived using data from the Pierre Auger Observatory [2].
The spectrum is calculated selecting data that fall inside a given region of the detector, and dividing the energy distribution by the corresponding exposure. If the showers have sufficient energy, the trigger efficiency of the surface detector becomes close to 100% and the exposure is independent of energy and simply obtained by integrating over the surface area, time and solid angle. The SD of the Pierre Auger Observatory becomes fully efficient above 3 EeV for events with zenith angle, θ, below 60°. For inclined events with θ exceeding 60° the energy above which the efficiency is approximately 100% is 4 EeV. For events detected with the 750 m array full efficiency is reached at energies greater than 0.3 EeV. Three independent fluxes have been obtained with the Auger Observatory at the highest energies [2, 3]. The data collected up to 31st December 2012 with $\theta < 60°$give the largest exposure corresponding to 82,318 events of energies above 3 EeV. The results of these three fluxes and the flux obtained at lower energies with the 750 m array are compared in Fig. 1.

This measurement provides evidence for the suppression of the flux above 4×10^{19} eV. The combined energy spectrum scaled with E^3 is shown in Fig. 1. The dominant systematic uncertainty of the spectrum stems from that of the overall energy scale, which is estimated to be 14%. The position of the ankle at $\log_{10}(E\text{ankle}/\text{eV}) = 18.72 \pm 0.01$ (stat.) ± 0.02 (sys.) has been determined by fitting the flux with a broken power law $E^{-\gamma}$. An index of $\gamma = 3.23 \pm 0.01 \pm 0.07$ is found below the ankle. Above the ankle the spectrum follows a power law with index $2.63 \pm 0.02 \pm 0.04$. In comparison to the power law extrapolation, the spectrum is suppressed by a factor two at $\log_{10}(E_{1/2}/\text{eV}) = 19.63 \pm 0.01 \pm 0.01$. The significance of the suppression is larger than 20σ. The suppression is similar to what is expected from the GZK effect for protons or nuclei as heavy as iron, but could in part also be related to a change of the shape of the average injection spectrum at the sources.

2.2 The mass composition

The atmospheric depth, $X_{\max}$, at which the longitudinal development of a shower reaches its maximum in terms of the number of secondary particles is correlated with the mass of the incident cosmic ray particle. With the generalization of Heitlers model of electron– photon cascades to hadron-induced showers and the superposition assumption for nuclear primaries of mass A, the average depth of the shower maximum, $X_{\max}$, at a given energy E is expected to follow [4]

$$\langle X_{\max} \rangle = \alpha(\ln E \langle \ln A \rangle) + \beta \tag{1}$$

where $\langle \ln A \rangle$ is the average of the logarithm of the primary masses. The coefficients α and β depend on the nature of hadronic interactions, most notably on the multiplicity, elasticity and cross-section in ultra-high energy collisions of hadrons with air, see e.g. [5].

A recent analysis [6] based on high quality and high statistics hybrid data collected with the southern site of the Pierre Auger Observatory has been addressed to the $\langle X_{\max} \rangle$ measurement and its energy dependence. A comparison of the predictions of the moments from simulations for proton- and iron-induced air showers to the data is shown in Fig. 2. Comparing the energy evolution of $\langle X_{\max} \rangle$ for data and simulations in Fig. 2 it can be seen that the slope of the data is different from what would be expected for either a pure-proton or pure-iron composition. The change of $\langle X_{\max} \rangle$ with the logarithm of energy is usually referred to as elongation rate D_{10}. A single linear fit of $X_{\max}$ as a function of $\lg(E)$ does not describe our data well. Allowing for a change in the elongation rate at a break point $\lg(E_0)$ yields a good χ^2/ndf of 8.2/14 with $\lg E_0/\text{eV} = 18.27$.
An interpretation in terms of mass composition of the moments of the $X_{\max}$ distribution was

given using air- shower simulations with contemporary hadronic interaction models. Assuming that the modeling of hadronic interactions gives a fair representation of the actual processes in air showers at ultra-high energies, our data suggest that the flux of cosmic rays is composed of predominantly light nuclei at around $10^{18.3}$ eV and that the fraction of heavy nuclei is increasing up to energies of $10^{19.6}$ eV. Estimates of the fractions of groups of nuclei contributing to the cosmic-ray flux can be derived by interpreting the full distributions as in [7].

Due to its hybrid design, the Pierre Auger Observatory also provides independent experimental observables obtained from the surface detector for the study of the shower development, as for example reported in [8].

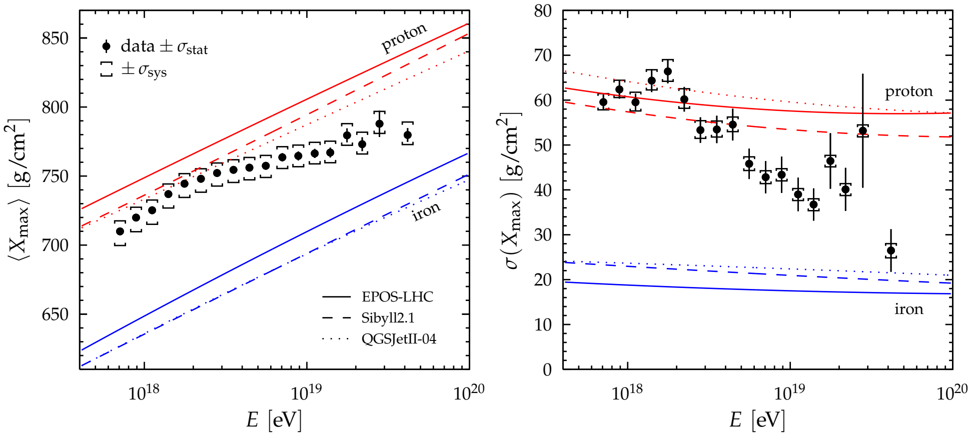

Figure 2: Energy evolution of the first two central moments of the $X_{\max}$ distribution compared to air-shower simulations for proton and iron primaries [6].

2.3 The Cosmic Ray Anisotropy

Between January 2004 and December 2009 the Pierre Auger Observatory has detected 69 cosmic rays events with energy in excess of 55 EeV. Their arrival directions are reported in [9]. This data set is more than twice as large as the one analyzed in [10], which provided evidence of anisotropy in CR arrival directions at the 99% confidence level. The anisotropy was tested with a priori parameters through the correlation between the arrival directions of CRs and the positions of nearby active galaxies from the 12th edition of the Veron-Cetty Veron catalog of quasars and active galactic nuclei. The degree of that observed correlation has decreased from $(69^{+11}_{-13})\%$ to $(38^{+7}_{-6})\%$, to be compared with the 21% expected to occur by chance if the flux were isotropic. More data are needed to determine this correlating fraction accurately. The evidence for anisotropy has not strengthened since the analysis reported in [10].

The correlation of recent data with objects in the VCV catalog is not as strong as that observed in 2007. If the evidence for anisotropy is substantiated by future data, then it should also become possible to discriminate between different astrophysical scenarios using techniques of the type that have been presented here to explore the compatibility of different models with the present set of arrival directions.

We have also compared the distribution of arrival directions with the positions of different populations of nearby extragalactic objects: galaxies in the 2MRS survey and AGNs detected in X-rays by Swift-BAT. These studies are a posteriori and do not constitute further quantitative evidence for anisotropy.

We have analyzed the region of the sky close to the location of the radiogalaxy Cen A, since this corresponds to the largest observed excess with respect to isotropic expectations. The region of Cen A is densely populated with different types of nearby extragalactic objects. From all the arrival directions of CRs with $E \geq 55$ EeV, 18.8% lie within 18° of Cen A, while 4.7% is the isotropic expectation. There are two arrival directions very close to the position of the Cen A nucleus. Aside from those two events, the excess is distributed rather broadly.

A knowledge of CR composition is important for deciding which of several source scenarios is more likely. The trajectories of highly charged nuclei are expected to undergo large deflections due to the Galactic magnetic fields. While a correlation of arrival directions with nearby matter on small angular scales is plausible for protons above 55 EeV, it is puzzling if the CR are heavy nuclei. If the particles responsible for the measured excesses for example around Centaurus A at $E > 55$ EeV are heavy nuclei with charge Z, the proton component of the sources should lead to excesses in the same regions at energies E/Z. In [12] the lack of anisotropies in the directions of the excesses at energies above E_{th}/Z is reported, setting constraints on the allowed proton fraction at the lower energies.

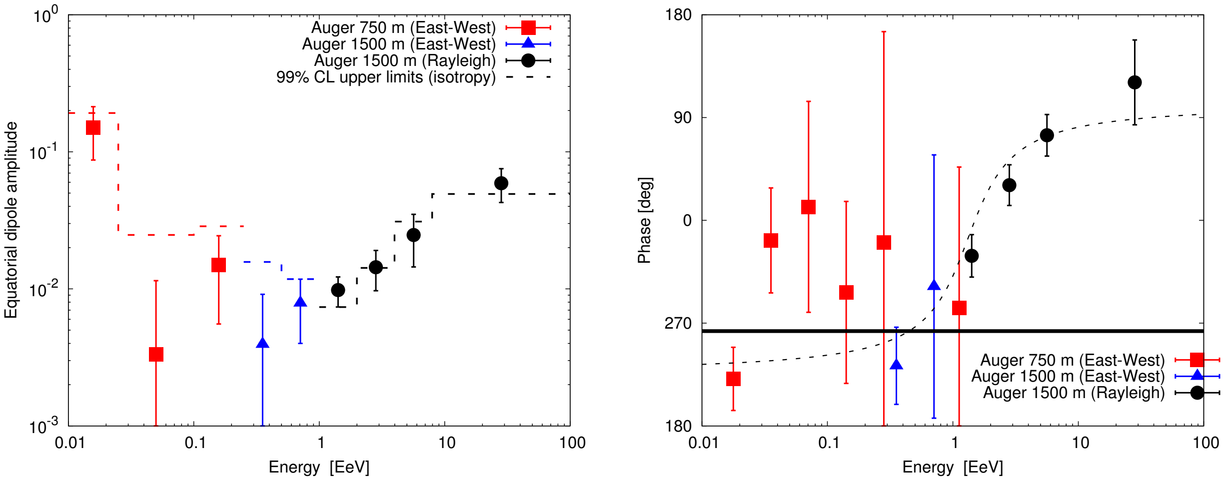

Figure 3: Left: Amplitude of the first term in the Fourier expansion of the flux measured at the Auger Observatory in terms of R.A. as a function of energy. It can be related to the projection of a dipole amplitude onto the equatorial plane [11]. Right: Phase of the first harmonic in R.A. as a function of energy using data from the Pierre Auger Observatory from January 1 2004 to December 31 2010 for the larger array, and from September 12 2007 to April 11 2011 for the infill [11].

The results of an analysis of the large angular scale distribution of the arrival directions of the Pierre Auger Observatory data has also been carried on, including for the first time inclined events with zenith angle between 60° and 80°. A prescription has been established to test these possible hints of anisotropy. The results obtained of the dipole amplitude compared to expectations from isotropy and the dipole phases presented when the prescription was midterm, are shown in Fig 3.

2.4 Searches for high-energy neutrinos and gamma rays

The limits on the fluxes of neutrinos [14] and photons [13] obtained from the Pierre Auger Observatory are shown in Fig. 5 and Fig. 4. Model scenarios for sources of UHECRs, in which

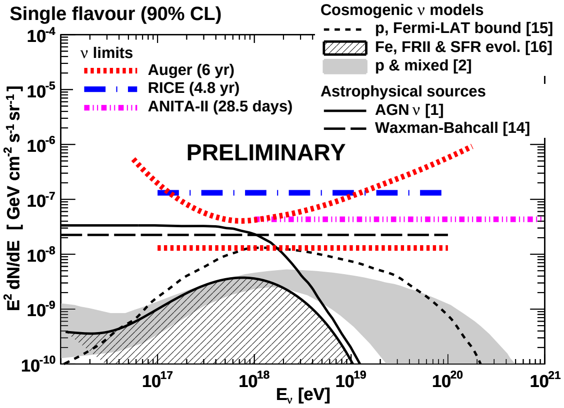

Figure 4: Differential and integrated upper limits (at 90% C.L.) from the Pierre Auger Observatory for a diffuse flux of UHE neutrinos. The search period corresponds to 6 yr of a complete SD. We also show the integrated limits from ANITAII, and RICE experiments, along with expected fluxes for several cosmogenic neutrino models as well as for astrophysical sources [14].

the observed particles are produced by the decay of other particles (top-down models), lead to large secondary fluxes of photons and neutrinos. Some representative examples of predicted secondary fluxes of such models are shown in Fig. 5 and Fig. 4 (photons: GZK, TD, Z-burst, and SHDM; neutrinos: TD, Z-burst). The neutrino flux limit of the Auger Observatory is now lower than the Waxman-Bahcall flux. The current flux limits rule out or strongly disfavor that top-down models can account for a significant part of the observed UHECR flux. The bounds are reliable as the photon flux limits depend only on the simulation of electromagnetic showers and, hence, are very robust against assumptions on hadronic interactions at very high energy.

3 Activity of the L'Aquila–Gran Sasso Group

The activity of the group has followed two main lines:

- Developement of a Monte Carlo code (*SimProp*) for the propagation of UHECR nuclei in extragalactic space, and its use for the study of physical observables
- Developement and test of the Raman Lidar system for an enhanced atmospheric test beam within the Observatory.

The first activity is carried on iside the Cosmic Ray Phenomenology task of the Pierre Auger Collaboration. Using outputs of *SimProp*, several physical analyses are in progress, concerning a combined fit of the energy spectrum and the mass composition of UHECRs detected in the Observatory. This analysis is also contributing to the scientific motivations for the upgrade of the Pierre Auger Observatory.
The study of predictions for the fluxes of cosmogenic neutrinos from GZK interactions has been also carried on.
Lorentz invariance violations are under study, from the point of view of their effects on UHECR propagation and on interactions of particles in the Earth atmosphere.

The second activity concerns the atmospheric monitoring. The Raman Lidar system has been fully operative at the Central Raman Laser Facility (CRLF). The measurements of the Vertical

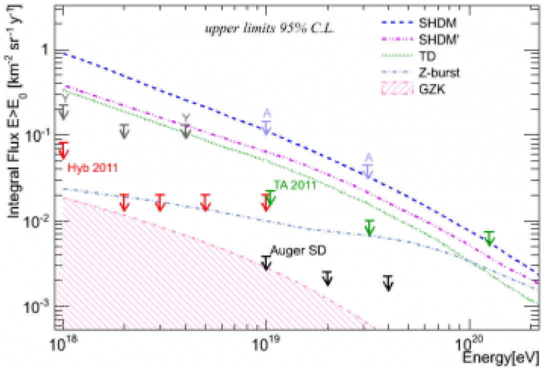

Figure 5: Upper limits on the photon flux above 1, 2, 3, 5 and 10 EeV (Auger ICRC 2011) compared to previous limits from Auger (SD and Hybrid 2009, from AGASA (A), Yakutsk (Y) and Telescope Array (TA 2011). The shaded region and the lines give the predictions for the GZK photon flux and for top-down models (TD, Z-Burst, SHDM, and SHDM) [13].

Aerosol Optical Depth (VAOD) have been taken from boundary layer to free troposphere from Raman scattering, together with elastic scattering and water vapor profiles; the Raman and elastic measurements can be combined to give (through the backscatter ratio) a precise determination of the aereosol profile. The measurements are performed every night: during nights with no FD measurements, they consist of one 12 minutes run. During the FD measurements there are three 12 minutes Raman runs, one before and after FD acquisition and (starting from 2014) one during the acquisition. Given the importance of the aerosol measurement for a precise FD reconstruction, it is foreseen to have longer runs during acquisition in selected, low aerosol content, nights. The CRLF Raman LIDAR has a sensitivity for which the minimum measurable VAOD is about 0.01 in 12 minutes, but a sensitivity of 0.005 can be reached in longer runs. After each Raman run, the data are copied to LNGS and CSM/USA servers, and a program computes preliminary VAOD values (which are sent by email immediately after the run) and generates preliminary VAOD plots (http://cetemps.aquila.infn.it/osservatorio/CLRF_raman_lidar/). The Raman LIDAR operations have been regular and smooth, and the automatic Raman LIDAR runs were done according to Before/During/After FD shift schedule without interferences with fluorescence detectors. The Raman LIDAR analysis has shown to be robust, and the data quality check quite positive. The Raman lidar database is now ready for an extended comparison between Raman lidar and side scattering techniques, but also for atmospheric studies.

3.1 Talks

- A. di Matteo has presented a talk with title “ Interaction of ultra-high-energy cosmic rays with cosmic background photons” at the International School of Space Science “Observing the Universe with the Cosmic Microwave Background”, L’Aquila, April 2014.
- A. di Matteo has presented a talk with title “Expected cosmogenic neutrino fluxes in various UHECR scenarios” at the “Multiple Messengers and Challenges in Astroparticle Physics” workshop at GSSI, L’Aquila, October 2014.
- A.F. Grillo has presented a talk with title “Are Cosmic Rays still a valuable probe of Lorentz Invariance Violations in the Auger era?” at the Vulcano Workshp “Frontier Ob-

jects in Astrophysics and Particle Physics", May 2014. The Proceeding has been published in Frascati Phys.Ser. 58 (2014) 274.
The same topic has been presented at the "Multiple Messengers and Challenges in Astroparticle Physics" workshop at GSSI, L'Aquila, October 2014 and at LNGS as a seminar.

- V. Rizi has presented a talk with title "Raman LIDARs for Pierre Auger Observatory: field experiences and results" at AtmoHEAD 2014, Padova, May 2014.
- S. Petrera has presented a talk with title "Auger - Telescope Array" at the "Multiple Messengers and Challenges in Astroparticle Physics" workshop at GSSI, L'Aquila, October 2014.
- The proceedings of the talk "Cosmic ray composition studies with the Pierre Auger Observatory" given by D. Boncioli on behalf of the Pierre Auger Collaboration at RICAP Conference (Roma, May 2013) has been published in Nucl.Instrum.Meth. A742 (2014) 22-28.

4 List of Publications

1. A. Aab *et al.* [Pierre Auger Collaboration], "Depth of maximum of air-shower profiles at the Pierre Auger Observatory. II. Composition implications," Phys. Rev. D **90** (2014) 12, 122006 [arXiv:1409.5083 [astro-ph.HE]].
2. A. Aab *et al.* [Pierre Auger Collaboration], "Depth of maximum of air-shower profiles at the Pierre Auger Observatory. I. Measurements at energies above $10^{17.8}$eV," Phys. Rev. D **90** (2014) 12, 122005 [arXiv:1409.4809 [astro-ph.HE]].
3. A. Aab *et al.* [Telescope Array and Pierre Auger Collaborations], "Searches for Large-Scale Anisotropy in the Arrival Directions of Cosmic Rays Detected above Energy of 10^{19} eV at the Pierre Auger Observatory and the Telescope Array," Astrophys. J. **794** (2014) 2, 172 [arXiv:1409.3128 [astro-ph.HE]].
4. A. Aab *et al.* [Pierre Auger Collaboration], "Muons in air showers at the Pierre Auger Observatory: Mean number in highly inclined events," Phys. Rev. D **91** (2015) 3, 032003 [Erratum-ibid. D **91** (2015) 5, 059901] [arXiv:1408.1421 [astro-ph.HE]].
5. A. Aab *et al.* [Pierre Auger Collaboration], "Reconstruction of inclined air showers detected with the Pierre Auger Observatory," JCAP **1408** (2014) 08, 019 [arXiv:1407.3214 [astro-ph.HE]]
6. A. Aab *et al.* [Pierre Auger Collaboration], "A Targeted Search for Point Sources of EeV Neutrons," Astrophys. J. **789** (2014) L34 [arXiv:1406.4038 [astro-ph.HE]]
7. A. Aab *et al.* [Pierre Auger Collaboration], "A Targeted Search for Point Sources of EeV Photons," Astrophys. J. **789** (2014) 160 [arXiv:1406.2912 [astro-ph.HE]]
8. A. Aab *et al.* [Pierre Auger Collaboration], "Probing the radio emission from air showers with polarization measurements," Phys. Rev. D **89** (2014) 5, 052002 [arXiv:1402.3677 [astro-ph.HE]].

References

[1] E. Zas, to be submitted to the proceedings of ECRS 2014

[2] A. Schulz for the Pierre Auger Collaboration, 33rd ICRC, Rio de Janeiro, Brazil, 2013, arXiv:1307.5059 [astro-ph.HE].

[3] A. Lettesier-Selvon for the Pierre Auger Collaboration . 2013 Proc. of the 33rd ICRC, Rio de Janeiro, (highlight talk) arXiv astro-ph:1310.4620.

[4] W. Heitler, Oxford University Press, 1954;
J. Matthews, Astropart. Phys. 22 (2005), 387

[5] T. Wibig, Phys. Rev. D 79, 094008;
R. Ulrich et al. for the Pierre Auger Collaboration, Proc. 32th ICRC (Beijing, China) 2011

[6] A. Aab *et al.* [Pierre Auger Collaboration], Phys. Rev. D **90** (2014) 12, 122005, [arXiv:1409.4809 [astro-ph.HE]].

[7] A. Aab *et al.* [Pierre Auger Collaboration], Phys. Rev. D **90** (2014) 12, 122006, [arXiv:1409.5083 [astro-ph.HE]].

[8] D. Boncioli for the Pierre Auger Collaboration, Nucl.Instrum.Meth. A742 (2014) 22-28

[9] P.Abreu et al. [The Pierre Auger Collaboration], Astropart. Phys. 34, 314-326 (2010). ([arXiv:1009.1855])

[10] Pierre Auger Collaboration [J. Abraham et al.], Science 318 (2007) 938. Astropart. Phys. 29 (2008) 188.

[11] A. Aab *et al.* [Telescope Array and Pierre Auger Collaborations], Astrophys. J. **794** (2014) 2, 172 [arXiv:1409.3128 [astro-ph.HE]].

[12] Pierre Auger Collaboration [J. Abraham et al.], JCAP 1106 (2011) 022 and arXiv:1106.3048 [astro-ph.HE].

[13] Pierre Auger Collab., J. Abraham et al., Astropart. Phys. 27, 155 (2007), astro-ph/0606619.
Pierre Auger Collab., J. Abraham et al., Astropart. Phys. 29, 243 (2008), arXiv:0712.1147.
Pierre Auger Collab., J. Abraham et al., Astropart. Phys. 31, 399 (2009), arXiv:0903.1127.
A. Aab *et al.* [Pierre Auger Collaboration], Astrophys. J. **789** (2014) 160 [arXiv:1406.2912 [astro-ph.HE]]

[14] Pierre Auger Collab., P. Pieroni, Proc. of 33rd Int. Cosmic Ray Conf., Rio de Janeiro, Brazil, #0697 (2013), arXiv:1307.5059.

The Pierre Auger Collaboration

A. Aab[41], P. Abreu[65], M. Aglietta[52], E.J. Ahn[82], I. Al Samarai[28], I.F.M. Albuquerque[16], I. Allekotte[1], P. Allison[87], A. Almela[11, 8], J. Alvarez Castillo[58], J. Alvarez-Muñiz[75], R. Alves Batista[40], M. Ambrosio[43], A. Aminaei[59], L. Anchordoqui[81], S. Andringa[65], C. Aramo[43], V.M. Aranda [72], F. Arqueros[72], N. Arsene[68], H. Asorey[1, 24], P. Assis[65], J. Aublin[30], M. Ave[1], M. Avenier[31], G. Avila[10], N. Awal[85], A.M. Badescu[69], K.B. Barber[12], J. Bäuml[35], C. Baus[35], J.J. Beatty[87], K.H. Becker[34], J.A. Bellido[12], C. Berat[31], M.E. Bertaina[52], X. Bertou[1], P.L. Biermann[38], P. Billoir[30], S.G. Blaess[12], A. Blanco[65], M. Blanco[30], C. Bleve[47], H. Blümer[35, 36], M. Boháčová[26],

D. Boncioli[51], C. Bonifazi[22], N. Borodai[63], J. Brack[79], I. Brancus[66], A. Bridgeman[36], P. Brogueira[65], W.C. Brown[80], P. Buchholz[41], A. Bueno[74], S. Buitink[59], M. Buscemi[43], K.S. Caballero-Mora[56], B. Caccianiga[42], L. Caccianiga[30], M. Candusso[44], L. Caramete[67], R. Caruso[45], A. Castellina[52], G. Cataldi[47], L. Cazon[65], R. Cester[46], A.G. Chavez[57], A. Chiavassa[52], J.A. Chinellato[17], J. Chudoba[26], M. Cilmo[43], R.W. Clay[12], G. Cocciolo[47], R. Colalillo[43], A. Coleman[88], L. Collica[42], M.R. Coluccia[47], R. Conceição[65], F. Contreras[9], M.J. Cooper[12], A. Cordier[29], S. Coutu[88], C.E. Covault[77], J. Cronin[89], R. Dallier[33, 32], B. Daniel[17], S. Dasso[5, 3], K. Daumiller[36], B.R. Dawson[12], R.M. de Almeida[23], S.J. de Jong[59, 61], G. De Mauro[59], J.R.T. de Mello Neto[22], I. De Mitri[47], J. de Oliveira[23], V. de Souza[15], L. del Peral[73], O. Deligny[28], H. Dembinski[36], N. Dhital[84], C. Di Giulio[44], A. Di Matteo[48], J.C. Diaz[84], M.L. Díaz Castro[17], F. Diogo[65], C. Dobrigkeit [17], W. Docters[60], J.C. D'Olivo[58], A. Dorofeev[79], Q. Dorosti Hasankiadeh[36], M.T. Dova[4], J. Ebr[26], R. Engel[36], M. Erdmann[39], M. Erfani[41], C.O. Escobar[82, 17], J. Espadanal[65], A. Etchegoyen[8, 11], H. Falcke[59, 62, 61], K. Fang[89], G. Farrar[85], A.C. Fauth[17], N. Fazzini[82], A.P. Ferguson[77], M. Fernandes[22], B. Fick[84], J.M. Figueira[8], A. Filevich[8], A. Filipčič[70, 71], B.D. Fox[90], O. Fratu[69], M.M. Freire[6], B. Fuchs[35], T. Fujii[89], B. García[7], D. Garcia-Pinto[72], F. Gate[33], H. Gemmeke[37], A. Gherghel-Lascu[66], P.L. Ghia[30], U. Giaccari[22], M. Giammarchi[42], M. Giller[64], D. Głas[64], C. Glaser[39], H. Glass[82], G. Golup[1], M. Gómez Berisso[1], P.F. Gómez Vitale[10], N. González[8], B. Gookin[79], J. Gordon[87], A. Gorgi[52], P. Gorham[90], P. Gouffon[16], N. Griffith[87], A.F. Grillo[51], T.D. Grubb[12], F. Guarino[43], G.P. Guedes[18], M.R. Hampel[8], P. Hansen[4], D. Harari[1], T.A. Harrison[12], S. Hartmann[39], J.L. Harton[79], A. Haungs[36], T. Hebbeker[39], D. Heck[36], P. Heimann[41], A.E. Herve[36], G.C. Hill[12], C. Hojvat[82], N. Hollon[89], E. Holt[36], P. Homola[34], J.R. Hörandel[59, 61], P. Horvath[27], M. Hrabovský[27, 26], D. Huber[35], T. Huege[36], A. Insolia[45], P.G. Isar[67], I. Jandt[34], S. Jansen[59, 61], C. Jarne[4], J.A. Johnsen[78], M. Josebachuili[8], A. Kääpä[34], O. Kambeitz[35], K.H. Kampert[34], P. Kasper[82], I. Katkov[35], B. Kégl[29], B. Keilhauer[36], A. Keivani[88], E. Kemp[17], R.M. Kieckhafer[84], H.O. Klages[36], M. Kleifges[37], J. Kleinfeller[9], R. Krause[39], N. Krohm[34], O. Krömer[37], D. Kuempel[39], N. Kunka[37], D. LaHurd[77], L. Latronico[52], R. Lauer[92], M. Lauscher[39], P. Lautridou[33], S. Le Coz[31], D. Lebrun[31], P. Lebrun[82], M.A. Leigui de Oliveira[21], A. Letessier-Selvon[30], I. Lhenry-Yvon[28], K. Link[35], L. Lopes[65], R. López[53], A. López Casado[75], K. Louedec[31], L. Lu[34, 76], A. Lucero[8], M. Malacari[12], S. Maldera[52], M. Mallamaci[42], J. Maller[33], D. Mandat[26], P. Mantsch[82], A.G. Mariazzi[4], V. Marin[33], I.C. Mariş[74], G. Marsella[47], D. Martello[47], L. Martin[33, 32], H. Martinez[54], O. Martínez Bravo[53], D. Martraire[28], J.J. Masías Meza[3], H.J. Mathes[36], S. Mathys[34], J. Matthews[83], J.A.J. Matthews[92], G. Matthiae[44], D. Maurel[35], D. Maurizio[13], E. Mayotte[78], P.O. Mazur[82], C. Medina[78], G. Medina-Tanco[58], R. Meissner[39], V.B.B. Mello[22], D. Melo[8], A. Menshikov[37], S. Messina[60], R. Meyhandan[90], M.I. Micheletti[6], L. Middendorf[39], I.A. Minaya[72], L. Miramonti[42], B. Mitrica[66], L. Molina-Bueno[74], S. Mollerach[1], F. Montanet[31], C. Morello[52], M. Mostafá[88], C.A. Moura[21], M.A. Muller[17, 20], G. Müller[39], S. Müller[36], R. Mussa[46], G. Navarra[52] ‡, S. Navas[74], P. Necesal[26], L. Nellen[58], A. Nelles[59, 61], J. Neuser[34], P.H. Nguyen[12], M. Niculescu-Oglinzanu[66], M. Niechciol[41], L. Niemietz[34], T. Niggemann[39], D. Nitz[84], D. Nosek[25], V. Novotny[25], L. Nožka[27], L. Ochilo[41], F. Oikonomou[88], A. Olinto[89], N. Pacheco[73], D. Pakk Selmi-Dei[17], M. Palatka[26], J. Pallotta[2], P. Papenbreer[34], G. Parente[75], A. Parra[53], T. Paul[81, 86], M. Pech[26], J. Pękala[63], R. Pelayo[55], I.M. Pepe[19], L. Perrone[47], E. Petermann[91], C. Peters[39], S. Petrera[48, 49], Y. Petrov[79], J. Phuntsok[88], R. Piegaia[3], T. Pierog[36], P. Pieroni[3], M. Pimenta[65], V. Pirronello[45], M. Platino[8], M. Plum[39], A. Porcelli[36], C. Porowski[63], R.R. Prado[15], P. Privitera[89], M. Prouza[26], V. Purrello[1], E.J. Quel[2], S. Querchfeld[34], S. Quinn[77], J. Rautenberg[34], O. Ravel[33], D. Ravignani[8], B. Revenu[33], J. Ridky[26], S. Riggi[45], M. Risse[41], P. Ristori[2], V. Rizi[48], W. Rodrigues de Carvalho[75], G. Rodriguez Fernandez[44], J. Rodriguez Rojo[9], M.D. Rodríguez-Frías[73], D. Rogozin[36], J. Rosado[72], M. Roth[36], E. Roulet[1], A.C. Rovero[5], S.J. Saffi[12], A. Saftoiu[66], F. Salamida[28], H. Salazar[53], A. Saleh[71], F. Salesa Greus[88], G. Salina[44], F. Sánchez[8], P. Sanchez-Lucas[74], E. Santos[17], E.M. Santos[16], F. Sarazin[78],

B. Sarkar[34], R. Sarmento[65], R. Sato[9], C. Scarso[9], M. Schauer[34], V. Scherini[47], H. Schieler[36], P. Schiffer[40], D. Schmidt[36], O. Scholten[60][a], H. Schoorlemmer[90], P. Schovánek[26], F.G. Schröder[36], A. Schulz[36], J. Schulz[59], J. Schumacher[39], S.J. Sciutto[4], A. Segreto[50], M. Settimo[30], A. Shadkam[83], R.C. Shellard[13], I. Sidelnik[1], G. Sigl[40], O. Sima[68], A. Śmiałkowski[64], R. Šmída[36], G.R. Snow[91], P. Sommers[88], J. Sorokin[12], R. Squartini[9], Y.N. Srivastava[86], D. Stanca[66], S. Stanič[71], J. Stapleton[87], J. Stasielak[63], M. Stephan[39], A. Stutz[31], F. Suarez[8], T. Suomijärvi[28], A.D. Supanitsky[5], M.S. Sutherland[87], J. Swain[86], Z. Szadkowski[64], O.A. Taborda[1], A. Tapia[8], A. Tepe[41], V.M. Theodoro[17], C. Timmermans[61,59], C.J. Todero Peixoto[14], G. Toma[66], L. Tomankova[36], B. Tomé[65], A. Tonachini[46], G. Torralba Elipe[75], D. Torres Machado[22], P. Travnicek[26], R. Ulrich[36], M. Unger[85], M. Urban[39], J.F. Valdés Galicia[58], I. Valiño[75], L. Valore[43], G. van Aar[59], P. van Bodegom[12], A.M. van den Berg[60], S. van Velzen[59], A. van Vliet[40], E. Varela[53], B. Vargas Cárdenas[58], G. Varner[90], R. Vasquez[22], J.R. Vázquez[72], R.A. Vázquez[75], D. Veberič[36], V. Verzi[44], J. Vicha[26], M. Videla[8], L. Villaseñor[57], B. Vlcek[73], S. Vorobiov[71], H. Wahlberg[4], O. Wainberg[8,11], D. Walz[39], A.A. Watson[76], M. Weber[37], K. Weidenhaupt[39], A. Weindl[36], F. Werner[35], A. Widom[86], L. Wiencke[78], H. Wilczyński[63], T. Winchen[34], D. Wittkowski[34], B. Wundheiler[8], S. Wykes[59], L. Yang [71], T. Yapici[84], A. Yushkov[41], E. Zas[75], D. Zavrtanik[71,70], M. Zavrtanik[70,71], A. Zepeda[54], Y. Zhu[37], B. Zimmermann[37], M. Ziolkowski[41], F. Zuccarello[45]

[1] Centro Atómico Bariloche and Instituto Balseiro (CNEA-UNCuyo-CONICET), San Carlos de Bariloche, Argentina

[2] Centro de Investigaciones en Láseres y Aplicaciones, CITEDEF and CONICET, Argentina

[3] Departamento de Física, FCEyN, Universidad de Buenos Aires and CONICET, Argentina

[4] IFLP, Universidad Nacional de La Plata and CONICET, La Plata, Argentina

[5] Instituto de Astronomía y Física del Espacio (IAFE, CONICET-UBA), Buenos Aires, Argentina

[6] Instituto de Física de Rosario (IFIR) - CONICET/U.N.R. and Facultad de Ciencias Bioquímicas y Farmacéuticas U.N.R., Rosario, Argentina

[7] Instituto de Tecnologías en Detección y Astropartículas (CNEA, CONICET, UNSAM), and Universidad Tecnológica Nacional - Facultad Regional Mendoza (CONICET/CNEA), Mendoza, Argentina

[8] Instituto de Tecnologías en Detección y Astropartículas (CNEA, CONICET, UNSAM), Buenos Aires, Argentina

[9] Observatorio Pierre Auger, Malargüe, Argentina

[10] Observatorio Pierre Auger and Comisión Nacional de Energía Atómica, Malargüe, Argentina

[11] Universidad Tecnológica Nacional - Facultad Regional Buenos Aires, Buenos Aires, Argentina

[12] University of Adelaide, Adelaide, S.A., Australia

[13] Centro Brasileiro de Pesquisas Fisicas, Rio de Janeiro, RJ, Brazil

[14] Universidade de São Paulo, Escola de Engenharia de Lorena, Lorena, SP, Brazil

[15] Universidade de São Paulo, Instituto de Física de São Carlos, São Carlos, SP, Brazil

[16] Universidade de São Paulo, Instituto de Física, São Paulo, SP, Brazil

[17] Universidade Estadual de Campinas, IFGW, Campinas, SP, Brazil

[18] Universidade Estadual de Feira de Santana, Brazil

[19] Universidade Federal da Bahia, Salvador, BA, Brazil

[20] Universidade Federal de Pelotas, Pelotas, RS, Brazil

[21] Universidade Federal do ABC, Santo André, SP, Brazil

[22] Universidade Federal do Rio de Janeiro, Instituto de Física, Rio de Janeiro, RJ, Brazil

[23] Universidade Federal Fluminense, EEIMVR, Volta Redonda, RJ, Brazil

[24] Universidad Industrial de Santander, Bucaramanga, Colombia

[25] Charles University, Faculty of Mathematics and Physics, Institute of Particle and Nuclear

Physics, Prague, Czech Republic
[26] Institute of Physics of the Academy of Sciences of the Czech Republic, Prague, Czech Republic
[27] Palacky University, RCPTM, Olomouc, Czech Republic
[28] Institut de Physique Nucléaire d'Orsay (IPNO), Université Paris 11, CNRS-IN2P3, Orsay, France
[29] Laboratoire de l'Accélérateur Linéaire (LAL), Université Paris 11, CNRS-IN2P3, France
[30] Laboratoire de Physique Nucléaire et de Hautes Energies (LPNHE), Universités Paris 6 et Paris 7, CNRS-IN2P3, Paris, France
[31] Laboratoire de Physique Subatomique et de Cosmologie (LPSC), Université Grenoble-Alpes, CNRS/IN2P3, France
[32] Station de Radioastronomie de Nançay, Observatoire de Paris, CNRS/INSU, France
[33] SUBATECH, École des Mines de Nantes, CNRS-IN2P3, Université de Nantes, France
[34] Bergische Universität Wuppertal, Wuppertal, Germany
[35] Karlsruhe Institute of Technology - Campus South - Institut für Experimentelle Kernphysik (IEKP), Karlsruhe, Germany
[36] Karlsruhe Institute of Technology - Campus North - Institut für Kernphysik, Karlsruhe, Germany
[37] Karlsruhe Institute of Technology - Campus North - Institut für Prozessdatenverarbeitung und Elektronik, Karlsruhe, Germany
[38] Max-Planck-Institut für Radioastronomie, Bonn, Germany
[39] RWTH Aachen University, III. Physikalisches Institut A, Aachen, Germany
[40] Universität Hamburg, Hamburg, Germany
[41] Universität Siegen, Siegen, Germany
[42] Università di Milano and Sezione INFN, Milan, Italy
[43] Università di Napoli "Federico II" and Sezione INFN, Napoli, Italy
[44] Università di Roma II "Tor Vergata" and Sezione INFN, Roma, Italy
[45] Università di Catania and Sezione INFN, Catania, Italy
[46] Università di Torino and Sezione INFN, Torino, Italy
[47] Dipartimento di Matematica e Fisica "E. De Giorgi" dell'Università del Salento and Sezione INFN, Lecce, Italy
[48] Dipartimento di Scienze Fisiche e Chimiche dell'Università dell'Aquila and INFN, Italy
[49] Gran Sasso Science Institute (INFN), L'Aquila, Italy
[50] Istituto di Astrofisica Spaziale e Fisica Cosmica di Palermo (INAF), Palermo, Italy
[51] INFN, Laboratori Nazionali del Gran Sasso, Assergi (L'Aquila), Italy
[52] Osservatorio Astrofisico di Torino (INAF), Università di Torino and Sezione INFN, Torino, Italy
[53] Benemérita Universidad Autónoma de Puebla, Puebla, México
[54] Centro de Investigación y de Estudios Avanzados del IPN (CINVESTAV), México, México
[55] Unidad Profesional Interdisciplinaria en Ingeniería y Tecnologías Avanzadas del Instituto Politécnico Nacional (UPIITA-IPN), México, D.F., México
[56] Universidad Autónoma de Chiapas, Tuxtla Gutiérrez, Chiapas, México
[57] Universidad Michoacana de San Nicolás de Hidalgo, Morelia, Michoacán, México
[58] Universidad Nacional Autónoma de México, México, D.F., México
[59] IMAPP, Radboud University Nijmegen, Netherlands
[60] KVI - Center for Advanced Radiation Technology, University of Groningen, Netherlands
[61] Nikhef, Science Park, Amsterdam, Netherlands
[62] ASTRON, Dwingeloo, Netherlands

[63] Institute of Nuclear Physics PAN, Krakow, Poland
[64] University of Łódź, Łódź, Poland
[65] Laboratório de Instrumentação e Física Experimental de Partículas - LIP and Instituto Superior Técnico - IST, Universidade de Lisboa - UL, Portugal
[66] 'Horia Hulubei' National Institute for Physics and Nuclear Engineering, Bucharest- Magurele, Romania
[67] Institute of Space Sciences, Bucharest, Romania
[68] University of Bucharest, Physics Department, Romania
[69] University Politehnica of Bucharest, Romania
[70] Experimental Particle Physics Department, J. Stefan Institute, Ljubljana, Slovenia
[71] Laboratory for Astroparticle Physics, University of Nova Gorica, Slovenia
[72] Universidad Complutense de Madrid, Madrid, Spain
[73] Universidad de Alcalá, Alcalá de Henares, Madrid, Spain
[74] Universidad de Granada and C.A.F.P.E., Granada, Spain
[75] Universidad de Santiago de Compostela, Spain
[76] School of Physics and Astronomy, University of Leeds, United Kingdom
[77] Case Western Reserve University, Cleveland, OH, USA
[78] Colorado School of Mines, Golden, CO, USA
[79] Colorado State University, Fort Collins, CO, USA
[80] Colorado State University, Pueblo, CO, USA
[81] Department of Physics and Astronomy, Lehman College, City University of New York, NY, USA
[82] Fermilab, Batavia, IL, USA
[83] Louisiana State University, Baton Rouge, LA, USA
[84] Michigan Technological University, Houghton, MI, USA
[85] New York University, New York, NY, USA
[86] Northeastern University, Boston, MA, USA
[87] Ohio State University, Columbus, OH, USA
[88] Pennsylvania State University, University Park, PA, USA
[89] University of Chicago, Enrico Fermi Institute, Chicago, IL, USA
[90] University of Hawaii, Honolulu, HI, USA
[91] University of Nebraska, Lincoln, NE, USA
[92] University of New Mexico, Albuquerque, NM, USA

(‡) Deceased
(a) Also at Vrije Universiteit Brussels, Belgium

High Voltage System for the Generation of High Energy X-rays: synchronization and improvement

Libero Palladino*,[a,b], Maurizio Di Paolo Emilio[a,b]

[a] Department of MeSVA, L'Aquila University
[b] INFN, Laboratorio Nazionale del Gran Sasso, Assergi (AQ)
* Scientific responsible

Abstract

The x-ray (3 keV - 25 keV) are produced by high voltage discharge applied inside plasma source interaction chamber by focusing a laser beam. The control system is based on a high voltage power supply and an LC-inverter circuit with Thyratron for the generation of the trigger signal increasing the efficiency of the system. In this report analysis of the system, layout of synchronization with YAG laser and a possible study for a new layout with solid-state element are presented and discussed.

1 Introduction

Different applications of soft X-rays (70 eV - 2 keV) and hard x-rays (3 keV - 25 keV) in biological, radiobiological and in medical imaging field, have encouraged the development of X ray sources based on the production of plasma. Plasmas produced by focusing pulsed laser beams on solid targets are currently recognized as one of the most promising alternative to conventional (X-ray tubes) and to synchrotron X-ray sources [1] [2]. Optimization of pulsed x-rays sources it is necessary to make x-rays source comparable with the most advanced current x-ray tubes (i.e. microfocus) for applications in the field of mammography and non-destructive inspection. The high energy x-ray (3 keV - 25 keV) are emitted by plasma on target driven by a control system that manages High Voltage power supply, an LC Inverter discharge and laser beam generation. Actually, in the LC-Inverter circuit the discharge is controlled by a spark gap and a trigger generator composed of Thyratron and a trigger high voltage power supply. Thyratrons are obsolete as fewer and fewer vendors are selling them in response to decreased demand. An alternate solid-state device, the insulated-gate bipolar transistor (IGBT), can readily operate at the speed needed to increase the efficiency of the system.

2 High Voltage System for high energy X-rays emission

The x-rays of the higher energy region (about 25 keV) is produced for bremmsthralung effect. The relative configuration of the interaction chamber is shown in figure 1 and 2. The main feature is to apply the High voltage (30 - 50 kV) from the target, on which the laser is focalized,

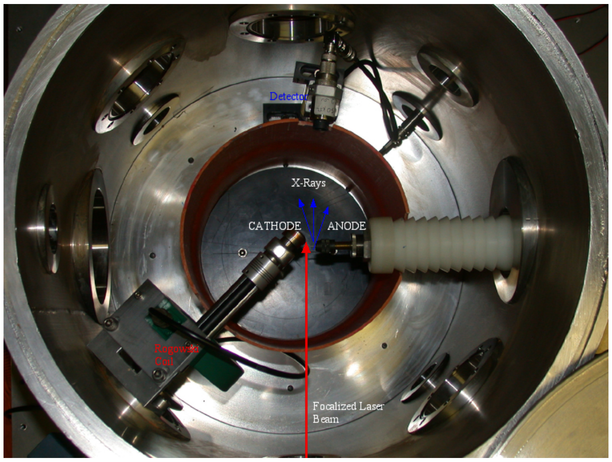

Figure 1: Interaction chamber (inside)

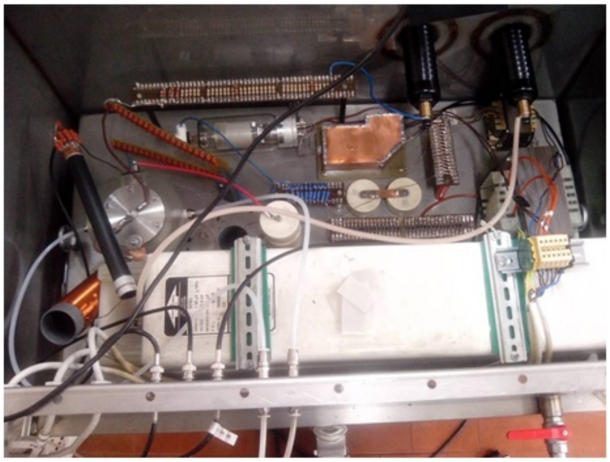

Figure 2: High Voltage system

(cathode) to the anode (such as metallic materials Mo or W) where x-rays are produced [3] [4]. The mechanism of x-rays production is based on the generation of a plasma obtained by focusing a laser beam NdYag (5J per pulse, duration 6 ns, 0.3 mrad divergence, 536 nm wavelength) on a target metal. The trigger high voltage power supply was designed with transformer and diodes rectifiers for obtaining DC voltage to send in the spark gap. This configuration was resulted electrically unstable due to the electromagnetic noise and return high voltage. For these reasons, a commercial High Voltage Power Supply must be used for the future implentations. The reason to obtain a high voltage through a LC inverter (Figure 3) is because of the system is working with high voltage in the discharge phase, but during the charge of the capacitors the system is isolated which is essential for the safety and average life of the electrical components. Thyratrons are obsolete, disadvantages can be the increase in delay time and jitter when the tube ages. These contribute significantly to the overall phase noise of the system. A new system (Figure 4) with IGBT to can reduce the complexity and improve the stability and synchronization [5].

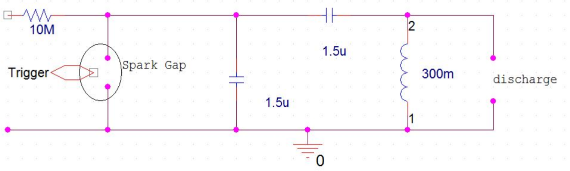

Figure 3: LC Inverter

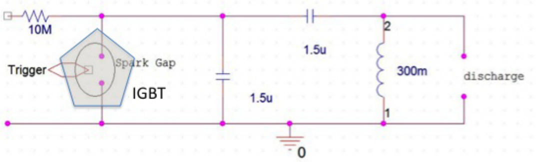

Figure 4: General New Layout of LC Inverter

3 Material and Preliminary results

A trigger circuit supplied the LC inverter with High Voltage power supply and is sent to the Spark Gap using a Thyratron, which is used as high electrical power switch. To increase the stability of the system, IGBT can be replaced to the Thyratron in according to the new design for combining high efficiency and fast switching.

The results of p-spice model in [6], let us to test the system using a High Voltage Power Supply at 15 kV. X- rays measured by photodetector (PD) with an aluminum foils of 15.8 m thickness (figure 5). The synchronization of the system (Figure 6) is made considering that the x-ray signal is started 13 us after the trigger signal. As indicated in figure 7 the total delay to set in the pulse generator should be around 600 us.

Actually, the time difference is around 2 us. The synchronization of laser beam and discharge using Pulse Generator of Quantum Components is very useful to synchronize all signals (figure 8 and 9).

4 Conclusions

In the range of x-ray energy of 3 keV - 25 keV, we have studied a possible model to evaluate the electrical characteristics of the high voltage system to optimize the emission of x-rays. A possible future configuration will be to use an IGBT (Insulated Gate Bipolar Transistor) instead of Thyratron to compact the system and increase the energy. In near future we will improve the synchronization of the system between trigger discharge with pulse laser beam. Moreover, we will examine x-rays emission by changing the distance from anode and cathode and power density of the laser. The synchronization can be improvement using a photodetector for detecting the light of discharge and synchronazing with laser beam and x-ray emission.

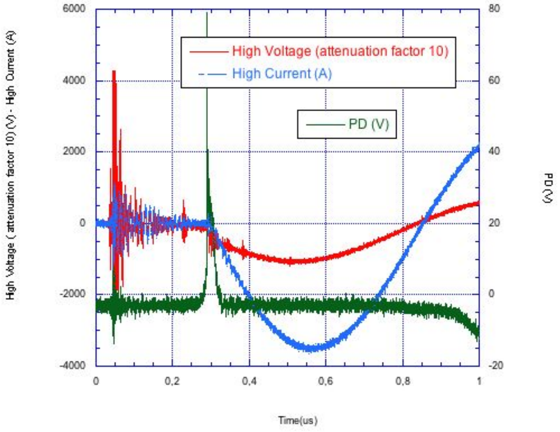

Figure 5: Experimental Signals in vacuum of 10^{-3} mbar with 15kV of Power supply: In blue line, High Current Signal, in red line the High Voltage with attenuation factor of 10 and in green line, the x-ray emission.

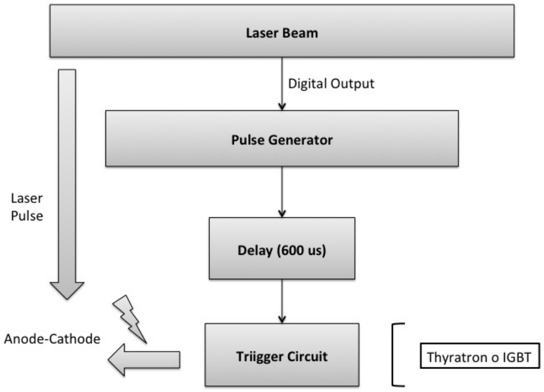

Figure 6: Synchronization Layout.

5 Acknowledgement

We would like to take this opportunity to thank Prof. S. Ragazzi, Director of Gran Sasso National Laboratories of INFN for scientific and financial support. Moreover, thank to Prof. M.G. Cifone director of MesVA Department of LAquila University for supporting us. This work is financially supported by INFN, PLAXA experiment.

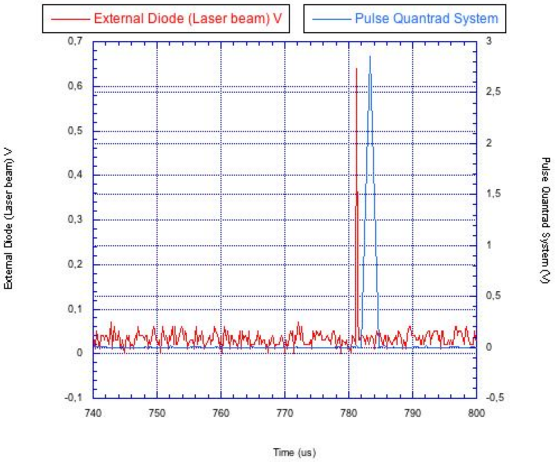

Figure 7: Preeliminary set-up of the synchronization: in red line, external diode to measure the laser beam (plasma source), in blue linee the trigger sent to the Thyratron.

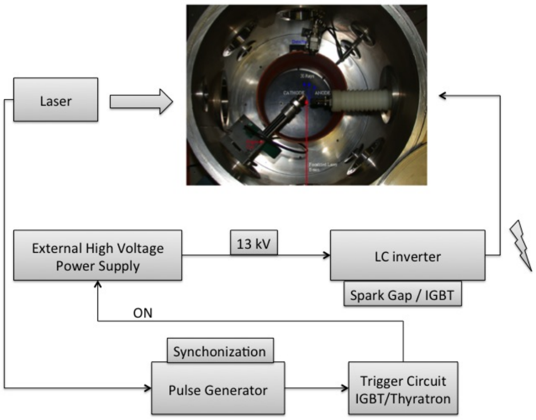

Figure 8: New complete layout.

Figure 9: Pulse Geenratore Quatum 9520.

References

[1] Gerardi S. (2009) **Ionizing radiation microbeam facilities for radiobiological studies in Europe**, *Journal of Radiation Research*, 50, A13- A 20.

[2] **Data sheet of commercial X-ray Tube** , *http://www.varian.com/media/xray/products/pdf/m105sp.pdf Varian Medical System*

[3] L. Palladino et all (2013), **X-ray emission analysis of a plasma source using an yttrium and a mylar target for the generation of 2.48 nm wavelength microbeam**, *Applied Surface Science, 272, 119-123*

[4] Habetler, T.G. et all, **Design and implementation of an inverter output LC filter used for dv/dt reduction**, *Power Electronics, IEEE Transactions on (Volume:17 , Issue: 3).*

[5] S.L. Gold, Thyratron-PFN, **IGBT Hybrid, and Direct Switched Modulator** *RD* **as it Effects** , *Klystron Protection SLAC-PUB-8475 June 2000*

[6] M. Di Paolo Emilio and L. Palladino , **High energy X-ray emission driven by high voltage circuit system**, *2014 J. Phys.: Conf. Ser. 508 012011*

6 Publication

M. Di Paolo Emilio and L. Palladino
High Voltage System for the Generation of High Energy X-rays: synchronization and improvement.
J. Physics: Conference Series Vol 508, 2014